Nitrogen Oxide Delivery Systems for Biological Media

by

Brian Thomas Skinn

B.S. Chemical Engineering (2004)
Case Western Reserve University

Submitted to the Department of Chemical Engineering
In Partial Fulfillment of the Requirements of the Degree of
DOCTOR OF PHILOSOPHY IN CHEMICAL ENGINEERING
at the
MASSACHUSETTS INSTITUTE OF TECHNOLOGY
February 2012

© Massachusetts Institute of Technology 2012
All Rights Reserved

Signature of Author .....
Department of Chemical Engineering
December 2, 2011

Certified by .....
William M. Deen
Carbon P. Dubbs Professor of Chemical Engineering
Thesis Supervisor

Accepted by .....
William M. Deen
Carbon P. Dubbs Professor of Chemical Engineering
Chairman, Committee for Graduate Students

Nitrogen Oxide Delivery Systems for Biological Media

by

Brian Thomas Skinn

Submitted to the Department of Chemical Engineering on December 2, 2011
in partial fulfillment of the requirements for the Degree of
Doctor of Philosophy in Chemical Engineering

ABSTRACT

Elevated levels of nitric oxide (NO) *in vivo* are associated with a variety of cellular modifications thought to be mutagenic or carcinogenic. These processes are likely mediated by reactive nitrogen species (RNS) such as nitrogen dioxide (NO_2) and peroxynitrite formed from the respective reactions of NO with oxygen and superoxide anion. Controlled delivery of these RNS at levels expected to occur *in vivo* is desirable in studying these processes and their role in the etiology of various diseases. Two delivery systems were developed that provide novel capabilities for steady, quantitative exposure of biological targets to RNS over periods from hours to days. Quantitative models are presented that accurately describe the behavior of both systems. The first system achieves NO concentrations of 0.6-3.0 μM in a stirred, liquid-filled vessel by diffusion from a gas stream through a porous poly(tetrafluoroethylene) membrane. Oxygen, consumed by reaction with NO or by other processes, is supplied by diffusion from a separate gas stream through a loop of poly(dimethylsiloxane) tubing. The adventitious chemistry observed in a prior device for NO delivery [Wang C. *Ann Biomed Eng* (2003) **31**:65-79] is eliminated in the present design, as evidenced by the close match to model predictions of the accumulation rate of nitrite, the stable end product of NO oxidation. The second system delivers NO_2 by direct contacting of a stirred liquid with an NO_2-containing gas mixture. Accumulation rates of products in the presence and absence of the NO_2-reactive substrate 2,2′-azino-bis(3-ethylbenzothiazoline-6-sulfonate) matched model predictions within 15% for all conditions studied. The predicted steady NO_2 concentration in the liquid is on the order of 400 pM, similar to what is expected to be present in extracellular fluids in the presence of 1 μM NO. This system appears to be the first reported with the capability for sustained, quantitative NO_2 delivery to suspended cell cultures. Results from initial efforts to test a novel mixing model for bolus delivery of peroxynitrite to agitated solutions imply that the proposed model might accurately describe mixing in bolus delivery experiments with agitation by vortex mixing, but further work is required to validate the model.

Thesis Supervisor: William M. Deen

Title: Professor of Chemical Engineering

Acknowledgements

This thesis would not have been possible without the assistance and encouragement of a number of people. Foremost among these is my advisor, Prof. William Deen, who has been an inexhaustible and invaluable source of guidance and input as I wrestled with the chemistry of nitrogen oxides. I am especially grateful for his assistance in improving the concision, precision, and clarity of my technical communication. I am also indebted to the members of my thesis committee, Professors Klavs F. Jensen (Chemical Engineering) and Steven R. Tannenbaum (Biological Engineering), whose comments, suggestions, and criticisms were invaluable in guiding my research.

Thanks also to the members of Deen group, including Kristin Mattern, Gaurav Bhalla, Chang Hoon Lim, and Melanie Chin, both for engaging and helpful technical discussions and for making the lab environment fun and easygoing. I greatly appreciate the experimental assistance provided by UROPs George Pratt and Deborah Markham. Debbie's patience and unflappable good cheer in the face of a long series of generally unsuccessful experiments were truly exemplary. I am also grateful for the technical assistance rendered by Mark Belanger (Edgerton student machine shop, MIT) in my efforts to fabricate the custom NO reactor components. I am indebted to Laura Trudel, Pete Wishnok, Yu Zeng, Vicki Dydek and Nick Zaborenko for their assistance with lines of experimental inquiry that were, in the end, unfruitful.

The social environment of the department was thoroughly enjoyable. Props go to Arman Haidari, Wyatt Tenhaeff and Michael Zahniser for enduring my idiosyncrasies during the Upland years. I also am grateful to Kristin, Jason, Sanjoy, Nick, Heather, and company for introducing me to the finer details of the sugar, coffee, and corn markets, and to Dave Adrian and Micah Green for the in-depth tours of the fast-paced and frequently explosive world of sprockets.

I would be remiss if I failed to acknowledge the innumerable ways in which my parents have assisted me throughout the years. They have provided much appreciated assistance in matters large and small throughout all of my (many!) years of education.

Finally, this thesis would not have been possible without the constant encouragement and unfailing support of my wife Lisa. She is always ready to celebrate any success, large or small, and was always there with a word of encouragement in those long days of, "Well, the data is good, but I have no idea what it means." I look forward to sharing with her all that awaits us in the years to come.

Table of Contents

Chapter 1 Introduction and Background 17

1.1 Nitric oxide in biology 17

1.2 Biological chemistry of nitrogen oxides 20

1.3 Delivery of nitrogen oxides 24

1.3.1 Reported methods 24

1.3.2 Overview and evaluation 29

1.4 Research objectives 33

Chapter 2 Nitric Oxide Delivery System for Biological Media 35

2.1 Introduction 35

2.2 Materials and methods 38

2.2.1 Chemicals 38

2.2.2 Gas delivery system 38

2.2.3 Apparatus 39

2.2.4 Concentration measurements 41

2.2.5 NO oxidation kinetics 41

2.2.5.1 Substrate-free media 41

2.2.5.2 NO oxidation of morpholine 42

2.2.6 Reactor model 43

2.2.6.1 Macroscopic model 43

2.2.6.2 Derivation of the correction factors χ_j and γ 44

2.2.7 Evaluation of mass transfer coefficients 47

2.2.7.1 Mass transfer coefficients for O_2 47

2.2.7.2 Mass transfer coefficients for NO 48

2.2.8 Tests using nitrite and NMor accumulation 49

2.2.9 Simultaneous delivery of NO and O_2 51

2.3 Results 52

2.3.1 Mass transfer coefficients 52

2.3.2 Tests using nitrite and NMor accumulation 52

2.3.3 Simultaneous delivery of NO and O_2 60

2.4 Discussion 64
2.4.1 Elimination of adventitious NO oxidation 64
2.4.2 Model performance 68
2.4.3 Estimation of parameter values at body temperature 70
2.4.4 Application of the delivery system 71
2.5 Conclusion 73
Chapter 3 Nitrogen Dioxide Delivery System for Biological Media 77
3.1 Introduction 77
3.2 Materials and methods 84
3.2.1 Chemicals 84
3.2.2 Gas delivery system 84
3.2.3 Apparatus 85
3.2.4 Concentration measurements 87
3.2.5 Reactor model 89
3.2.5.1 H_2O gas-phase mass transfer coefficient 92
3.2.5.2 O_2 liquid-phase mass transfer coefficient 93
3.2.5.3 Macroscopic model for NO_2/N_2O_4 delivery 95
3.2.5.4 Microscopic model for NO_2/N_2O_4 delivery 96
3.2.5.5 Non-dimensional NO_2/N_2O_4 model 102
3.2.5.6 Parameter corrections at body temperature 105
3.2.6 Measurement of mass transfer coefficients 106
3.2.7 Reactor characterization using product accumulation rates 106
3.3 Results 107
3.3.1 Mass transfer coefficients 107
3.3.2 Tests using product accumulation rates 110
3.3.3 Simulated accumulation rates 117
3.4 Discussion 117
3.4.1 Application to cell experiments 122
3.4.1.1 RN concentrations at body temperature 122
3.4.1.2 Effect of NO_2-reactive substrates in culture medium 123
3.4.1.3 Maintenance of reactor O_2 and H_2O levels 128

3.4.2 Supplemental analysis of data and macroscopic model 130
3.4.2.1 Nitric acid impurity 130
3.4.2.2 Power-law dependence of nitrite accumulation rate on f_N 133
3.4.2.3 Liquid-phase relaxation time scale for RN 135
3.4.2.4 Uncertainty in the gas-phase mass transfer coefficient 139
3.4.3 Supplemental analysis of microscopic model 140
3.4.3.1 Computation of lag times 140
3.4.3.2 Model sensitivity study 143
3.4.3.3 Microscopic model concentration profiles 149
3.4.3.4 Model dependence on film thickness 157
3.4.4 Delivery of NO_2 via PDMS and porous PTFE 164
3.5 Conclusion 166
Chapter 4 Bolus Delivery of Peroxynitrite to Biological Media 169
4.1 Introduction 169
4.1.1 Peroxynitrite biology and chemistry 169
4.1.2 Peroxynitrite delivery 171
4.1.3 Modeling of mixing in agitated vessels 172
4.1.4 Chemical systems as probes for mixing time scales 174
4.1.5 Present work 176
4.2 Materials and methods 177
4.2.1 Chemicals 178
4.2.2 Reaction mechanisms 178
4.2.2.1 Peroxynitrite decomposition and thiol reaction 178
4.2.2.2 Diazenyl dye formation from 1-naphthol and diazotized sulfanilic acid 182
4.2.2.3 Copper(II) salt precipitation and alkaline hydrolysis of ethyl chloroacetate 184
4.2.3 Concentration measurements 186
4.2.4 Peroxynitrite synthesis 189
4.2.5 Bolus delivery model 192
4.2.6 Bolus delivery experiments 198

4.2.6.1 Preparation of reactant solutions 198
4.2.6.2 Delivery experiments 199
4.3 Results and Discussion 201
4.3.1 Peroxynitrite synthesis 201
4.3.2 Preliminary tests of the chemical systems 202
4.3.3 Reproducibility of bolus delivery 203
4.3.4 Evaluation of bolus mixing model for orbital mixer agitation 206
4.3.5 Evaluation of bolus mixing model for vortexer agitation 211
4.4 Conclusion 214
Appendix A Experimental Data from Nitric Oxide Delivery System 217
Appendix B Experimental Data from Nitrogen Dioxide Delivery System 243
Appendix C Thermodynamic Constraints for Aqueous N_2O_3 and N_2O_4 Solubilities 271
Appendix D Base Well and Membrane Scaling Arguments for Delivery of NO 275
Appendix E Gas-Phase Scaling Arguments for Delivery of NO_2 299
Appendix F Fabrication and Assembly Instructions and Parts List for NO Delivery Apparatus 315
Appendix G Parts List and Assembly Instructions for NO_2 Delivery Apparatus 341
Bibliography 345

List of Figures

Figure 1.1. Schematic of some key physiologically-relevant reactions of the nitrogen oxides. 22
Figure 1.2. Schematic of 'coexistence regions' for delivery of various RNS. 26
Figure 2.1. Schematic of NO delivery system 40
Figure 2.2. Measured O_2 concentration in representative O_2 depletion experiments. 53
Figure 2.3. Measured NO and O_2 concentrations during delivery of 10% NO to oxygenated buffer without O_2 replenishment. 55
Figure 2.4. Nitrite concentration during delivery of 10% NO to oxygenated buffer without O_2 replenishment in the absence of morpholine. 57
Figure 2.5. Nitrite and N-nitrosomorpholine concentrations in delivery of 10% NO to oxygenated buffer without O_2 replenishment in the presence of morpholine. 59
Figure 2.6. Measured O_2 and NO concentrations during simultaneous delivery of 20% O_2 and 1% NO to oxygenated buffer. 61
Figure 2.7. Measured and predicted NO concentrations during simultaneous delivery of O_2 and NO at three steady-state O_2 partial pressures in the liquid ($\overline{P}_{O_2}$). 62
Figure 2.8. Composition of NO gas and PDMS tubing length required to give a desired steady value of $\overline{C}_{NO}$ 72
Figure 3.1. Molecular structure of ABTS species. 81
Figure 3.2. Schematic of NO_2 reactor. 86
Figure 3.3. Measured O_2 concentration during representative O_2 depletion-repletion experiment. 109
Figure 3.4. Nitrite, nitrate and ABTS radical concentrations during a representative 0.01% NO_2 delivery experiment to buffer initially with 107 μM ABTS. 111
Figure 3.5. Measured nitrite accumulation rate during delivery of various NO_2-containing gas mixtures to buffer in the absence of ABTS. 114
Figure 3.6. Measured nitrite and nitrate accumulation rates during delivery of various NO_2-containing gas mixtures to buffer in the absence of ABTS. 116

Figure 3.7. Measured and predicted nitrite accumulation rates during delivery of various NO_2-containing gas mixtures to buffer in the absence of ABTS. 118
Figure 3.8. Measured and predicted nitrite and $ABTS^+$ accumulation rates during delivery of 0.001% and 0.01% NO_2 to buffer in the presence of ABTS. 119
Figure 3.9. Predicted bulk and well-mixed region NO_2 concentrations at ambient and body temperature, as a function of the % NO_2 in the feed gas. 124
Figure 3.10. Predicted lag time as a function of the initial concentration of various NO_2-reactive substrates. 126
Figure 3.11. Predicted bulk volumetric ABTS consumption rate as a function of bulk ABTS concentration. 142
Figure 3.12. Sensitivity study: percent change from reference case in simulated nitrite accumulation rate in the absence of ABTS. 146
Figure 3.13. Sensitivity study: percent change from reference case in simulated product accumulation rates in the presence of ABTS (0.001% NO_2). 147
Figure 3.14. Sensitivity study: percent change from reference case in simulated product accumulation rates in the presence of ABTS (0.01% NO_2). 148
Figure 3.15. Percent deviation of model predictions from nitrite accumulation rate data in the absence of ABTS. 150
Figure 3.16. Percent deviation of model predictions from product accumulation rate data in the presence of ABTS. 151
Figure 3.17. Concentration scale for RN as a function of the NO_2 gas mixture. 153
Figure 3.18. Simulated non-dimensional RN concentration and NO_2 fraction profiles. 154
Figure 3.19. Simulated non-dimensional NO_2 and N_2O_4 concentration profiles. 156
Figure 3.20. Simulated non-dimensional RN concentration profiles neglecting gas-phase phenomena. 158
Figure 3.21. Dependence of simulated bulk and well-mixed RN concentrations on stagnant film thickness. 160
Figure 3.22. Dependence of simulated non-dimensional RN concentration profile on stagnant film thickness. 161
Figure 3.23. Simulated non-dimensional NO_2 and ABTS concentration profiles. 163
Figure 4.1. Molecular structures of species in the diazenyl dye reaction system. 183

Figure 4.2. Schematic of peroxynitrite synthesis apparatus. 191
Figure 4.3. Schematic representation of proposed reactive mixing model. 193
Figure 4.4. Consumption of cysteine in bolus delivery of alkaline peroxynitrite during agitation by orbital mixing. 204
Figure 4.5. Diazenyl dye formation from addition of diazo-SAA to 1-NA during agitation by orbital mixing. 205
Figure 4.6. Comparison of best-fit mixing times in Cys/Per and diazenyl dye systems with orbital mixing agitation. 208
Figure 4.7. Comparison between observed and predicted diazenyl dye concentrations with orbital mixing agitation. 209
Figure 4.8. Comparison of thiol consumption in delivery of peroxynitrite with orbital mixing agitation. 210
Figure 4.9. Best-fit mixing times for bolus delivery with vortexing agitation. 213
Figure 4.10. Comparison between observed and predicted diazenyl dye concentrations with vortexing agitation. 215
Figure A.1. O_2 depletion experiments for PTFE base membrane. 221
Figure A.2. O_2 depletion experiments for PDMS tubing. 224
Figure A.3. Measured NO, O_2 and NO_2^- concentrations in delivery of 10% NO in the absence of Mor without O_2 replenishment. 232
Figure A.4. Measured NO, O_2, NO_2^-, and NMor concentrations in delivery of 10% NO in the presence of 2 mM Mor without O_2 replenishment. 236
Figure A.5. Measured NO and O_2 concentrations in simultaneous delivery of NO and O_2 in the absence of Mor. 242
Figure B.1. O_2 depletion-repletion experiments. 247
Figure B.2. H_2O evaporation during flow of N_2 through reactor headspace. 249
Figure B.3. Delivery of 1% NO_2 by direct gas-liquid contacting in the absence of ABTS (Q = 250 sccm). 252
Figure B.4. Delivery of 1% NO_2 by direct gas-liquid contacting in the absence of ABTS (Q = 365 sccm). 254
Figure B.5. Delivery of 0.1% NO_2 by direct gas-liquid contacting in the absence of ABTS. 255

Figure B.6. Delivery of 0.01% NO_2 by direct gas-liquid contacting in the absence of ABTS. 256
Figure B.7. Delivery of 0.001% NO_2 by direct gas-liquid contacting in the absence of ABTS. 258
Figure B.8. Delivery of 0.01% NO_2 by direct gas-liquid contacting in the presence of ABTS. 260
Figure B.9. Delivery of 0.001% NO_2 by direct gas-liquid contacting in the presence of ABTS. 262
Figure B.10. Delivery of NO_2 by diffusion through PDMS tubing in the absence of ABTS. 265
Figure B.11. Delivery of NO_2 by diffusion through PDMS tubing in the presence of ABTS. 267
Figure B.12. Delivery of NO_2 by diffusion through a porous PTFE membrane in the absence of ABTS. 269
Figure D.1. Predicted reaction correction factor (γ) as a function of NO_2 abundance. . 278
Figure F.1. Images of laminated membrane fabrication procedure. 318
Figure F.2. Schematic for reactor base insert. 321
Figure F.3. Schematic for reactor cap. 327
Figure F.4. Fitting assembly schematic for the custom soda lime column. 336
Figure F.5. Photograph of the assembled soda lime column. 337
Figure F.6. Photograph of the assembled NO reactor. 340
Figure G.1. Schematic of NO_2 reactor with small parts detail 342
Figure G.2. Photograph of assembled NO_2 reactor 344

List of Tables

Table 1.1. Summary of species, targets and modes in RNS delivery. 30
Table 2.1. Physicochemical parameters 50
Table 2.2. Mass transfer coefficients for O_2 and NO at the base membrane and tubing in the absence of reactions 54
Table 2.3. Simulated and observed NO and O_2 concentrations and NO rise times for simultaneous NO and O_2 delivery at various O_2 concentrations 65
Table 2.4. Extrapolation of room-temperature parameter values to body temperature ... 69
Table 3.1. Physicochemical parameters and reactor specifications. 101
Table 3.2. Product accumulation rates in headspace delivery of NO_2. 112
Table 3.3. Diffusivities, NO_2 reaction rate constants, and lag-phase endpoint concentrations for lag time calculations 127
Table 3.4. Data used for estimation of feed gas nitric acid impurity and for correction of simulated nitrate accumulation rates in the presence of ABTS. 132
Table 3.5. Comparison of predicted relaxation times and experimental sampling times for NO_2 delivery in the absence of ABTS. 138
Table 3.6. Codes and descriptions for model sensitivity study 144
Table 4.1. Rate constants for chemical mechanisms used to test the delivery model. .. 185
Table 4.2. Extinction coefficients for the diazenyl dye products of the 1-NA/diazo-SAA chemical system 188
Table 4.3. Differential equations and algebraic constraints used in model simulations 196
Table 4.4. Reaction time scales for the test chemical systems. 200
Table D.1. Mass transfer resistances and overall mass transfer coefficients for base well and membrane boundary layers. 287
Table D.2. Quantities used to estimate the gas-phase NO_2 concentration scale. 290
Table D.3. Estimation of the significance of NO oxidation on gas-phase boundary layer and porous membrane transport. 293
Table E.1. Gas-phase rate and equilibrium constants for NO_2/N_2O_4 mechanism. 304
Table E.2. Gas-phase chemistry scaling estimates for Q = 365 sccm. 313
Table G.1. Parts information for NO_2 reactor components. 343

Chapter 1

Introduction and Background

1.1 Nitric oxide in biology

The concurrent identification by Ignarro et al. (1987) and Palmer et al. (1987) of endothelium-derived relaxing factor as the moderately stable radical nitric oxide (NO) initiated extensive, prolonged study of what has been revealed to be its highly complex chemistry, biochemistry, and signaling physiology. A search of the Web of Science database (Thomson Reuters, New York, NY) indicates that for the period 1899-1986, an estimated 28 articles per year were published that return hits for the topic keyword "nitric oxide." For the period spanning 1987 through September of 2011, the average is over 7500 articles per year, corresponding to a frequency of approximately 1 in 180 of all publications indexed. Not all of these articles pertain to the physiological role of NO, but it is remarkable that such a large fraction of the scholarly work published in the last two and a half decades has been dedicated in some fashion to the study of this small molecule.

Nitric oxide is generated within the body by the action of the nitric oxide synthases (NOS) on L-arginine, with concomitant consumption of NADPH and O_2 and generation of L-citrulline (Stuehr, 1999). Specifically, NO is synthesized from the terminal guanido nitrogen atom(s) of L-arginine (Moncada et al., 1989). The enzyme activity is stereospecific for L-Arg. Three NOS isoforms are known: neuronal (nNOS; Bredt et al., 1991a; Bredt et al., 1991b), inducible (iNOS; Xie et al., 1992), and endothelial (eNOS; Lamas et al., 1992). The nNOS and eNOS isoforms are named for

the cell types from which they were first isolated and are generally considered to be constitutively expressed, though mechanisms to modulate their expression have been identified (Forstermann et al., 1998; Rafikov et al., 2011). Inducible NOS is so named because it is typically expressed only under conditions of immune or inflammatory stimulation (Geller and Billiar, 1998). Work in solving the NOS protein structures has revealed that all three isoforms are homodimers, where each monomer comprises separate reductase and oxygenase domains connected by a calmodulin-binding region. The activity of both nNOS and eNOS is regulated by Ca^{2+} via reversible calmodulin binding, whereas iNOS binds calmodulin at all physiological Ca^{2+} concentrations and thus is not subject to Ca^{2+}-dependent regulation (Daff, 2010).

The earliest investigations of the biological role of NO pertained to its vasodilatory effects (Ignarro et al., 1999) and its interactions with guanylate cyclase and other heme proteins (Henry and Guissani, 1999). However, the regulatory activity of NO is quite diverse: a few of its targets include the pancreas (Spinas, 1999), the kidneys (Kone and Baylis, 1997), the intestines (Alican and Kubes, 1996), the urinary tract (Mumtaz et al., 1999), and the central nervous system (Szabo, 1996). Elucidation of NO-dependent functions continues at a rapid pace, in some cases describing refinements of previously known interactions [e.g., in myocardial function (Ziolo et al., 2008) and steroidogenesis (Ducsay and Myers, 2011)] and in others bringing to light novel functions or behaviors of NO and NOS. Examples include modulation of the expression levels of the "constitutive" eNOS isoform (Rafikov et al., 2011) and the existence of a regulatory role of iNOS in healthy neural function (Amitai, 2010).

Properly controlled generation of NO is necessary for a healthy organism, as evidenced by the pathologies observed in the mice bred by Tsutsui et al. (2006) with homozygous knockouts for all three NOS isoforms. These mice exhibited polyuria, polydipsia, renal insensitivity to vasopressin, arteriosclerosis, and overall reduction in viability and fertility. Misregulation of NO signaling is thought to be a factor in a number of disease states; improper signaling is implicated in hypertensive and/or circulatory complications in sickle cell disease (Akinsheye and Klings, 2010) and diabetes mellitus (Masha et al., 2011), as well as in mediation of demyelination in multiple sclerosis (Parkinson et al., 1997). Excessive production of NO is also problematic, independent of its signaling implications, as it can lead to NO concentrations sufficiently high to create mutagenic or carcinogenic levels of reactive nitrogen species (RNS) (Burney et al., 1997; Tamir et al., 1996). Indeed, the correlation between chronic inflammation, entailing significant, prolonged iNOS upregulation and NO production, and development of various cancers is well established (Tamir and Tannenbaum, 1996). The situation is complicated further once a tumor has formed: there is evidence that significantly elevated local NO concentrations are tumoricidal (and thus beneficial), whereas normal or slightly elevated concentrations are tumorigenic (Jenkins et al., 1995; Singh and Gupta, 2011). It is thus impossible to assert unequivocally that elevated NO levels are deleterious. This complexity in the chemical and regulatory effects of NO necessitates careful design and interpretation of experiments.

The regulatory significance of NO makes it a natural therapeutic target. Ignarro (1989) notes retrospectively that identification of the vascular signaling functions of NO provides a great deal of insight into the pharmacological efficacy of nitroglycerin, nitrate

and nitrite esters, and nitroprusside, all of which are believed to act via the eventual release of NO. Various other NO-releasing species have been studied for potential pharmacological effects, including the S-nitrosothiols (RSNOs; Al-Sa'doni and Ferro, 2000) and sydnonimine derivatives (Lehmann, 2000). Numerous studies have also examined NOS as drug targets (Fukuto and Chaudhuri, 1995; Joubert and Malan, 2011; McCarthy et al., 2008; O'Connor and O'Brien, 2009; Paige and Jaffrey, 2007). Therapeutic use of NO has been attempted by direct administration of the gas, typically by inhalation (Weimann et al., 1997). The efficacy of such treatment is controversial, however. In reviewing portions of the clinical literature, Donohue et al. (2011) conclude that "there is currently no evidence to support the use of [inhaled NO] in preterm infants with respiratory failure outside the context of rigorously conducted randomized clinical trials" and, similarly, Afshari et al. (2011) argue that "[inhaled NO] cannot be recommended for [adult or child] patients with acute hypoxemic respiratory failure. [It] results in a transient improvement in oxygenation but does not reduce mortality and may be harmful." Conversely, Steinhorn (2011) finds NO to be a "highly effective pulmonary vasodilator for newborn infants with [persistent pulmonary hypertension] or hypoxemic respiratory failure." A clearer understanding of the physiological, pharmacological, and toxicological actions of NO and its derivatives should help to resolve these questions.

1.2 Biological chemistry of nitrogen oxides

The biologically relevant chemistry of NO and related nitrogen oxides is quite complex; a subset of these reactions is presented in Figure 1.1. Although a radical, NO itself is comparatively stable, reacting with few biological molecules in most

circumstances. As shown in the upper left of Figure 1.1, one significant reaction pathway for NO *in vivo* is the formation of nitroso adducts with metal centers of proteins, such as the heme in guanylate cyclase and hemoglobin (Ignarro, 1989) and the Cu^{2+} centers of cytochrome c oxidase and ceruloplasmin (Torres and Wilson, 1999). NO also reacts relatively quickly with molecular O_2 to form nitrogen dioxide (NO_2; Lewis and Deen, 1994), and reacts near the diffusion-controlled limit with superoxide radical (O_2^-), an inevitable byproduct of cellular respiration (Blough and Zafiriou, 1985; Huie and Padmaja, 1993), to form the strong oxidant peroxynitrite ($ONOO^-$). There is also evidence that NO reacts to form nitroso adducts with various organic radical species present *in vivo*, including thiyl (Goldstein and Czapski, 1996) and tyrosyl (Goldstein et al., 2000) radicals, though the biological significance of the former reaction pathway is disputed on kinetic grounds.

As shown in the central portion of Figure 1.1, NO_2 is formed by multiple pathways *in vivo*. These include NO oxidation by O_2, reaction of peroxynitrite with CO_2 (Goldstein et al., 2001), and reaction of hydroxyl radical (HO) with nitrite (Treinin and Hayon, 1970), where HO is generated from hydrogen peroxide either by Fenton chemistry (Thomas et al., 2002) or by the enzymatic action of, for example, myeloperoxidase (Sampson et al., 1998). Once formed, it rapidly combines with NO to form nitrous anhydride (N_2O_3; Graetzel et al., 1970) which, as depicted in the lower left of Figure 1.1, readily nitrosates sulfhydryls (Goldstein and Czapski, 1996; Keshive et al., 1996) and amines (Lewis et al., 1995b; Liu and Hotchkiss, 1995) and deaminates nucleobases (Liu and Hotchkiss, 1995). NO_2 itself is thought to react with many classes of biomolecules (Figure 1.1, center left and bottom right), including lipids (Balazy and

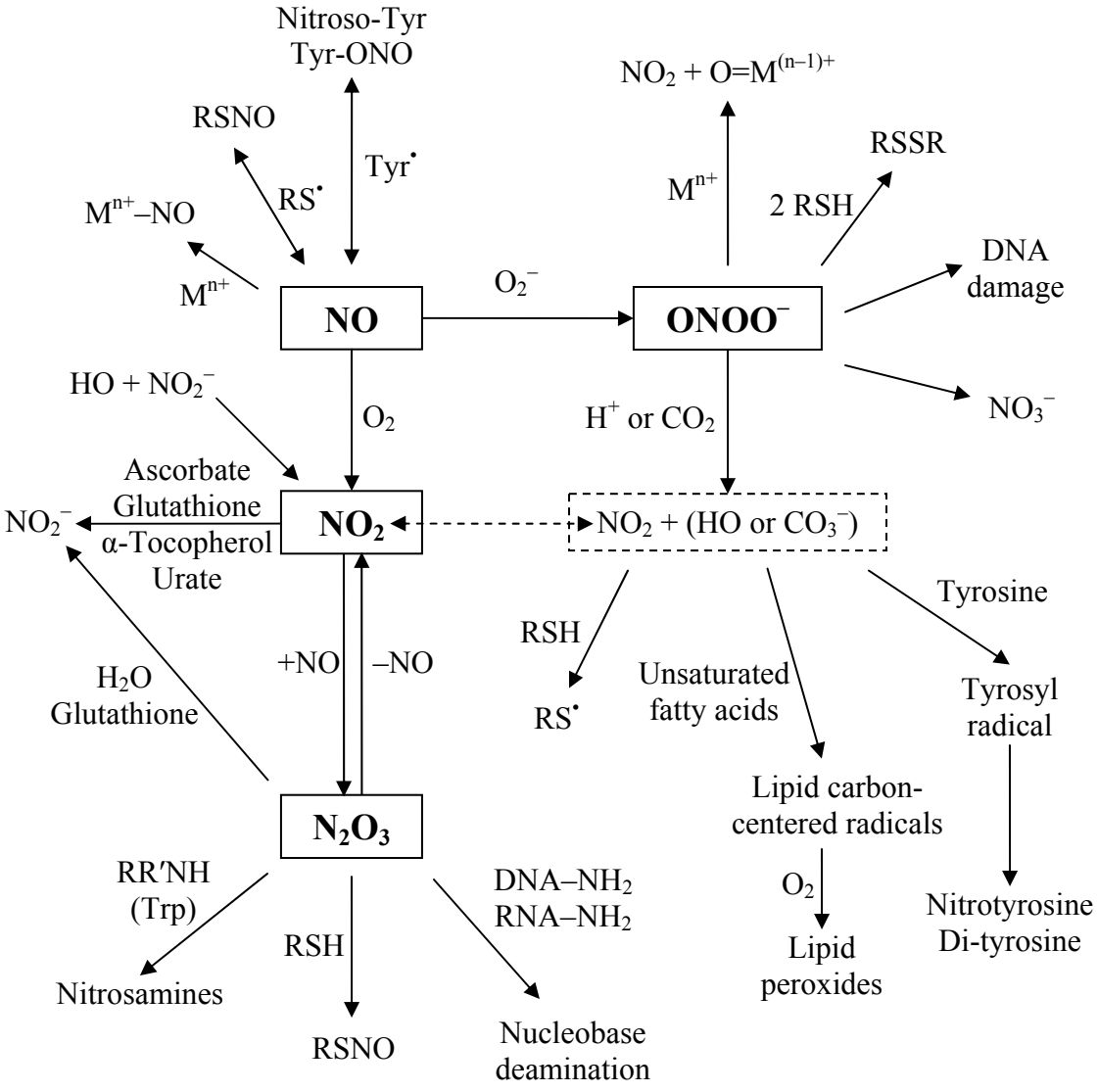

Figure 1.1. Schematic of some key physiologically-relevant reactions of the nitrogen oxides.

Chemtob, 2008; Halliwell et al., 1992), proteins (Bartesaghi et al., 2007), nucleic acids (Beda and Nedospasov, 2007; Shafirovich et al., 2001), and physiologically significant small molecules such as ascorbate and α-tocopherol (Forni et al., 1986). Glutathione is a significant scavenger *in vivo* of both NO_2 and N_2O_3; NO_2 is also scavenged by urate and ascorbate, if the latter are present at sufficient levels (Lim et al., 2008).

Peroxynitrite ($ONOO^-$) is formed from the extremely rapid reaction between NO and O_2^-, which is one of the few reactions fast enough to compete with superoxide dismutase for O_2^-. $ONOO^-$ is a weak base; its conjugate acid, peroxynitrous acid (ONOOH), has a pK_a of 6.8. $ONOO^-$ is relatively stable in aqueous solution, but ONOOH decomposes rapidly to HO and NO_2. Some of these radicals recombine into nitric acid at the site of formation, while others diffuse away into the medium (Ferrer-Sueta and Radi, 2009). Evidence has also been reported of a non-radical decomposition pathway for $ONOO^-$, generating NO_2^- and singlet oxygen (Miyamoto et al., 2009; Pfeiffer et al., 1997), but this reaction is sufficiently slow as to be negligible *in vivo*. $ONOO^-$ reacts rapidly with dissolved CO_2 to form CO_3^- (carbonate radical anion) and NO_2; in a similar fashion to the decomposition of ONOOH, some of these radicals recombine to form CO_2 and NO_3^- while others escape and are able to react with other substrates. As shown in the upper right of Figure 1.1, $ONOO^-$ is also capable of direct, two-electron oxidation of certain substrates, including thiols (Landino et al., 2008; Quijano et al., 1997), metal centers (Alvarez and Radi, 2003), and thioethers such as methionine (Perrin and Koppenol, 2000; Pryor et al., 1994; Rebrin et al., 2008).

In order to gain understanding of the effects of RNS *in vitro* and *in vivo*, it is necessary to estimate or quantify the RNS concentrations. Detailed models have been

published describing the spatial distributions of RNS generated by macrophages in plate cultures (Chen and Deen, 2001; Nalwaya and Deen, 2004a, b) and by macrophages attached to carrier beads in suspension (Chen et al., 1998). Similarly, models have been developed to predict NO concentration profiles within inflamed colonic crypts (Chin et al., 2008) and within the microvasculature (Lamkin-Kennard et al., 2004), as well as intracellular concentrations of RNS under inflammatory conditions (Lim et al., 2008). All of these models require careful consideration of the chemistry described above as well as the spatial distribution of the various RNS and reactive substrates involved.

1.3 Delivery of nitrogen oxides

1.3.1 Reported methods

Given the toxicological and pathophysiological significance of the reactions of RNS with cellular components, it is desirable to develop systems capable of delivering these species to targets of interest under conditions similar to those predicted to occur *in vivo*. Since the kinetics of many of the key reaction steps are nonlinear (including NO oxidation and the radical reactions of NO_2), in order to capture physiologically relevant phenomena RNS levels must be realistic. For example, in plated co-cultures of target cells with macrophages (Nalwaya and Deen, 2004a) and in inflamed colonic crypts (Chin et al., 2008) the maximum NO concentration is predicted to be ~ 1 μM and 0.3 μM, respectively. Further, the RNS concentrations must be maintained for prolonged periods of time—at least hours to days.

As an additional complication, in most cases delivery of one RNS leads to the presence of at least one other. A schematic of these intrinsic 'coexistence regions' of

RNS delivery is presented in Figure 1.2. As can be seen, only NO_2 can be delivered in isolation from the other RNS of interest, as under properly selected delivery conditions the effects of N_2O_4 can be made negligible (see Chapter 3). Homolysis of ONOOH and/or reaction of $ONOO^-$ with CO_2 both entail formation of NO_2, as does oxidation of NO in the absence of O_2^-. Delivery of $ONOO^-$ in a fashion that mimics the physiological route of formation by reaction of NO and O_2^- is the most complex scenario considered, which results in the simultaneous presence of all the RNS of interest. It is thus desirable to develop methods for controlled, sustained delivery of each RNS in order to more clearly distinguish the effects of one RNS from another.

Nitric oxide

Methods that have been used for NO delivery include direct infusion of O_2-free, NO-saturated solutions (Liu et al., 1998; Thomas et al., 2001), addition of NO-releasing compounds (e.g., NONOates; Kröncke et al., 1993; Maragos et al., 1991), co-culture of target cells with activated macrophages (Pfeiffer et al., 2001), and diffusion of gaseous NO through permeable membranes (Kavdia et al., 2000; Tamir et al., 1993; Wang and Deen, 2003). None of these methods is completely free from problems. The utility of infusion of NO-saturated solutions and NO donor compounds is limited because of their inherently transient nature: both the NO and the donor compounds are consumed on a time scale of 3-30 min (Maragos et al., 1991). Further, some the NO donor compounds may exert NO-independent toxicity. Recently, photo-controlled NO donors have been described (Nakagawa, 2011), which release NO at a rate proportional to an irradiating light source. Since the rate of NO generation from these compounds is not dependent on their instantaneous concentrations, they have the potential to provide steady NO

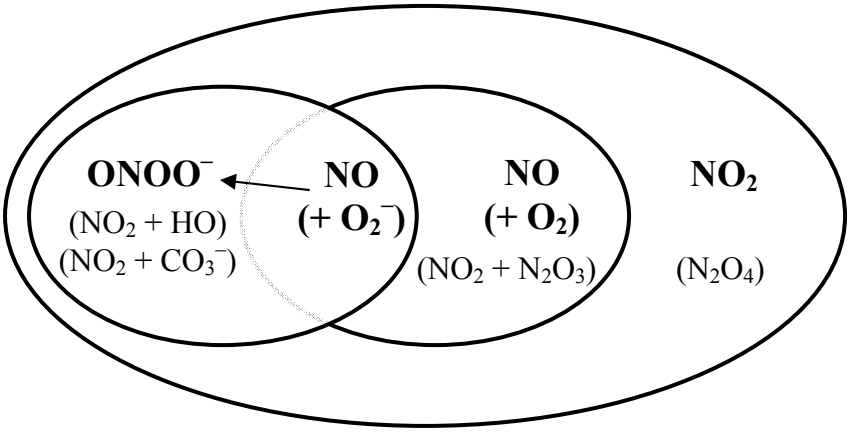

Figure 1.2. Schematic of 'coexistence regions' for delivery of various RNS.

Bolded formulas indicate primary species delivered. Non-bolded, parenthetical formulas indicate secondary species generated from primary species. Peroxynitrite and NO can be delivered independently, but both (with NO, in the presence of O_2) entail concomitant formation of NO_2. Hydroxyl radical and carbonate radical anion result from $ONOO^-$ delivery in the absence and presence of CO_2, respectively.

concentrations, as desired. Macrophage co-culture is an unattractive NO delivery option for studies not concerned specifically with the effects of activated macrophages, due to the need for device sterility and the prospect of NO-independent effects. Delivery by diffusion through permeable membranes seems the most promising means for achieving controlled NO delivery. Sustained, physiologically relevant NO concentrations were achieved by Wang and Deen (2003) via delivery of gaseous NO through PDMS tubing, though characterization of their system was complicated by unanticipated chemistry postulated to occur within the PDMS tubing used. While this phenomenon complicated applications of the device to the study of the reactions of RNS with molecular substrates (Dong et al., 2003), the reactor has been successfully used in studies of the effects of NO on a variety of cell lines (Dong and Dedon, 2006; Kiziltepe et al., 2005; Li et al., 2009; Li et al., 2006; Li et al., 2005; Wang et al., 2003).

Nitrogen dioxide

Controlled delivery of NO_2 to cells and biomolecules has been attempted in a number of configurations, none of which seem particularly relevant to the study of elevated production of RNS in a toxicological or pathological setting. Pulse radiolytic and flash photolytic techniques have been used extensively to probe the reactions of NO_2 with specific molecules (Bartesaghi et al., 2004; Forni et al., 1986; Goldstein et al., 2004a), but no studies were found that attempted exposures to cells using this technique. Presumably, the cytotoxicity of the radiation and/or particle beams used in these studies would confound any such study attempted. The phenol nitrating agent tetranitromethane (TNM) has been used to mimic the activity of NO_2 [as in, e.g., Lennon et al. (2007)] but TNM is not useful for simulating the biological or biochemical action of NO_2 as it does

not release NO_2 as a free radical under most conditions. Most of the remaining literature on biological exposures appears to focus on the delivery of gaseous NO_2 to cells (Ayyagari et al., 2007; Bakand et al., 2006; Bombick et al., 1998; Komori et al., 2008; Persinger et al., 2001), tissues (Bion et al., 2002; Postlethwait and Mustafa, 1989; Switalla et al., 2010), or entire organisms (Douglas et al., 1994) as a model airborne pollutant. Most of these studies used lung tissue or cultured bronchial or alveolar cells, and most delivered NO_2 in a configuration attempting to mimic that of actual environmental NO_2 exposure. No studies were found that attempted delivery of NO_2 to cells under conditions pertinent to prolonged immune stimulation.

Peroxynitrite

Two main routes are available for delivery of peroxynitrite: addition of pre-formed, alkaline $ONOO^-$ either as a bolus or in a steady stream (Kuhn et al., 1999; Pfeiffer and Mayer, 1998; Pfeiffer et al., 2000; Wang and Deen, 2004; Zhang et al., 2003) and *in situ* generation from simultaneous production of NO and O_2^-. The latter can potentially be achieved by combination of an NO donor species with a chemical [e.g., Hodges et al. (2000)], enzymatic [e.g., Radi et al. (1990)], or cellular [e.g., Nakamura et al. (2002)] source of O_2^-. While well suited for exposure of chemical species, the Hodges et al. O_2^- source is possibly cytotoxic and thus may not be usable in delivery of $ONOO^-$ to cells. As well, it was demonstrated by Wang and Deen (2004) that the xanthine oxidase O_2^- generation system is inactivated by $ONOO^-$, and is thus also not a viable option. It would be necessary to identify an enzymatic O_2^--generating system that is not sensitive to $ONOO^-$ in order for this approach to be useful. Finally, the complexity of the

culture media required for cellular generation of O_2^- likely would confound any effort to draw detailed mechanistic conclusions from experiments using such a technique.

The main complications of peroxynitrite delivery by the addition of pre-formed $ONOO^-$ are its decomposition via ONOOH and its reaction with CO_2, both of which are sufficiently rapid that uniform concentrations cannot be assumed in most settings, even with very aggressive mixing. Wang and Deen (2004) were still able to obtain good agreement between their data and a model assuming perfect mixing, however, and concluded that bolus or continuous infusion represented the best available option for $ONOO^-$ delivery at that time. It should be noted that different product distributions have been observed in experiments delivering equal amounts of NO and O_2^- as compared to experiments delivering 'authentic' peroxynitrite (Goldstein and Merenyi, 2008). Accordingly, it would be desirable to develop well-controlled, quantitative delivery methods using both approaches.

1.3.2 Overview and evaluation

Development of separate methods for specific delivery of each RNS predicted to occur *in vivo* (viz., NO, NO_2, and $ONOO^-$) to biomolecules and/or cells is desirable due to the inevitable cross-generation of these RNS. While transient methods may be sufficient for chemical studies with sufficiently simple mechanisms, a more physiologically relevant, steady delivery mode will frequently be required, as in the study of NO signaling. Table 1.1 presents one possible schematization of the various possible delivery configurations and provides representative citations for modes with established methods, as described above. For the others, brief notes on the outstanding challenges

Table 1.1. Summary of species, targets and modes in RNS delivery.

Examples of successful applications of the techniques listed are noted where relevant. See text for discussion of bolded chapter references and italicized comments.

RNS	Delivery Mode	Delivery to: Molecules	Delivery to: Cells
NO (+ O_2)	Transient	Donor compounds (Lehmann, 2000) Bolus infusion of NO-saturated solutions (Thomas et al., 2001)	
	Steady	Photo-controlled NO donors (Nakagawa, 2011) Porous PTFE membrane **See Chapter 2**	PDMS tubing (Wang and Deen, 2003)
NO_2	Transient	Pulse radiolysis (Goldstein et al., 2006)	*Pulse radiolysis feasible?*
	Steady	*Continuous radiolysis feasible?* Direct gas-liquid contacting of NO_2 gas mixture **See Chapter 3**	
$ONOO^-$ (authentic)	Transient	Bolus infusion (Wang and Deen, 2004) **See Chapter 4**	Bolus infusion (Minetti et al., 2008) *Microfluidics?*
	Steady	*Steady, uniform delivery is challenging*	
$ONOO^-$ ($NO + O_2^-$)	Transient	Chemical NO, O_2^- sources (Hodges et al., 2000; Kirsch et al., 1998)	SIN-1 (Li et al., 2002a; Lomonosova et al., 1998)
	Steady	*Photo-controlled NO & O_2^- donors?*	*Cell-safe delivery is challenging* (Wang and Deen, 2004)

are given; more detail on these difficulties is provided below. Methods with bolded references are addressed by this research in the chapters indicated.

Challenges in radiolytic NO_2 delivery

Within certain limits, radiolytic methods are attractive tools for NO_2 exposure. Their main downside stems from the potential of the photon and/or electron beams used to disrupt the molecules or cells under study, as well as the potential adverse effects of the high concentrations of hydroxyl radical and solvated electron scavengers required (e.g., N_2O and NO_2^-). It seems likely that pulse radiolytic exposure of cells to NO_2 would cause significant NO_2-independent cell damage. Further, the complex composition of most culture media would possibly interfere with the radical-generating chemistry. In terms of steady NO_2 exposures, no studies were identified that used continuous radiolysis in order to deliver NO_2 in this fashion. As long as the target species in a chemical study is not sensitive to the incident beam and can be included at a sufficiently low concentration that it will react with a negligible fraction of the radiolytic precursor radicals, the method is theoretically feasible.

Challenges in bolus peroxynitrite delivery

Steady exposure of targets to known concentrations of authentic peroxynitrite under physiological conditions is extremely challenging due to its short lifetime at neutral pH. The intensity of mixing required to achieve uniform concentrations is not feasible by most standard laboratory techniques. The agreement between predicted and observed product formation rates in the bolus infusion system of Wang and Deen (2004) is encouraging, but the perfect-mixing assumption that was invoked is likely not strictly

valid. The requirement to stabilize pre-formed $ONOO^-$ by storage in strongly alkaline solutions is a further complication of this method. Addition of a sufficiently large volume of the peroxynitrite solution will require either strong buffering or concomitant addition of acid. The infusant volumes involved may cause undesirable chemical dilution or alterations to the hydrodynamic behavior of the system. One solution to this problem is to use $ONOO^-$ stock solutions of higher concentration, but decomposition of peroxynitrite starts to become problematic at concentrations around 200 mM (Koppenol et al., 1996). Also, as the concentration of $ONOO^-$ is increased, the possible effects of contaminants in the peroxynitrite preparation and the strength of the localized 'burst' of RNS at the point of infusion both increase accordingly. As an additional consideration in exposing cells to pre-formed $ONOO^-$, it is possible that the mixing required to achieve spatial uniformity will be sufficiently intense to harm the cells under study (Kunas and Papoutsakis, 2009). At the very least, alterations in cell behavior such as modulation of protein expression (Morga-Ramirez et al., 2010) and disruption of respiratory function (Abu-Reesh and Kargi, 1989) are to be expected.

In situ *peroxynitrite delivery*

The development of photo-controlled NO donors (Nakagawa, 2011) is a major first step toward simultaneous generation of NO and O_2^- in true steady-state fashion. Development of a comparable controlled-release donor of superoxide would potentially eliminate the technical barriers to exposures of chemical targets to *in situ*-generated $ONOO^-$. A key point of feasibility would be the requirement for negligible consumption of the donor species by peroxynitrite or its radical byproducts. Given this, as long as the substrate is unaffected by the light or other stimulus needed to trigger NO and O_2^- release

and there is no cross-reactivity between the NO and O_2^- donors and the substrate of interest, the method should be sound. Further, as long as the NO- and O_2^--generating species do not display $ONOO^-$-independent toxicity, they should also be suitable for long-term, steady exposure of cells. Replenishment of the donor species would be necessary in long experiments, but this should be unproblematic.

1.4 Research objectives

The initial objective of this research was to develop well-controlled delivery methods for peroxynitrite, both to molecules and to cells. The short lifetime of $ONOO^-$ in neutral solution makes it almost inevitable that concentrations will be non-uniform when pre-formed $ONOO^-$ is infused into a reaction vessel, even with very vigorous stirring. Chapter 4 describes a novel bolus mixing model that was conceived in an attempt to quantify the 'vortexing method' for delivery of pre-formed $ONOO^-$, where a drop of alkaline $ONOO^-$ is added to target-containing medium during vigorous vortexing [see, e.g., Pamir and Wogan (2003)]. Not described are preliminary efforts to develop a microfluidic system for exposing individual cells to pre-formed $ONOO^-$. It was hypothesized that the short length scales and controlled, laminar flow conditions in a microfluidic device would enable quantifiable, reproducible delivery conditions. Preliminary tests of material compatibility with alkaline peroxynitrite solutions were encouraging, but attempts to attach peroxynitrite-reactive ligands to small, neutrally-buoyant particles were unsuccessful. (In theory, these particles would have permitted characterization of the transport of peroxynitrite to the surface of cell-sized particles

within the proposed device.) Assistance was provided in these efforts by Ms. Deborah Markham (UROP, Department of Chemistry, MIT).

After some preliminary discussions of prospective uses of the proposed microfluidic delivery method with Dr. Steven Tannenbaum (Biological Engineering, MIT), it became clear that a better understanding of some fundamental aspects of intracellular RNS chemistry was needed. Accordingly, the peroxynitrite delivery efforts were set aside and focus was turned to development of a new system for NO delivery that eliminated the adventitious chemistry occurring in the system of Wang and Deen (2003), so as to make available a tool suitable for NO exposure of biologically-relevant molecules in addition to exposure of cells (Chapter 2). Initial attempts to apply this new system to NO exposures of tyrosine revealed unanticipated complications, attributed to cross-reactions of tyrosyl radical with NO (Goldstein et al., 2000). Since NO_2 is the primary RNS in the Tyr reaction system, the system of Wang and Deen (2003) was adapted for controlled delivery of NO_2 (Chapter 3). Analysis of various aspects of the systems reported in Chapters 2 and 3 was performed in collaboration with Chang Hoon Lim (graduate student, Chemical Engineering, MIT).

One article has already been published from this work (portions of Chapter 2; Skinn et al., 2011), and another manuscript is in preparation (portions of Chapter 3).

Chapter 2

Nitric Oxide Delivery System for Biological Media

2.1 Introduction

In addition to its multiple signaling functions in the body, NO is a source of reactive nitrogen species (RNS), which can be toxic or mutagenic (Burney et al., 1997). Elucidation of the role of NO-derived RNS in the etiology of cancer and other diseases requires that their rates of reaction with nucleic acids, proteins, and other biomolecules be characterized. Such kinetic studies can require prolonged exposure of the target molecule to NO and O_2. For example, in a study of nitrosative damage to plasmid DNA, 12 h exposures were needed to obtain readily detectable amounts of the modified bases (Dong et al., 2003). Likewise, in characterizing the effects of NO on cells, there is a need to achieve predictable, constant concentrations for periods ranging from hours to days.

Among the methods which have been used to expose biomolecules or cells to NO are bolus injection of NO-saturated aqueous solutions (Liu et al., 1998; Thomas et al., 2001) and generation of NO from donor compounds (Kröncke et al., 1993; Maragos et al., 1991). Both approaches are simple and do not require special equipment, but the NO concentration decreases markedly within a few minutes, due to depletion of the source material. Another method is simultaneous culture of macrophages with target cells (Lewis et al., 1995a; Pfeiffer et al., 2001). After an induction period of a few hours, activated macrophages can synthesize NO at a constant rate (Chin et al., 2010), permitting maintenance of physiological concentrations for days. However, cellular

generation of NO is too complicated for routine use in kinetic studies: the apparatus must be sterile, the culture medium creates unwanted chemical complexity, and co-culture of target cells with macrophages introduces the possibility of NO-independent effects.

A more promising strategy for achieving sustained, constant, and predictable NO concentrations is delivery by diffusion through gas-permeable membranes. Simultaneous replenishment of the O_2 that is consumed chemically or by cellular respiration is also desirable. An early implementation of this idea involved NO delivery via a loop of poly(dimethylsiloxane) (PDMS) tubing inserted into a stirred vessel (Tamir et al., 1993). Limitations of that approach included the absence of O_2 delivery and the presence of a head space in which gas-phase oxidation of NO could occur. Gas-phase reactions complicate the kinetics and may lead to RNS levels that are unphysiological. A later improvement was to resupply O_2 by flowing an air/CO_2 mixture through the headspace (Kavdia et al., 2000). The most recent refinement involves a liquid-filled, stirred chamber fitted with two loops of PDMS tubing, one each for NO and O_2 delivery (Wang and Deen, 2003). The head space is eliminated and the NO and O_2 concentrations can be maintained at predictable, physiological levels indefinitely. This apparatus has been employed both for exposure of cells to NO (Chin et al., 2010; Dong and Dedon, 2006; Kiziltepe et al., 2005; Li et al., 2009; Li et al., 2006; Li et al., 2005; Wang et al., 2003) and for kinetic studies (Dong et al., 2003).

However, delivery of NO by diffusion through PDMS tubing has been found to be less satisfactory for kinetic studies than for studies with cells, because some of the NO is evidently oxidized to NO_2 within the wall of the tubing. The presence of O_2 in the membrane is inevitable, because some will diffuse from the aqueous solution into the NO

tubing, and from there to the NO gas stream. The evidence for adventitious NO oxidation was a rate of NO_2^- accumulation in the solution that was some nine times higher than could be attributed to oxidation in the bulk liquid (Wang and Deen, 2003). It was inferred that the aqueous concentrations of two RNS of interest (NO_2 and N_2O_3) were elevated by several orders of magnitude within about 1 μm of the NO tubing. This "hot spot" does not affect results with adherent cells, which are placed in a dish at the bottom of the reactor, and is unlikely to affect studies with suspended cells, because steric and hydrodynamic interactions will tend to exclude them from the vicinity of the tubing. However, for kinetic studies it requires correction factors which complicate the analysis of data and create uncertainty in the measured rate constants (Dong et al., 2003).

The objective of the present work was to eliminate the region of high RNS concentrations, while retaining the advantages of NO and O_2 delivery through gas-permeable membranes. It was reasoned that if NO were delivered through a porous, hydrophobic membrane, the intramembrane O_2 level would be minimized by rapid escape of O_2 via the gas-filled pores. Because the mass transfer resistance in the liquid is significant, the resulting loss of O_2 from the reactor and the contamination of the NO stream would still be minor. Although we were unable to find a suitable source of porous, hydrophobic tubing, porous poly(tetrafluoroethylene) (PTFE) with the desired properties is available in sheet form. Thus, the NO delivery tubing was replaced by a flat sheet of porous PTFE in the base of a stirred reactor, with O_2 delivery through PDMS tubing as before. The reactor was characterized by continuous monitoring of aqueous NO and O_2 concentrations and by periodic liquid sampling and NO_2^- analysis. As will be described, the results confirm the elimination of the hot spot and show that constant, physiological

levels of NO and O_2 can be maintained indefinitely. A model is presented which allows the aqueous NO and O_2 concentrations to be predicted as a function of the compositions of the NO and O_2 gas mixtures and the length of the O_2 delivery tubing.

2.2 Materials and methods

2.2.1 Chemicals

Griess assay reagents were from Cayman Chemical (Ann Arbor, MI) or were prepared in deionized water from sulfanilamide (1% in 5% phosphoric acid) and N-1-naphthyl-ethylene-diamine (0.1%) from Sigma-Aldrich (St. Louis, MO). All other chemicals were from Sigma-Aldrich. All experiments were performed using 50 mM sodium phosphate buffer at pH 7.4, prepared using deionized water.

2.2.2 Gas delivery system

Pure N_2 and mixtures of 50% O_2 in N_2, 10% NO in N_2, 1% NO in N_2, and 5% O_2 plus 5% CO_2 in N_2 were obtained from Airgas East (Salem, NH). There were two gas streams to the reactor: one was 100-1000 standard cubic centimeters per minute (sccm) of N_2 or the 10% or 1% NO mixtures, and the other was 100-400 sccm of O_2/N_2 mixtures ranging from 0%-50% O_2. Gas flow rates were controlled by Porter Instruments mass flow controllers (Parker-Hannefin, Hatfield, PA). To rigorously exclude O_2 entry, stainless steel tubing and fittings were used in the NO delivery line; the O_2 delivery tubing was PTFE. Higher nitrogen oxides were eliminated from the NO gas stream by reactive absorption in an oxygen trap repacked with pulverized, indicating soda lime.

Outlet pressures of both gas lines under delivery conditions were at most 1% above ambient.

2.2.3 Apparatus

As shown in Figure 2.1, the reactor consisted of a closed, liquid-filled container (65 mL volume), with O_2 supply via a loop of PDMS tubing (Silastic®, 1.96 mm o.d., 1.47 mm i.d., Dow Corning, Midland, MI) and NO entry across a flat, porous PTFE membrane (75 μm thick, 3.0 μm pore size, 83% porosity; Advantec MFS, Dublin, CA). The cell body, magnetic stirrer, and baseplate from an Amicon 8050 ultrafiltration cell (Millipore, Billerica, MA) were used. A custom baseplate insert was machined from non-porous PTFE rod to give a ½″-diameter well facing the porous membrane. The active area of the membrane was restricted to match the well by laminating the membrane to two sheets of poly(vinylidene fluoride) (PVDF) (0.005″ thickness, McMaster-Carr, Dayton, NJ). This was done by clamping the membrane and PVDF sheets between glass plates and heating at 180 °C for 12 min. The membrane was sealed to the cell body and the custom insert using petrolatum grease. A cap machined from polycarbonate rod held an NO electrode (World Precision Instruments, Sarasota, FL; ISO-NOP system) and a fiber-optic O_2 sensor (Instech Laboratories, Inc., Plymouth Meeting, PA). Additional ports accommodated the inlet and outlet of the tubing loop and permitted liquid sampling by syringe. All experiments were performed at room temperature (22-24 °C) and a stirring rate of 165 ± 10 rpm, as determined by a strobe tachometer. Detailed fabrication instructions for the apparatus can be found in Appendix F.

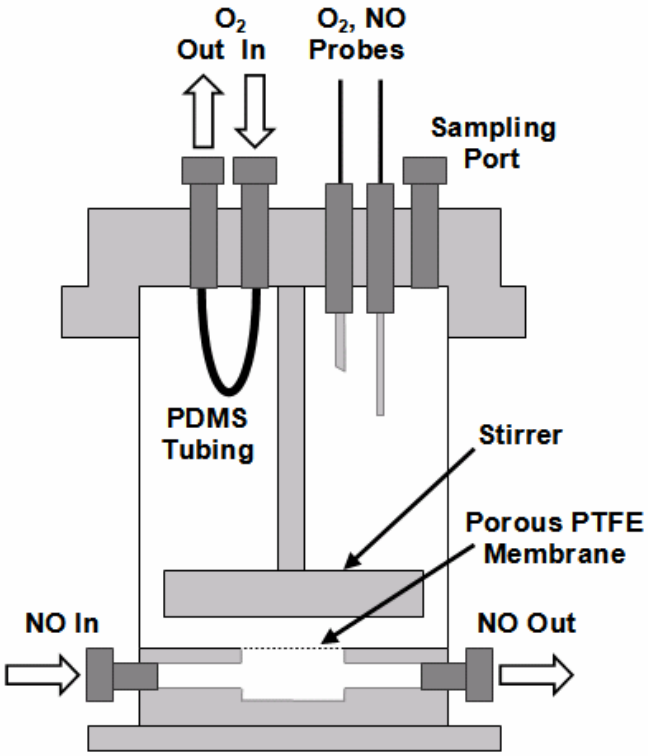

Figure 2.1. Schematic of NO delivery system

2.2.4 Concentration measurements

The O_2 sensor, calibrated as recommended by the manufacturer, had a linear response for concentrations up to ambient levels (0-255 μM), but not above that. The NO probe was calibrated by adding known quantities of NO_2^- to a solution of excess KI in 0.1 M H_2SO_4, which generates equimolar amounts of NO (Zhang, 2008). A linear response was obtained for the concentrations of interest (0-3.5 μM). Nitrite concentrations were measured by the Griess method (see Section 3.2.4). N-nitroso-morpholine (NMor) concentrations were measured by spectrophotometric assay at 250 nm against a blank of NO_2^-- and NMor-free buffer. The extinction coefficient (ε_{250} = 6390 ± 160 M^{-1} cm^{-1}, n = 8) was determined from the absorbance of solutions of authentic NMor at various dilutions. The NMor concentration of each sample was corrected for the presence of nitrite (ε_{250} = 30.9 ± 1.1 M^{-1} cm^{-1}, n = 3), which typically contributed no more than approximately 10% to the measured absorbance. (CAUTION: N-nitrosomorpholine is a suspected carcinogen and should be handled with care.)

2.2.5 NO oxidation kinetics

2.2.5.1 Substrate-free media

In simple aqueous media at physiological pH, NO is oxidized to NO_2^- via the following multistep mechanism, in which NO_2 and N_2O_3 are intermediates (Lewis and Deen, 1994):

$$2\,NO + O_2 \xrightarrow{k_1} 2\,NO_2\,. \tag{2.1}$$

$$NO + NO_2 \underset{k_{-2}}{\overset{k_2}{\rightleftharpoons}} N_2O_3\,. \tag{2.2}$$

$$N_2O_3 + H_2O \xrightarrow{k_3} 2\,NO_2^- + 2\,H^+ . \quad (2.3)$$

The hydrolysis of N_2O_3 is enhanced by phosphate ion (Lewis et al., 1995b), as

$$N_2O_3 + H_2O + P_i \xrightarrow{k_4} 2\,NO_2^- + 2\,H^+ + P_i . \quad (2.4)$$

Under the conditions of the following analysis, Reaction (2.1) is rate-limiting and only the overall reaction need be considered:

$$4\,NO + O_2 + 2\,H_2O \xrightarrow{k_1} 4\,NO_2^- + 4\,H^+ . \quad (2.5)$$

Denoting the concentration of species j as C_j, the rate of NO_2^- formation per unit volume is

$$R = 4k_1 C_{NO}^2 C_{O_2} . \quad (2.6)$$

The corresponding rates of NO and O_2 consumption are R and $R/4$, respectively.

2.2.5.2 NO oxidation of morpholine

In the presence of the saturated heterocycle morpholine (Mor; tetrahydro-1,4-oxazine), an additional reaction occurs. The deprotonated secondary amine of Mor (Mor^o) reacts with N_2O_3 to form NMor and nitrite (Lewis et al., 1995b):

$$N_2O_3 + Mor^o \xrightarrow{k_5} NO_2^- + NMor + H^+ . \quad (2.7)$$

The protonated amine of morpholine has a pK_a of 8.5 (Hetzer et al., 1966), and thus at pH 7.4 the fraction of total Mor existing in the deprotonated state is $f_{Mor^o} = 0.074$.

Reaction (2.1) remains rate-limiting even in the presence of Mor, so the consumption rates of NO and O_2 are unchanged at R and $R/4$, respectively, with R as in

Eq. (2.6). The distribution of products between nitrite and NMor is determined by the competition among Reactions (2.3), (2.4) and (2.7). Since all three product-forming reactions are first order in N_2O_3, the yield of NMor (Y_{NMor}) is independent of the N_2O_3 concentration and takes the form

$$Y_{\mathrm{NMor}} = \frac{R_{\mathrm{NMor}}}{R_{\mathrm{NO_2^-}} + R_{\mathrm{NMor}}} = \frac{k_5 f_{\mathrm{Mor^o}} C_{\mathrm{Mor}}}{2\left[k_3 + k_4 \mathrm{P_i} + k_5 f_{\mathrm{Mor^o}} C_{\mathrm{Mor}}\right]}. \tag{2.8}$$

Regardless of the distribution predicted by Eq. (2.8), the sum of the nitrite and NMor accumulation rates is expected to remain unchanged at R [Eq. (2.6)].

2.2.6 Reactor model

2.2.6.1 Macroscopic model

The concentration of species j averaged over the reactor volume is denoted as $\overline{C}_j$ and is a function only of time (t). It is assumed that the concentrations measured using the NO electrode, O_2 probe, Griess assay, and spectrophotometric measurements are the same as $\overline{C}_{\mathrm{NO}}$, $\overline{C}_{\mathrm{O_2}}$, $\overline{C}_{\mathrm{NO_2^-}}$ and $\overline{C}_{\mathrm{NMor}}$, respectively. Assuming the rate of depletion of Mor in the reactor is sufficiently slow that its concentration remains pseudosteady, the mass balances for the key species are

$$\frac{d\overline{C}_{\mathrm{NO}}}{dt} = \frac{\chi_{\mathrm{NO}} A_m k^{\mathrm{o}}_{m,\mathrm{NO}}}{V}\left(\alpha_{\mathrm{NO}} P_{m,\mathrm{NO}} - \overline{C}_{\mathrm{NO}}\right) - \frac{A_t k^{\mathrm{o}}_{t,\mathrm{NO}}}{V}\overline{C}_{\mathrm{NO}} - 4\gamma k_1 \overline{C}^2_{\mathrm{NO}} \overline{C}_{\mathrm{O_2}}. \tag{2.9}$$

$$\frac{d\overline{C}_{\mathrm{O_2}}}{dt} = \frac{A_t k^{\mathrm{o}}_{t,\mathrm{O_2}}}{V}\left(\alpha_{\mathrm{O_2}} P_{t,\mathrm{O_2}} - \overline{C}_{\mathrm{O_2}}\right) - \frac{\chi_{\mathrm{O_2}} A_m k^{\mathrm{o}}_{m,\mathrm{O_2}}}{V}\overline{C}_{\mathrm{O_2}} - \gamma k_1 \overline{C}^2_{\mathrm{NO}} \overline{C}_{\mathrm{O_2}}. \tag{2.10}$$

$$\frac{d\overline{C}_{NO_2^-}}{dt} = 4\gamma\left(1 - Y_{Mor^o}\right)k_1\overline{C}_{NO}^2\overline{C}_{O_2} . \quad (2.11)$$

$$\frac{d\overline{C}_{NMor}}{dt} = 4\gamma Y_{NMor}k_1\overline{C}_{NO}^2\overline{C}_{O_2} . \quad (2.12)$$

In Eqs. (2.9) and (2.10) the terms on the right-hand side correspond to entry across the primary barrier (PTFE membrane for NO and PDMS tubing for O_2), loss across the other barrier, and consumption via NO oxidation, respectively. The subscripts *m* and *t* refer to the PTFE membrane and PDMS tubing, respectively. The total liquid volume is *V* and α_j, $P_{i,j}$, and A_i are the solubilities, gas-phase partial pressures, and active areas, respectively, for barrier *i* and species *j*. The area A_m was the same in all experiments, whereas A_t (based on the outer diameter of the tubing) was adjusted by altering the tubing length.

The mass transfer coefficient for species *j* at barrier *i*, under unreactive conditions, is denoted as $k_{i,j}^o$. These coefficients were measured in separate experiments, as will be described. The values for NO and O_2 are predicted to be influenced slightly by NO oxidation. This was taken into account by introducing correction factors (χ_j) which were estimated as described next, in Section 2.2.6.2. Also described is the calculation of a correction factor for the reaction rate (γ), which stems from the presence of concentration boundary layers.

2.2.6.2 Derivation of the correction factors χ_j and γ

Oxidation of NO in the concentration boundary layer next to the NO delivery membrane might influence the observed rates of mass transfer and reaction. This possibility was examined computationally by considering two regions, the boundary layer

at the reactor base and the well-mixed fluid region. The boundary layer next to the O_2 delivery tubing could be ignored for this purpose, because the relatively low NO concentration makes oxidation unimportant there (Wang and Deen, 2003). The well mixed region was treated as uniform with concentrations $C_{w,j}$ and the boundary layer next to the PTFE membrane was modeled as a stagnant film extending from $x = 0$ (membrane) to $x = \delta$ (well mixed region). The concentrations in the film are denoted as $\hat{C}_j(x)$ and its thickness is $\delta = D_{O_2} \big/ k^{o}_{m,O_2}$ = 68 μm. Accordingly, the film volume corresponding to an exposed membrane area A_m of 1.27 cm^2 is 8.6 μL, as compared to the total volume of 65 mL.

The characteristic times for diffusion across the film (δ^2 / D_j = 2 s) are small enough to make the system pseudosteady. Denoting the volumetric rates of formation in the film region as $\hat{R}_j$, the conservation equations and boundary conditions are

$$D_j \frac{d^2 \hat{C}_j}{dx^2} = -\hat{R}_j, \qquad \hat{C}_j(0) = \alpha_j P_{m,j}, \qquad \hat{C}_j(\delta) = C_{w,j}. \tag{2.13}$$

These equations for NO and O_2 were solved in MAPLE 10 to obtain $\hat{C}_{NO}(x)$ and $\hat{C}_{O_2}(x)$. Although both concentrations varied considerably across the film, when the relative volumes were taken into account it was found that $\overline{C}_j \big/ C_{w,j} = 1.00$ for all conditions studied. Thus, the difference between the volume-average and well-mixed concentrations is negligible for both NO and O_2, as assumed in interpreting the concentration measurements.

In these computations the concentration of Mor was assumed to be uniform and the concentrations of NO_2 and N_2O_3 were calculated using the quasi-equilibrium assumption [QEA; see Lim (2011)]. That is, it was assumed that the rates of formation and consumption of the two latter species were locally equal at all points within the boundary layer. From the kinetics of Reactions (2.1)-(2.4) and (2.7), the QEA concentrations were calculated to be

$$C_{\mathrm{NO_2}} = \frac{2k_1\left(k_{-2}+k_P'\right)}{k_2 k_P'} C_{\mathrm{NO}} C_{\mathrm{O_2}}\,, \tag{2.14}$$

$$C_{\mathrm{N_2O_3}} = \frac{2k_1}{k_P'} C_{\mathrm{NO}}^2 C_{\mathrm{O_2}}\,, \tag{2.15}$$

where the pseudo-first-order rate constant k_P' for product formation from N_2O_3 (nitrite or NMor) in this system is defined as

$$k_P' = k_3 + k_4 \mathrm{P_i} + k_5 f_{\mathrm{Mor^o}} C_{\mathrm{Mor}}\,. \tag{2.16}$$

Given that $A_m \delta << V$, the correction factor for the reaction rate was calculated as

$$\gamma = 1 + \frac{A_m}{V R_{w,j}} \int_0^{\delta} \hat{R}_j \, dx \tag{2.17}$$

where $R_{w,j}$ is the rate based on the well-mixed (or volume-average) concentrations. Because the rates for NO, O_2, NO_2^- and NMor are all proportional to one another, γ is the same for each of these species. The mass transfer coefficient with oxidation, divided by that for an unreactive system, was calculated as

$$\chi_j = \frac{k_{m,j}}{k_{m,j}^{\mathrm{o}}} = -\frac{D_j}{k_{m,j}^{\mathrm{o}}\left(\alpha_j P_{m,j} - C_{w,j}\right)} \frac{d\hat{C}_j}{dx}(0)\,. \tag{2.18}$$

Neither type of correction was found to be very important. That is, with 10% NO gas and $\bar{P}_{O_2}$ = 160 mmHg, γ= 1.07, χ_{NO} = 1.05, and χ_{O_2} = 0.99. At 1% NO, all of these factors equaled 1.00.

2.2.7 Evaluation of mass transfer coefficients

2.2.7.1 Mass transfer coefficients for O_2

The mass transfer coefficients for O_2 at the two barriers were found by measuring the rate of depletion of O_2 from an air-equilibrated buffer in the absence of NO. This was done by passing N_2 through the flow space in question, with the other one sealed; either the tubing was removed or the PTFE membrane was replaced by an impermeable PVDF disc. When the tubing was present, the lengths ranged from 4-8 cm. For either configuration, Eq. (2.10) reduces to

$$\frac{d\bar{C}_{O_2}}{dt} = -\frac{A_i k^{o}_{i,O_2}}{V}\bar{C}_{O_2} \tag{2.19}$$

the solution for which is

$$\bar{C}_{O_2}(t) = \bar{C}_{O_2}(0)\exp[-t/\tau], \qquad \tau = \frac{V}{A_i k^{o}_{i,O_2}}. \tag{2.20}$$

The O_2 concentration was measured as a function of time and the data were regressed against Eq. (2.20) to find k^{o}_{i,O_2}.

2.2.7.2 Mass transfer coefficients for NO

The O_2 results were extrapolated to NO as follows. Laminar boundary-layer theory (Deen, 1998) indicates that for transport from a solid surface to a liquid $k^{o}_{i,j} \propto D_j^{2/3}$, where D_j is the aqueous diffusivity of species j. Thus

$$k^{o}_{i,\mathrm{NO}} = k^{o}_{i,\mathrm{O_2}} \left(\frac{D_{\mathrm{NO}}}{D_{\mathrm{O_2}}} \right)^{2/3} . \tag{2.21}$$

This is all that was needed to find $k^{o}_{m,\mathrm{NO}}$, because the diffusional resistance in the gas-filled pores of the PTFE membrane is negligible. For $k^{o}_{t,\mathrm{NO}}$, however, the resistances in the tubing wall and liquid are both significant.

The mass transfer coefficients at the PDMS tubing under unreactive conditions are determined by the resistances of the tubing wall and aqueous boundary layer. Defining the driving force as the concentration difference, the resistance in the aqueous film for species j is $1/k^{o}_{f,j}$, where $k^{o}_{f,j}$ is the unreactive mass transfer coefficient for just the film. Using liquid-equivalent concentrations, the resistance of the wall is

$$\frac{1}{k^{o}_{w,j}} = \frac{\alpha_j r_o}{\tilde{\alpha}_j \tilde{D}_j} \ln\left(\frac{r_o}{r_i} \right), \tag{2.22}$$

where $\tilde{\alpha}_j \tilde{D}_j$ is the permeability of gas j in the PDMS tubing. This wall resistance is roughly comparable to that in the film. Thus, the overall resistance is

$$\frac{1}{k^{o}_{t,j}} = \frac{1}{k^{o}_{f,j}} + \frac{\alpha_j r_o}{\tilde{\alpha}_j \tilde{D}_j} \ln\left(\frac{r_o}{r_i} \right). \tag{2.23}$$

Eq. (2.23) was applied to both NO and O_2 and $k^{o}_{f,NO}$ was related to k^{o}_{f,O_2} using Eq. (2.21). Algebraic rearrangement led then to the following expression for $k^{o}_{t,NO}$:

$$k^{o}_{t,NO} = \left[\frac{1}{k^{o}_{t,O_2}} \left(\frac{D_{O_2}}{D_{NO}} \right)^{2/3} + r_o \ln\left(\frac{r_o}{r_i} \right) \left\{ \frac{\alpha_{NO}}{\tilde{\alpha}_{NO}\tilde{D}_{NO}} - \left(\frac{\alpha_{O_2}}{\tilde{\alpha}_{NO}\tilde{D}_{NO}} \right) \left(\frac{D_{O_2}}{D_{NO}} \right)^{2/3} \right\} \right]^{-1} . \quad (2.24)$$

The values for the physicochemical parameters and reactor dimensions are given in Table 2.1.

2.2.8 Tests using nitrite and NMor accumulation

Nitric oxide delivery in the presence of O_2 was examined first by comparing observed NO_2^- and NMor accumulation rates to those predicted using measured NO and O_2 concentrations. For this purpose, the reactor was filled with air-equilibrated buffer and equipped only with the PTFE membrane. When present, the Mor concentration was 2 mM. Pure N_2 gas (350 sccm) was flowed beneath the PTFE membrane for at least 20 min and then a 10% NO mixture (350 sccm) was introduced. Nitric oxide and O_2 concentrations were monitored continuously and the liquid was sampled periodically for NO_2^- and NMor assays. The samples were stored in sealed vials and were replaced with fresh buffer. The NO concentrations at each sampling time were subtracted from the measured NO_2^- and NMor concentrations (weighted by $1-Y_{NMor}$ and Y_{NMor}, respectively), because the residual NO in each sample is expected to be oxidized to NO_2^- and NMor within the sealed vials according to the competing stoichiometry of Reactions (2.3), (2.4) and (2.7). The rates of product accumulation calculated by substituting the measured NO and O_2 concentrations into Eqs. (2.11) and (2.12) was compared to that found from the

Table 2.1. Physicochemical parameters

Quantity	Value [a]	Units	Reference
α_{NO}	1.9×10^{-3}	M atm^{-1}	Zacharia and Deen, 2005
α_{O_2}	1.2×10^{-3}	M atm^{-1}	Weiss, 1970 Hermann et al., 1995
$\tilde{\alpha}_{NO}\tilde{D}_{NO}$	3.1×10^{-11}	M m^2 atm^{-1} s^{-1}	Zacharia and Deen, 2005
$\tilde{\alpha}_{O_2}\tilde{D}_{O_2}$	2.1×10^{-11}	M m^2 atm^{-1} s^{-1}	Robb, 1968
D_{NO}	2.2×10^{-9}	m^2 s^{-1}	Zacharia and Deen, 2005
D_{O_2}	2.1×10^{-9}	m^2 s^{-1}	Goldstick and Fatt, 1970
k_1	2.1×10^{6}	M^{-2} s^{-1}	Lewis and Deen, 1994
k_2	1.1×10^{9}	M^{-1} s^{-1}	Graetzel et al., 1970
k_{-2}	4.8×10^{4}	s^{-1}	Graetzel et al., 1970
k_3	1.6×10^{3}	s^{-1}	Licht et al., 1988
k_4	6.4×10^{5}	M^{-1} s^{-1}	Lewis et al., 1995b
k_5	6.4×10^{7}	M^{-1} s^{-1}	Lewis et al., 1995b
A_m	1.27×10^{-4}	m^2	-
r_o	9.80×10^{-4}	m	-
r_i	7.35×10^{-4}	m	-
L	$(4 \text{ to } 8) \times 10^{-2}$	m	-
V	6.5×10^{-5}	m^3	-

[a] All parameter values here are for 23-25 °C.

Griess and spectrophotometric assays. As will be discussed, the total product accumulation rate is expected to remain nearly constant in such experiments, despite the changing O_2 and NO concentrations and regardless of the presence of Mor.

2.2.9 Simultaneous delivery of NO and O_2

The approach of the NO and O_2 concentrations to steady-state was examined during simultaneous delivery of both gases in the absence of Mor. In the analysis of these experiments the O_2 level in the liquid will be expressed as a partial pressure, $\overline{P}_{O_2}$. Both ambient ($\overline{P}_{O_2}$ = 160 mmHg) and sub-ambient O_2 levels were investigated. The sub-ambient O_2 partial pressures of 100, 40, and 25 mmHg, correspond to arterial, venous/tissue, and slightly hypoxic conditions, respectively. The reactor was filled with air-equilibrated buffer and equipped with both the PTFE membrane and PDMS tubing loop. Mixtures between 5% and 35% O_2 were used to supply O_2, and the length of the PDMS tubing loop was adjusted to provide the desired steady-state O_2 concentration. For experiments at ambient O_2 levels, the O_2 mixture (100-250 sccm) and pure N_2 (350 sccm) were first flowed through the tubing and the reactor base, respectively, for at least 20 min. At t = 0, the gas beneath the PTFE membrane was switched to 10% or 1% NO (350 sccm) and the O_2 and NO concentrations were monitored until steady values were obtained. For experiments at sub-ambient O_2 levels, pure N_2 was flowed through both the PDMS tubing and the reactor base until the desired $\overline{P}_{O_2}$ was reached, at which time the gas streams were switched to the appropriate O_2 and NO mixtures. In both types of experiments the rise of $\overline{C}_{NO}$ to its steady value was fitted with an exponential function, to find the time constant for the approach to steady-state (τ_{NO}). These experiments were

simulated by solving Eqs. (2.9) and (2.10) numerically using MAPLE 10 (Waterloo Maple, Waterloo, ON, Canada).

2.3 Results

Plots of the data from all experiments reported in this chapter are included in Appendix A.

2.3.1 Mass transfer coefficients

Figure 2.2 presents representative O_2 concentrations for depletion experiments with either the PDMS tubing or the PTFE membrane, with $t = 0$ being the moment the N_2 flow was started. Eq. (2.20) yielded excellent fits to the data, as shown by the solid curves. The k°_{i,O_2} values so obtained are summarized in Table 2.2, along with $k^{\circ}_{i,NO}$ calculated using Eqs. (2.21) and (2.24). As shown, the mass transfer coefficients for O_2 and NO were found to be nearly identical. The O_2 values for the PDMS tubing represent the average of experiments with tubing lengths of 4, 6, and 8 cm, as no dependence of k°_{t,O_2} on length was observed. At the end of some experiments the reactor was sealed, after which $\overline{C}_{O_2}$ consistently stabilized at a sub-ambient level, confirming that the reactor was gas-tight.

2.3.2 Tests using nitrite and NMor accumulation

Figure 2.3 shows O_2 and NO profiles for a representative experiment with 10% NO and no PDMS tubing loop. In this case $t = 0$ is when the NO flow was started. There was a rapid increase in NO concentration during the first few minutes, followed by a slow

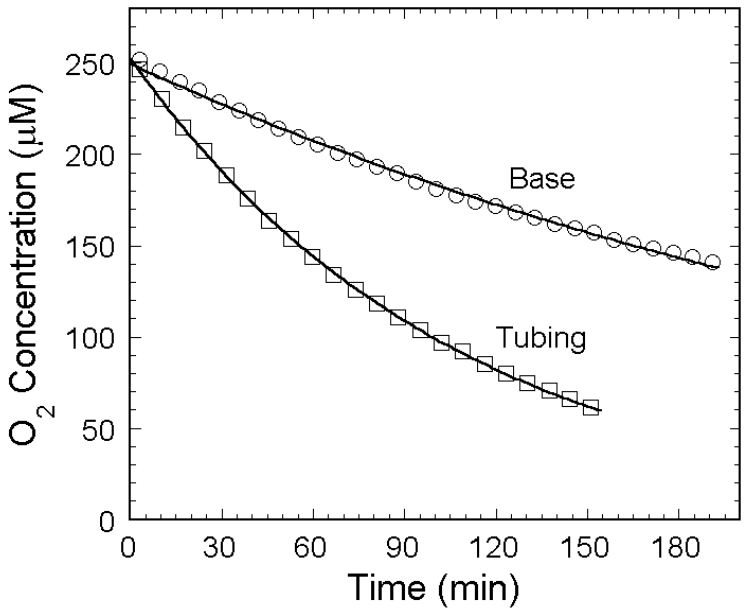

Figure 2.2. Measured O_2 concentration in representative O_2 depletion experiments.

For the data marked 'Base', the PTFE membrane was present and the PDMS tubing was absent. For the data marked 'Tubing', 6 cm of PDMS tubing was used and the PTFE membrane was replaced with a PVDF barrier. The solid curves were calculated using the best-fit value of the mass transfer coefficient for the data shown.

Table 2.2. Mass transfer coefficients for O_2 and NO at the base membrane and tubing in the absence of reactions

	Base (n = 7)	Tubing (n = 5)
	$A_m k^{o}_{m,j}$ ($m^3\ s^{-1}$)	$k^{o}_{t,j}$ ($m\ s^{-1}$)
O_2	$4.0 \pm 0.9 \times 10^{-9}$	$2.5 \pm 0.3 \times 10^{-5}$
NO	$4.1 \pm 0.9 \times 10^{-9}$ [a]	$2.5 \pm 0.3 \times 10^{-5}$ [b]

[a] Calculated using Eq. (2.21)

[b] Calculated using Eq. (2.24)

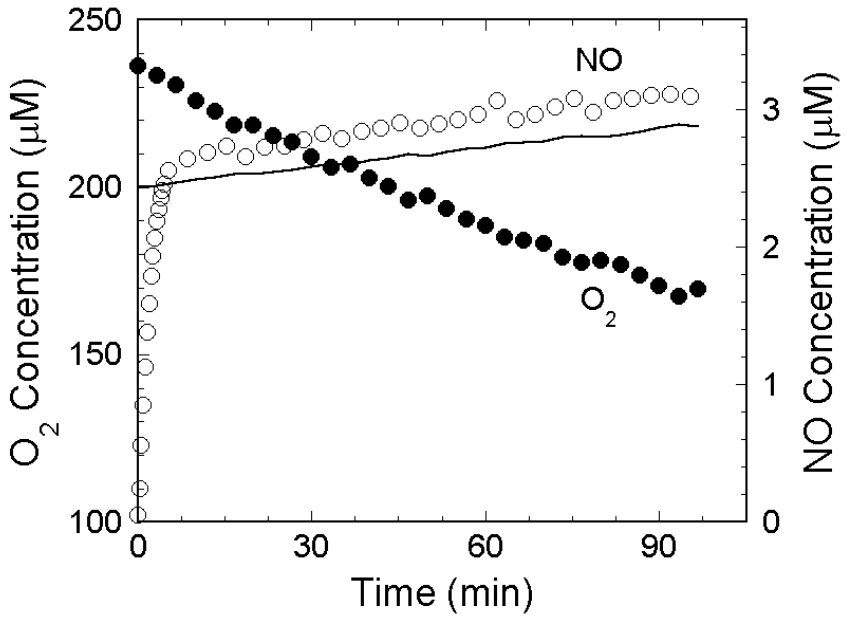

Figure 2.3. Measured NO and O_2 concentrations during delivery of 10% NO to oxygenated buffer without O_2 replenishment.

The discrete symbols are experimental data and the solid curve is the NO concentration calculated from the O_2 data using Eq. (2.25).

upward drift. In the absence of replenishment, the O_2 concentration fell by about 30% over 90 min. The periodic upsets in $\bar{C}_{NO}$ and $\bar{C}_{O_2}$ are due to the liquid sampling and replacement; the NO probe, in particular, was very sensitive to handling. It was postulated that, after the first 10 min, $\bar{C}_{NO}$ is determined by a pseudosteady balance between NO entry and oxidation. Neglecting the time derivative and tubing terms in Eq. (2.9) and noting that $\alpha_{NO} P_{m,NO} >> \bar{C}_{NO}$, the NO concentration is predicted to vary with the O_2 concentration as

$$\bar{C}_{NO} = \sqrt{\frac{\chi_{NO} A_m k^{o}_{m,NO} \alpha_{NO} P_{m,NO}}{4\gamma k_1 \bar{C}_{O_2} V}} . \tag{2.25}$$

The solid curve in Figure 2.3 was obtained by using the measured values of $\bar{C}_{O_2}$ in Eq. (2.25). The prediction of Eq. (2.25) matches the data within 10%, confirming the pseudosteady balance between the entry and oxidation of NO.

Nitrite data from multiple delivery experiments in the absence of Mor with 10% NO and no O_2 replenishment are shown in Figure 2.4. After an initial transient, the rate of NO_2^- accumulation was constant at 53 ± 2 μM/hr (mean ± s. d., n = 8). This stems from the fact that $\alpha_{NO} P_{m,NO} >> \bar{C}_{NO}$, so that the entry rate of NO is constant. The results were highly reproducible, and the NO_2^- accumulation rate calculated from the experimental NO and O_2 concentrations (52 ± 3 μM/hr, n = 8) was indistinguishable from that measured. The correction of the nitrite data for residual NO, which ranged between 2.7 and 3.5 μM, was 15% for the data points at t = 15 min and decreased to less than 5% by t = 60 min.

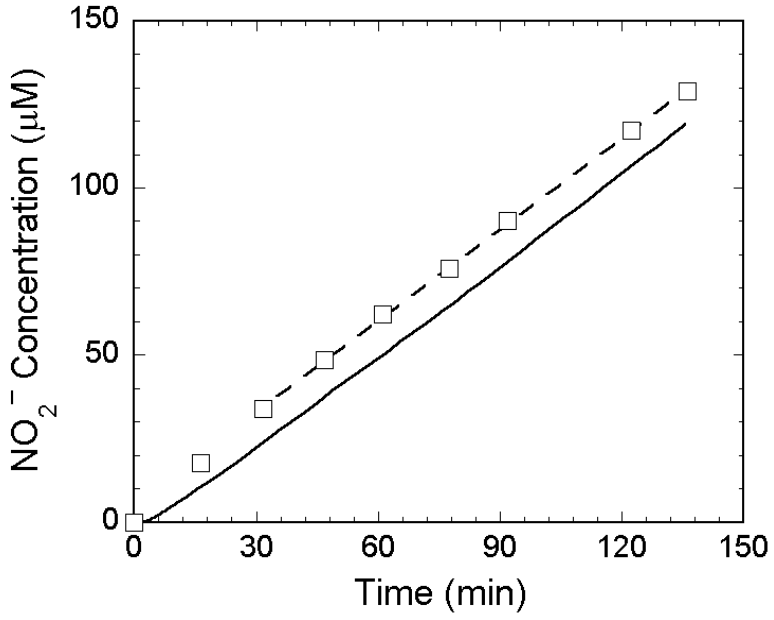

Figure 2.4. Nitrite concentration during delivery of 10% NO to oxygenated buffer without O_2 replenishment in the absence of morpholine.

The discrete symbols are averages of results from the Griess assays (n = 4); error bars of ± 1 s.d. for both time and NO_2^- concentration are smaller than the symbols. The dashed line is a linear fit of the data for $t \geq 30$ min, and the solid line is the prediction obtained by integrating Eq. (2.11) using the NO and O_2 data for one representative experiment.

The one unexpected finding in Figure 2.4 is the positive intercept that was obtained when extrapolating a linear fit to the data for $t \geq 30$ min back to $t = 0$. A negative intercept should result from the initial absence of NO. This discrepancy may have resulted from incomplete elimination of O_2 from the NO delivery space and/or the PTFE membrane prior to introducing the NO gas mixture. The intercept corresponds to a NO_2^- concentration of 9 μM, which [from Reaction (2.5)] would require an excess O_2 concentration of 2.25 μM. With $V = 65$ mL, the corresponding excess quantity of O_2 is 150 nmol. The void volume of the membrane is calculated to contain 260 nmol of O_2 when equilibrated with ambient air. Much of this could react with NO to form NO_2 within the membrane, during a brief period after initiating the NO-containing gas flow. This NO_2 could create the excess NO_2^- by reacting with NO within the liquid.

Nitrite and NMor data from one representative delivery experiment in the presence of 2 mM Mor with 10% NO and no O_2 replenishment is shown in Figure 2.5. As with the data in Figure 2.4, after a brief transient the rate of nitrite accumulation was linear, while that of NMor was linear from the start of the experiment. The NO_2^- and NMor accumulation rates under these conditions were 49 ± 1 and 4.2 ± 0.1 μM h^{-1}, respectively (mean ± s.d.; n = 4). These accumulation rates correspond to an NMor yield of $Y_{NMor} = 0.079$, which is in good agreement with the value of 0.11 predicted by Eq. (2.8) for the morpholine (2 mM) and phosphate (50 mM) concentrations used. The sum of the NO_2^- and NMor accumulation rates (53 ± 1 μM h^{-1}) is indistinguishable from the Mor-free nitrite accumulation rate, which is as expected if Reaction (2.1) is rate limiting. The small intercept at $t = 0$ seen in the NMor data was reproducible and statistically different from zero ($p = 0.01$). This intercept presumably stems from some

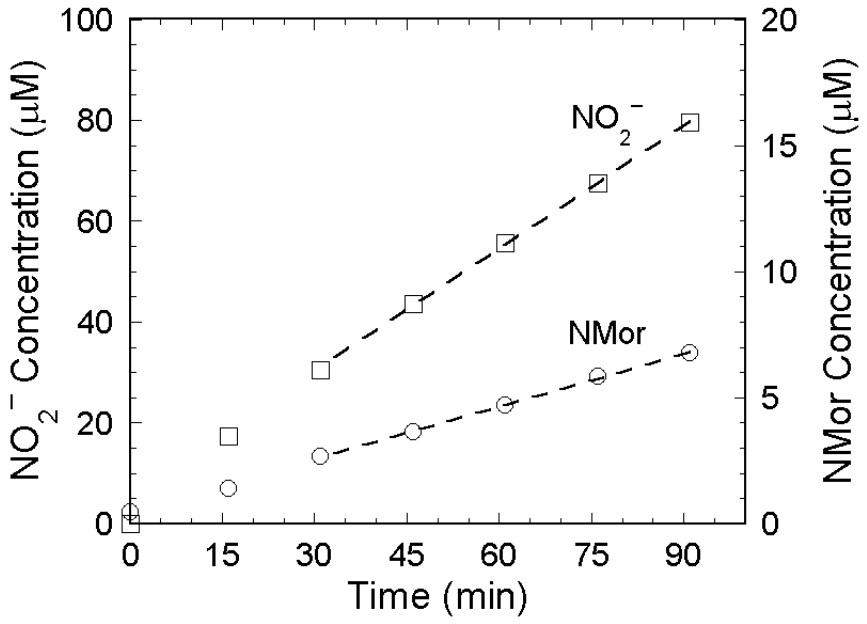

Figure 2.5. Nitrite and N-nitrosomorpholine concentrations in delivery of 10% NO to oxygenated buffer without O_2 replenishment in the presence of morpholine.

The discrete symbols are results from the Griess and spectrophotometric assays for one representative experiment. Error bars of ± 1 s.d. for both sets of concentration data are smaller than the symbols. The dashed lines are linear fits of the data for $t \geq 30$ min.

contamination of the reactor contents, possibly due to dissolution of an optically absorptive component of the grease used to seal the laminated membrane.

2.3.3 Simultaneous delivery of NO and O_2

A representative plot of NO and O_2 concentrations measured during simultaneous delivery is shown in Figure 2.6. In this experiment 1% NO and 20% O_2 were used, resulting in sub-ambient O_2 ($\bar{P}_{O_2}$ = 100 mmHg). An initial N_2 purge of 37 min was needed to lower $\bar{C}_{O_2}$ to the desired level. After the NO and O_2 mixtures were introduced at $t = 0$, $\bar{C}_{NO}$ rose to a steady value of 0.84 μM within approximately 15 min, while $\bar{C}_{O_2}$ remained stable at 155 μM. The steady concentrations were in good agreement with those predicted using the model (horizontal dashed lines).

The O_2 concentration affects both the steady value of $\bar{C}_{NO}$ and the time required to reach that value (the "rise time"), as shown in Figure 2.7. These data are for 1% NO at three O_2 levels in the liquid. Higher O_2 concentrations depress $\bar{C}_{NO}$ by increasing the rate of NO oxidation, and also lead to shorter rise times. These trends are captured well by the model (solid curves). The 25% discrepancy in the steady value of $\bar{C}_{NO}$ at $\bar{P}_{O_2}$ = 25 mmHg is probably due largely to a measurement error, as discussed later. Noteworthy in Figure 2.7 is that the initial value of $d\bar{C}_{NO}/dt$ is independent of $\bar{P}_{O_2}$. This can be explained by observing that $\bar{C}_{NO}(0) = 0$, for which Eq. (2.9) gives

$$\frac{d\bar{C}_{NO}}{dt}(0) = \frac{\chi_{NO} A_m k^{o}_{m,NO} \alpha_{NO} P_{m,NO}}{V}. \qquad (2.26)$$

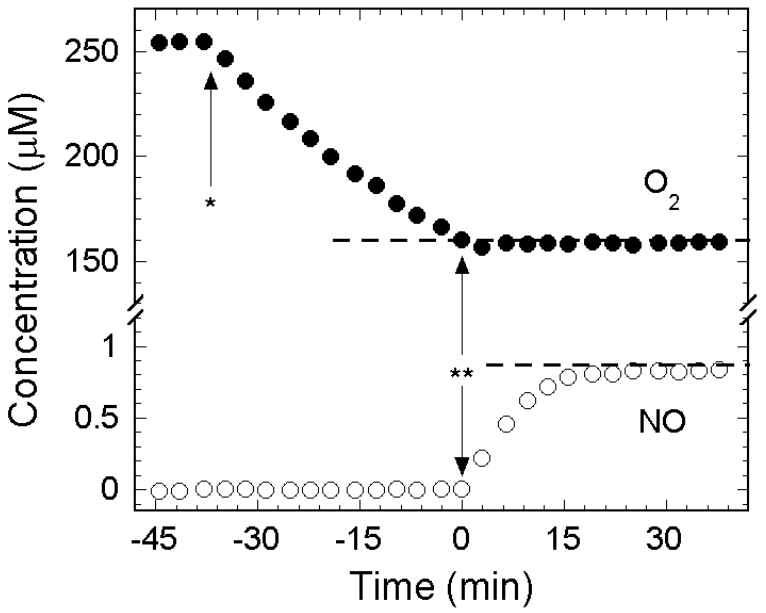

Figure 2.6. Measured O_2 and NO concentrations during simultaneous delivery of 20% O_2 and 1% NO to oxygenated buffer.

The PDMS tubing length was 5.2 cm. The flow of pure N_2 through the tubing and reactor base was begun at the time marked by "*" and the flow of the O_2 and NO mixtures was begun at the time marked by "**". The dashed lines are the steady-state concentrations predicted using Eqs. (2.9) and (2.10).

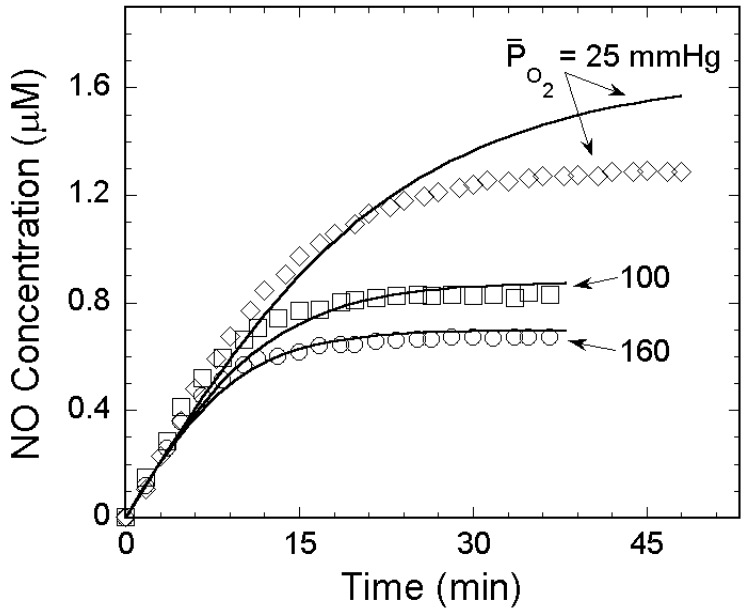

Figure 2.7. Measured and predicted NO concentrations during simultaneous delivery of O_2 and NO at three steady-state O_2 partial pressures in the liquid ($\bar{P}_{O_2}$).

A 1% NO mixture was used in each case. The O_2 gas mixtures and tubing lengths were as shown in Table 2.3. The data are shown by the discrete symbols and the solid curves are the predictions using Eqs. (2.9) and (2.10).

The time constant for the approach of $\bar{C}_{NO}$ to steady state was inferred by recognizing that the escape of NO through the PDMS tubing is usually small relative to its consumption by O_2. Moreover, $\alpha_{NO} P_{m,NO} >> \bar{C}_{NO}$, in which case Eq. (2.9) can be reduced to

$$\frac{d\bar{C}_{NO}}{dt} = \frac{\chi_{NO} A_m k^{o}_{m,NO}}{V} \alpha_{NO} P_{m,NO} - 4\gamma k_1 \bar{C}^2_{NO} \bar{C}_{O_2} . \tag{2.27}$$

Converting to dimensionless variables gives

$$\frac{d\Theta}{d\eta} = 1 - B^2 \Theta^2 \; ; \; \Theta(0) = 0 \tag{2.28}$$

where

$$\Theta = \frac{\bar{C}_{NO}}{C^*_{NO}} , \; \eta = \frac{t}{t^*} , \; t^* = \frac{V C^*_{NO}}{\chi_{NO} A_m k^{o}_{m,NO} \alpha_{NO} P_{m,NO}} , \; B^2 = \frac{4\gamma k_1 \left(C^*_{NO} \right)^2 \bar{C}_{O_2} V}{\chi_{NO} A_m k^{o}_{m,NO} \alpha_{NO} P_{m,NO}} . \tag{2.29}$$

The concentration scale C^*_{NO} is the predicted steady-state value of $\bar{C}_{NO}$, and $\bar{C}_{O_2}$ is assumed to be constant at its steady-state value. The time scale t^* was chosen to make the constant term in Eq. (2.28) unity. The solution is

$$\Theta(\eta) = \frac{1}{B} \left[\frac{1 - \exp(-2B\eta)}{1 + \exp(-2B\eta)} \right] . \tag{2.30}$$

The fact that both exponential arguments have pre-factors of $2B$ indicates that the transient rise in $\bar{C}_{NO}$ should have a single characteristic time scale, $\tau_{NO} = t^*/2B$. Substitution of Eq. (2.29) into this expression for τ_{NO} yields

$$\tau_{NO} = \frac{1}{4}\sqrt{\frac{V}{\chi_{NO} A_m k_{m,NO} k_1 \bar{C}_{O_2} \alpha_{NO} P_{m,NO}}}, \tag{2.31}$$

which is consistent with the shorter rise times seen at higher O_2 levels.

Table 2.3 summarizes the data and simulation results for all experiments involving simultaneous NO and O_2 delivery. Included are the gas mixtures and tubing lengths (L) that were used, the steady-state concentrations, and the time constants for the approach of $\bar{C}_{NO}$ to its steady value. The final NO concentrations ranged from 0.7 to 2.3 μM, depending on the conditions used. The time constants predicted from Eq. (2.31) were in excellent agreement with those measured, as were the steady values of $\bar{C}_{O_2}$ and $\bar{C}_{NO}$ obtained from Eqs. (2.9) and (2.10).

2.4 Discussion

2.4.1 Elimination of adventitious NO oxidation

The continuous delivery of NO and O_2 by diffusion through gas-permeable membranes appears to be the most practical way to expose cells or biomolecules to constant levels of NO for hours to days. However, great care is needed to avoid artifacts caused by unrealistic levels of RNS. The present work was motivated by an unexpected aspect of a delivery system that is similar to the one described here, but which uses loops of PDMS tubing for both NO and O_2 delivery (Wang and Deen, 2003). In both designs the NO and O_2 concentrations can be maintained indefinitely at levels representative of those in macrophage-infiltrated tissues. [For example, the NO concentration in inflamed colonic crypts has been estimated as 0.3 μM (Chin et al., 2008)]. However, when NO

Table 2.3. Simulated and observed NO and O_2 concentrations and NO rise times for simultaneous NO and O_2 delivery at various O_2 concentrations

				Predicted			Observed		
$\bar{P}_{O_2}$ mmHg	%O_2	%NO	L cm	$\bar{C}_{NO}$ μM	$\bar{C}_{O_2}$ μM	τ_{NO} min	$\bar{C}_{NO}$ μM	$\bar{C}_{O_2}$ μM	τ_{NO} min
	30%	10%	8.0	2.2	270	1.6	2.2	260	1.7
160	35%	10%	5.1	2.2	270	1.6	2.3	260	1.6
	30% [a]	1%	6.3	0.69	260	5.2	0.67	260	5.7
100	20%	1%	5.2	0.86	160	6.6	0.84	160	6.5
40	8%	1%	5.3	1.3	64	10	-	-	-
25	5%	1%	5.3	1.6	40	13	1.3	43	11

[a] O_2 mixture to be used in combination with Figure 2.8 at $\bar{P}_{O_2}$ = 160 mmHg

was delivered via PDMS tubing, the rate of NO_2^- formation was approximately nine times that calculated by using the measured NO and O_2 concentrations in Eq. (2.11). The enhanced NO_2^- production was explained by postulating that there is oxidation of NO to NO_2 within the wall of the PDMS tubing loop that supplies NO (Wang and Deen, 2003). A predicted consequence of this is greatly elevated concentrations of NO_2 and N_2O_3 in a very thin (~1 μm) layer of liquid next to the NO tubing. Although this "hot spot" should not affect experiments involving cells, which are unlikely to enter the thin layer with elevated RNS concentrations, it greatly complicates the interpretation of kinetic data for substrates that react with NO_2 or N_2O_3.

The evidence that this problem was eliminated in the present apparatus is that the predicted and observed rates of NO_2^- formation are now indistinguishable (Figure 2.4). In other words, replacing the NO delivery tubing with a porous PTFE membrane apparently avoids adventitious oxidation of NO. The reason this works is that O_2 diffuses much more rapidly through gas-filled pores than through PDMS, and its ability to escape into the NO gas keeps its concentration within and near the PTFE membrane very low. At the same time, the mass transfer resistance in the liquid keeps the loss of O_2 via this route small. Scaling arguments to support this hypothesis are presented in Appendix D. That PDMS tubing can continue to be used for O_2 delivery is consistent with the model proposed previously (Wang and Deen, 2003), which predicted that NO oxidation within the tubing wall would be significant only in the NO loop. Elimination of the "hot spot" and knowledge of the NO concentration enables prediction of the steady-state RNS concentrations in defined aqueous solutions (Lewis and Deen, 1994) and in cells (Lim et al., 2008).

In addition to the use of a porous, hydrophobic membrane for NO delivery, avoiding undesired RNS in the membrane or gas space requires that there be a sufficient flow rate (at least 350 sccm) through the base of the reactor, that a soda lime column be used to remove higher nitrogen oxides (primarily NO_2), and that O_2 be excluded from the NO gas line by using only stainless steel and glass components. [This last point was noted also by Thomas et al. (2001).] The thermal lamination of the PTFE membrane with the PVDF mask was found to be important also. Preliminary experiments with no mask and with an unlaminated mask both showed dramatically increased NO_2^- accumulation rates, because of poor sealing from the atmosphere and/or the ability of NO and O_2 to coexist within the unmasked portions of the PTFE membrane (see Section D.5).

To note, the success of the reactor design in preventing adventitious NO oxidation permitted invocation of the QEA for both NO_2 and N_2O_3 (Section 2.2.6.2). In any attempt to develop a model for a system where significant quantities of contaminating NO_2 or N_2O_3 are present in the NO feed stream as in Wang and Deen (2003), however, it would be necessary to simulate one or both of the contaminating species explicitly. As with N_2O_4 (Section 3.2.5.4), it would probably be sufficient to continue treating N_2O_3 as a quasi-equilibrium species, while simulating NO_2 directly. Any differences in diffusivity or solubility between NO, NO_2, and N_2O_3 would potentially become significant in this more general model. Again as with N_2O_4 (Section 3.2.5.4), it would likely be acceptable to assume that $D_{NO_2} \approx D_{N_2O_3}$ but not that $\alpha_{NO_2} \approx \alpha_{N_2O_3}$. Since both the gas- and liquid-phase equilibrium constants for Reaction (2.2) are well established (Graetzel et al., 1970; Wiberg and Aylett, 2001), estimation of $\alpha_{N_2O_3}$ using thermodynamic constraints as in Appendix C should provide a sufficiently accurate value.

2.4.2 Model performance

A model was developed to predict the effects of gas composition and tubing length on the steady-state concentrations of NO and O_2 in the liquid, and to provide guidance on how quickly those concentrations can be achieved. As shown by the results in Figures 2.6 and 2.7 and Table 2.3, the simulation results were consistent with all of the observed trends. The O_2 concentrations, NO concentrations, and time constants were all predicted quite accurately. A likely cause of the discrepancy in $\overline{C}_{NO}$ at $\overline{P}_{O_2} = 25$ mmHg is the presence of 5% CO_2 in this particular O_2 mixture. Acidification of the internal electrolyte of the NO probe, such as by introduction of CO_2, is expected to depress the sensor response (Zhang, 2008). Thus, the measured value of $\overline{C}_{NO}$ may be too low in this one case. In addition to accurately describing the NO and O_2 concentrations within the reactor, the model also described well the rates of formation of NO oxidation end products within the system. The good agreement between model and data in the test experiments (Section 2.3.2) permits a great deal of confidence in applications of the reactor to other chemical systems of interest.

Although all of the experiments were performed at room temperature, the various parameter values can be extrapolated from 23 °C to 37 °C with reasonable confidence, as explained in Section 2.4.3. The temperature-correction factors, which range from an 18% decrease in an input to a 38% increase, are listed in Table 2.4 along with the corrected parameter values. Employing these corrections, the model can be used to predict the NO and O_2 concentrations that would be obtained at body temperature.

Table 2.4. Extrapolation of room-temperature parameter values to body temperature

The correction factors for NO and O_2 were assumed to be equal. The units of each quantity are as in Tables 2.1 and 2.2.

Parameter (X)	$\frac{X^{37°C}}{X^{23°C}}$	$X^{37°C}$	
		NO	O_2
α_j	0.82	1.5×10^{-3}	0.98×10^{-3}
$\tilde{\alpha}_j\tilde{D}_j$	1.17	3.6×10^{-11}	2.5×10^{-11}
D_j	1.38	3.0×10^{-9}	2.9×10^{-9}
$k^{o}_{m,j}$	1.30	5.3×10^{-9}	5.2×10^{-9}
$k^{o}_{t,j}$	1.35	1.9×10^{-5}	1.9×10^{-5}
k_1	1.14	2.4×10^{6}	

2.4.3 Estimation of parameter values at body temperature

The temperature dependence of the aqueous solubilities (α_j) was estimated from tabulated data (Green and Maloney, 1997), while that for the aqueous diffusivities (D_j) was assumed to follow the Stokes-Einstein relationship (Deen, 1998). The PDMS permeabilities ($\tilde{\alpha}_j \tilde{D}_j$) and the autoxidation rate constant (k_1) were assumed to exhibit an Arrhenius-type temperature dependence, based on the data of Robb (1968) and Lewis and Deen (1994), respectively. Because variations in $k^{\circ}_{m,j}$ are due only to changes in D_j, temperature corrections were made using an expression analogous to Eq. (2.21).

The values of $k^{\circ}_{t,j}$ at 37°C were estimated as follows. Values of $k^{\circ}_{f,j}$ at 23°C were obtained by rearrangement of Eq. (2.23) and substitution of the parameters from Tables 2.1 and 2.2. Values for $k^{\circ}_{f,j}$ at 37°C were found then by analogy with Eq. (2.21). The values for $k^{\circ}_{t,j}$ at 37°C were then calculated from Eq. (2.23) using the estimated parameter values at 37°C. The final correction factors for $k^{\circ}_{t,\mathrm{O_2}}$ and $k^{\circ}_{t,\mathrm{NO}}$ were slightly different (1.34 and 1.36, respectively); the mean of these two values is reported in Table 2.4.

The effects of temperature on the film and bulk reaction rates in Eq. (2.17) cancel, and the effective film thickness was assumed to be constant. Accordingly, the correction factor for the reaction rate (γ) at body temperature is the same as that given in the text for room temperature. Likewise, in calculating the correction factors for the mass transfer coefficients (χ_j) from Eq. (2.18), the effects of temperature cancel.

2.4.4 Application of the delivery system

The gas compositions and tubing lengths needed to give desired steady-state NO and O_2 concentrations can be obtained either via simulations using Eqs. (2.9) and (2.10) or graphically, as follows. The O_2 gas mixtures needed to give any of four steady O_2 partial pressures in the liquid ($\overline{P}_{O_2}$ = 160, 100, 40, or 25 mmHg) are as in Table 2.3. Figure 2.8(a) shows the NO gas composition that is needed to achieve a given NO concentration in the liquid, at either 23 or 37 °C. Once the values of $\overline{C}_{NO}$ and $\overline{P}_{O_2}$ are selected, the corresponding %NO can be read from the ordinate. As can be seen, the differing temperatures have almost no effect on the required NO gas composition. The required tubing length can be determined in a similar fashion from Figure 2.8(b). Note that this is the exposed length, and that it is constrained to 4-8 cm to avoiding kinking or interference with the stirrer. The tubing lengths needed at 37 °C are predicted to be approximately 2 mm shorter than those for 23 °C.

The use of sub-ambient levels of O_2 requires an initial purge before NO is introduced, as illustrated in Figure 2.6. The reduction of $\overline{P}_{O_2}$ to the desired level can be done most rapidly by flowing pure N_2 through both the PDMS tubing and the base of the reactor. During this period there are no reactions and $P_{t,O_2} = P_{m,O_2} = 0$. The solution to Eq. (2.10) for the purge period has the same exponential form as Eq. (2.20), but with a time constant given by

$$\tau_{\text{purge}} = \frac{V}{\chi_{m,O_2} A_m k^{o}_{m,O_2} + 2\pi r_o L k^{o}_{t,O_2}} . \tag{2.32}$$

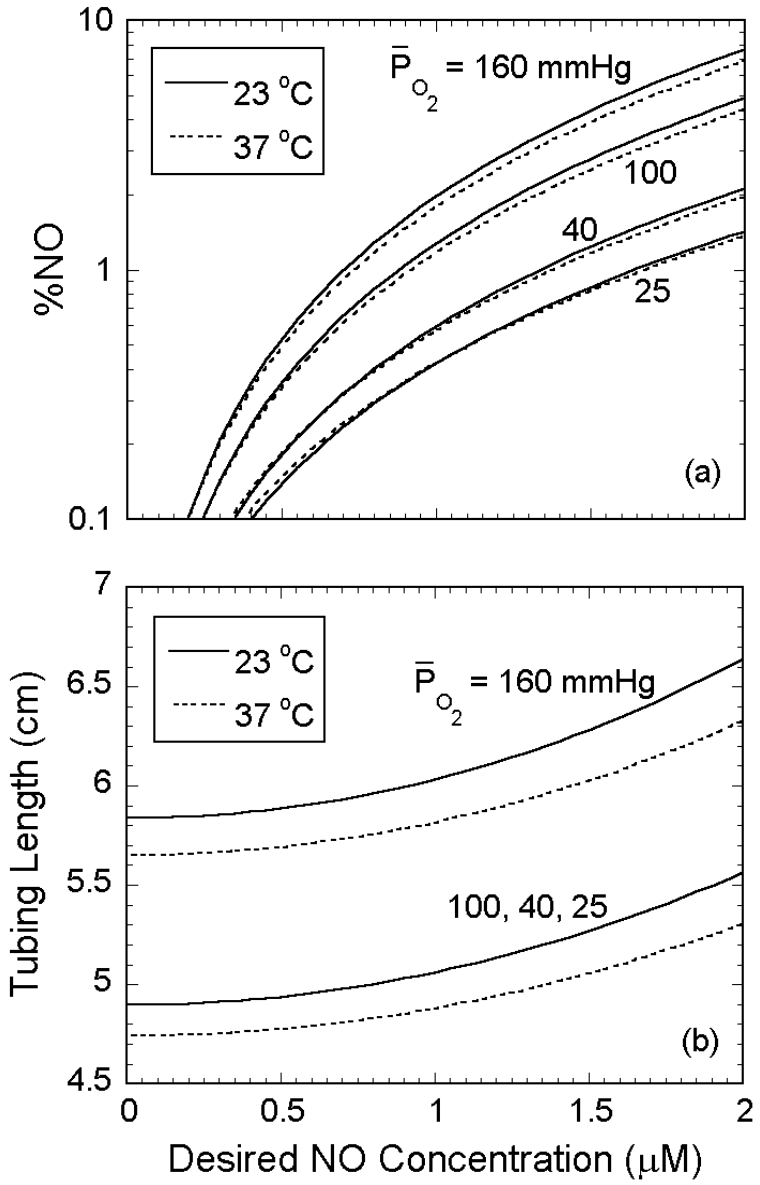

Figure 2.8. Composition of NO gas and PDMS tubing length required to give a desired steady value of $\bar{C}_{NO}$.

NO composition (a) and tubing length (b) results are shown for four values of the steady O_2 partial pressure in the liquid ($\bar{P}_{O_2}$) and two temperatures, 23°C and 37°C. To achieve these partial pressures, the O_2 gas mixture must be selected as shown in Table 2.3.

Using the parameter values in Tables 2.1 and 2.2, the time required to reach a desired $\overline{P}_{O_2}$ level at 23°C is

$$t_{\text{purge}}^{23°C}[\text{min}] = \left(\frac{1000}{3.63 + 1.42\, L[\text{cm}]} \right) \cdot \ln\left(\frac{161}{\overline{P}_{O_2}[\text{mmHg}]} \right). \tag{2.33}$$

Using also Table 2.4, the purge time for 37°C is

$$t_{\text{purge}}^{37°C}[\text{min}] = \left(\frac{1000}{4.72 + 1.92\, L[\text{cm}]} \right) \cdot \ln\left(\frac{161}{\overline{P}_{O_2}[\text{mmHg}]} \right) \tag{2.34}$$

Once this time is reached, the tubing gas stream should be switched to the appropriate O_2 mixture. If desired, the sub-ambient $\overline{P}_{O_2}$ can be maintained indefinitely by continuing the flow of O_2 through the tubing and pure N_2 through the reactor base. Or, NO flow through the base of the reactor can be initiated immediately.

2.5 Conclusion

A novel apparatus for the continuous supply of NO and O_2 to biological media has been fabricated and characterized. It avoids the adventitious oxidation of NO that complicates data interpretation with earlier designs, while retaining the advantages of diffusion through gas-permeable membranes into a small liquid-filled vessel. The concentrations of NO and O_2 can be adjusted in a predictable manner and physiologically relevant levels maintained indefinitely.

Elimination of the adventitious NO oxidation makes this reactor a promising tool for chemical kinetic experiments involving the reactive byproducts of NO. The good agreement of experimental and simulated product yields implies that the system should

permit reliable inference of unknown rate constants in mechanisms of interest. Further confirmation of the reactor behavior could be obtained by delivering NO to ABTS, which is oxidized by NO_2 with elementary second-order chemistry (Section 2.1). One possible application of the device would be to reproduce the experiments of Dong et al. (2003) and Dendroulakis et al. (2007), which investigated the rates of formation of nucleic acid damage products after exposure to nitric oxide. Dong et al. (2003) attempted to correct for the effects of adventitious NO oxidation by comparing the observed product formation rates to those of morpholine, but it should be possible to obtain a more confident estimate of the relevant rates of reaction in the present device where the unwanted chemical complexity is absent.

Another potential application of this system is re-examination of the mechanism of nitro-tyrosine (N-Tyr) and di-tyrosine (di-Tyr) formation from the reaction of tyrosine with NO-derived RNS. The rate constant most frequently used in the literature for the reaction of NO_2 and tyrosine [see, e.g., Goldstein et al. (2000) and Hodges et al. (2000)] is that of Prutz et al. (1985), which actually pertains to the reaction of NO_2 and the tyrosine moiety of a glycyl-tyrosine dipeptide. *N*-terminal functionalization of tryptophan has been shown to modulate its reactivity with N_2O_3 (Bonnett and Holleyhead, 1974; Kirsch et al., 2003; Zhang et al., 1996), and it is thus reasonable to question whether equating the reactivities of Tyr and Gly-Tyr can be justified. Preliminary experiments delivering NO to Tyr solutions yielded much smaller rates of formation of N-Tyr and di-Tyr than expected, even accounting for the formation of an adduct between NO and tyrosyl radical (Goldstein et al., 2000). In combination with specific delivery of NO_2 using the system described in Chapter 3 and applying recently developed techniques

for assay of sub-picomole quantities of N-Tyr and di-Tyr (Zeng et al., 2010), direct elucidation of these rate constants would be useful in (re-)interpreting the results of studies of this tyrosine oxidation/nitration mechanism.

Chapter 3

Nitrogen Dioxide Delivery System for Biological Media

3.1 Introduction

Nitrogen dioxide is an inorganic radical capable of reaction with a variety of substrates. While it lacks the more ubiquitous reactivity of hydroxyl radical (Buxton et al., 1988) and carbonate radical anion (CO_3^-; Augusto et al., 2002), a number of biologically significant molecules are susceptible to attack by NO_2, including proteins (Bartesaghi et al., 2007), nucleic acids (Beda and Nedospasov, 2007; Shafirovich et al., 2001), lipids (Balazy and Chemtob, 2008; Halliwell et al., 1992), and numerous smaller molecules [e.g., ascorbate and α-tocopherol (Forni et al., 1986)]. Cytotoxic, mutagenic or carcinogenic effects are expected from many of these reactions.

Environmental exposures to NO_2 as a pollutant have been studied in some depth (Hesterberg et al., 2009; Monn, 2001; Weichenthal et al., 2007). The formation of NO_2 by endogenous processes is also well established (Augusto et al., 2002). Reaction of elevated levels of NO with O_2 generates NO_2 and N_2O_3 (Lewis et al., 1995b) at concentrations sufficiently high to be toxic or mutagenic (Burney et al., 1997). NO also reacts with superoxide radical anion (O_2^-), a byproduct of cellular respiration, at a near diffusion-controlled rate to form peroxynitrite anion ($ONOO^-$; Nauser and Koppenol, 2002). $ONOO^-$ subsequently reacts rapidly with CO_2 to produce NO_2 and CO_3^- at a yield of approximately 33% (Goldstein et al., 2001). Neutrophils recruited to sites of inflammation or infection also may generate NO_2 directly from NO_2^-, via externally

expressed myeloperoxidase (Sampson et al., 1998). Finally, Fenton chemistry in the presence of NO_2^- is a possible route for NO_2 formation *in vivo* (Thomas et al., 2002).

The complex mixture of reactive nitrogen species (RNS) generated in the presence of micromolar levels of NO can complicate attribution of a given mode of damage to a particular RNS. Methods for delivery of each of these species in isolation would therefore be useful in determining which species is responsible for a particular type of chemical modification. It is thus of interest to study the effects on cells and biomolecules of NO_2 exposure mimicking that expected *in vivo*. As the free radical nature of many reactions of NO_2 causes their rates to be nonlinear in the NO_2 concentration (e.g., the reaction of NO_2 with tyrosine; Goldstein et al., 2000), in these exposures the NO_2 concentration should be well quantified and comparable to that predicted to occur *in vivo* [ranging between an extracellular concentration of 500 pM in the presence of 1 μM NO in buffer [estimated from rate data of Lewis et al. (1995b)] and an intracellular concentration of 5 pM in cells exposed to 1 μM NO (Lim et al., 2008)]. Also, the exposures ideally will be steady and sustainable for hours to days.

Study of NO_2 is complicated by the absence of reliable methods for direct concentration measurements in solution, as well as the rapid hydrolysis of its dimer, dinitrogen tetroxide (N_2O_4) (Graetzel et al., 1969), to equal quantities of nitrous and nitric acids. The dimerization and hydrolysis are written as

$$2\,NO_2 \underset{}{\overset{K_1}{\rightleftharpoons}} N_2O_4\,. \tag{3.1}$$

$$N_2O_4 + H_2O \xrightarrow{k_2} HNO_2 + HNO_3\,. \tag{3.2}$$

These reactions often require that characterization of the solubility, diffusivity, and mass transfer of NO_2, as well as its rate of reaction with particular species, must be performed based upon analysis of the rate of formation of end products (Lee and Schwartz, 1981; Mertes and Wahner, 1995) and/or from thermodynamic arguments based on related systems (Schwartz and White, 1981). In certain cases, kinetic information can be inferred from analysis of intermediates with favorable spectrophotometric, fluorimetric, or electron spin resonance properties (Alfassi et al., 1990; Bielski and Gebicki, 1969; Lagercrantz, 1969; Mahal et al., 1999), but such techniques are often inapplicable in the complex media required for cell culture. Study of delivery of NO_2 to neutrally-buffered or alkaline solution is simplified somewhat by the rapid dissociation of the nitrous and nitric acids formed from Reaction (3.2) to stable nitrite and nitrate ions, respectively.

Numerous reactions of NO_2 with various substrates have been studied using pulse radiolysis or flash photolysis techniques: irradiation of N_2O-saturated solutions in the presence of sufficient levels of NO_2^- and NO_3^- generates primarily NO_2 (Bartesaghi et al., 2004; Forni et al., 1986; Goldstein et al., 2004b). One substrate of particular relevance is 2,2′-azino-bis(3-ethylbenzothiazoline-6-sulfonate) (ABTS), which is oxidized by NO_2 to form NO_2^- and the moderately stable, strongly colored ABTS radical ($ABTS^+$; Goldstein and Czapski, 1995):

$$NO_2 + ABTS \xrightarrow{k_3} NO_2^- + ABTS^+ . \qquad (3.3)$$

$ABTS^+$ has a lifetime sufficient to permit accurate off-line spectrophotometric quantitation, instead of requiring *in situ* analysis The chemical structures of ABTS and $ABTS^+$ are presented in Figure 3.. As pulse radiolysis is inherently a transient method, it is poorly suited for experiments where prolonged exposure to NO_2 is required. While

continuous irradiation would provide a steady NO_2 concentration, the apparatus complexity and possibility for NO_2-independent radiative degradation of toxicologically relevant biomolecules limit the usefulness of this method. The difficulty of appropriate sterilization and environmental control (humidity, O_2, CO_2 levels, etc.) in the radiolysis apparatus is also of significant concern.

There appear to be no known NO_2 analogues of the various types of "NO donors," such as the NONOates (Li and Lancaster, 2009; Ramamurthi and Lewis, 1997) and S-nitroso-N-acetyl-penicillamine (Williams, 1985), though chemicals that mimic the activity of NO_2 do exist, such as the phenol-nitrating agent tetranitromethane (Lennon et al., 2007). Diaf and Beckman, 1995 describe a 'polymeric sorbent' material capable of reversibly binding NO_2, but give no data on its stability or NO_2-releasing properties in aqueous suspension. As with most NO donors, however, a donor material would be depleted in the process of generating NO_2, leading to a corresponding decline over time in the NO_2 concentration. Any NO_2-independent toxicity of the donor materials themselves would make them even less attractive for NO_2 delivery to cells.

Based upon our past success in developing methods for generating steady, controlled NO concentrations in small, liquid-filled vessels by the diffusion of NO through gas-permeable membranes [Skinn et al., 2011 (see Chapter 2); Wang and Deen, 2003], we sought to develop an analogous method for NO_2 delivery. Preliminary experiments attempting delivery of NO_2 to a neutrally-buffered aqueous medium via diffusion through poly(dimethylsiloxane) (PDMS) tubing or a flat, porous poly(tetrafluoroethylene) (PTFE) membrane in the manner of Wang and Deen and Skinn et al., respectively, gave results that were not readily interpretable. Specifically, the

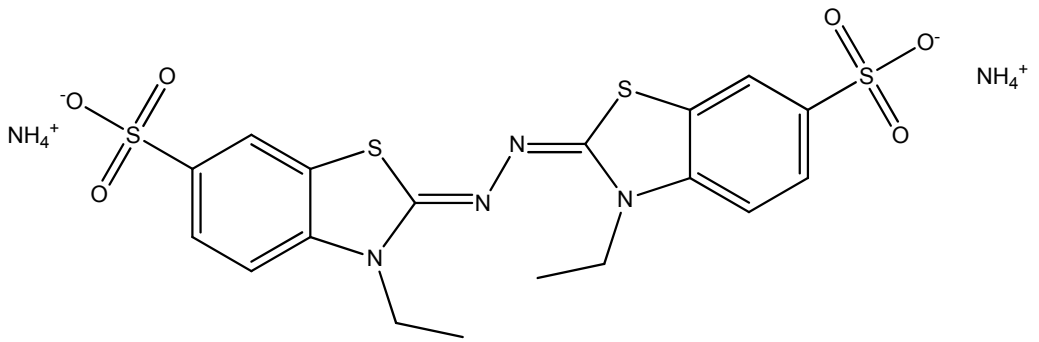

(a)

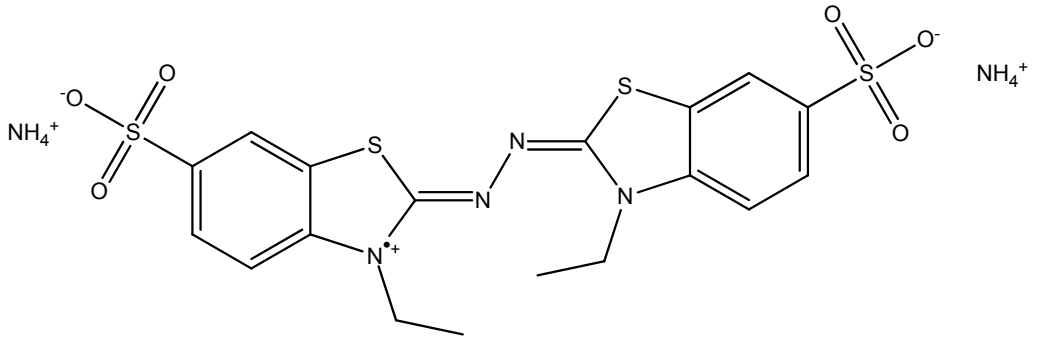

(b)

Figure 3.1. Molecular structure of ABTS species.

Structures for ABTS (a) and ABTS radical (b) were generated by ChemBioDraw Ultra 12 (CambridgeSoft, Cambridge, MA).

observed accumulation rates of the stable end products (NO_2^- and NO_3^- in this buffered system) deviated significantly from the one-to-one ratio predicted by Reaction (3.2) (see Section 3.4.4 for a brief discussion of these results). Adventitious chemistry occurring within the membranes seems the most likely cause of these discrepancies. Intramembrane oxidation chemistry was hypothesized to be significant in the PDMS tubing delivery system of Wang and Deen (2003), leading to unexpectedly high nitrite accumulation rates. Pasternak et al. (1970) found that while the solubilities of CO_2, O_2, N_2 and N_2O_4 in PTFE correlated well with their boiling points, the solubility of NO_2 deviated from this correlation by orders of magnitude. Further, the measured diffusivity of NO_2 in PTFE also differed from that of CO_2 by orders of magnitude, despite the similar sizes of the two molecules. The authors explained this behavior by positing a strong, reversible interaction between NO_2 and PTFE. In other words, it is likely that neither PDMS nor PTFE membranes are passive facilitators of NO_2 transport.

The poor results obtained from membrane-mediated diffusion led us to investigate direct contacting of an NO_2-containing gas with a target-containing liquid. Unlike NO, where gas-phase oxidation reactions introduce unwanted complexity, with NO_2 there is no reason to avoid having a headspace above the stirred liquid. NO_2 is unreactive toward O_2 and, in certain reactor configurations, all gas phase chemistry save the equilibrium of Reaction (3.1) can be neglected. Much of the literature on NO_2 absorption into aqueous solutions addresses the scrubbing of gaseous mixtures of reactive nitrogen species, primarily NO + NO_2 in varying ratios (Atsukawa et al., 1968; Chappell, 1973). Other studies examine atmospheric dynamics such as NO_2 uptake into particulate aerosols, clouds, etc. (Bambauer et al., 1994; Daum et al., 1984) or seek to develop tools for

measurement of atmospheric NO_2 levels (Gerboles et al., 2005; Palmes et al., 1976). The overarching goal of most of this work is to understand and control the polluting effects of nitrogen oxides found in the exhaust from motor vehicles and electrical or chemical production facilities, and the apparatus configurations used therein are consequently poorly suited for examining NO_2 exposure of cells. Another aspect of these systems making them unhelpful for cell exposures is that various species are often added to the aqueous medium in an attempt to enhance uptake of pollutant nitrogen species either by reactive enhancement of mass transfer or by 'trapping' of various intermediates to avoid formation of volatile and relatively unreactive NO (Jin et al., 2006; Khan and Adewuyi, 2010; Kobayashi et al., 1977). Even in the absence of chemical additives, the chemical and physical mechanisms invoked to describe these systems are often prohibitively complex.

We present here a novel system that delivers NO_2 in a controlled and predictable fashion to a stirred, buffered aqueous solution by direct contacting with an NO_2-containing gas stream. A model was developed that describes well the accumulation rates of stable end products both in the absence of substrates and in the presence of ABTS, after correcting for a putative HNO_3 impurity in the feed gas stream. The reactor is inexpensive, of simple construction, easy to sterilize by autoclave, and has been successfully used in the configuration of Wang and Deen (2003) for study of the effects of nitric oxide on a variety of cell lines, including wild-type and p53-null TK6 cells (Dong and Dedon, 2006; Li et al., 2006; Li et al., 2005; Wang et al., 2003), murine embryonic stem cells (Kiziltepe et al., 2005) and human colon cancer HCT116 cells (Li et al., 2009). Considerations pertaining to application of the system in delivery to cells

(Section 3.4.1) and analysis of the system dynamics (Sections 3.4.2 and 3.4.3) are both presented.

3.2 Materials and methods

3.2.1 Chemicals

All chemicals were from Sigma-Aldrich (St. Louis, MO). All reagent solutions were prepared using deionized (DI) water. All experiments were performed using 50 mM sodium phosphate buffer at pH 7.5 prepared using DI water.

3.2.2 Gas delivery system

Pure N_2 and mixtures of 0.001%, 0.01%, 0.1% and 1% NO_2 in N_2 were obtained from Airgas East (Salem, NH). All NO_2 mixtures contained a 3:1 excess of O_2 for stability. The manufacturer's specification is defined as the mole percent of NO_2 in the limit as pressure goes to zero (that is, if all N_2O_4 is dissociated to NO_2). The building lab air supply (filtered and dried by the utility) was used directly. The flow rate of the gas stream to the reactor was controlled by a Porter Instruments mass flow controller (Parker-Hannefin, Hatfield, PA) to 365 standard cubic centimeters per minute (sccm), except as noted. The gas flow rate was measured directly with a Porter Instruments rotameter connected to the reactor outlet. Continuous flow rate measurement was made in experiments with pure N_2 or lab air, but in experiments with NO_2 only a single measurement was made before each experiment using a N_2 test flow, to avoid possible damage to the rotameter. Stainless steel tubing and fittings were used in the NO_2 delivery line; the lab air and N_2 delivery tubing was poly(tetrafluoroethylene) (PTFE). The

pressure within the reactor headspace conditions was measured to be no more than 1% above ambient (1 atm) in test N_2 flows at 365 sccm.

3.2.3 Apparatus

Unless otherwise specified, the reactor consisted of a closed perfluoroalkoxy (PFA) container (110 mL total volume) with both liquid (80 mL) and gas (30 mL) spaces (Figure 3.2). The diameter of the vessel was 6 cm, resulting in a gas-liquid interfacial area of 28.3 cm^2. The container lid was modified to hold a fiber-optic O_2 sensor (Instech Laboratories, Inc., Plymouth Meeting, PA) and a septum port for liquid sampling. Two additional ports served as inlet and outlet for gas flow to the headspace. All reactor components were composed of PFA, PTFE, poly(chlorotrifluoroethylene), or poly(vinylidene fluoride). Detailed parts information for the reactor can be found in Appendix G. All experiments were performed at room temperature (22-24 °C) and with a stirring rate of 100 ± 5 rpm, as determined by a strobe tachometer.

In a few experiments, NO_2 (1% or 0.1%) was delivered either by the method of Wang and Deen (2003) or by that of Skinn et al. (2011)—that is, by diffusion through poly(dimethylsiloxane) (PDMS) tubing or through a flat porous PTFE membrane, respectively—to a liquid-filled reactor with no headspace. In the former case, the NO_2 mixture was flowed through a single tubing loop of active length 7.6 cm, omitting the second loop used by Wang and Deen for O_2 replenishment. In the latter case, the NO_2 mixture was flowed through the base well of the Skinn et al. reactor in the same fashion as the NO stream in that study.

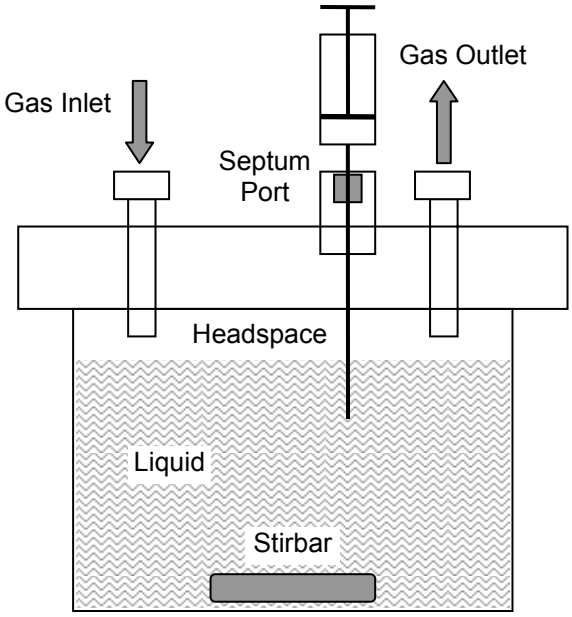

Figure 3.2. Schematic of NO_2 reactor.

3.2.4 Concentration measurements

The O_2 sensor, calibrated as recommended by the manufacturer, had a linear response for concentrations up to ambient levels (0-255 μM), but not above that. Nitrite concentrations were measured by the Griess method. Briefly, to 400 μL of NO_2^- standard solution (0-50 μM) or sample (diluted to 0-50 μM) were added 200 μL of 1% sulfanilamide (SAN) in 5% phosphoric acid ("Griess R1") and 200 μL of 0.1% N-(1-naphthyl)ethylenediamine (NED; "Griess R2"). The absorbance at 540 nm (A_{540}) was read after a 10-min incubation period (BioSpec-1601, Shimadzu Scientific Instruments, Columbia, MD]). Nitrite concentrations were determined by comparison to a calibration curve generated from a NO_2^- standard solution.

Total nitrate plus nitrite was measured by the Griess method after enzymatic reduction of nitrate to nitrite via a protocol modified from that of Grisham et al. (1996). Briefly, for each sample a cuvette was charged with the following (all concentrations listed are for the stock solutions): DI H_2O (250 μL), 1 M HEPES (25 μL), 100 μM FAD (25 μL), 860 μM NADPH (50 μL), and 1.4 U mL^{-1} Aspergillus nitrate reductase (50 μL). To this was added 100 μL either of a NO_3^- or NO_2^- standard (0-50 μM) or of a sample (pre-diluted to 0-50 μM total nitrite plus nitrate). The cuvette was covered with Parafilm M (Bemis Co., Neenah, WI) and incubated at 37 °C for 30 min. Potassium ferricyanide [$K_3Fe(CN)_6$, 11 mM, 50 μL] was added and the sample further incubated for 10 min to consume any remaining NADPH. Griess R1 and R2 (200 μL each) were added and A_{540} was measured after a 10-min incubation period. The concentration of NO_3^- in each sample was determined by comparison with separate NO_3^- and NO_2^- calibration curves and the separately measured NO_2^- concentration. The A_{540} of test samples

containing known amounts of both NO_3^- and NO_2^- matched calibration curve predictions to within 5%. NADPH and nitrate reductase solutions were prepared daily and kept at room temperature. Nitrate reductase was reconstituted with DI H_2O 30-45 min before use, with occasional gentle vortexing. FAD solutions prepared with DI H_2O were stable for approximately one month when stored at 4 °C in a foil-wrapped glass bottle. HEPES and $K_3Fe(CN)_6$ solutions prepared with DI H_2O and stored at 4 °C in glass bottles were stable for at least six months.

The concentration of ABTS in the stock buffer and in samples withdrawn from the reactor was determined spectrophotometrically ($\varepsilon_{340} = 3.6 \times 10^4$ $M^{-1} \cdot cm^{-1}$; Childs and Bardsley, 1975; Wolfenden and Willson, 1982) by comparison against a reference of ABTS-free buffer. The value of ε_{340} for $ABTS^+$ is reported as being 15% of that of ABTS (Childs and Bardsley, 1975); based on this, the contribution of $ABTS^+$ to A_{340} was estimated to be less than 4% for all samples collected and was thus neglected. The concentration of $ABTS^+$ in each sample was also measured spectrophotometrically, with $\varepsilon_{416} = 3.6 \times 10^4$ $M^{-1} \cdot cm^{-1}$ (Goldstein and Czapski, 1995). $ABTS^+$ was found to be the only component of the system with appreciable absorbance at 416 nm, and the $ABTS^+$ absorption was stable for up to two hours at $ABTS^+$ concentrations no greater than 20 μM. After measuring the A_{416} of each NO_2-exposed sample, 0.15 ml of the metal ion chelator diethylene-triamine-pentaacetic acid (DTPA; 5 mM in buffer) was added to 1.5 ml of the sample to consume the $ABTS^+$ (Balcerczyk et al., 2007) before assaying for ABTS, NO_2^-, and NO_3^-.

The presence of ABTS in the samples complicated measurement of NO_2^- and NO_3^-. Addition of Griess R1 to samples containing ABTS and NO_2^- resulted in slow

formation of the blue-green color characteristic of $ABTS^+$. Given the relatively rapid reaction between acidified nitrite and SAN (Fox, 1985), it is likely the $ABTS^+$ formation originates from reaction between ABTS and the diazonium intermediate in the Griess system as opposed to, say, intermediate formation of NO_2 in the assay milieu. This interference was eliminated by reversing the order of addition of Griess R1 and R2. In the NO_2^--only assay, the ABTS concentration was sufficiently high to result in formation of a fine precipitate after addition of Griess R2 and Griess R1, which dramatically affected measurement of A_{540}. This precipitate was eliminated by reducing the sample volume to 100 µl and diluting with 550 µl of ABTS-free buffer before adding Griess R2 and R1. No modifications to the ABTS-free NO_2^- + NO_3^- assay protocol were necessary to avoid precipitate formation in experiments with ABTS. The presence of 50-100 µM ABTS had a small but significant effect on the NO_2^- and NO_3^- calibration curves, independent of the ABTS concentration. As such, 100 µM ABTS (final concentration) was added to all NO_2^- and NO_3^- calibration standards. Neither ABTS nor DTPA appeared to have an effect on the enzymatic reduction of NO_3^- to NO_2^-.

3.2.5 Reactor model

The model for the reactor was constructed as follows. The gas and liquid phases within the reactor were modeled as well-mixed (uniform concentrations of all species), except for thin boundary layers adjacent to the gas-liquid interface in each phase. The headspace mass balance for species *j* was thus written as

$$\tilde{V}\frac{d\tilde{C}_j}{dt} = Q\left(\tilde{C}_{j,f} - \tilde{C}_j\right) - \tilde{k}_j A\left(\tilde{C}_j - \tilde{C}_{j,i}\right) + \tilde{V}\tilde{R}_j . \qquad (3.4)$$

The terms on the right hand side of Eq. (3.4) represent headspace inflow/outflow, mass transfer to/from the interface, and gas-phase reaction, respectively. The well-mixed concentration, the inlet (feed) stream concentration, and the gas-phase interfacial concentration of species *j* are denoted as $\tilde{C}_j$, $\tilde{C}_{j,f}$ and $\tilde{C}_{j,i}$, respectively. The composition of the outlet stream is assumed identical to that of the well-mixed region, and the volumetric flow rate *Q* for both the inlet and outlet streams is assumed to be identical. Mass transfer from the well-mixed region to the interface is described using an average mass transfer coefficient $\tilde{k}_j$ and interfacial area *A*. The headspace volume and the gas-phase volumetric rate of reaction are denoted as $\tilde{V}$ and $\tilde{R}_j$, respectively.

In the liquid phase, only two terms are necessary to describe the reactor dynamics, in addition to the accumulation term, as

. $$V\frac{d\overline{C}_j}{dt} = k_j A\left(C_{j,i} - \overline{C}_j\right) + V\overline{R}_j . \qquad (3.5)$$

The liquid-phase concentration of species *j* at the interface is $C_{j,i}$, and the concentration of species *j* averaged over the entire liquid volume (boundary layer plus well-mixed region) is $\overline{C}_j$. (This 'bulk' concentration was used because it is more representative of what a typical cell or molecule will experience as it traverses the liquid.) Mass transfer from the interface to the liquid was represented using an average mass transfer coefficient k_j and interfacial area *A*. The liquid volume and bulk liquid-phase volumetric rate of reaction were *V* and $\overline{R}_j$, respectively. Eqs. (3.4) and (3.5) both assume constant liquid and headspace volumes.

Eq. (3.4) could be simplified by noting that the upper limit of the relaxation time scale of a transient differential equation of this form is controlled by the time scale of the fastest process represented on the right hand side of the equation. That is, if the time scale of one of the processes is known, the relaxation time scale must be less than or equal to this known process time scale (see Appendix E). The residence time for the headspace, $t_{res} = \tilde{V}/Q$, has a maximum value of 7.2 s (for Q = 250 sccm), which is approximately 25-fold smaller than the shortest sampling interval used, 3 min (in delivery of 1% NO_2; see Table 3.5). This indicates that transient phenomena are negligible in the headspace under all experimental conditions, permitting reduction of the headspace mass balance to

$$0 = Q\left(\tilde{C}_{j,f} - \tilde{C}_j\right) - \tilde{k}_j A\left(\tilde{C}_j - \tilde{C}_{j,i}\right) + \tilde{V}\tilde{R}_j \,. \tag{3.6}$$

The interfacial transport terms in Eqs. (3.5) and (3.6) can be related by assuming that the gas and liquid phases are in equilibrium at the interface and that no interfacial reaction is occurring. The equilibrium condition is represented as $C_{j,i}/\tilde{C}_{j,i} = K_j$, where $K_j = \alpha_j RT$ is the partition coefficient for species *j* assuming ideal gas behavior and α_j is the solubility (Henry's coefficient) for species *j*. Assumption of no interfacial reaction requires that the flux of species *j* from the well-mixed region of the headspace to the interface must equal the flux of species *j* from the interface to the liquid, as $N_j = \tilde{k}_j\left(\tilde{C}_j - \tilde{C}_{j,i}\right) = k_j\left(C_{j,i} - \overline{C}_j\right)$. Substitution of the equilibrium condition into this expression and rewriting in terms of an overall driving force $\left(K_j\tilde{C}_j - \overline{C}_j\right)$ yields an expression for the overall interfacial flux of

$$N_j = k_{j,T}\left(K_j\tilde{C}_j - \bar{C}_j\right);\ k_{j,T} = \left(\frac{K_j}{\tilde{k}_j} + \frac{1}{k_j}\right)^{-1}, \tag{3.7}$$

where $K_j/\tilde{k}_j$ and $1/k_j$ are defined as the gas- and liquid-phase resistances, respectively. The form of $k_{j,T}$ in Eq. (3.7), is useful for determining whether the liquid or the gas boundary layer represents the dominant resistance to mass transfer across the interface, or whether contributions from both boundary layers must be considered.

3.2.5.1 H_2O gas-phase mass transfer coefficient

The mass transfer coefficients for a given species *j* are functions of a number of system parameters, including the vessel geometry, the stir rate, the liquid and gas viscosities, and the reactions in which species *j* participates. The most reliable way to obtain values for these coefficients is by experimental measurement of systems where one phase represents the dominant resistance to mass transfer. Further, it is useful to obtain mass transfer coefficients under unreactive conditions, as such values represent starting points from which corrections can be applied to estimate the effect of reactions on the mass transfer behavior.

Flow of pure N_2 over DI H_2O is a special case where no reactions will occur and the gas phase is expected to be the only resistance to H_2O transport in the system, since the liquid-phase water concentration will be uniform and constant at 55.6 M. Evaporation of H_2O and subsequent loss by outflow results in a decrease in the liquid volume over time, which can be measured simply by weighing the reactor. For sufficiently small $\Delta V/V$, the liquid-phase dynamics can be ignored entirely and the gas-phase mass transfer coefficient can be assumed to be constant. Under these conditions

only Eq. (3.6) need be considered. Given that the feed gas is dry and that the gas phase at the interface will be saturated with water (concentration $\tilde{C}_{H_2O,sat}$), the mass balance becomes

$$0 = -Q\tilde{C}_{H_2O} - \tilde{k}_{H_2O} A\left(\tilde{C}_{H_2O} - \tilde{C}_{H_2O,sat}\right). \tag{3.8}$$

The solution to Eq. (3.8) is

$$\tilde{C}_{H_2O} = \tilde{C}_{H_2O,sat}\left(\frac{\tilde{\kappa}_{H_2O}}{1+\tilde{\kappa}_{H_2O}}\right);\ \tilde{\kappa}_{H_2O} = \frac{\tilde{k}_{H_2O} A}{Q}, \tag{3.9}$$

with the rate of loss of mass from the reactor predicted to be constant and equal to

$$-\tilde{C}_{H_2O} \cdot Q \cdot \mathrm{M}_{H_2O}, \tag{3.10}$$

where M_{H_2O} is the molecular weight of water.

3.2.5.2 O_2 liquid-phase mass transfer coefficient

A representative liquid-phase mass transfer coefficient can be obtained by examining the transport of O_2 into and out of aqueous solution. Boundary-layer theory predicts that $\tilde{k}_{O_2}$ will be larger than k_{O_2} by approximately two orders of magnitude (Deen, 1998), and the partition coefficient for O_2 in buffer is small, with a value of 0.029. The expression for $k_{j,T}$ in Eq. (3.7) indicates then that the liquid mass transfer resistance should dominate. Accordingly, Eq. (3.6) can be rewritten as

$$0 = Q\left(\tilde{C}_{O_2,f} - \tilde{C}_{O_2}\right) - k_{O_2} A\left(K_{O_2}\tilde{C}_{O_2} - \bar{C}_{O_2}\right). \tag{3.11}$$

A further consequence of the dominance of the liquid-phase resistance is that $\tilde{C}_{O_2,i}$ should be nearly equal to $\tilde{C}_{O_2}$. Eq. (3.11) can be solved for the concentration difference between the feed gas and the headspace in terms of the total difference in (gas-equivalent) concentration between the feed gas and the bulk liquid, giving

$$\tilde{C}_{O_2,f} - \tilde{C}_{O_2} = \frac{K_{O_2}\kappa_{O_2}}{1+K_{O_2}\kappa_{O_2}}\left(\tilde{C}_{O_2,f} - \frac{\bar{C}_{O_2}}{K_{O_2}}\right);\ \kappa_{O_2} = \frac{k_{O_2}A}{Q}. \tag{3.12}$$

Boundary-layer theory predicts that k_{O_2} should be no greater than ~ 10^{-4} m s^{-1}, giving an upper limit of $\kappa_{O_2} \leq 0.05$. In combination with the small value of K_{O_2} this means that the change in the O_2 concentration from the inlet to the outlet of the headspace should be negligible, and thus the entire gas-phase dynamics can be represented as $\tilde{C}_{O_2,i} \approx \tilde{C}_{O_2} \approx \tilde{C}_{O_2,f}$.

Writing Eq. (3.5) now with these simplified gas-phase dynamics and no liquid-phase reactions of O_2 gives

$$V\frac{d\bar{C}_{O_2}}{dt} = k_{O_2}A\left(K_{O_2}\tilde{C}_{O_2,f} - \bar{C}_{O_2}\right). \tag{3.13}$$

Solving Eq. (3.13) assuming a bulk O_2 concentration at $t = 0$ of $\bar{C}_{O_2}(0)$ yields

$$\bar{C}_{O_2}(t) = K_{O_2}\tilde{C}_{O_2,f} + \left[\bar{C}_{O_2}(0) - K_{O_2}\tilde{C}_{O_2,f}\right]\cdot\exp\left[-\frac{t}{\tau}\right];\ \tau = \frac{V}{k_{O_2}A}. \tag{3.14}$$

Fitting of experimental O_2 concentration profiles with Eq. (3.14) provides values for τ and k_{O_2}.

3.2.5.3 *Macroscopic model for NO_2/N_2O_4 delivery*

It was assumed that the forward and reverse reactions of (3.1) are sufficiently fast that NO_2 and N_2O_4 are nearly in equilibrium at every point within the reactor (quasi-equilibrium assumption, or QEA; see Lim (2011) for a more in-depth discussion). This motivates definition of a total reactive nitrogen (RN) concentration, C_N, as

$$C_N = C_{\mathrm{NO_2}} + 2\,C_{\mathrm{N_2O_4}}\,. \tag{3.15}$$

The total RN concentration can be defined for both the gas ($\tilde{C}_N$) and liquid (C_N) phases. Substituting the equilibrium relationship $C_{\mathrm{N_2O_4}} = K_1\left(C_{\mathrm{NO_2}}\right)^2$ into Eq. (3.15) yields a quadratic expression in $C_{\mathrm{NO_2}}$; applying the quadratic formula and dividing the result by C_N gives φ, the fraction of RN that is present as NO_2:

$$\varphi = \frac{C_{\mathrm{NO_2}}}{C_N} = \frac{\sqrt{1+8\,C_N K_1}-1}{4\,C_N K_1}\,. \tag{3.16}$$

An expression analogous to Eq. (3.16) for $\tilde{\varphi}$, the fraction of RN present as NO_2 in the gas phase, can be constructed by substituting $\tilde{C}_N$ and $\tilde{K}_1 RT$ for C_N and K_1, respectively:

$$\tilde{\varphi} = \frac{\tilde{C}_{\mathrm{NO_2}}}{\tilde{C}_N} = \frac{\sqrt{1+8\,\tilde{C}_N \tilde{K}_1 RT}-1}{4\,\tilde{C}_N \tilde{K}_1 RT}\,. \tag{3.17}$$

Note that the N_2O_4 concentration written in terms of φ and C_N is thus $C_{\mathrm{N_2O_4}} = C_N\left(1-\varphi\right)/2$. Note also that if C_N is position-dependent, φ will be as well.

Rewriting all of the governing equations in terms of RN eliminates the need to consider either fast reaction of (3.1) explicitly. To do this, the conservation equation for

NO_2 is added to twice that equation for N_2O_4. The headspace mass balance for RN is thus derived from Eq. (3.6) as

$$0 = Q\left(\tilde{C}_{N,f} - \tilde{C}_N\right) - \tilde{k}_N A\left(\tilde{C}_N - \tilde{C}_{N,i}\right) - \tilde{k}_2 \tilde{V}\left(1-\tilde{\varphi}\right)\tilde{C}_{\mathrm{H_2O}}\tilde{C}_N\,, \tag{3.18}$$

where $\tilde{k}_{\mathrm{NO_2}} \approx \tilde{k}_{\mathrm{N_2O_4}} = \tilde{k}_N$ is assumed and $\tilde{C}_{\mathrm{N_2O_4}}$ in the reaction term is written in terms of $\tilde{C}_N$ and $\tilde{\varphi}$. While other gas-phase reactions are possible, such as the reaction of two HNO_2 molecules to form H_2O and N_2O_3 (Chan et al., 1976), scaling estimates (see Appendix E) predict that only N_2O_4 hydrolysis may proceed to an extent sufficient to influence the behavior of the reactor.

3.2.5.4 Microscopic model for NO_2/N_2O_4 delivery

In the liquid phase, hydrolysis of N_2O_4 is expected to be sufficiently fast that C_N, and thus φ, will be a strong function of position. Accordingly, the spatial averaging implicit in the bulk quantities in Eq. (3.5) cannot accurately represent the non-linear kinetics of C_N. A microscopic model describing RN entry into and reaction within the reactor was constructed as follows. The boundary layer adjacent to the gas-liquid interface is modeled as a stagnant film extending a distance x_f from the interface, which is defined as $x = 0$. The remainder of the liquid is assumed to be well-mixed. The concentration of species j within the stagnant film and in the well-mixed region is denoted as $C_j(x)$ and $C_{j,m}$, respectively, and it is assumed that $C_{j,m} = C_j(x_f)$. The value of x_f was estimated from the liquid-phase mass transfer coefficient for O_2 as $x_f = D_{\mathrm{O_2}} / k_{\mathrm{O_2}}$, where $D_{\mathrm{O_2}}$ is the liquid-phase diffusivity of O_2. (Note that the choice of x_f has a significant effect on the performance of the model; see Section 3.4.3.4.) The

experimentally determined value of k_{O_2} (see Section 3.3.1) corresponds to a film thickness x_f = 78 μm, which in turn gives a characteristic diffusion time for ABTS (the slowest-diffusing species in the system) of $t_{diff} = x_f^2 / D_{\mathrm{ABTS}} \approx 20\ \mathrm{s}$. This time scale is sufficiently small that the transient terms in the reaction-diffusion differential equations governing the RN and ABTS concentrations can be neglected. These equations are

$$0 = D_N \frac{d^2 C_N}{dx^2} - k_2 \left[1 - \varphi(x)\right] C_N(x) - k_3 \varphi(x) C_N(x) C_{\mathrm{ABTS}}(x). \tag{3.19}$$

$$0 = D_{\mathrm{ABTS}} \frac{d^2 C_{\mathrm{ABTS}}}{dx^2} - k_3 \varphi(x) C_N(x) C_{\mathrm{ABTS}}(x). \tag{3.20}$$

Eq. (3.19) is constructed from the differential equations for NO_2 and N_2O_4 as with Eq. (3.18). The diffusivity of N_2O_4 is assumed to be approximately equal to that of NO_2, with $D_{\mathrm{NO_2}} \approx D_{\mathrm{N_2O_4}} = D_N$, and φ is written as a function of x to highlight its position dependence. Given that ABTS is a non-volatile solute, the boundary conditions for C_{ABTS} are

$$\frac{dC_{\mathrm{ABTS}}}{dx}(0) = 0;\ C_{\mathrm{ABTS}}(x_f) = C_{\mathrm{ABTS},m}. \tag{3.21}$$

Derivation of the boundary conditions for RN is more complicated. The boundary condition for C_N at $x = x_f$ was constructed by equating the flux of RN out of the stagnant film with the consumption of RN in the well-mixed region, as

$$-D_N A \frac{dC_N}{dx}(x_f) - \left\{k_2 \left[1 - \varphi(x_f)\right] + k_3 \varphi(x_f) C_{\mathrm{ABTS}}(x_f)\right\} C_N(x_f) V = 0. \tag{3.22}$$

V appears in the reaction term of Eq. (3.22) since the volume of the boundary layer is negligible with respect to the total liquid volume ($x_f A / V \approx 0.003$), and thus the well-

mixed volume is nearly equal to V. For the boundary at $x = 0$, assuming that the gas-phase mass transfer coefficients for all species j are approximately equal to $\tilde{k}_{H_2O} \equiv \tilde{k}$, the flux-matching condition at the gas-liquid interface gives a boundary condition of

$$\tilde{k}\left[\tilde{C}_N - \left(\frac{C_{NO_2}(0)}{K_{NO_2}} + 2\frac{C_{N_2O_4}(0)}{K_{N_2O_4}}\right)\right] = -D_N \frac{dC_N}{dx}(0). \tag{3.23}$$

The unequal partition coefficients of NO_2 and N_2O_4 prevent simply using $C_N(0)$ in the left-hand side of Eq. (3.23). Multiplying the $C_{N_2O_4}(0)$ term by K_{NO_2}/K_{NO_2} and rewriting the ratio $K_{NO_2}/K_{N_2O_4}$ as

$$\frac{K_{NO_2}}{K_{N_2O_4}} = 1 - \rho_N \; ; \; \rho_N \equiv \frac{K_{N_2O_4} - K_{NO_2}}{K_{N_2O_4}}, \tag{3.24}$$

Eq. (3.23) can be written as

$$\frac{\tilde{k}}{K_{NO_2}}\left[K_{NO_2}\tilde{C}_N - \left\{1 - \rho_N\left[1 - \varphi(0)\right]\right\}C_N(0)\right] = -D_N \frac{dC_N}{dx}(0). \tag{3.25}$$

$\tilde{C}_N$ must be eliminated from Eq. (3.25) in order to use this condition in numerical simulations. Since the non-linearity of $\tilde{\varphi}$ prevents explicit solution of Eq. (3.18) for $\tilde{C}_N$, Eq. (3.25) was solved for $\tilde{C}_N$, giving

$$\tilde{C}_N = \frac{1}{K_{NO_2}}\left\{1 - \rho_N\left[1 - \varphi(0)\right]\right\}C_N(0) - \frac{D_N}{\tilde{k}}\frac{dC_N(0)}{dx}. \tag{3.26}$$

Substitution of Eq. (3.26) into Eq. (3.18) leaves $\tilde{C}_{N,i}$ as the only remaining undetermined variable quantity, which can be expressed in terms of $C_N(0)$ and $\varphi(0)$ as

$$\tilde{C}_{N,i} = \left[\frac{\varphi(0)}{K_{\mathrm{NO_2}}} + \frac{1-\varphi(0)}{K_{\mathrm{N_2O_4}}} \right] C_N(0) \,. \tag{3.27}$$

The RN concentration in the feed gas, $\tilde{C}_{N,f}$, is governed by two constraints: the manufacturer's specification (f_N) and the composition of the gas stream at the finite total pressure within the delivery tubing ($P_{T,f}$ = 1 atm). The manufacturer's specification written in terms of $\tilde{C}_{N,f}$ is

$$f_N = \frac{\tilde{C}_{N,f}}{\tilde{C}_{N,f} + \tilde{C}_{inert,f}} \,, \tag{3.28}$$

where '*inert*' here means N_2 plus O_2. Assuming ideal gas behavior, the composition constraint is

$$\tilde{C}_{\mathrm{NO_2},f} + \tilde{C}_{\mathrm{N_2O_4},f} + \tilde{C}_{inert,f} = \left(\frac{1+\tilde{\varphi}_f}{2} \right) \tilde{C}_{N,f} + \tilde{C}_{inert,f} = \frac{P_{T,f}}{RT} \,. \tag{3.29}$$

Simultaneous solution of Eqs. (3.28) and (3.29) provides the $\tilde{C}_{N,f}$ values for the various NO_2 gas mixtures. Though complicated, this combination of Eqs. (3.18), (3.26) and (3.27) represents an explicit boundary condition expression in terms of $C_N(0)$ and $dC_N/dx(0)$ that is suitable for use in numerical simulations.

The above system of differential equations and boundary conditions was converted into non-dimensional form (see Section 3.2.5.5) and simulated in MAPLE 11 (Maplesoft, Waterloo, Ontario, Canada). Early simulations indicated that elimination of gas-phase hydrolysis [omitting the rightmost term in Eq. (3.18)] had at most a 5% effect on the simulation predictions (see Section 3.4.3.2). As the non-linearity of this term is

responsible for much of the complexity of the boundary condition at $x = 0$, all subsequent simulations neglected gas-phase reactions. The bulk accumulation rates of NO_2^-, NO_3^- and $ABTS^+$ were calculated from the simulation results as

$$\frac{d\overline{C}_{NO_2^-}}{dt} = C_N(x_f)\left(k_2 \frac{1-\varphi(x_f)}{2} + k_3\varphi(x_f) C_{ABTS}(x_f) \right) + \frac{A}{V}\int_0^{x_f} C_N(x)\left[k_2 \frac{1-\varphi(x)}{2} + k_3\varphi(x) C_{ABTS}(x) \right] dx. \tag{3.30}$$

$$\frac{d\overline{C}_{NO_3^-}}{dt} = k_2 C_N(x_f)\frac{1-\varphi(x_f)}{2} + \frac{A}{V}\int_0^{x_f} k_2 C_N(x)\frac{1-\varphi(x)}{2} dx. \tag{3.31}$$

$$\frac{d\overline{C}_{ABTS^+}}{dt} = k_3 C_N(x_f)\varphi(x_f) C_{ABTS}(x_f) + \frac{A}{V}\int_0^{x_f} k_3 C_N(x)\varphi(x) C_{ABTS}(x) dx. \tag{3.32}$$

As in Eq. (3.22), the negligible volume of the stagnant film relative to the liquid volume was invoked to simplify the form of Eqs. (3.30)–(3.32). The bulk NO_2 and N_2O_4 concentrations at pseudo-steady-state were calculated as

$$\overline{C}_{NO_2} = C_N(x_f)\varphi(x_f) + \frac{A}{V}\int_0^{x_f} C_N(x)\varphi(x) dx. \tag{3.33}$$

$$\overline{C}_{N_2O_4} = C_N(x_f)\frac{1-\varphi(x_f)}{2} + \frac{A}{V}\int_0^{x_f} C_N(x)\frac{1-\varphi(x)}{2} dx. \tag{3.34}$$

The values for the physicochemical parameters and reactor dimensions used in the simulations are given in Table 3.1. Ideal gas behavior is assumed to govern the behavior of all species in the gas phase. Calculations using the NO_2 and N_2O_4 parameters of Horstmann et al. (2005) for the PSRK equation of state indicate that the gas-phase system behavior should deviate by less than 2% from ideal (that is, $P_j = \tilde{C}_j RT$ within 2%).

Table 3.1. Physicochemical parameters and reactor specifications.

Parameter	Value [a]		Units	Reference
	23 °C	37 °C		
Q	6.1×10^{-6}	6.3×10^{-6}	$m^3\ s^{-1}$	–
A	2.8×10^{-3}	2.8×10^{-3}	m^2	–
$\tilde{V}$	3×10^{-5}	3×10^{-5}	m^3	–
V	8×10^{-5}	8×10^{-5}	m^3	–
$\tilde{k}_{H_2O}$	$3.0 \pm 1.7 \times 10^{-2}$	3.1×10^{-2}	$m\ s^{-1}$	(this work)
k_{O_2}	$2.7 \pm 0.5 \times 10^{-5}$	3.2×10^{-5}	$m\ s^{-1}$	(this work)
$\tilde{C}_{H_2O,sat}$	1.14×10^{-3}	—	M	Lange, 1999
α_{O_2}	1.2×10^{-3} [b]	1.0×10^{-3} [b]	$M\ atm^{-1}$	Weiss, 1970 Hermann et al., 1995
α_{NO_2}	9×10^{-3} [c]	6.5×10^{-3}	$M\ atm^{-1}$	Schwartz and White, 1981
$\alpha_{N_2O_4}$	0.77	0.62	$M\ atm^{-1}$	(see Appendix C)
D_{O_2}	2.1×10^{-9}	2.9×10^{-9}	$m^2\ s^{-1}$	Goldstick and Fatt, 1970
D_{NO_2}	1.85×10^{-9}	2.6×10^{-9}	$m^2\ s^{-1}$	Mertes and Wahner, 1995
D_{ABTS}	3.1×10^{-10}	4.3×10^{-10}	$m^2\ s^{-1}$	Kim, 2006
K_1	6.54×10^{4}	3.94×10^{4}	M^{-1}	Graetzel et al., 1969
$\tilde{K}_1$	6.86	2.7	atm^{-1}	Schwartz and White, 1981
k_2	1×10^{3}	2.3×10^{3}	s^{-1}	Graetzel et al., 1969
k_3	2.8×10^{7}	6.4×10^{7}	$M^{-1}\ s^{-1}$	Goldstein and Czapski, 1995

[a] References give parameter values for 22–25 °C. Methods used to estimate parameter values at 37 °C are described in Section 3.2.5.6

[b] Reduced by approximately 4% from its value in pure H_2O to account for salt effects

[c] Reduced by 25% from value of Schwartz and White, 1981; see Section 3.4.3

3.2.5.5 Non-dimensional NO_2/N_2O_4 model

The reaction-diffusion problem in the liquid boundary layer was non-dimensionalized as follows. The ABTS concentration was scaled by its bulk concentration, as

$$\psi = \frac{C_{\mathrm{ABTS}}}{\bar{C}_{\mathrm{ABTS}}}. \tag{3.35}$$

(To note, since the ABTS concentration will not be elevated within the liquid-phase boundary layer, the bulk and well-mixed ABTS concentrations will be nearly identical.) The scale C_N^* for the RN concentration was chosen as the concentration in the liquid that would be in equilibrium with the feed gas, assuming negligible N_2O_4 hydrolysis. Since the partition coefficients for NO_2 and N_2O_4 differ, this definition requires separate calculation of the respective NO_2 and N_2O_4 concentrations in equilibrium with the feed gas. The expression for C_N^* is then obtained using Eq. (3.15) as

$$C_N^* = \left[\tilde{\varphi}_f K_{\mathrm{NO_2}} + \left(1 - \tilde{\varphi}_f\right) K_{\mathrm{N_2O_4}} \right] \tilde{C}_{N,f}, \tag{3.36}$$

which permits the definition

$$\theta = \frac{C_N}{C_N^*}. \tag{3.37}$$

The length scale δ for the system was selected as a linearized penetration depth for RN in the absence of substrates. The differential equation for RN [Eq. (3.19)] was first reduced to

$$0 = D_N \frac{d^2 C_N}{dx^2} - k_2 \left(1 - \varphi\right) C_N. \tag{3.38}$$

After defining $\eta \equiv x/\delta$ and non-dimensionalizing Eq. (3.38), the scales for C_N cancel, leaving

$$0 = \frac{D_N}{\delta^2}\frac{d^2\theta}{d\eta^2} - k_2(1-\varphi)\theta\,. \tag{3.39}$$

Ignoring for the moment that $(1-\varphi)$ is expected to be significantly less than unity in a number of cases, it is natural to choose $\delta = \sqrt{D_N/k_2}$. Though leaving φ out of the definition of δ may cause η to be poorly scaled, it simplifies non-dimensionalization of the remainder of the system and avoids the need for *a priori* knowledge of the scale of φ, which is difficult to obtain. The domain of the problem thus becomes $0 \le \eta \le \eta_f$, where $\eta_f = x_f/\delta$. With x_f = 78 μm as calculated in Section 3.2.5.4 above, η_f = 58.

With the above concentration and length scales, the differential equations describing reactive transport in the liquid boundary layer become [from Eqs. (3.19) and (3.20), respectively]

$$0 = \frac{d^2\theta}{d\eta^2} - (1-\varphi)\theta - \mathrm{Da}_3\,\varphi\,\theta\psi\,;\ \mathrm{Da}_3 = \frac{k_3 C_{\mathrm{ABTS},m}\delta^2}{D_N} = \frac{k_3}{k_2}C_{\mathrm{ABTS},m}\,. \tag{3.40}$$

$$0 = \frac{d^2\psi}{d\eta^2} - \mathrm{Da}_{\mathrm{ABTS}}\,\varphi\,\theta\psi\,;\ \mathrm{Da}_{\mathrm{ABTS}} = \frac{k_3 D_N C_N^*}{k_2 D_{\mathrm{ABTS}}}\,. \tag{3.41}$$

Note that θ, ψ, and φ are all functions of position. However, only two differential equations are needed because φ can be written as an explicit algebraic function of θ [Eq. (3.16)]. The boundary conditions for the dimensionless ABTS concentration [Eq. (3.21)] are

$$\frac{d\psi}{d\eta}(0)=0;\ \psi(\eta_f)=1. \tag{3.42}$$

The boundary condition for RN at $\eta = \eta_f$ becomes

$$0=\frac{d\theta}{d\eta}(\eta_f)+B_2(1-\varphi)\theta(\eta_f)+B_3\varphi\,\theta(\eta_f)\psi(\eta_f);\ B_2=\frac{k_2\delta V}{D_N A};\ B_3=\frac{k_3\delta V C_{\mathrm{ABTS},m}}{D_N A}. \tag{3.43}$$

Eqs. (3.26) and (3.27) were non-dimensionalized respectively to

$$\tilde{C}_N=\frac{C_N^*}{K_{\mathrm{NO_2}}}\left[\{1-\rho_N(1-\varphi)\}\theta(0)-B_0\frac{d\theta}{d\eta}(0)\right];\ B_0=\frac{D_N K_{\mathrm{NO_2}}}{\tilde{k}\delta} \tag{3.44}$$

and

$$\tilde{C}_{N,i}=C_N^*\left[\frac{\varphi}{K_{\mathrm{NO_2}}}+\frac{1-\varphi}{K_{\mathrm{N_2O_4}}}\right]\theta(0). \tag{3.45}$$

Substitution of Eqs. (3.44) and (3.45) into Eq. (3.18), being careful to retain the dependence of $\tilde{\varphi}$ on $\tilde{C}_N$, generated the final boundary condition.

Eq. (3.18) (Section 3.2.5.3) and Eqs. (3.40) through (3.45) represent the full system of equations input to the numerical solver in MAPLE. Non-dimensionalization of the simulation outputs [i.e., Eqs. (3.30) through (3.34)] was achieved by universal substitution of $C_N = C_N^*\,\theta$, $C_{\mathrm{ABTS}} = \bar{C}_{\mathrm{ABTS}}\,\psi$, $x = \eta\,\delta$, and $x_f = \eta_f\,\delta$ in those expressions. Plots of representative dimensionless RN concentration profiles are provided in Section 3.4.3.3.

3.2.5.6 Parameter corrections at body temperature

The temperature dependences of the gas- ($\tilde{D}_j$) and aqueous-phase (D_j) diffusivities were assumed to follow the Maxwell-Boltzmann and Stokes-Einstein relationships, respectively (Deen, 1998). Per the predictions of boundary-layer theory for a fluid-fluid interface (Deen, 1998), mass transfer coefficients in both phases ($\tilde{k}_j$, k_j) were assumed to obey the relationship $k_j \propto D_j^{1/2}$. The volumetric flow rate of the gas (Q) was corrected assuming ideal gas behavior. The gas-phase NO_2/N_2O_4 equilibrium constant ($\tilde{K}_1$) and the NO_2 solubility (α_{NO_2}) were adjusted using the van 't Hoff equation. The value of $-\Delta H/R$ used for $\tilde{K}_1$ was the mean of those reported by Dunn et al. (1962), Srivastava and Barua (1961), and Verhoek and Daniels (1931); and that used for α_{NO_2} was from Schwartz and White (1981).

In the absence of reliable literature data on the temperature dependence of Reactions (3.2) and (3.3), the heuristic rule of a two-fold increase for each 10 °C increase in temperature was applied to k_2 and k_3. The same rule was applied for the reactions between NO_2 and GSH, Asc, and Cys (Table 3.3). As well, no reliable estimate of the temperature dependence of the aqueous NO_2/N_2O_4 equilibrium constant (K_1) was available. As a best estimate, the forward reaction was approximated as diffusion-limited and the activation energy of the reverse reaction was assumed equal to the gas-phase value reported by Atkinson et al. (2004). The N_2O_4 solubility ($\alpha_{N_2O_4}$) was calculated as at room temperature, using corrected values of α_{NO_2}, $\tilde{K}_1$, and K_1 in Eq. (C.4).

3.2.6 Measurement of mass transfer coefficients

The gas-phase mass transfer coefficient for H_2O was determined as follows. The reactor was charged with 81-82 ml of DI H_2O and its initial weight was measured on a Sartorius analytical balance (Bohemia, NY). The reactor was connected to the gas manifold and pure N_2 was flowed through the headspace. The N_2 flow was periodically halted and the reactor was disconnected from the gas manifold and weighed. The rate of loss of mass of the reactor and its contents, corrected for the short intervals where the N_2 flow was disconnected, was used in Eqs. (3.9) and (3.10) to determine $\tilde{k}_{H_2O}$.

The liquid-phase mass transfer coefficient for O_2 was determined as follows. The reactor was charged with 80 ml of air-equilibrated buffer and fitted with the O_2 probe. At the start of each experiment, a flow of pure N_2 (365 or 250 sccm) was initiated through the headspace and the O_2 concentration was monitored. When the liquid had been substantially depleted of O_2, the gas flow was switched to lab air and the O_2 concentration was monitored until the O_2 level in the liquid had been substantially replenished. These O_2 data were regressed against Eq. (3.14) to obtain values for τ, from which k_{O_2} was estimated.

3.2.7 Reactor characterization using product accumulation rates

Nitrogen dioxide delivery in the absence and presence of ABTS was examined by measuring the accumulation rates of NO_2^-, NO_3^- and $ABTS^+$. For this purpose, the reactor was filled with 80 ml of buffer either with or without ABTS and connected to the gas delivery system. At $t = 0$, flow of one of the NO_2 gas mixtures was initiated through the headspace. Liquid samples (2.0-2.5 ml) were withdrawn from the reactor prior to

initiating the gas flow and periodically thereafter. The sampling interval varied between 3 min and 30 min, depending on the accumulation rates of the end products. Each sample was stored in a sealed vial and was replaced with fresh buffer. In experiments with ABTS the samples were assayed for $ABTS^+$ and ABTS within 5 min and 30 min of withdrawal from the reactor, respectively. The 1.5-ml portions of each sample were treated with DTPA immediately after assaying for $ABTS^+$. All DTPA-treated samples were assayed for ABTS and analyzed at least in duplicate for NO_2^- and NO_3^- on the day of generation. Experimental durations were selected such that the $ABTS^+$ concentration never exceeded 20 μM; sampling intervals were selected such that the accumulation rates of all three products remained nearly constant (see Section 3.4.2.3).

In experiments delivering NO_2 via PDMS tubing or porous PTFE membrane, the appropriate reactor was completely filled with buffer (110 ml and 65 ml reactor volumes, respectively) and connected to the gas handling system. Samples were withdrawn before initiating gas flow and typically at 30-min intervals thereafter. Sample processing and analysis procedures were identical to those described above, except that no assays for unreacted ABTS were performed.

3.3 Results

Plots of all experimental data collected can be found in Appendix B.

3.3.1 Mass transfer coefficients

The change in mass of the reactor during flow of pure N_2 over DI H_2O was linear with time with a slope of -0.420 ± 0.020 g h^{-1} (n = 3). From Eqs. (3.9) and (3.10), this

corresponds to a headspace H_2O concentration of $\tilde{C}_{H_2O}$ = 1.07 ± 0.04 mM, which is close to the literature value for the water saturation concentration at 23 °C, $\tilde{C}_{H_2O,sat} = P_{H_2O,sat}/RT$ = 1.14 mM (Table 3.1). Defining $\gamma = \tilde{C}_{H_2O}/\tilde{C}_{H_2O,sat}$, algebraic rearrangement of Eq. (3.9) yields $\tilde{\kappa}_{H_2O} = \gamma/(1-\gamma)$. Standard error propagation calculations indicate that the uncertainties of $\tilde{\kappa}_{H_2O}$ and γ are related by

$$\Delta\tilde{\kappa}_{H_2O} = \frac{d\tilde{\kappa}_{H_2O}}{d\gamma}\cdot\Delta\gamma = \frac{1}{(1-\gamma)^2}\Delta\gamma. \tag{3.46}$$

Per the form of Eq. (3.46), the close approach of $\tilde{C}_{H_2O}$ to $\tilde{C}_{H_2O,sat}$ (alternatively, the close approach of γ to unity) amplifies the uncertainty of $\tilde{\kappa}_{H_2O}$, yielding $\tilde{\kappa}_{H_2O}$ = 16 ± 10. The mass transfer coefficient obtained from Eq. (3.9) and this value of $\tilde{\kappa}_{H_2O}$ is reported in Table 3.1.

Figure 3.3 presents representative O_2 concentrations for a depletion-repletion experiment (365 sccm), with t = 0 being the moment the N_2 flow was started for the depletion phase. Eq. (3.14) yielded excellent fits to the data, as shown by the solid curves. In each experiment, values of k_{O_2} were approximately 20% higher for the repletion phase as compared to the depletion phase (presumably due in part to losses of liquid volume due to evaporation). Also, values of k_{O_2} for a given phase (depletion or repletion) were approximately 10% higher at 365 sccm as compared to 250 sccm. Due to the small magnitude of these variations, the value of k_{O_2} reported in Table 3.1 is the mean of all values obtained, regardless of delivery mode (depletion or repletion) and Q.

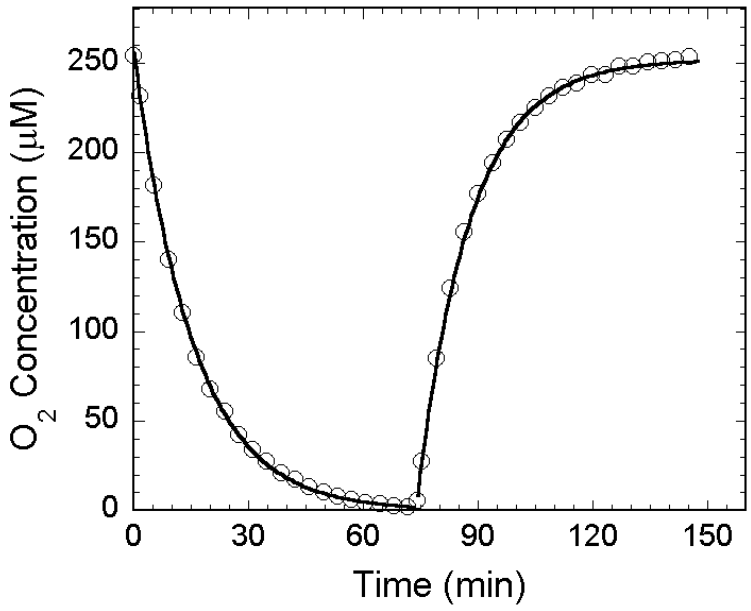

Figure 3.3. Measured O_2 concentration during representative O_2 depletion-repletion experiment.

The solid curves were calculated using the best-fit values of the mass transfer coefficient for the relevant portion of the data.

3.3.2 Tests using product accumulation rates

Figure 3.4 shows NO_2^-, NO_3^-, and $ABTS^+$ concentrations for a representative experiment with 0.01% NO_2 and an ABTS concentration of 107 μM. After initiating flow of the NO_2-containing gas mixtures, the rates of accumulation of all three products were constant, at 68, 23, and 48 μM h^{-1}, respectively. Due to uncertainty in the time required for the gas mixture to traverse the manifold, and thus in the 'true' $t = 0$, only the slopes of the linear fits shown in Figure 3.4 were examined. Constant rates of formation of all products were observed in all experiments; this constancy can be attributed to a rapid approach to pseudo-steady state in all experiments, as well as sufficiently early termination of the experiments with ABTS such that most ABTS remained unreacted ($[ABTS]_f/[ABTS]_o > 77\%$ in all experiments).

Table 3.2 summarizes the experimental data and simulation results for all of the experiments performed. Accumulation rates of nitrite and nitrate were a strong function of f_N, spanning more than four orders of magnitude over the range of f_N studied. The nitrite and nitrate rates were similar at 1% and 0.1% NO_2, but the latter significantly exceeded the former at 0.01% and 0.001% NO_2. Decreasing the gas flow rate from 365 sccm to 250 sccm had a relatively strong effect on the accumulation rates observed at 1% NO_2. This effect can be explained in terms of the relative resistances argument presented in Section 3.4.2.4. In the presence of ABTS, the nitrite accumulation rate increased significantly while the nitrate rate either decreased moderately or was unaffected. The $ABTS^+$ accumulation rate increased moderately with the tenfold increase in f_N from 0.001% to 0.01%.

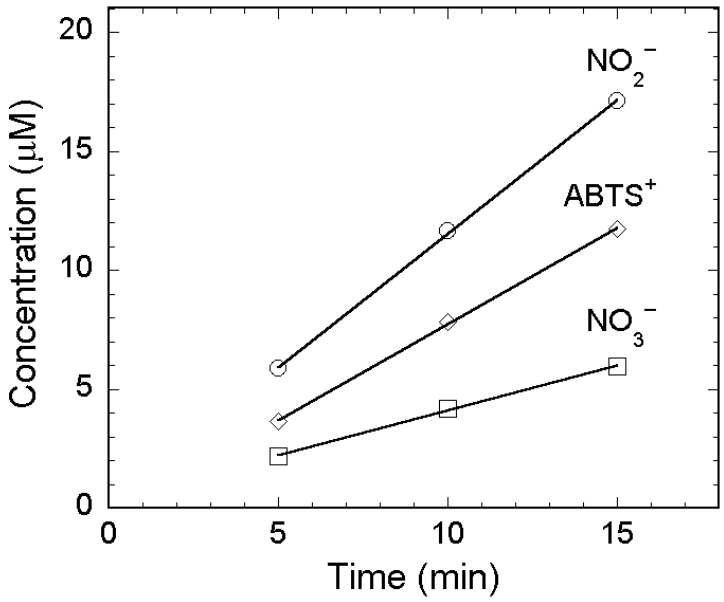

Figure 3.4. Nitrite, nitrate and ABTS radical concentrations during a representative 0.01% NO_2 delivery experiment to buffer initially with 107 μM ABTS.

The discrete symbols for NO_2^- and NO_3^- are averages from the respective Griess methods (each sample assayed at least in duplicate), and those for $ABTS^+$ are calculated from the A_{416} read for each sample prior to DTPA treatment. Error bars for NO_2^- and NO_3^- are smaller than the symbols. The solid lines are linear fits of the respective data; the slopes of these lines are reported in Table 3.2 for each of the various experimental conditions examined.

Table 3.2. Product accumulation rates in headspace delivery of NO_2.

f_N	ABTS	n	$\frac{dC_{NO_2^-}}{dt}$	$\frac{dC_{NO_3^-}}{dt}$	$\frac{dC_{ABTS^+}}{dt}$
1%	-	3	21,000 ± 300 (24,000)	17,000 ± 1600 (24,000)	-
0.1%	-	2	840 ± 30 (870)	900 ± 20 (940)	-
0.01%	-	2	20 ± 1 (21)	38 ± 1 (39)	-
0.001%	-	4	0.66 ± 0.05 (0.76)	6.0 ± 0.4 (6.4)	-
1% [a]	-	5	15,000 ± 300 (19,000)	12,000 ± 500 (19,000)	-
0.01%	107 μM	4	71 ± 9 (62)	24 ± 6 (27)	51 ± 9 (54)
0.001%	107 μM	4	22 ± 1 (19)	5.7 ± 1.6 (5.6)	20 ± 1 (19)

All accumulation rates are in μM h^{-1} and are reported as mean ± s.d, rounded to two significant figures. Model predictions are given in parentheses below each measurement; values for the nitrate accumulation rate at 0.1% NO_2 and below are corrected for the assumed nitric acid impurity in the feed gas as described in Section 3.4.2.1. Uncorrected predictions for nitrate in the absence of ABTS are identical to those for nitrite.

[a] 250 sccm gas flow rate

It is noteworthy that, in all experiments, concentrations of all three product species were negligible in the samples withdrawn prior to initiation of the flow of the NO_2 gas mixture, and the product accumulation rates were reproducible at each condition studied. Assays for NO_2^- and NO_3^- were performed at least in duplicate for each sample. Repeated measurements of A_{416} for each sample prior to DTPA treatment were consistently identical within the precision of the spectrophotometer. This indicates that the main source of error in the $ABTS^+$ determinations is derived from uncertainty in the literature value of the extinction coefficient.

Figure 3.5 is a log-log plot of the nitrite accumulation rate observed in the absence of ABTS as a function of the NO_2 mixture used. As can be seen, the nitrite accumulation rate is described well by a 3/2-power dependence on the RN abundance in the gas mixture. As will be discussed (Section 3.4.2.2), this relationship can be rationalized with a simple scaling argument considering the effects of Reaction (3.2) on the liquid-phase mass transfer coefficient, assuming that NO_2 is the primary species responsible for RN transport.

As shown in Table 3.2, in experiments with ABTS, NO_2^- and $ABTS^+$ accumulation rates were comparable and the NO_2^- accumulation rate was enhanced relative to the ABTS-free experiments with the same gas mixture. Of note, the relative enhancement of the NO_2^- accumulation rate was much greater at 0.001% NO_2 than at 0.01%. Conversely, addition of ABTS either decreased or had no effect on the NO_3^- accumulation rate. The sum of the measured concentrations of ABTS and $ABTS^+$ in NO_2-exposed samples prior to treatment with DTPA consistently equaled the concentration of ABTS in the stock buffer to within a few percent. Similarly, the

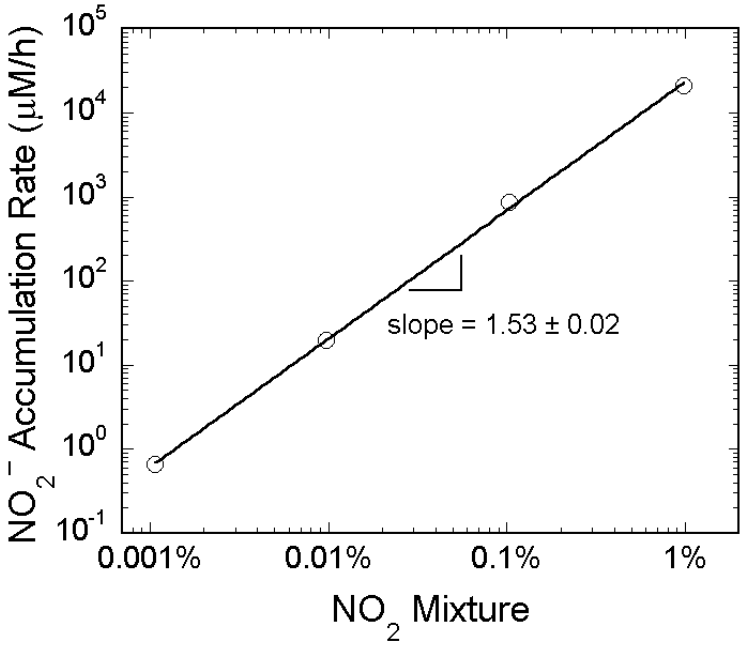

Figure 3.5. Measured nitrite accumulation rate during delivery of various NO_2-containing gas mixtures to buffer in the absence of ABTS.

Data are plotted as a function of the abundance of NO_2 in the feed gas mixture. Discrete symbols are experimental data; error bars are smaller than the symbols. The data closely follow a power-law dependence of the accumulation rate on % NO_2, as denoted by the solid line. See Section 3.4.2.2 for discussion of this behavior.

measured ABTS concentration in samples after DTPA treatment also consistently matched the stock buffer ABTS concentration. The simplest interpretation of this result is that the contribution of $ABTS^+$ to A_{340} was indeed negligible in these experiments, and that DTPA reacts with $ABTS^+$ to re-form ABTS.

The stoichiometry of Reaction (3.2) indicates that, presuming that N_2O_4 hydrolysis is the only pathway for consumption of RN, the accumulation rates of NO_2^- and NO_3^- in the absence of ABTS should be equal. That is, the nitrite yield, defined as

$$Y_{NO_2^-} = \frac{\dfrac{dC_{NO_2^-}}{dt}}{\dfrac{dC_{NO_2^-}}{dt} + \dfrac{dC_{NO_3^-}}{dt}}, \tag{3.47}$$

should have a value of 0.5, independent of the delivery conditions. Figure 3.6 plots the observed nitrite and nitrate accumulation rates for all four NO_2 gas mixtures used, along with values of $Y_{NO_2^-}$. While $Y_{NO_2^-}$ is close to the predicted value of 0.5 for 1% and 0.1% NO_2, the nitrate accumulation rate substantially exceeds that of nitrite at the two lowest % NO_2. This behavior is hypothesized to stem from a nitric acid impurity in the feed gas and will be examined further in Section 3.4.2.1.

The data from delivery experiments using the PDMS tubing and the porous PTFE membrane deviated significantly both from the stoichiometric predictions of Reaction (3.2) and from the data obtained via direct gas-liquid contacting. Nitrite yields [Eq. (3.47)] were aberrantly low in experiments with delivery through PDMS tubing, with values of 0.22 ± 0.01 and 0.31 ± 0.03 using 0.1% (n = 4) and 1% (n = 6) NO_2 gas mixtures, respectively. Conversely, the nitrite yields were inexplicably high in

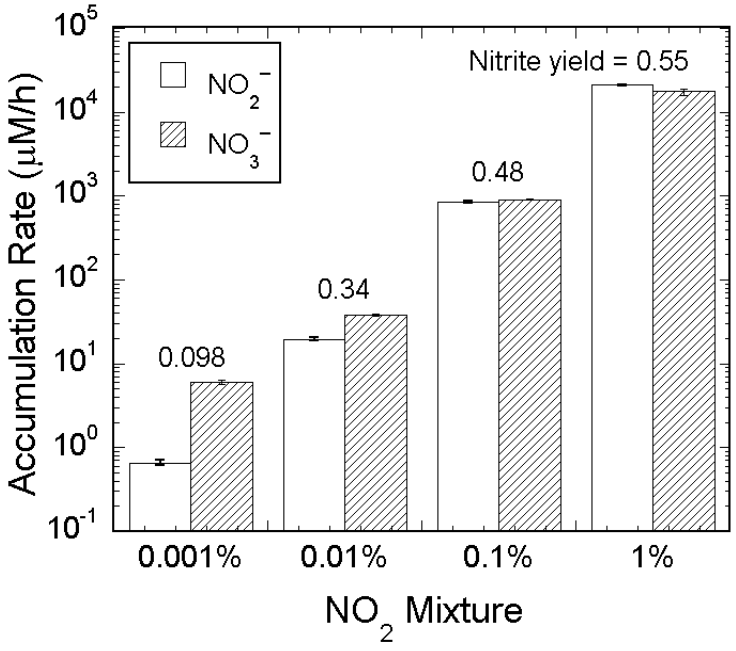

Figure 3.6. Measured nitrite and nitrate accumulation rates during delivery of various NO_2-containing gas mixtures to buffer in the absence of ABTS.

Nitrite yields [see Eq. (3.47)] are reported for each mixture; increasing deviation from the yield of 0.5 expected on the basis of Reaction (3.2) is observed with decreasing % NO_2. See Section 3.4.2.1 for discussion of this behavior.

experiments with delivery through the porous PTFE membrane, with values of 0.64 ± 0.04 and 0.62 ± 0.02 using 0.1% (n = 2) and 1% (n = 3) NO_2. The experimental data from the PDMS and PTFE delivery experiments is included in Appendix B.

3.3.3 Simulated accumulation rates

Figure 3.7 plots on a log scale the nitrite accumulation rate in the absence of ABTS, along with the corresponding simulation results. The bar heights and error bars for the experimental data are the mean and standard deviation, respectively, reported in Table 3.2. Figure 3.8 plots on a linear scale the NO_2^- and $ABTS^+$ accumulation rates in experiments with 107 μM ABTS, again paired with the corresponding simulation results. The model predictions from both types of experiment are in excellent agreement with the data, with deviations of no more than approximately ± 15% in all cases. In both figures, the upper and lower error bars for the model were calculated by running simulations at the respective upper and lower extremes of the uncertainties for $\tilde{k}_{H_2O}$ and k_{O_2} (Table 3.1).

3.4 Discussion

While existing methods for generation of NO_2 have been used in the study of its reactions with biomolecules, these methods are poorly suited for exposing cells to concentrations that mimic the steady conditions estimated to be present in inflamed tissues. Given the success in development of systems suitable for delivery of NO to cells and biomolecules over prolonged periods [Skinn et al., 2011 (see Chapter 2); Wang and Deen, 2003] we sought to develop a similar system for NO_2. Initial efforts to deliver NO_2 by diffusion through PDMS tubing [as in Wang and Deen (2003)] and through a flat,

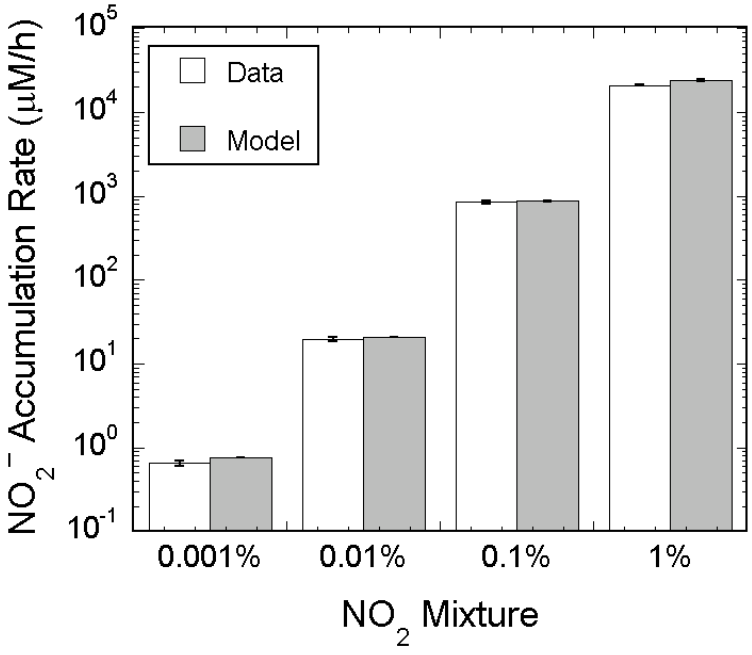

Figure 3.7. Measured and predicted nitrite accumulation rates during delivery of various NO_2-containing gas mixtures to buffer in the absence of ABTS.

The discrepancies between model and data are 15% or less at all conditions studied.

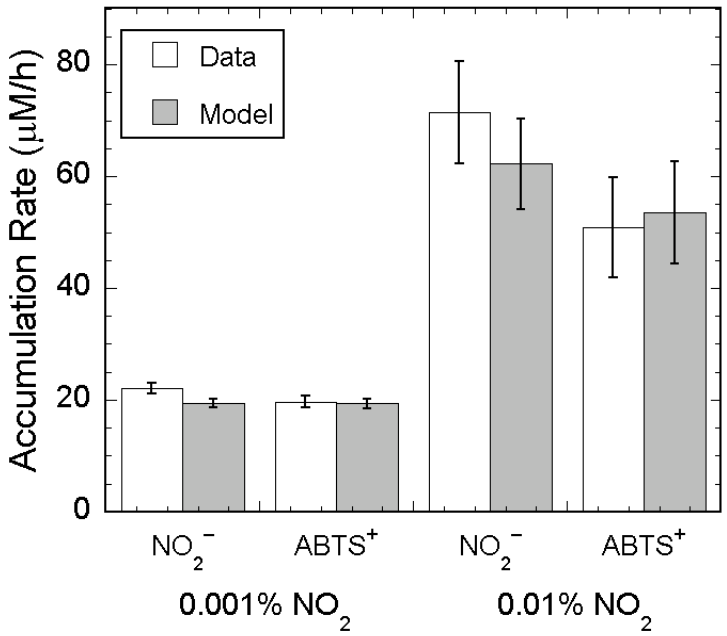

Figure 3.8. Measured and predicted nitrite and $ABTS^+$ accumulation rates during delivery of 0.001% and 0.01% NO_2 to buffer in the presence of ABTS.

The discrepancies between model and data are 15% or less at all conditions studied.

porous PTFE membrane [as in Skinn et al. (2011)] resulted in product accumulation rates that were not well described by models incorporating only mass transfer and the comparatively simple kinetic mechanism of Reactions (3.1)–(3.3). Presumably, additional NO_2 or N_2O_4 chemistry occurs within these membranes. In the former case, the solubility of water vapor in PDMS is relatively high (approx. 1.8×10^{-2} M atm^{-1}; Sato et al., 2010), possibly permitting N_2O_4 hydrolysis or other reactions to occur within the tubing; further, reaction between NO_2 and/or N_2O_4 and the PDMS tubing itself cannot be ruled out. In the latter case, NO_2 has been shown to interact with PTFE [as evidenced by the aberrant diffusivity and solubility of NO_2 in PTFE as measured by Pasternak et al. (1970)], and it is possible that the porous PTFE matrix transforms NO_2 in some fashion as it traverses the membrane.

Given the poor results from delivery of NO_2 by diffusion through permeable membranes, delivery by direct gas-liquid contacting was used to examine whether elimination of the interposed membrane would lead to more predictable results. Direct contacting of NO_2-containing gas streams with aqueous media is relatively well studied, though few, if any, of the systems reported in the literature could be readily adapted for NO_2 exposures of biological materials, particularly cells. As the reactor of Wang and Deen (2003) was successful in achieving steady exposure of cells to NO, it was adapted to the purpose of NO_2 delivery by reducing the liquid volume and introducing a head-space. Passage of NO_2-containing gas mixtures through this headspace at controlled flow rates enabled steady, reproducible delivery of NO_2 to the liquid in the absence of cells; proceeding with application of the system to cellular exposures should be straightforward.

The first sub-section of the following analysis, Section 3.4.1, discusses various considerations related to application of the delivery system to cell experiments. Section 3.4.1.1 presents the NO_2 and N_2O_4 (together 'reactive nitrogen' or 'RN') concentrations expected to occur within the reactor at room and body temperature. Section 3.4.1.2 describes the confounding effect of NO_2-reactive substrates on NO_2 exposures of cells and proposes re-suspension of the target cells in substrate-free medium as means to avoid this problem. Section 3.4.1.3 provides suggestions for how to replenish the dissolved oxygen and liquid volume lost to the headspace over the course of an experiment.

The next sub-section (Section 3.4.2) presents further analysis of the data and macroscopic model. Section 3.4.2.1 rationalizes the deviation of the nitrite yield for the 0.01% and 0.001% NO_2 mixtures from the predicted value of 0.5 (see Section 3.3.2 and Figure 3.6) in terms of a putative nitric acid impurity in the NO_2 gas cylinders. The remainder of Section 3.4.2 presents various scaling arguments. Section 3.4.2.2 explains the 3/2-power relationship observed between the nitrite accumulation rate and f_N (see Figure 3.5) in terms of a simplified model that assumes RN is transported primarily as NO_2. Section 3.4.2.3 explains the constant observed product accumulation rates (see, e.g., Figure 3.4) by comparing the time scales of the approach to steady-state of the volume-averaged RN concentration with the experimental sampling intervals. Section 3.4.2.4 invokes a series resistances argument to argue that the significant uncertainty in the measured gas-phase mass transfer coefficient for H_2O (Table 3.1) is of minimal concern in terms of the accuracy of the proposed model.

Section 3.4.3 begins with a detailed description (Section 3.4.3.1) of the method used to calculate the 'lag times' of Section 3.4.1.2. The remainder of the sub-section is dedicated to analysis of the output from the microscopic model of Section 3.2.5.4. The sensitivity of the simulated nitrite and $ABTS^+$ accumulation rates to the various system parameters is described in Section 3.4.3.2. Section 3.4.3.3 presents some representative dimensionless concentration profiles for RN and ABTS, and Section 3.4.3.4 describes the dependence of some of the simulation outputs on the stagnant film thickness (η_f from Section 3.2.5.5).

Section 3.4.4 concludes the discussion with some brief remarks on the attempts to deliver NO_2 by diffusion through PDMS tubing and porous PTFE membranes, as described in Section 3.1.

3.4.1 Application to cell experiments

3.4.1.1 RN concentrations at body temperature

In order to predict the behavior of the system at body temperature, temperature corrections were made in the parameter values, as given in Table 3.1 and explained in Section 3.2.5.6. Figure 3.9 plots the predicted bulk and well-mixed NO_2 concentrations at room and body temperature. The bulk and well-mixed NO_2 concentrations should be representative of those encountered within the reactor by suspended and adherent cells, respectively. Both concentrations increase with increasing f_N, with the well-mixed and bulk concentrations ranging between 0.3-0.8 nM and 0.4-6.0 nM, respectively. At a given f_N, both concentrations are predicted to decrease when the temperature is increased from 23 °C to 37 °C. This is primarily due to the decrease in the NO_2 solubility (α_{NO_2}).

Of note, in delivery of 0.001% NO_2 both the bulk and well-mixed concentrations are similar to that predicted to exist in oxygenated buffer containing 1 μM NO (0.3-0.4 nM, compared to a predicted 0.5 nM; Lewis et al., 1995b). This NO concentration is on the order of that predicted to occur in an inflamed colonic crypt (Chin et al., 2010). A further advantage of the 0.001% mixture is that the accumulation rates of nitrous and nitric acids are small enough to permit the use of weakly-buffered (≥ 1 mM) solutions if necessary, but are large enough that quantification of the final nitrite and nitrate by Griess techniques is uncomplicated. As such, mixtures of 0.001% NO_2 are recommended for most applications of this reactor.

3.4.1.2 Effect of NO_2-reactive substrates in culture medium

Simulation of delivery to solutions containing 107 μM ABTS indicated that essentially all of the RN was consumed within a few microns of the gas-liquid interface (see, e.g., Figure 3.23). It is reasonable to assume that similar behavior would result in the presence of other NO_2-reactive substrates. This spatial confinement is expected to practically eliminate contact between NO_2 and any cells in the reactor, as only a small portion of a suspended cell would ever contact the RN-rich region—and then only transiently—and adherent cells will remain far from the interface at all times. In effect, NO_2 exposure of cells occurs only in the absence of NO_2-reactive substrates: it is necessary either to wait a sufficient time after initiation of NO_2 delivery for these substrates to be consumed, or to resuspend/re-plate the target cells in substrate-free buffer. This behavior is similar, for example, to the protective effect of ascorbate and other antioxidants against lipid peroxidation by NO_2 as reported by Halliwell et al. (1992).

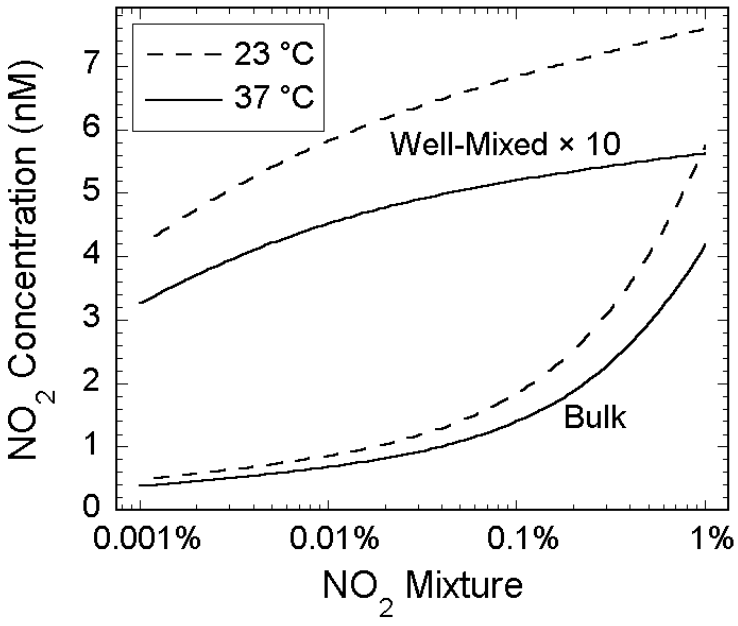

Figure 3.9. Predicted bulk and well-mixed region NO_2 concentrations at ambient and body temperature, as a function of the % NO_2 in the feed gas.

The bulk and well-mixed concentrations are predicted to apply to delivery to suspended- and adherent-culture cells, respectively. The moderate decrease in both NO_2 concentrations with the increase to 37 °C is due primarily to decreasing NO_2 solubility with increasing temperature.

The 'lag time' for a substrate is defined here as the NO_2 delivery time required to reduce the bulk concentration of that substrate sufficiently that the predicted bulk NO_2 concentration rises to 95% of its value in the absence of the substrate. For compactness, define this substrate concentration as the 'lag-phase endpoint concentration,' $\overline{C}_{j,e}$.

Figure 3.10 plots the estimated lag times at 37 °C for ABTS and three substrates commonly found in cell culture media, glutathione (GSH), ascorbate (Asc), and cysteine (Cys); details of these lag time calculations are presented in Section 3.4.3.1. The rate constants and diffusivities for GSH, Asc, and Cys that were used in generating the lag time curves are listed in Table 3.3, along with the calculated endpoint concentrations for all four species. When present, typical concentrations for GSH, Asc, and Cys in culture medium (RPMI, DMEM, Ham's and McCoy's were taken as representative; formulations were from https://shop.lonza.com) are 2, 3, and 290 μM, respectively, corresponding to lag times of 3, 3.5, and 12 h.

Note that other components of the culture medium are also likely to be NO_2-reactive, such as free tyrosine and the pH indicator Phenol Red. The lag time in experiments with multiple substrates is expected to be a nonlinear, additive combination of the lag times of the individual species, which may extend to dozens of hours. Fetal serum commonly added to culture media for mammalian cells also contains a complex spectrum of potential substrates for NO_2, further extending the lag time. Thus, despite the inevitable complications that will result, such as limitations on the duration of experiments because of diminished cell viability in the absence of proper culture medium, re-suspension or re-plating of target cells in, for example, Hank's balanced salt solution (HBSS) is the recommended course for NO_2 exposures. The inorganic salts in HBSS are

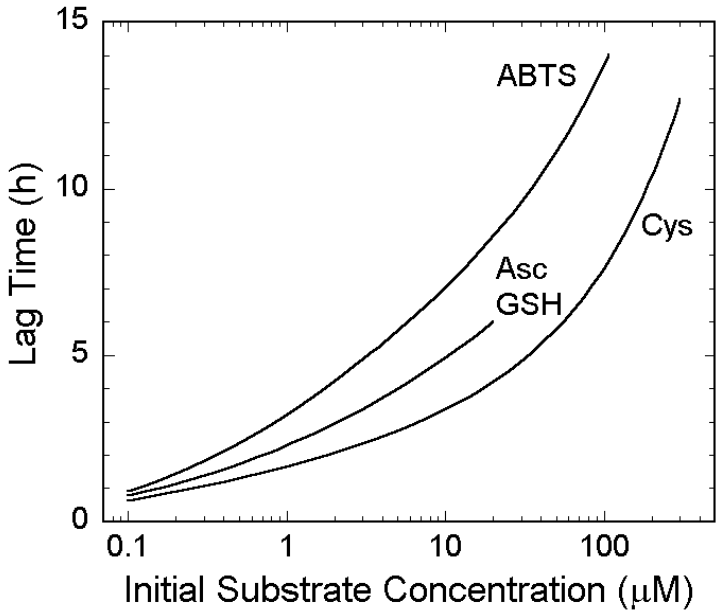

Figure 3.10. Predicted lag time as a function of the initial concentration of various NO_2-reactive substrates.

Asc, GSH and Cys are ascorbate, glutathione, and cysteine, respectively. Lag times were estimated assuming single-step, second-order reactions of substrate and NO_2 and are primarily dependent on the reaction rate constant and the substrate diffusivity (see Section 3.4.3.1). Lag time estimates are for 37 °C.

Table 3.3. Diffusivities, NO_2 reaction rate constants, and lag-phase endpoint concentrations for lag time calculations

Parameter	Value	Units	Reference
k_{GSH}	4.4×10^{7}	$M^{-1}\ s^{-1}$	Ford et al., 2002
k_{Asc}	1.5×10^{8}	$M^{-1}\ s^{-1}$	Alfassi et al., 1990
k_{Cys}	1.1×10^{8}	$M^{-1}\ s^{-1}$	Ford et al., 2002
D_{GSH}	1.1×10^{-9}	$m^2\ s^{-1}$	Jin and Chen, 2000
D_{Asc}	7.3×10^{-10}	$m^2\ s^{-1}$	Gerhardt and Adams, 1982
D_{Cys}	1.4×10^{-9}	$m^2\ s^{-1}$	Jin and Chen, 2000
$\bar{C}_{\mathrm{ABTS},e}$	106	pM	(this work)
$\bar{C}_{\mathrm{GSH},e}$	174	pM	
$\bar{C}_{\mathrm{Asc},e}$	95	pM	
$\bar{C}_{\mathrm{Cys},e}$	40	pM	

Rate constants and diffusivities are for 37 °C and were adjusted from literature values as described in Section 3.2.5.6. See text for definition of lag-phase endpoint concentrations.

expected to be inert to NO_2; although a reaction of NO_2/N_2O_4 with glucose has been reported (Degering and Berntsen, 1951), hours-long exposures to relatively high RN levels were required to obtain moderate conversions. As such, the glucose in HBSS should be effectively inert and HBSS is expected to behave as a substrate-free medium for the purposes of NO_2 delivery. Maintenance of baseline cell viability for 4 h should be feasible in freshly prepared HBSS (Chrungoo et al., 1997; De Souza et al., 2010; Li et al., 2002a; Yoshikawa et al., 1997); depending on the cell line longer experiments may be possible.

3.4.1.3 Maintenance of reactor O_2 and H_2O levels

Note that O_2 levels can be maintained in the reactor by including a sufficient amount of O_2 in the NO_2 gas mixture. Unlike with NO, where the co-existence of O_2 and NO has significant undesired consequences (Wang and Deen, 2003), O_2 is typically added to NO_2 gas mixtures in order to inhibit slow, equilibrium formation of NO and O_2 (Atkinson et al., 2004). The only route for O_2 consumption in the liquid is expected to be cellular respiration, which can be accounted for in the O_2 mass balance as follows. The volumetric O_2 consumption rate can be represented as

$$\overline{R}_{O_2} = -\rho_c \cdot q_{O_2}, \tag{3.48}$$

where ρ_c is the cell density in units of cells ml^{-1} and q_{O_2} is the specific O_2 consumption rate in units of mol s^{-1} cell^{-1}. Under steady-state conditions, the liquid-phase mass balance for O_2 [Eq. (3.5)] written in terms of O_2 partial pressures is

$$0 = \frac{\alpha_{O_2} k_{O_2} A}{V}\left(\tilde{P}_{O_2,f} - \overline{P}_{O_2}\right) - \rho_c q_{O_2}, \tag{3.49}$$

where $\overline{P}_{O_2}$ is the desired volume-averaged O_2 partial pressure in the liquid and $\tilde{P}_{O_2,i} \approx \tilde{P}_{O_2,f}$ is assumed as per the scaling analysis described in Section 3.2.5.2. Algebraic rearrangement of Eq. (3.49) provides a specification for the abundance of O_2 in the NO_2 mixture:

$$\tilde{P}_{T,f} f_{O_2} - \overline{P}_{O_2} = \frac{V}{\alpha_{O_2} k_{O_2} A} \cdot \left(\rho_c q_{O_2} \right). \tag{3.50}$$

In Eq. (3.50) $\tilde{P}_{T,f}$ is the total pressure of the gas feed stream at the reactor inlet (1.00 atm in the present system configuration) and f_{O_2} is the fraction of O_2 in the feed gas mixture, typically expressed as a percentage. To note, it should be feasible to include CO_2 in the feed gas mixture as well, per the requirements of many mammalian cell lines (Chin et al., 2010; Li et al., 2009; Wang et al., 2003). This ability to supply all three gases (NO_2, CO_2, and O_2) in a single feed stream is an appealing feature of the system design.

As an example, consider delivery of NO_2 to TK6 cells, a human lymphoblastoid cell line that has been studied extensively in the context of exposure to nitric oxide (Dong and Dedon, 2006; Li et al., 2006; Li et al., 2002b; Li et al., 2005; Wang et al., 2003). The specific O_2 consumption rate of this cell line at 37 °C in phosphate-buffered saline is 0.65 ± 0.16 nmol min^{-1} $(10^6 \text{ cells})^{-1}$ as reported by Wang et al. (2003). For delivery of NO_2 at 37 °C to a TK6 cell suspension at a density of $\rho_c = 2 \times 10^6$ cells ml^{-1} and at air-equilibrated oxygen levels ($\overline{P}_{O_2} = 0.21$ atm), Eq. (3.50) and the parameter values in Table 3.1 indicate that the NO_2 gas mixture should include 23% O_2.

Since experiments delivering NO_2 to cells will last at least a few hours, the rate of loss of water from the reactor may be significant: the rate of loss of liquid volume will

be approximately 0.5 and 1.0 ml h^{-1} at 23 °C and 37 °C, respectively, based on the saturation water vapor pressures reported in Green and Maloney (1997). It is not possible to prevent water loss by using a 'wet' NO_2 mixture, because of the inevitable hydrolysis of N_2O_4 that would occur within the supply cylinder [Reaction (3.2)]. Accordingly, it may be necessary to replenish the reactor volume by injecting appropriate quantities of sterile water. The volume should be replenished with sterile water instead of with, e.g., HBSS since only the H_2O is volatile; loss of buffer salts or glucose should be negligible.

3.4.2 Supplemental analysis of data and macroscopic model

3.4.2.1 Nitric acid impurity

Certain aspects of the simulation and experimental results demand closer scrutiny. For example, a notable feature of the experimental data (Table 3.2, Figure 3.6) is the increasing deviation of the nitrite yield [$Y_{NO_2^-}$, Eq. (3.47)] from the stoichiometric prediction of Reaction (3.2) with decreasing abundance of NO_2 in the gas mixture. With 1% and 0.1% NO_2 mixtures, the observed nitrite yield was close to the expected value of 0.5, whereas with 0.01% and 0.001% NO_2 the nitrate accumulation rate was significantly greater than the nitrite rate. One possible explanation for this deviation is a nitric acid impurity in the gas mixture: the gas manufacturer confirmed that they expect a "0.2% to 2% relative level of nitric acid" in their NO_2 mixtures (M. Birch, personal communication), though the impurity is not assayed on a cylinder-by-cylinder basis. HNO_3 impurities at roughly this level (~1.5%) have been observed previously in commercial NO_2 mixtures (Bambauer et al., 1994). We hypothesize that the deviation of

the product distribution from the expected $Y_{NO_2^-} = 0.5$ is due to such an impurity. Quantitative support for this hypothesis is provided in what follows.

The rapid deprotonation of HNO_3 upon entering the buffered liquid media is assumed to drive $\tilde{C}_{HNO_3,i}$ nearly to zero. Thus, neglecting gas-phase reactions, Eq. (3.6) written for nitric acid becomes

$$0 = Q\left(\tilde{C}_{HNO_3,f} - \tilde{C}_{HNO_3}\right) - \tilde{k}_{HNO_3} A \tilde{C}_{HNO_3} . \tag{3.51}$$

Assuming $\tilde{k}_{HNO_3} \approx \tilde{k}_{H_2O}$ it follows that $\tilde{C}_{HNO_3} = \tilde{C}_{HNO_3,f}\left(1+\tilde{\kappa}_{H_2O}\right)^{-1}$, with $\tilde{\kappa}_{H_2O}$ as in Eq. (3.9), and the predicted contribution of the impurity to the nitrate accumulation rate in the absence of ABTS is

$$\Delta dC \equiv \frac{dC_{NO_3^-}}{dt} - \frac{dC_{NO_2^-}}{dt} = \tilde{C}_{HNO_3,f} \frac{\tilde{k}_{H_2O} A}{V} \frac{1}{1+\tilde{\kappa}_{H_2O}} . \tag{3.52}$$

Eq. (3.52) assumes that in the absence of ABTS the nitrite and nitrate accumulation rates are equal and that all excess nitrate accumulation is attributable to the nitric acid impurity.

Table 3.4 summarizes the information required to estimate the magnitude of the impurity and to calculate corrected nitrate accumulation rates in the presence of ABTS. Per Eq. (3.52), the difference ΔdC between the observed nitrate and nitrite accumulation rates in the absence of ABTS was used to estimate the concentrations (at 25 °C and 1 atm) of the nitric acid impurities as 21 nM and 70 nM, respectively, in the 0.001% and 0.01% NO_2 mixtures. These concentrations represent 5.1% and 1.7% relative impurities compared to the NO_2 concentrations in the gas mixtures (0.41 μM and 4.1 μM, respectively). Both of the former are in reasonable agreement with the manufacturer's

Table 3.4. Data used for estimation of feed gas nitric acid impurity and for correction of simulated nitrate accumulation rates in the presence of ABTS.

	Quantity	Source	NO_2 Mixture	
			0.001%	0.01%
No ABTS	$\frac{dC_{NO_3^-}}{dt}$	Data	6.0	38
	$\frac{dC_{NO_2^-}}{dt}$	Data	0.66	20
	$\Delta dC \equiv \frac{dC_{NO_3^-}}{dt} - \frac{dC_{NO_2^-}}{dt}$	Data	5.3	18
	$\tilde{C}_{HNO_3,f}$	Eq. (3.52)	21 nM (5.1%)	70 nM (1.7%)
107 μM ABTS	$\frac{dC_{NO_3^-}}{dt}$	Data	5.7	24
		Simulation	0.26	9.0
		Simulation + ΔdC	5.6	27

Experimental data are reproduced from Table 3.2; uncertainties in the accumulation rates are omitted for clarity. Units for all quantities are μM h^{-1} except those for $\tilde{C}_{HNO_3,f}$, as indicated. The relative nitric acid impurity for each gas mixture, $\tilde{C}_{HNO_3,f} / \tilde{C}_{N,f}$, is given in parentheses below the corresponding values of $\tilde{C}_{HNO_3,f}$. The procedure for correcting the simulated nitrate accumulation rate in the presence of ABTS is described in the text.

estimate. Further, as can be seen in Table 3.4, correction of the simulated nitrate accumulation rate by the ΔdC calculated from the ABTS-free data markedly improves the quality of the prediction for both NO_2 mixtures studied. The consistency of these results indicates that the nitric acid impurity hypothesis is quite plausible.

The lack of direct measurement of the proposed nitric acid impurity negates the usefulness of the NO_3^- accumulation data in the quantitative characterization of the reactor. As such, the remainder of Section 3.4 will focus exclusively on the NO_2^- and $ABTS^+$ data. It is worthwhile to note, though, that methods exist for the assay of HNO_3 even in the presence of a relative excess of NO_2 [see, e.g., Appel et al. (1980) and Goldan et al. (1983)] and thus it would have been feasible to quantify the impurity more rigorously had it been necessary in order to validate the proposed model.

3.4.2.2 Power-law dependence of nitrite accumulation rate on f_N

The quality of the fit shown in Figure 3.5 and its close match to a 3/2-power dependence can be rationalized by assuming that RN is primarily transported as NO_2. In the present configuration, scaling arguments can be made based upon boundary layer theory (Deen, 1998) that the hydrolysis of N_2O_4 is sufficiently fast that convective effects can be neglected near the interface and thus transport will be effected only by diffusion. If N_2O_4 is a negligible contributor to RN transport, the diffusion of NO_2 will be balanced by N_2O_4 hydrolysis, as

$$D_{NO_2} \frac{d^2 C_{NO_2}}{dx^2} \sim k_2 C_{N_2O_4} \approx k_2 K_1 C_{NO_2}^2 , \tag{3.53}$$

where the symbol '~' indicates an order of magnitude equality. A penetration depth δ for NO_2 can be derived from Eq. (3.53) by noting that $D_{NO_2} C_{NO_2,i} / \delta^2 \sim k_2 K_1 C_{NO_2,i}^2$,

giving $\delta \sim \left(D_{NO_2} / k_2 K_1 C_{NO_2,i} \right)^{1/2}$. The absorptive flux of NO_2 can thus be estimated as

$$N_{NO_2} = -D_{NO_2} \frac{dC_{NO_2}}{dx} \sim \frac{D_{NO_2} C_{NO_2,i}}{\delta} \sim \left(k_2 K_1 D_{NO_2} \right)^{1/2} C_{NO_2,i}^{3/2} . \qquad (3.54)$$

Assuming that $C_{NO_2,i} \propto f_N$, it follows directly from Eq. (3.54) that N_{NO_2}, and thus $dC_{NO_2^-} / dt$, will obey a 3/2-power relationship with f_N.

This behavior matches the 'diffusive mass-transport controlled' case of Lee and Schwartz (1981), with NO_2 as the diffusing species. Note however that this apparatus configuration differs sufficiently from that of Lee and Schwartz, in which the NO_2 gas mixture was delivered by bubbling through a glass frit, that their criteria for determining the operative 'limiting regime' are not applicable. Interestingly, despite the success of the above simplified model in rationalizing the observed 3/2-power dependence, NO_2 is not always the primary carrier of RN. For example, at 1% NO_2 the numerical model of Sections 3.2.5.3 and 3.2.5.4 predicts that while 93% of RN is present as NO_2 in the gas phase, only about 7% is in the form of NO_2 on the liquid side of the gas-liquid interface [cf. Figure 3.18(b)]. It may be that since f_N is directly proportional to $\tilde{C}_N$ (the *gas-phase* RN concentration), the variation of overall RN transport with f_N is primarily dependent upon the gas-phase distribution of RN between NO_2 and N_2O_4.

It is interesting to note that the prediction of Danckwerts (1970) for the uptake rate of NO_2 in this system is nearly a quantitative match for the observed uptake rate.

Assuming quasi-equilibrium behavior of N_2O_4, Reactions (3.1) and (3.2) taken together represent an irreversible second-order reaction of NO_2 with rate expression

$$R = -2\frac{K_1 k_2}{1 + k_2/k_{-1}} C_{NO_2}^2 \tag{3.55}$$

where k_2/k_{-1} = 0.145 (Graetzel et al., 1969). Eq. (5-59c) of Danckwerts written in the present notation for this overall reaction, assuming that RN exists primarily as NO_2, is

$$\frac{d\bar{C}_{NO_x^-}}{dt} = \frac{A}{V}\left(\frac{4}{3}\frac{D_{NO_2} K_1 k_2}{1 + k_2/k_{-1}}\right)^{1/2}\left(\frac{\alpha_{NO_2} P_T}{100}\right)^{3/2}(\%\,NO_2)^{3/2}. \tag{3.56}$$

NO_x^- indicates the sum of NO_2^- and NO_3^-, and the $\left(\alpha_{NO_2} P_T/100\right)^{3/2}(\%\,NO_2)^{3/2}$ term is equivalent to $C_{NO_2,i}^{3/2}$ assuming that $\tilde{C}_{NO_2,f} = \tilde{C}_{NO_2,i}$ for all f_N. The leading coefficient of the power-law fit for the nitrite accumulation rate in Figure 3.5 is 23.4 mM h^{-1}. Neglecting the nitric acid impurity, the coefficient for a fit of the combined nitrite and nitrate rates would be twice that number, or 46.8 mM h^{-1}. The corresponding coefficient calculated from Eq. (3.56) is 40.8 mM h^{-1}, which differs only by about 15% from the experimental result. Further, the observed power of 1.53 differs from the Danckwerts prediction of 1.5 by only 2%.

3.4.2.3 Liquid-phase relaxation time scale for RN

In describing the transport of RN into the liquid, Eq. (3.5) does not necessarily preclude the possibility of transient behavior on a time scale sufficiently long to have an experimentally observable effect on the product accumulation. The constancy of the observed rates, however, implies that the RN concentration profile consistently reached

steady-state prior to withdrawal of the first sample (t_{sample}). The relaxation time scale (t_{relax}) of the $\overline{C}_N$ transient is determined by the interfacial transport term of Eq. (3.5), since the reaction term is consumptive in RN and thus can only respond to changes in C_N originating from other phenomena. Neglecting the reaction term in Eq. (3.5) and non-dimensionalizing with $\theta = \overline{C}_N / \overline{C}_N^*$ and $\tau = t/t_{relax}$ yields

$$\frac{d\theta}{d\tau} = \frac{k_N A}{V} t_{relax} \left(\frac{C_{N,i}}{\overline{C}_N^*} - \theta \right). \tag{3.57}$$

Since the only source for RN within the liquid is transport from the gas, the RN concentration at any point within the liquid can be no greater than that at the interface. Thus, it is required that $C_{N,i} / \overline{C}_N^* \geq 1$. Per the form of Eq. (3.57), t_{relax} is inversely proportional to $C_{N,i} / \overline{C}_N^*$ and thus choosing $t_{relax} = V / k_N A$ represents an upper bound on the relaxation time of the RN concentration. That is, in the case that $C_{N,i} / \overline{C}_N^* \gg 1$, the actual relaxation time will be much smaller than t_{relax}.

In the absence of reactions, the value of k_N would not be very different from the value of k_{O_2}. However, the rapid hydrolysis of N_2O_4 and the reaction of NO_2 with ABTS are expected to increase k_N relative to its unreactive value. The magnitude of this increase can be estimated for delivery in the absence of ABTS, as follows. The flux expression of Eq. (3.54), rewritten for RN, can be related to k_N as

$$D_N \frac{dC_N}{dx} \sim \frac{D_N}{\delta_N} C_{N,i} \sim k_N C_{N,i}, \tag{3.58}$$

where $C_{N,i}$ is chosen as the scale for C_N and δ_N is the penetration depth for RN, analogous to the definition of δ of Section 3.4.2.2. An expression for δ_N can be determined by a method similar to that of Eq. (3.53); the order of magnitude relationship is

$$D_N \frac{d^2 C_N}{dx^2} \sim \frac{D_N}{\delta_N^2} C_{N,i} \sim k_2 (1-\varphi_i) C_{N,i}, \tag{3.59}$$

where φ_i is the value of φ calculated from $C_{N,i}$. The resulting expression for the penetration depth is $\delta_N \sim \left[D_N / k_2 (1-\varphi_i) \right]^{1/2}$, which in combination with Eq. (3.58) gives

$$k_N \sim \left[D_N k_2 (1-\varphi_i) \right]^{1/2}. \tag{3.60}$$

No straightforward method was identified for estimation of φ_i at the various f_N of interest, so values were taken from the simulations. Given that higher RN concentrations favor N_2O_4 formation, however, a positive correlation between f_N and $(1-\varphi_i)$ is expected. Table 3.5 presents for the various f_N the values of $(1-\varphi_i)$ from simulations, the corresponding estimates of k_N and t_{relax}, and experimental values of t_{sample}. As can be seen, in all cases the first sample was drawn at an interval of at least eight times the corresponding estimate of the relaxation time. It is thus reasonable to argue that no transient behavior should be observed, in agreement with the experimental data. Also included in Table 3.5 is an estimate of the relaxation time as calculated from the unreactive mass transfer coefficient (i.e., assuming $k_N = k_{O_2}$), corresponding to the limit $f_N \to 0$. As can be seen, reactive enhancement of RN uptake is significant; further, the unreactive t_{relax} indicates that transient behavior would likely have been observed in most experiments without ABTS were it not for the effect of N_2O_4 hydrolysis.

Table 3.5. Comparison of predicted relaxation times and experimental sampling times for NO_2 delivery in the absence of ABTS.

f_N	$(1-\varphi_i)$	$k_N \times 10^5$ ($m\ s^{-1}$)	t_{relax} (min)	t_{sample} (min)	t_{sample}/t_{relax}
(unreactive)	0	2.5	17.5	–	–
0.001%	0.0140	16.1	2.94	40	14
0.01%	0.147	52.1	0.904	15	17
0.1%	0.557	102	0.464	5	11
1%	0.854	126	0.375	3	8.0

3.4.2.4 Uncertainty in the gas-phase mass transfer coefficient

The large uncertainty in the experimentally-determined gas-phase mass transfer coefficient for H_2O (± 60%) is troubling. However, varying $\tilde{k}_{H_2O}$ across its full ± 60% range of uncertainty has in most cases no more than a 5% effect on simulated product accumulation rates, with the magnitude of the effect decreasing as the NO_2 abundance of the gas mixture decreases. This weak dependence can be rationalized by noting that three main transport processes are represented in Eqs. (3.5) and (3.6): convective transport (inflow) into the headspace via the feed gas, transport from the headspace gas to the interface, and transport from the interface into the liquid. Expressions for the resistance to transport through the gas- and liquid-phase boundary layers ('gas-BL' and 'liq-BL' resistances, respectively) have already been described in Eq. (3.7). The 'inflow resistance' for a driving force expressed in terms of liquid-equivalent concentrations is AK_N/Q. The 'partition coefficient' for RN, $K_N = C_N/\tilde{C}_N = K_{NO_2}\tilde{\varphi} + K_{N_2O_4}(1-\tilde{\varphi})$, varies in a nonlinear, monotonic fashion between K_{NO_2} and $K_{N_2O_4}$ as $\tilde{C}_N$ increases. For the feed concentrations $\tilde{C}_{N,f}$ corresponding to the experimental f_N values of 0.001%, 0.01%, 0.1% and 1%, K_N has estimated values of 0.22, 0.25, 0.47, and 2.3, respectively.

At f_N = 0.001%, both the gas-BL and inflow resistances (7.3 s m^{-1} and 100 s m^{-1}, respectively) are insignificant compared to the liq-BL resistance (6200 s m^{-1}; k_N from Table 3.5). As the richness of the gas mixture is increased to 1% NO_2, however, the greater relative abundance of N_2O_4 in the liquid phase (due to the nonlinearity of the equilibrium of Reaction (3.1) and the significantly greater solubility of N_2O_4) enhances RN transport in the liq-BL and correspondingly decreases the liq-BL resistance

(790 s m^{-1}). While the value of K_N at 1% NO_2 is large enough to make the inflow resistance significant (1000 s m^{-1}), it is still small enough that the gas-BL resistance remains insignificant (73 s m^{-1}). Changes in $\tilde{k}$ are thus expected to have a small effect on the overall transport of RN regardless of f_N, as observed in the simulations. Support for the prediction of comparable inflow and liq-BL resistances at 1% NO_2 can be found in the results from delivery experiments at 365 and 250 sccm: decreasing Q by 32% resulted in a 21% decrease in the nitrite accumulation rate, which is on the order of what would be expected in the case of a significant inflow resistance.

3.4.3 Supplemental analysis of microscopic model

3.4.3.1 Computation of lag times

The lag times described in Section 3.4.1.2 and presented in Figure 3.10 were determined as follows. While conversion of the pseudo-steady-state, non-dimensionalized model presented in Section 3.2.5.5 into a transient form is trivial (viz., by introducing appropriate time derivatives), implementing such a model in MAPLE is challenging. It is further uncertain whether simulation of such a model would have been within the computational capabilities of MAPLE. Instead, the following numerical approach was used. The instantaneous pseudo-steady volumetric consumption rate of a given substrate was determined as a discrete function Φ_j of the bulk substrate concentration (units of μM and μM h^{-1} for $\overline{C}_j$ and $d\overline{C}_j/dt$, respectively) via simulations. That is,

$$\Phi_j\left(\overline{C}_j\right) \equiv \left.\frac{d\overline{C}_j}{dt}\right|_{\overline{C}_j} . \tag{3.61}$$

Since the substrate concentration is not elevated in the liquid-phase boundary layer, the well-mixed and bulk concentrations are essentially equal and thus are freely interchangeable. The maximum of the domain of each Φ_j was selected to be on the order of the concentration of species *j* found in typical cell culture media; the minimum was selected to be at least an order of magnitude smaller than the lag-phase endpoint concentration as defined in Section 3.4.1. Each function Φ_j was meshed at approximately equal log-spacing in $\bar{C}_j$ throughout the domain, due to complex behavior of the functions Φ_j at small $\bar{C}_j$ and to the accuracy required for the inversion in Eq. (3.62), below. Figure 3.11 plots Φ_{ABTS} versus $\bar{C}_{ABTS}$ as a representative example; the inset shows the behavior of Φ_{ABTS} at low ABTS concentrations.

The discrete function Φ_j for each substrate was fitted with a cubic spline function (via the MAPLE function 'CurveFitting[Spline]'), which is a piecewise-continuous function F_j composed of a sequence of third-order polynomials that "is smooth in the first derivative and continuous in the second derivative" across the full domain of interpolation (p121, Press, 2007). The spacing between each pair (Φ_j,Φ_{j+1}) was sufficiently close that the second derivative of F_j was approximately constant across that interval, making the error in the fit minimal. The mesh density in $\bar{C}_j$ was selected such that the relative error between Φ_j and F_j, as well as between $1/\Phi_j$ and $1/F_j$, was less than 10^{-6} for all Φ_j. Rearrangement and definite integration of Eq. (3.61) (substituting the continuous F_j for the discrete Φ_j) from the initial substrate concentration $\bar{C}_{j,o}$ at $t = 0$ to the lag-phase endpoint concentration $\bar{C}_{j,e}$ at the lag time yields an expression for $t_{lag,j}$

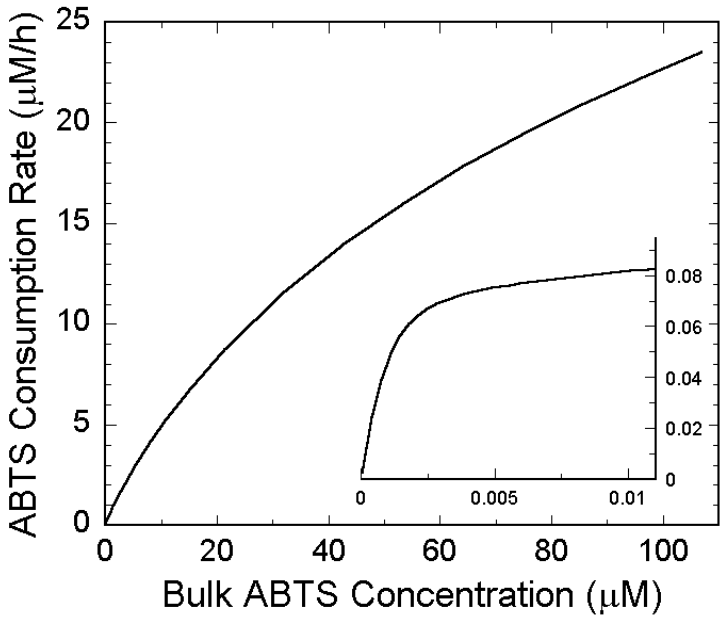

Figure 3.11. Predicted bulk volumetric ABTS consumption rate as a function of bulk ABTS concentration.

Plotted ABTS concentration range covers the domain necessary for calculation of the lag times of Figure 3.10. Inset highlights the deviation of the consumption rate profile at small $\overline{C}_{\mathrm{ABTS}}$. Variation in the consumption rate is approximately proportional to the square root of the bulk ABTS concentration over most of the concentration range shown.

for a particular initial concentration of the substrate species *j*:

$$t_{lag,j}\left(\bar{C}_{j,o}\right) = \int_{\bar{C}_{j,o}}^{\bar{C}_{j,e}} \frac{1}{F_j(c)}\, dc \,. \tag{3.62}$$

To note, a non-zero endpoint concentration is used in the definition of $t_{lag,j}$ because integration to $c = 0$ in Eq. (3.62) would be undefined.

3.4.3.2 Model sensitivity study

A sensitivity study was performed to examine the effects of variability in the system parameters (Table 3.1) on the behavior of the stagnant film model described in Section 3.2.5.5. Table 3.6 delineates the shorthand notation used in Figures 3.12 through 3.16 to indicate the various cases studied. For the reference case, Case (o), the Schwartz and White (1981) value of α_{NO_2} (12 mM atm^{-1}) was used and gas-phase N_2O_4 hydrolysis was neglected ($\tilde{k}_2 = 0$). The significance of the gas phase dynamics was examined by separately increasing $\tilde{k}$ and Q by a factor of 10^4 [Cases (A) and (B)], approximating "infinite" values of those parameters, and by introducing gas-phase hydrolysis [Case (C)]. Otherwise, model parameters were typically increased by 20% from their nominal values. Changes in α_{NO_2} (or K_1) were always accompanied by corresponding changes in $\alpha_{N_2O_4}$ assuming constant K_1 (or α_{NO_2}) and $\tilde{K}_1$ (see Appendix C). Changes to k_2 and D_N influenced the linearized penetration depth δ (see Section 3.2.5.5); the value of η_f was recalculated appropriately in each case. In all cases the predicted NO_2^- and $ABTS^+$ accumulation rates were compared to the rates from Case (o).

Table 3.6. Codes and descriptions for model sensitivity study.

Code	Parameter adjusted	Notes
(o)	(reference case)	α_{NO_2} = 12 mM atm^{-1}; $\tilde{k}_2 = 0$
(A)	$Q \rightarrow \infty$	Multiplied by 10^4
(B)	$\tilde{k} \rightarrow \infty$	Multiplied by 10^4
(C)	$\tilde{k}_2$ = 328 M^{-1} s^{-1}	Gas-phase hydrolysis included
(D)	α_{NO_2} + 20%	$\alpha_{N_2O_4}$ adjusted to maintain thermodynamic consistency (Appendix C)
(D–)	α_{NO_2} – 25%	
(E)	K_1 + 20%	
(F)	k_2 + 20%	These define $\delta = \sqrt{D_N / k_2}$; $\eta_f = x_f/\delta$ recalculated appropriately (Section 3.2.5.5)
(G)	D_N + 20%	
(H)	D_{ABTS} + 20%	–

Except for α_{NO_2} and as otherwise indicated, all parameter values were as in Table 3.1.

In most cases the effect of a 20% increase in a parameter was minimal: typically less than 10% for the NO_2^- accumulation rate in the absence of ABTS (Figure 3.12), and less than 15% for the NO_2^- and $ABTS^+$ accumulation rates in the presence of ABTS (Figures 3.13 and 3.14). Inclusion of gas-phase N_2O_4 hydrolysis had at most a 5% effect on the nitrite accumulation rate [ABTS-free, Case (C), 1% NO_2], with most cases seeing much smaller effects. Neglecting this reaction was thus deemed appropriate, as noted in Section 3.2.5.4. The parameters to which the model showed notable sensitivity in the absence of ABTS were the NO_2 solubility [Cases (D) and (D–)] and the volumetric flow rate through the headspace [Case (A)], especially the latter. This strong sensitivity to Q is in good agreement with the mass transfer resistance argument described previously (Section 3.4.2.4). Interestingly, the magnitude of the effect of increasing a given liquid-phase parameter [Cases (D) through (G)] typically decreased with increasing richness of the NO_2 mixture, perhaps because of the greater significance of the gas-phase dynamics at high % NO_2. In the presence of ABTS, no parameters induced dramatic changes in the model results. At 0.001% NO_2, variations in the $ABTS^+$ and NO_2^- accumulation rates were nearly identical (Figure 3.13) because essentially all NO_2 entering the reactor is expected to react with ABTS, as opposed to undergoing dimerization and hydrolysis. At 0.01% NO_2, the relationship between the effects on NO_2^- and $ABTS^+$ rates was less straightforward (Figure 3.14), presumably because a change in any given parameter had different effects on the competing N_2O_4 hydrolysis and ABTS oxidation reactions.

The relatively strong effect of the NO_2 solubility compared to the other parameters made it a natural subject of study in an attempt to bring the model predictions in better agreement with the data. The high reactivity of NO_2 in water complicates

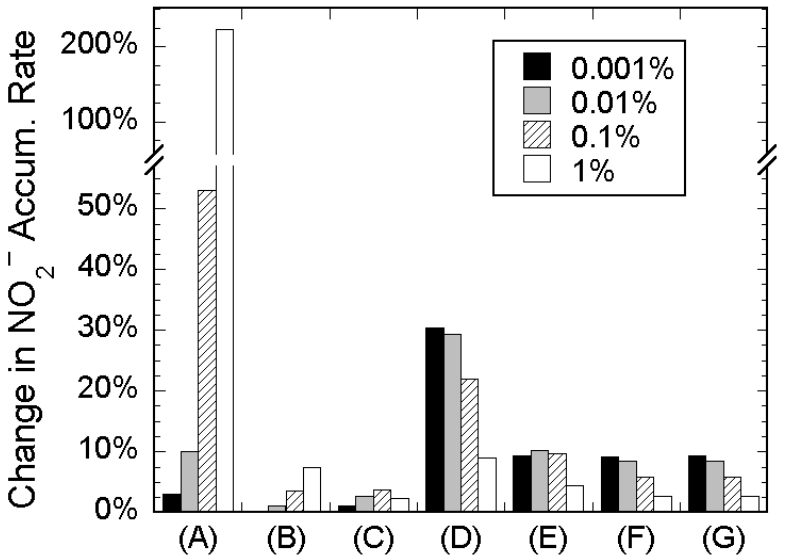

Figure 3.12. Sensitivity study: percent change from reference case in simulated nitrite accumulation rate in the absence of ABTS.

Simulation conditions and codes for the various test cases are described in Table 3.6. The dramatically increasing sensitivity of the predicted accumulation rate to Q [Case (A)] as the % NO_2 increases is explained well by the mass transfer resistance analysis in Section 3.4.2.4.

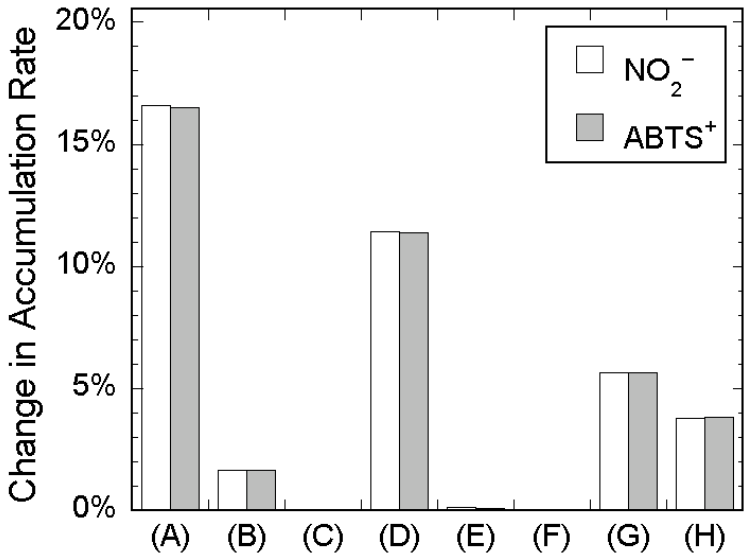

Figure 3.13. Sensitivity study: percent change from reference case in simulated product accumulation rates in the presence of ABTS (0.001% NO_2).

Reference simulation conditions and meanings for the codes for the various test cases are described in Table 3.6.

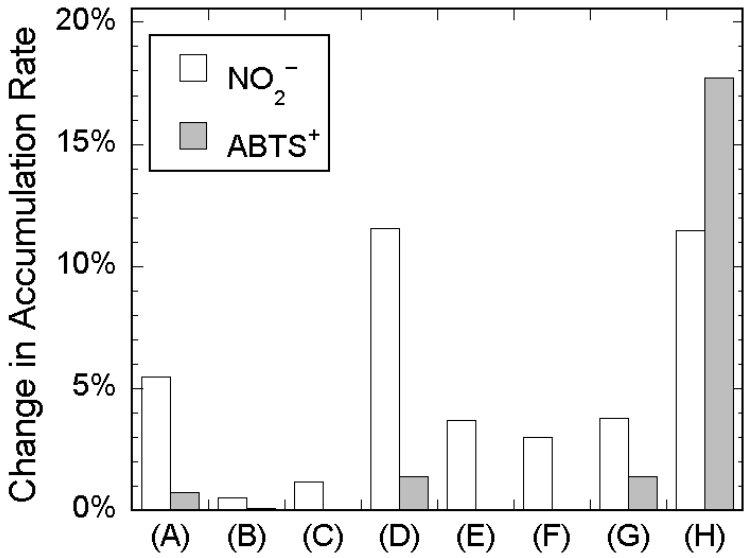

Figure 3.14. Sensitivity study: percent change from reference case in simulated product accumulation rates in the presence of ABTS (0.01% NO_2).

Reference simulation conditions and meanings for the codes for the various test cases are described in Table 3.6.

measurement of the NO_2 solubility, resulting in significant uncertainty in the literature values of this parameter ($0.1\text{-}7.0 \times 10^{-2}$ M atm^{-1}; Schwartz and White, 1981), which further strengthens the justification for using α_{NO_2} as an adjustable parameter. Simulations using Schwartz and White's recommended value, $\alpha_{NO_2} = 1.2 \times 10^{-2}$ M atm^{-1} [Case (o)], resulted in over-prediction of nitrite accumulation rate by as much as 80% in experiments without ABTS (Figure 3.15). Since the predicted nitrite accumulation rate increased as α_{NO_2} was increased, simulations were performed using various smaller values of α_{NO_2} in an attempt to improve the quality of the fit. As can be seen in Figures 3.15 and 3.16, decreasing α_{NO_2} by 25% [Case (D–)] yielded significant improvements in the model fit in the absence of ABTS, without substantially harming the quality of the fit in the presence of ABTS. The Case (D–) value of 9 mM atm^{-1} is bracketed by the Schwartz and White value of 12 mM atm^{-1} and by an experimental estimate from the same group, determined as 7 mM atm^{-1} (Lee and Schwartz, 1981). Fitting of the model to the data by means of a 25% decrease in the NO_2 solubility was thus deemed acceptable.

3.4.3.3 Microscopic model concentration profiles

In order to better understand the phenomena occurring within the liquid-phase boundary layer and the sensitivity of the model predictions to various parameters, concentration profiles generated by the model of Section 3.2.5.5 were examined. Except where noted, parameters in this section and the next correspond to Case (C) in Table 3.6. Results for Case (C) are presented because they incorporate all phenomena having at least a moderate effect on the system behavior. As will be discussed, the differences

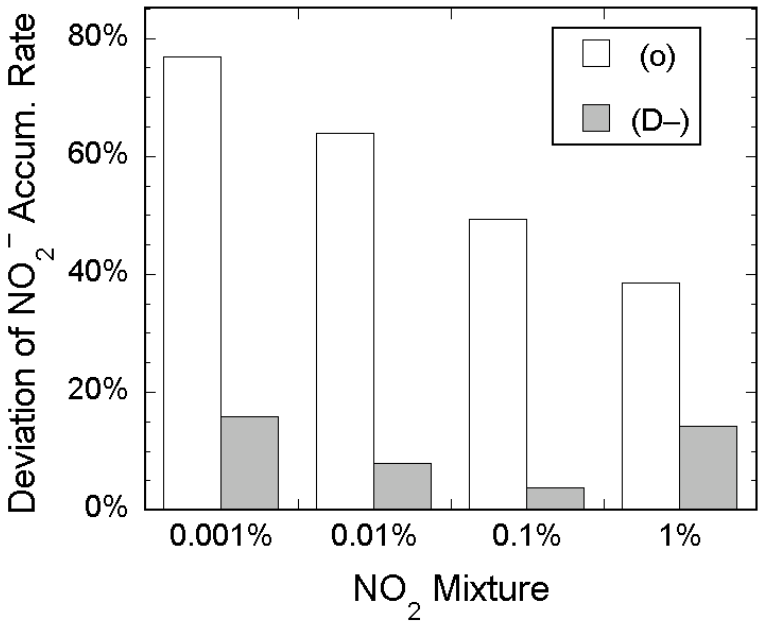

Figure 3.15. Percent deviation of model predictions from nitrite accumulation rate data in the absence of ABTS.

The conditions of Cases (o) and (D–) are described in Table 3.6.

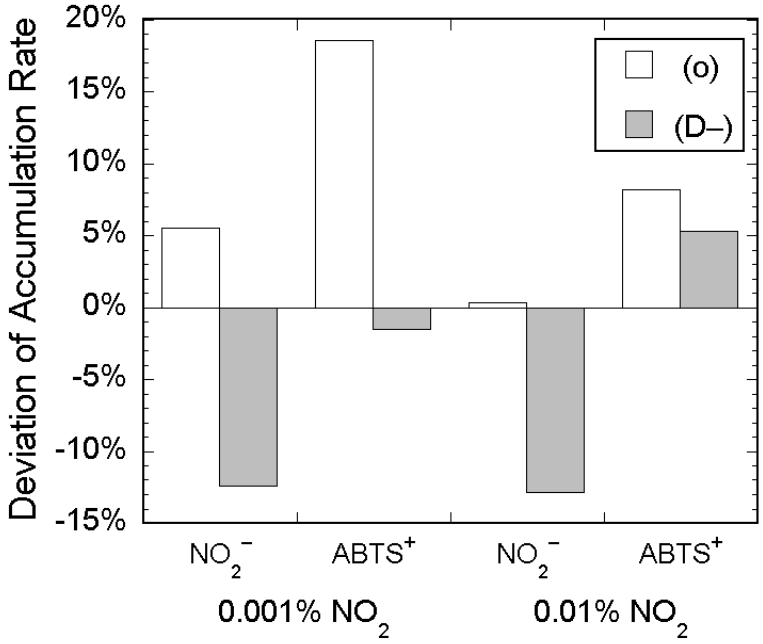

Figure 3.16. Percent deviation of model predictions from product accumulation rate data in the presence of ABTS.

The conditions of Cases (o) and (D–) are described in Table 3.6

between these results and those generated using the parameters of Case (o) or of Table 3.1 should be minor. The scale for ψ was the same in all simulations, $\bar{C}_{ABTS}$ = 107 μM. The scale for θ, C_N^*, was a nonlinear function of f_N, as plotted in Figure 3.17 for α_{NO_2} equal to 9 and 12 mM atm^{-1}. The ratio of the value of C_N^* at 12 mM atm^{-1} to that at 9 mM atm^{-1} is approximately 1.5 and 2.0 at 0.001% and 1% NO_2, respectively. This difference, as well as the deviation of the C_N^* profile from log-linearity, is due to a transition from NO_2 to N_2O_4 as the primary RN species (as can be seen in Figure 3.19 below) and the significantly higher solubility of N_2O_4 (Table 3.1).

Profiles of θ versus η for the four experimental NO_2 gas mixtures in the absence of ABTS are presented in Figure 3.18(a), with both the baseline parameter set of Table 3.1 and the modified set of Case (C) from Table 3.6. The profiles are nearly identical for the two parameter sets. Accordingly, the trends in the Case (C) simulation results should be representative of those with the baseline parameters. In all cases, θ decreases with η in a nonlinear fashion, with rates of fall-off increasing and values of $\theta(0)$ decreasing with increasing f_N. The decreasing θ at $\eta = 0$ can be explained by the decreasing liquid-phase resistance with increasing f_N (see Section 3.4.2.4), since a decrease in the liquid-phase resistance will result in a greater fraction of the concentration change occurring between the feed gas and the interface. The increasing rates of fall-off follow naturally from the penetration depth δ_N derived in Section 3.4.2.3, since φ decreases with increasing C_N and thus with increasing f_N. Figure 3.18(b) plots Case (C) profiles of φ versus η for the four NO_2 mixtures in the absence of ABTS, illustrating the expected inverse relationship between φ and C_N. Figures 3.19(a)–3.19(d) present the non-dimensional NO_2 and N_2O_4 concentrations for the four gas mixtures, with abscissa

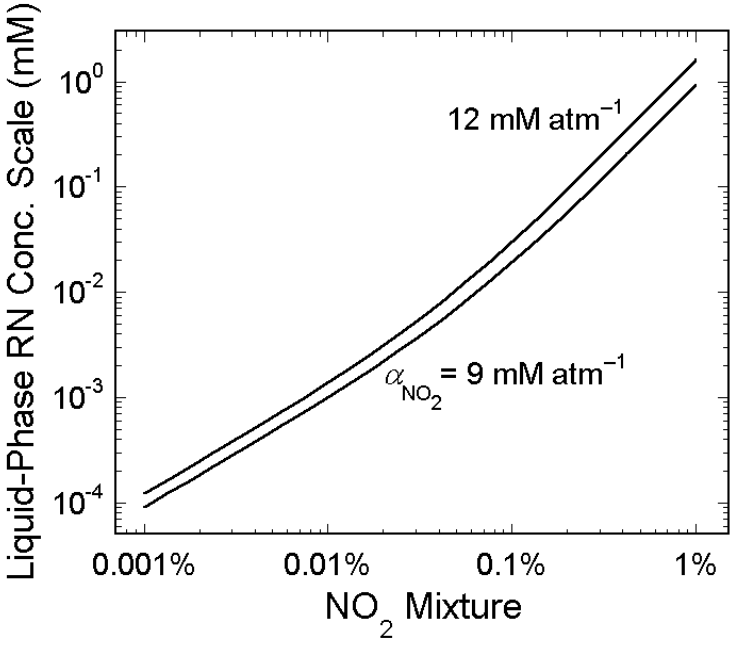

Figure 3.17. Concentration scale for RN as a function of the NO_2 gas mixture.

Deviation from log-linearity originates from the transition from NO_2 to N_2O_4 as the dominant RN species.

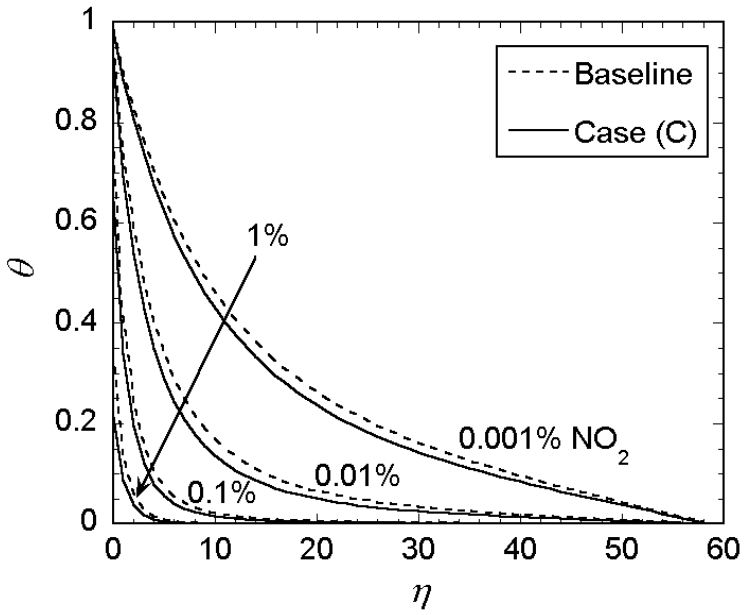

(a)

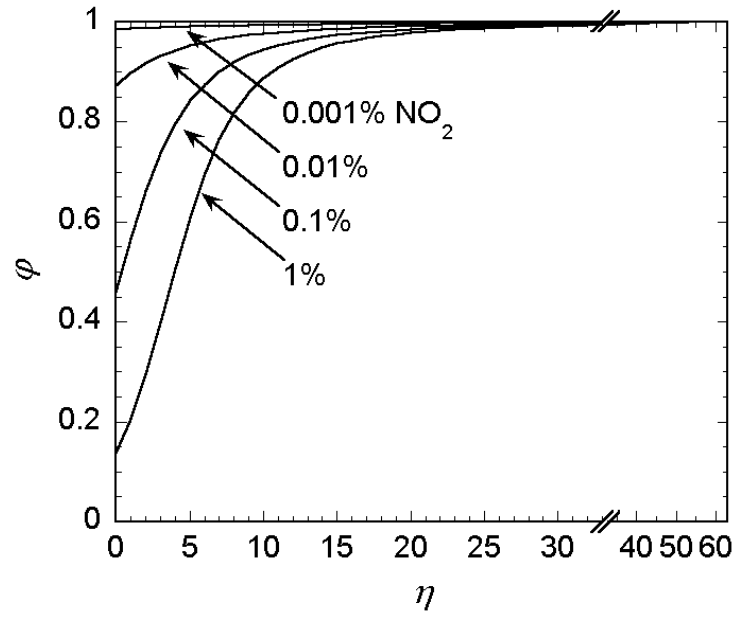

(b)

Figure 3.18. Simulated non-dimensional RN concentration and NO_2 fraction profiles.

Parameter values for (b) and for Case (C) curves in (a) are from Case (C) of Table 3.6. Those for 'Baseline' curves of (a) are from Table 3.1. Definitions of θ and φ are in Section 3.2.5.5.

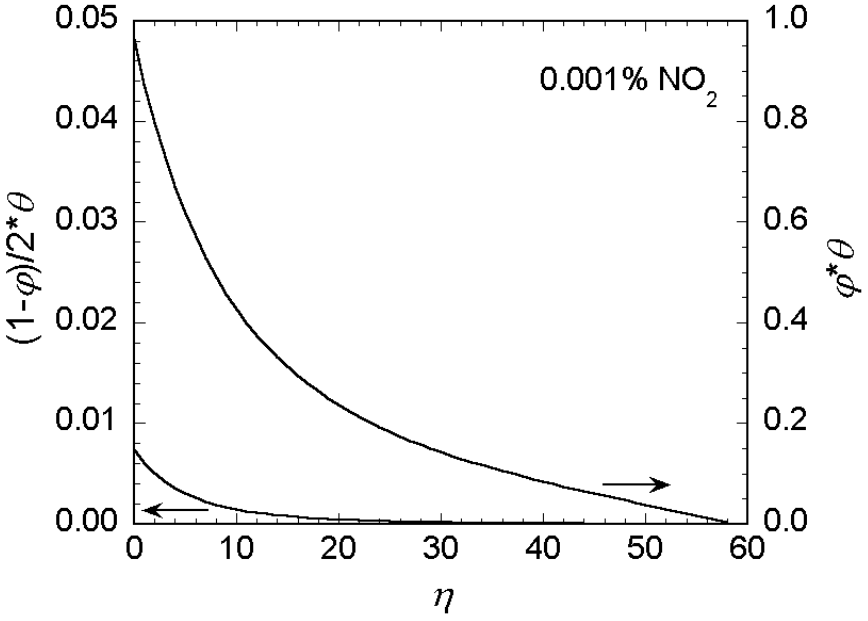

(a)

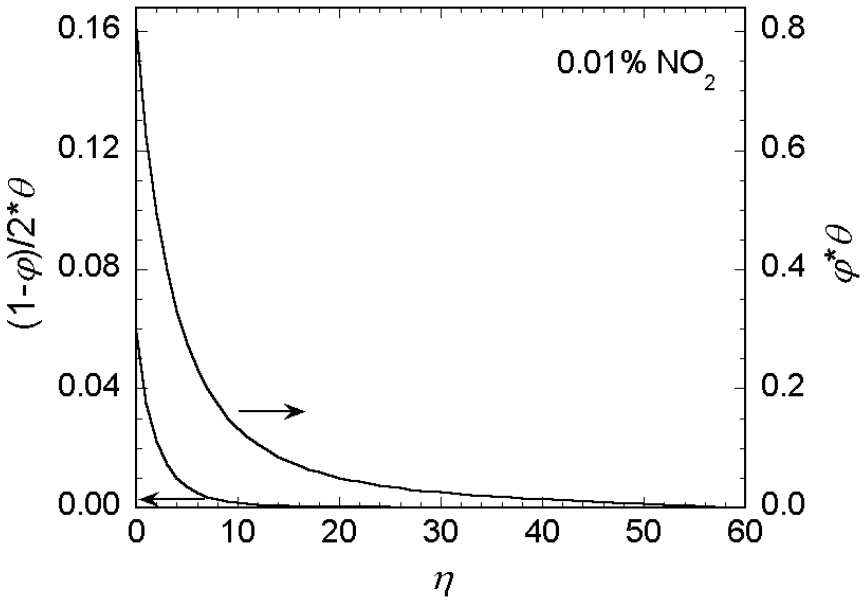

(b)

(Figure 3.19)

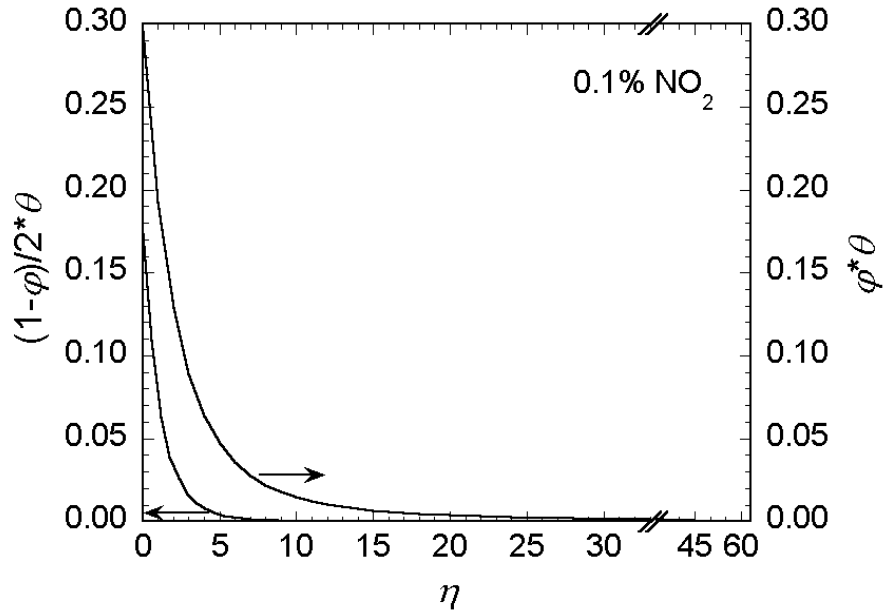

(c)

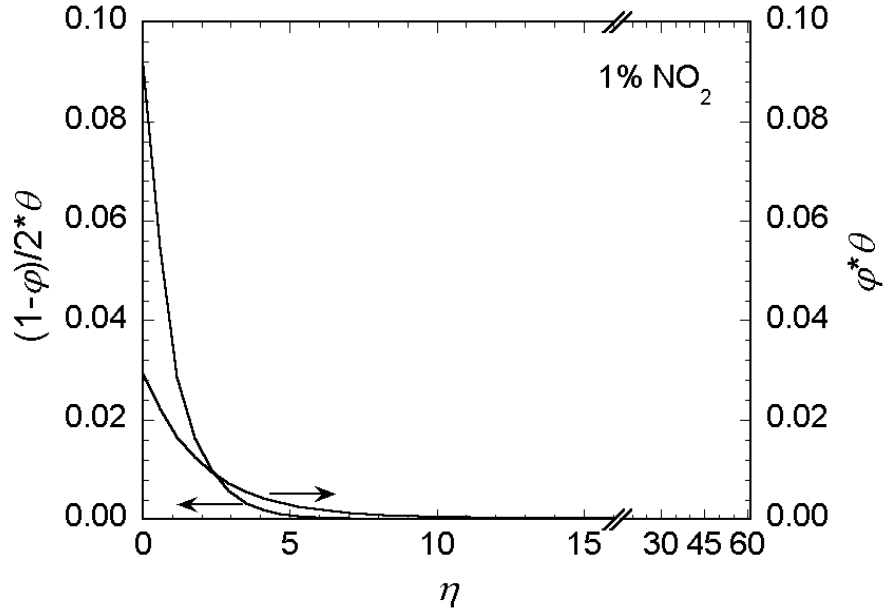

(d)

Figure 3.19. Simulated non-dimensional NO_2 and N_2O_4 concentration profiles.

NO_2 ($\varphi^*\theta$) and N_2O_4 [$(1-\varphi)/2^*\theta$] concentration profiles are for (a) 0.001%, (b) 0.01%, (c) 0.1%, and (d) 1% NO_2 mixtures. Abscissas and ordinates were separately adjusted to best display curves. Parameters were those of Case (C) from Table 3.6.

and ordinate scales separately adjusted in each figure to show more clearly the respective profiles. The same trends as above are evident here: decreasing non-dimensional concentrations and increasing relative N_2O_4 concentration with increasing f_N. Of note, at 1% NO_2, the absolute concentration of N_2O_4 at the gas-liquid interface is predicted to exceed the NO_2 concentration by approximately threefold.

Figure 3.20 presents profiles of θ versus η for simulations under conditions combining Cases (A) and (B) of Table 3.6. That is, the volumetric gas flow rate and gas-phase mass transfer coefficient were simulated as being functionally infinite, and gas-phase hydrolysis was neglected. Thus, gas phase phenomena were expected to be essentially absent. Indeed, the value of $\theta(0)$ deviated negligibly from unity for all four gas mixtures simulated, in contrast to the results of Figure 3.18(a). This result further emphasizes the significance of gas-phase phenomena in an accurate model of the system, supporting the conclusions of Sections 3.4.2.4 and 3.4.3.2.

3.4.3.4 Model dependence on film thickness

One feature of NO_2 delivery that complicates development of accurate models is the inverse dependence of the rate of Reaction (3.2) on C_N: as RN is consumed, the equilibrium of Reaction (3.1) disfavors N_2O_4 and thus also disfavors further consumption of RN. Thus the penetration depth δ_N derived in Section 3.4.2.3, which is a function of φ_i (the fraction of RN present as NO_2 on the liquid side of the gas-liquid interface), does not uniformly apply throughout the liquid boundary layer. In the absence of substrates, consumption of RN as it diffuses into the liquid causes the quantity $(1 - \varphi)$ to decrease locally, which in turn increases the 'local penetration depth.' Eventually, the latter

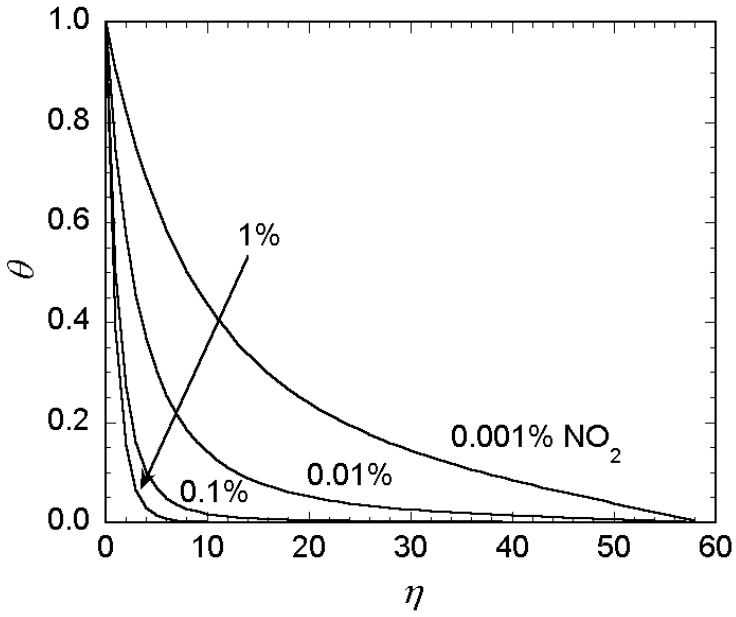

Figure 3.20. Simulated non-dimensional RN concentration profiles neglecting gas-phase phenomena.

Parameters were those of a combination of Cases (A) and (B) from Table 3.6, with negligible inflow and gas-phase boundary layer resistances and no gas-phase N_2O_4 hydrolysis. As anticipated, $\theta(0)$ is negligibly different from unity regardless of the $\%NO_2$ in the gas mixture.

quantity will increase to the point where it exceeds both the (fictitious) stagnant film thickness and the physical dimensions of the reactor. The geometric simplification inherent in the imposition of a film thickness thus introduces into the model an intrinsic sensitivity to the film thickness chosen. Similar difficulties would be present in any of the more complex reactive absorption models described in, e.g., Danckwerts (1970), so the simplicity of the stagnant film model still leaves it as the most appealing option. Lacking any other specific basis for estimating a film thickness, the most reasonable value is that calculated from the measured k_{O_2} as in Section 3.2.5.4.

Given its likely influence on the model behavior, the sensitivity of the various simulation outputs to changes in the film thickness was examined. Figure 3.21(a) presents the simulated bulk NO_2 and N_2O_4 concentrations for delivery of 0.001% and 0.01% NO_2 mixtures for a range of non-dimensional film thicknesses, and Figure 3.21(b) presents the simulated well-mixed NO_2 concentrations for delivery at all four experimental gas mixtures. Both plots were generated using the parameter values of Case (C) from Table 3.6. Interestingly, while the dependence of the bulk and well-mixed NO_2 concentrations on film thickness varies continuously across the range of η_f examined, the bulk N_2O_4 concentration rapidly approaches asymptotic values at well below the $\eta_f = 58$ calculated from k_{O_2}. Similar behavior (not shown) is also observed in simulation of 0.1% and 1% NO_2 mixtures.

Empirically, the behavior of the bulk N_2O_4 concentration can be rationalized as follows. Figure 3.22 presents simulated non-dimensional RN concentration profiles [0.01% NO_2; Case (C), Table 3.6] for various values of η_f. As can be seen from the figure and the inset, both θ and its η-derivative at $\eta = 0$ approach limiting values at

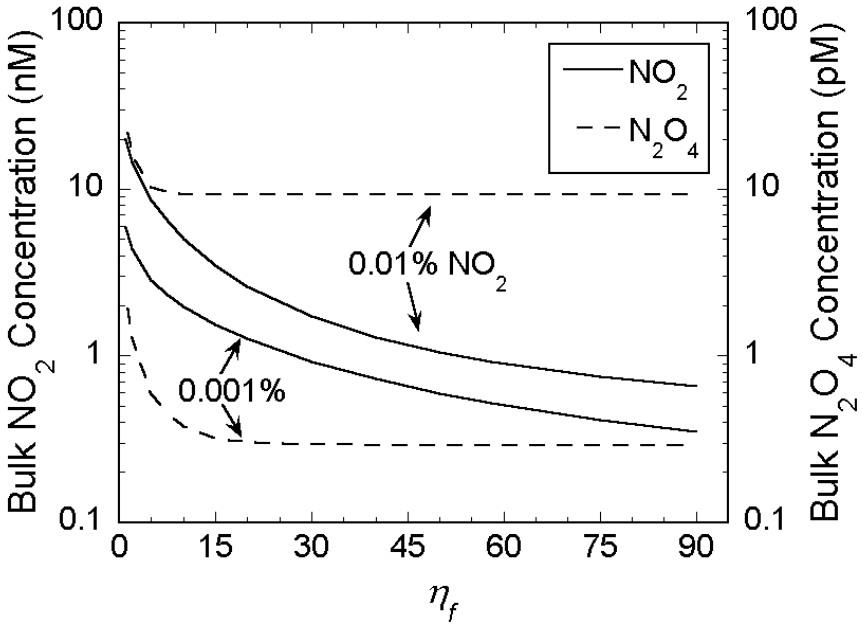

(a)

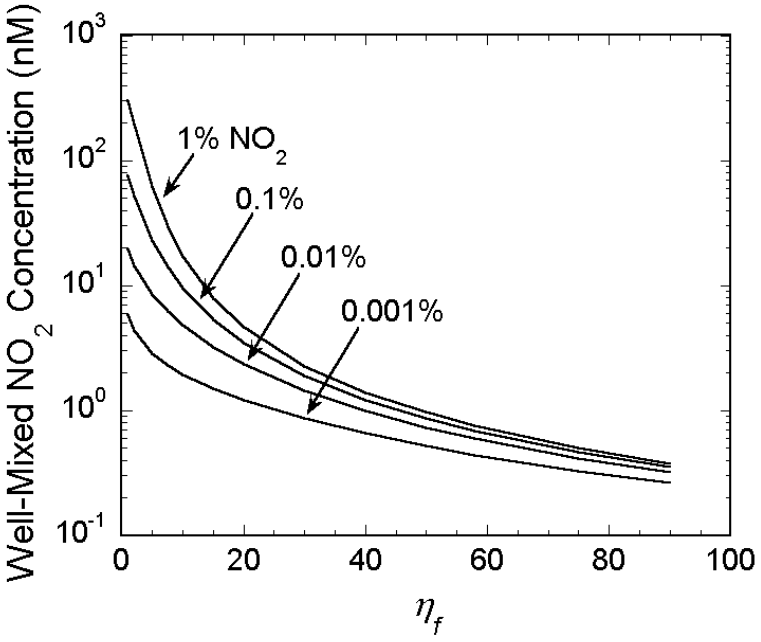

(b)

Figure 3.21. Dependence of simulated bulk and well-mixed RN concentrations on stagnant film thickness.

Bulk (a) and well-mixed (b) concentrations are defined in Section 3.2.5.

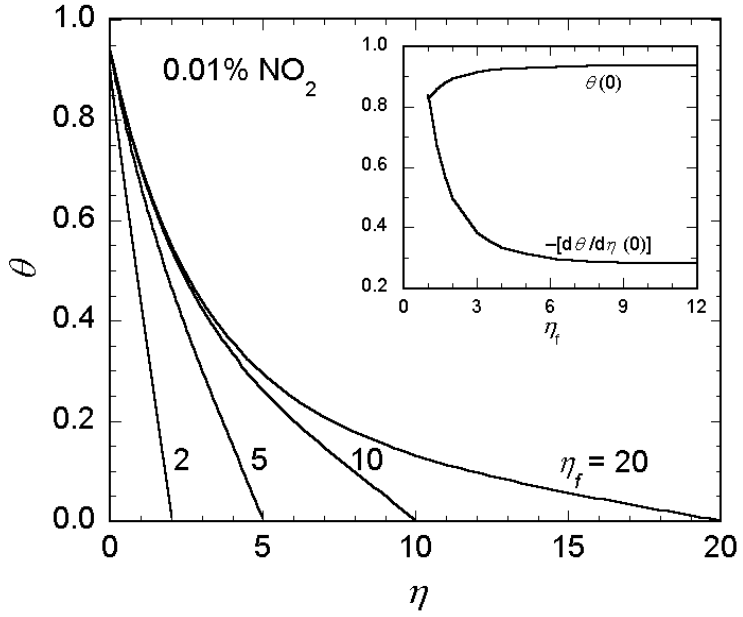

Figure 3.22. Dependence of simulated non-dimensional RN concentration profile on stagnant film thickness.

Simulation conditions were a combination of Cases (A) and (B) from Table 3.6, modeling reactor behavior in the limiting case of negligible gas-phase dynamics. Inset figure plots the value of θ and its η derivative at $\eta = 0$ as a function of the non-dimensional film thickness η_f.

comparatively small values of η_f. This is presumably because the artificial constraint of the film thickness is 'sufficiently far away' from the interface ($\eta = 0$) that the simulation behavior at the interface does not feel the effects of the constraint at $\eta = \eta_f$. The flux of RN into the reactor is directly proportional to $C_N^* \cdot d\theta/d\eta(0)$; if this quantity plateaus then the rate of entry of RN will plateau also. At steady-state, the entry of RN must exactly equal its total (volume-averaged) consumption within the reactor. Since the consumption of RN in substrate-free medium proceeds only through N_2O_4 hydrolysis, a reaction first-order in N_2O_4, the bulk (volume-averaged) N_2O_4 concentration must plateau along with the derivative of θ at the interface. This behavior indicates that the predictions for the nitrite and nitrate accumulation rates, at least, are not sensitive to the choice of film thickness and thus can be compared with the experimental data (as in Table 3.2 and Figure 3.7) with relatively high confidence. The bulk and well-mixed NO_2 concentrations reported in Figure 3.9, however, must be considered as best estimates given the limitations of the model.

Simulations of delivery of NO_2 to ABTS also exhibit dependence on the choice of film thickness, but for a different reason. This phenomenon is illustrated in Figure 3.23, which plots non-dimensional NO_2 and ABTS profiles (0.001% NO_2; Case (C), Table 3.6) within the stagnant film for three values of η_f, 30, 58 (nominal), and 80. The NO_2 profiles at these three η_f were nearly identical, so only one curve is shown in Figure 3.23. As can be seen, in the film model ABTS from the well-mixed region must diffuse through a region devoid of NO_2 in order to reach a reaction zone near the interface. Increasing the film thickness thus increases the decline in ABTS concentration between the well-mixed region and the reaction zone at the interface. However, the lower

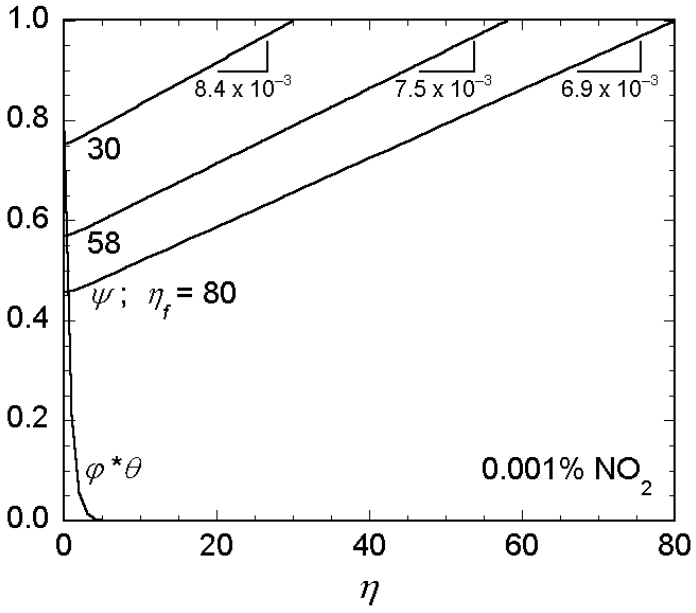

Figure 3.23. Simulated non-dimensional NO_2 and ABTS concentration profiles.

Simulations used the parameters of Case (C) from Table 3.6 with $\overline{C}_{ABTS}$ = 107 μM and a 0.001% NO_2 gas mixture. The NO_2 ($\varphi^*\theta$) profiles were visually indistinguishable for the three values of η_f shown; the curve here is for η_f = 58. The slopes of the ABTS (ψ) profiles are shown below each curve and vary inversely with η_f.

interfacial ABTS concentration in turn lowers the rate of reaction with NO_2 there, decreasing both the pseudo-steady flux of ABTS through the film (as represented by the slopes marked in Figure 3.23) and the overall rate of consumption of ABTS in the reactor. Of note, since the slope of the ABTS concentration profile within the film, and thus the decrease in the interfacial concentration for a given flux of ABTS, is determined in part by the ABTS diffusivity, identification of a reliable value of D_{ABTS} was critical in obtaining accurate model predictions. Depending on the NO_2 gas mixture and the bulk ABTS concentration, changes in the film thickness separately affect the formation rates of all three product species (NO_2^-, NO_3^- and $ABTS^+$) to varying degrees.

3.4.4 Delivery of NO_2 via PDMS and porous PTFE

No scheme was identified by which the PDMS and PTFE data could be reconciled with a model similar to that of Section 3.2.5, where the membranes were assumed to represent passive barriers to diffusive transport of NO_2/N_2O_4. As described below, the $ABTS^+$ accumulation rate was aberrantly low in the system of Wang and Deen (2003). Further, the observed nitrite yields were significantly greater in the Skinn et al. (2011) system ($Y_{NO_2^-} > 0.6$, see Figure B.12) compared to the data of Figure 3.6, as was expected. Wang and Deen (2003) postulated the occurrence of oxidation of NO within the PDMS tubing to explain aberrantly high observed rates of nitrite accumulation during delivery of NO in their system. It is possible that similar dynamics are occurring in these experiments: specifically, given the comparatively high solubility of water in PDMS, one or more of Reactions (E.11)-(E.14) in Appendix E could be operative within the PDMS tubing in addition to Reaction (3.1). A direct reaction of NO_2 or N_2O_4 with the PDMS

matrix itself is also possible. As for delivery through the porous PTFE membrane, Pasternak et al. (1970) report that NO_2 "interacts strongly, though reversibly" with PTFE based upon its aberrantly low diffusivity and high solubility in that material compared with gases of similar size. It is thus conceivable that the porous membrane modifies the NO_2 as it diffuses through from the base well to the liquid.

Interestingly, in delivery of 1% NO_2 to buffer containing ~100 μM ABTS via PDMS tubing (Figure B.11, Appendix B) the observed $ABTS^+$ accumulation rate is more than one order of magnitude below what would be expected from a comparison with the results in Section 3.3.2. Based upon the observed nitrite accumulation rate of 63 μM h^{-1}, if the RN were to transit the PDMS tubing without modification, the power-law fit of Figure 3.5 predicts an equivalent f_N in the direct-contacting system of approximately 0.02%. Thus, it is expected that the $ABTS^+$ accumulation rate would be at least as great as the 51 μM h^{-1} rate observed in delivery of 0.01% NO_2 (Table 3.2), as opposed to the 1 μM h^{-1} rate actually observed at $t \geq 30$ min. This behavior is similar to that noted by Dong et al. (2003) in their study of the delivery of NO to buffer containing morpholine (Mor; see Section 2.2.5.2 for the relevant kinetics). The accumulation rate of nitrite (the sole stable end product in delivery of NO to oxygenated aqueous solutions) was essentially identical in deliveries in the presence (Dong et al., 2003) and absence (Wang and Deen, 2003) of Mor, but the observed accumulation rate of N-nitrosomorpholine (NMor) was "about 4-5-fold lower than expected from the rate constants…" (Dong et al., 2003). One potential explanation for these results is that NO and NO_2 are converted into nitrous and/or nitric acids during transit through the PDMS tubing (Reactions (E.10)-(E.13) in Appendix E). These acids are essentially unreactive to Mor and ABTS in a

neutrally-buffered liquid. Sufficient conversion of NO and NO_2 in this manner could explain the depression of the observed NMor and $ABTS^+$ accumulation rates from expectations. Such intramembrane conversion, if it occurs, is not especially problematic in delivery of NO, since the technology exists to directly measure NO concentrations in solution (see Section 2.2.4). It would represent a fatal problem for delivery of NO_2, however, due to the lack of established methods for direct sensing of NO_2 concentrations in aqueous solution.

3.5 Conclusion

A novel apparatus for the continuous supply of NO_2 to biological media has been fabricated and characterized. The reactor is of simple construction and can easily be sterilized for cell studies. The concentration of NO_2 is predicted to fall within a relatively narrow range (0.3-6 nM) that is similar to the NO_2 concentration predicted to occur in oxygenated buffer containing 1 μM NO. This reactor is a promising tool for chemical kinetic or cellular experiments requiring prolonged, constant exposures to NO_2.

One potential refinement to the NO_2 delivery apparatus would be to attempt to scrub the nitric acid impurity (Section 3.4.2.1) from the feed gas. A 'nylon mesh column,' similar to the soda lime column in the NO delivery system (Section F.7), might permit substantial adsorption of the nitric acid while leaving the NO_2 concentration nearly unchanged [see, e.g., Appel et al. (1980) and Goldan et al. (1983)]. While nitric acid scrubbing was found to be unnecessary in the present work, the study of certain reaction mechanisms might require accurate determination of the accumulation rates of both nitrite and nitrate due specifically to hydrolysis of NO_2/N_2O_4, and thus require an

effectively HNO_3-free gas feed. Careful characterization experiments would be required in order to confirm that the column adsorption is specific to nitric acid. It would also be useful to develop methods for visual identification the saturation point of the column and for regeneration of a saturated column, which would simplify and economize its use.

In addition to NO_2 delivery to cells, a number of possibilities exist for studies of small-molecule reactions of NO_2 using the present system. For example, the preliminary experiments in delivery of NO to free Tyr (see Section 2.5) implied that the presence of NO introduces additional mechanistic complexity into the system. Exposure of free Tyr specifically to NO_2 could permit estimation of the rate constants in that system without the interfering effects of NO. Also, given the common use of the pH indicator Phenol Red in cell culture media, estimates of its rate of reaction with NO_2 would be useful in determining whether it is likely to interfere with NO_2 delivery to cells (see Section 3.4.1). At minimum, given sufficient analytical capacity it should be feasible to estimate a rate constant for any initial reaction between NO_2 and Phenol Red, even if a complex following mechanism occurs. Finally, Childs and Bardsley (1975), Brausam et al. (2009), and others report a reversible disproportionation reaction of $ABTS^+$,

$$2\,ABTS^+ \rightleftharpoons ABTS + ABTS^{2+}, \tag{3.63}$$

where $ABTS^{2+}$ is a nonradical species with an absorption peak in the vicinity of 510 nm (Venkatasubramanian and Maruthamuthu, 1989). The rate of disproportionation is pH-dependent and is sufficiently fast to require consideration in studies using the ABTS/$ABTS^+$ reaction—as an example, it necessitated maintaining $ABTS^+$ concentrations below 20 μM in this study (see Section 3.2.7). However, no estimates of the forward or reverse rate constants for Reaction (3.63) are given in these studies.

Assuming that any reactions between NO_2 and $ABTS^+$ or $ABTS^{2+}$ are sufficiently slow, estimation of one or both of the rate constants of Reaction (3.63) using methods similar to those described here should be relatively straightforward.

Chapter 4

Bolus Delivery of Peroxynitrite to Biological Media

4.1 Introduction

4.1.1 Peroxynitrite biology and chemistry

Peroxynitrite anion ($ONOO^-$) is formed *in vivo* from the near-diffusion-limited reaction between nitric oxide and superoxide anion (O_2^-; Nauser and Koppenol, 2002), both of which are generated endogenously (Blough and Zafiriou, 1985; Ignarro et al., 1987) It exists in equilibrium with its conjugate acid, peroxynitrous acid (ONOOH; Pryor and Squadrito, 1995):

$$ONOO^- + H^+ \underset{}{\overset{K_1}{\rightleftharpoons}} ONOOH\,. \qquad (4.1)$$

In the absence of reactive substrates $ONOO^-$ is relatively stable, but ONOOH is not, decomposing by homolysis to form a caged pair of hydroxyl (HO) and nitrogen dioxide (NO_2) radicals. Approximately 70% of these radical pairs recombine to form nitric acid, while others diffuse away from the solvent cage and become available for reaction with other species (Gerasimov and Lymar, 1999):

$$ONOOH \xrightarrow{k_2} 0.3\left(HO + NO_2\right) + 0.7\left(H^+ + NO_3^-\right). \qquad (4.2)$$

Both $ONOO^-$ and ONOOH (together 'Per') participate in additional reactions of physiological significance. For example, peroxynitrite anion reacts rapidly with CO_2 giving a similar product distribution as in Reaction (4.2), save for the production of

carbonate radical anion ($CO_3^{\cdot-}$) instead of HO (Lymar et al., 1996). Both ONOOH decomposition and the $ONOO^-$ reaction with CO_2 are sufficiently fast that the half-life of Per in physiological media is less than 1 s (Goldstein et al., 2005).

Along with the reaction of $ONOO^-$ with CO_2, oxidation of metal centers and direct reaction with proteins (Alvarez and Radi, 2003) are predicted to be the primary sinks for Per *in vivo* (Lim et al., 2008). However, numerous other physiologically-significant reactions are mediated by Per and the radicals formed from its decomposition. Peroxynitrous acid reacts directly with thiols (e.g., cysteine and glutathione; Trujillo and Radi, 2002; see Section 4.2.2.1) and both forms of peroxynitrite have been shown to oxidize thioethers such as methionine (Perrin and Koppenol, 2000; Pryor et al., 1994). The radical products of Per decomposition exhibit a broad reactivity (see Figure 1.1), including a number of pathways for oxidative DNA and lipid damage (Balazy and Chemtob, 2008; Halliwell et al., 1992; Lee et al., 2007; Niles et al., 2006). One peroxynitrite-derived modification of particular interest is the nitration of protein tyrosine, which has been investigated as a biomarker of the action of Per (Greenacre and Ischiropoulos, 2001). Recent evidence has indicated, however, that the formation of protein nitro-tyrosine may not be a merely random mechanism of chemical protein damage and instead may serve a number of physiological functions, including modulation of enzymatic activity and signaling behavior, as well as modulation of the susceptibility of proteins to degradation (Abello et al., 2009; Ischiropoulos, 2009). Elucidation of the mechanisms by which Per exposure leads to the formation of nitro-tyrosine and other oxidation and nitration products is thus an important component in developing an understanding of the effects of elevated levels of reactive nitrogen species in the body.

4.1.2 Peroxynitrite delivery

Two strategies are typically used to deliver peroxynitrite to biological media, addition of pre-formed, alkaline $ONOO^-$ (Kuhn et al., 1999; Pfeiffer and Mayer, 1998; Pfeiffer et al., 2000) and *in situ* generation from NO and O_2^- (Hodges et al., 2000; Radi et al., 1990; Wang and Deen, 2004). Bolus or steady infusion of pre-formed Per is complicated by its rapid decomposition [Reaction (4.2)], even in the absence of CO_2. As discussed later (Section 4.2.5), it is challenging to reduce the mixing time of a stirred liquid volume (the time scale over which the contents of that volume approach uniform composition) much below the order of one second. Modeling of the resulting exposures thus is typically semi-quantitative, at best. While *in situ* generation more closely mimics the conditions thought to occur *in vivo*, no robust system has been developed for this exposure method. The chemical superoxide source of Hodges et al. (2000) is possibly cytotoxic, and Per has been shown to inactivate the enzymes in the xanthine oxidase system for O_2^- synthesis (Wang and Deen, 2004). Nakamura et al (2002) used activated polymorphonuclear neutrophils as a superoxide source in combination with a chemical NO donor to study peroxynitrite exposure of folate, but the complex media required for cell culture makes it difficult to draw specific mechanistic inferences from the resulting data.

It is worthwhile to note that delivery of Per by transport from a gaseous stream in the manner described in Chapters 2 and 3 would be appealing, if it were feasible. Peroxynitrous acid is slightly volatile, with an estimated Henry's coefficient of 4×10^4 M atm^{-1} (Lobachev and Rudakov, 2005). Upon contacting gaseous ONOOH with a liquid surface, its rapid decomposition would confine it to a film adjacent to the gas-

liquid interface with a thickness on the order of 80 μm. Its chemistry could be modeled in much the same fashion as in the liquid-phase boundary layer in delivery of NO_2 (Section 3.2.5.4). However, ONOOH decomposes to HO and NO_2 radicals even more rapidly in the gas phase than in aqueous solution (gas-phase $k \sim 4 \times 10^4$ s^{-1}; Lobachev and Rudakov, 2005). The gas-phase recombination of these two radicals is yet faster ($k \geq 3 \times 10^9$ M^{-1} s^{-1}; Dransfield et al., 1999), and yields primarily nitric acid, with no more than 10% regeneration of ONOOH (Lobachev and Rudakov, 2005; Nizkorodov and Wennberg, 2002). The resulting rapid and irreversible conversion to HNO_3 makes it practically impossible to store gaseous ONOOH or to transport it from some steady generation source, such as the acidified mixture of nitrous acid and hydrogen peroxide of Lobachev and Rudakov (2005).

4.1.3 Modeling of mixing in agitated vessels

As noted above, the rapid decomposition reactions of peroxynitrite greatly complicate its delivery to stirred solutions due to their invalidation of the well-mixed assumption. From a scaling perspective, in order to consider a vessel well mixed relative to a particular reaction of interest, the mixing time scale must be much shorter than the time scale of that reaction. One dye tracer study of baffled, stirred vessels indicated that "the mixing time was comparable to the time required for the dye to be transported from the top of the vessel to the bottom part plus the time required for a further two rotations of the bulk flow in the circumferential direction" (Distelhoff et al., 1997). In a review of studies of tank mixing [Table 3 of Nere et al. (2003)] the shortest and longest mixing times achieved were 5 s and 25 s, in agitated vessels approximately 15 cm and 150 cm in diameter. These experiments were performed with similar specific power input (P/M;

power per unit mass of fluid), and from that perspective are comparable. The ten-fold decrease in reactor size resulted in only a five-fold decrease in mixing time and thus, if extrapolation of this correlation is valid, reduction of the diameter of the reactor by another factor of ten (to an extremely small reactor of diameter 1.5 cm) likely cannot reduce the mixing time below the order of 1 s. The dependence of the mixing time on P/M as reported in Tables 3 and 4 of Nere et al (2003) is relatively weak, with a two-fold decrease in mixing time requiring on average a six-fold increase in specific power input for a given vessel configuration. Implementing a mode of agitation sufficiently vigorous to permit consideration of the entire contents of any reactor of practical laboratory utility well-mixed on the time scale of Per decomposition (4 s) is thus quite difficult, if not impossible.

A variety of models have been published that attempt to describe the key features of the mixing processes occurring in stirred vessels. These models span a range of complexities, from empirical models based on scaling parameters [reviewed in Ranade et al. (1991)], to semi-empirical models that invoke turbulent eddy diffusivities and Kolmogorov scales (Bourne et al., 1995; Oh et al., 1989), to detailed, multi-dimensional computational models attempting to solve the full fluid dynamical and mass transfer problem (Brucato et al., 2000; Campolo and Soldati, 2004; Guha et al., 2006; Zauner and Jones, 2002). Most of these models address the problem of mixing in larger, pilot- or production-scale equipment because of the clear advantages of scale-up in an industrial setting. However, a robust model describing mixing in small, laboratory-scale vessels such as beakers and centrifuge tubes would be extremely useful in the more flexible research environment.

4.1.4 Chemical systems as probes for mixing time scales

It is obvious that in order for a chemical system to provide insight into the rate of mixing in a vessel, the distribution of reaction products in the solutions being mixed must depend on the rate of mixing. One of the simplest suitable mechanisms is the parallel competition of two reactants **B** and **C** for a common substrate **A**:

(R1): $$\mathbf{A} + \mathbf{B} \xrightarrow{k_{R1}} \mathbf{P}\,. \tag{4.3}$$

(R2): $$\mathbf{A} + \mathbf{C} \xrightarrow{k_{R2}} \mathbf{Q}\,. \tag{4.4}$$

In the following discussion, Reactions (4.3) and (4.4) will be abbreviated as "R1" and "R2", respectively. The species names in R1 and R2 (**A**, **B**, etc.) are bolded to distinguish them from the surrounding text. Upon addition of a solution containing **A** to another that contains an excess of both **B** and **C**, certain amounts of the products **P** and **Q** will form. The resulting product distribution is a function of the initial concentrations of **A**, **B** and **C**, the rate constants k_{R1} and k_{R2} and, in a well-designed experiment, the rate of mixing in the system. If the kinetics of R1 and R2 are known, the mixing time in the system can be inferred from the observed product distribution. Experiments performed using the same delivery method but a different chemical system where the constant k_{R2} is known but k_{R1} is unknown (with the time scales of R1 and R2 adjusted according to the formalism below) will then permit estimation of the unknown k_{R1}.

The rate of mixing influences the product distribution in a chemical system only under certain conditions, which can be defined in terms of time scales. The time scale for mixing is simply denoted as τ. The intrinsic time scales for R1 and R2, which are defined as the reaction time scales in the absence of any mixing considerations, are the inverse of

the pseudo-first-order rate constants for **A** in each reaction: $\tau_{R1} = [k_{R1} C_B]^{-1}$ and $\tau_{R2} = [k_{R2} C_C]^{-1}$, respectively. The observed reaction time scales, τ'_{R1} and τ'_{R2}, are the time scales on which R1 and R2 actually occur in the system. These latter scales can be no less than τ_{R1} and τ_{R2}, respectively, but under mixing-limited conditions they may take values $\tau'_{Rn} \sim \tau$ that are greater than the respective τ_{Rn}. In designing experiments either to characterize mixing rates or to infer unknown rate constants it is instructive first to examine certain limiting cases. For example, if either τ_{R1} or τ_{R2} is significantly greater than τ (that is, if either reaction is much slower than the mixing), then mixing will be essentially completed before the reaction in question proceeds appreciably. As a result, the value of τ will have a negligible effect on the product distribution regardless of the rapidity of the other reaction. Conversely, if both τ_{R1} and τ_{R2} are significantly smaller than τ (that is, if both reactions are much faster than the mixing), both τ'_{Rn} will be on the order of τ since the rate at which **A** is introduced to **B** and **C** is governed by τ^{-1}. This configuration is not useful for estimating τ, however, because the product distribution from each differential quantity of **A** that encounters the solution of **B** and **C** will be identical and a function only of the intrinsic values of τ_{Rn}. The value of τ merely controls the rate at which the differential 'parcels' of **A** are contacted with the other substrates.

The two limiting cases described above together require that $\tau_{Rn} \sim \tau$ for at least one reaction in order for the product distribution to be sensitive to mixing. Arbitrarily choosing R1 as the reaction satisfying this condition, the value of τ'_{R1} will thus be some unknown function g of τ_{R1}, τ, and possibly of τ_{R2}. The only remaining scaling constraint to be determined is that governing τ_{R2}. Since the goal is to make the product distribution

maximally sensitive to the rate of mixing, the optimal constraint to impose is $\tau_{R2} \ll \tau$. If $\tau_{R1} \sim \tau_{R2} \sim \tau$, the dependence of both observed scales τ'_{Rn} on the values of τ_{Rn} and τ will be similar, and the uncertainty of the mixing time scale derived from the experimental data will be relatively large. If $\tau_{R2} \ll \tau$, τ'_{R2} will be approximately equal to τ with little to no dependence on τ_{R1}, and the sensitivity of τ'_{R1} to the value of τ_{R2} will likewise be small. The scaling relationship $\tau_{R2} \ll \tau \sim \tau_{R1}$ thus results in the simplest non-zero functional dependence of the product distribution on τ: $\tau'_{R1} = g(\tau_{R1}, \tau)$ and $\tau'_{R2} \approx \tau$. Note that an estimate of τ is required in order to select both a suitable reaction system and appropriate initial reactant concentrations. If the actual value of τ for the mixing behavior of interest is significantly different from this estimate, either different substrate concentrations or an alternative chemical system will be required.

The time scales of the three chemical systems described in Section 4.2.2 as interpreted using the above formalism are presented in Table 4.4.

4.1.5 Present work

An ideal method for delivery of pre-formed peroxynitrite, as well as the study of other reactions on a laboratory scale, would be experimentally simple but also easily and accurately quantifiable. Invoking the well-mixed assumption results in by far the simplest model of reactive mixing, as it represents a significant dimensional reduction: it eliminates the three spatial dimensions, leaving time as the only independent variable. (This is a far simpler form of dimensional reduction that that of, e.g., Bhattacharya et al. (2004) which, though it is much more robust, entails significant mathematical complexity.) However, as noted above, it is not reasonable to apply this simplification to

the entire contents of the reactor from the moment a bolus of peroxynitrite is introduced. The model proposed in this chapter (Section 4.2.5) is based upon the hypothesis that invoking the perfect mixing assumption on a carefully selected sub-region of the reactor volume might be acceptable. As long as the agitation is sufficiently intense to keep this sub-volume well mixed, the model should represent the mixing process with reasonable accuracy. [To note, this isolation of a subset of the reactor volume from the surrounding fluid is similar to the "pseudo-multiphase" model of Akiti and Armenante (2004).]

The proposed model poorly describes bolus delivery experiments where the contents of a beaker are agitated using an orbital mixer (laboratory shaker; Section 4.3.4), but it shows promise for experiments with agitation by vortexing (Section 4.3.5). More work is required before it can be confidently argued that the model is quantitatively accurate, but these preliminary results are encouraging. Much of the work described here was performed with the assistance of two undergraduate students, George Pratt (Chemical Engineering, MIT) and Deborah Markham (Department of Chemistry, MIT). Mr. Pratt performed some of the experiments with the thiol/peroxynitrite system. Ms. Markham contributed extensively to the development of the diazenyl dye assay and collected the majority of the data for the Cu^{2+}/ECA and diazenyl dye systems.

4.2 Materials and methods

Three different chemical systems were used in the tests of the proposed mixing model. These systems and the various assays used to analyze the product mixtures are described in Sections 4.2.2 and 4.2.3, respectively. Details of the method used to synthesize peroxynitrite for the thiol oxidation system (Section 4.2.2.1) is described in

Section 4.2.4, along with a brief overview of published peroxynitrite synthesis methods. The proposed bolus mixing model is described in Section 4.2.5 and the methods used to test it are presented in Section 4.2.6.

4.2.1 Chemicals

Sodium peroxynitrite and manganese(II) oxide were synthesized as described in Section 4.2.4. All other chemicals were obtained from Sigma-Aldrich (St. Louis, MO). All solutions were prepared using deionized (DI) water.

4.2.2 Reaction mechanisms

Values for the rate constants specified in the following mechanisms are provided in Table 4.1. Species are marked as **A**, **B** or **C** to indicate their role in the formalism of Section 4.1.4. Estimates of the reaction time scales for each system are presented in Table 4.4.

4.2.2.1 Peroxynitrite decomposition and thiol reaction

When alkaline, pre-formed $ONOO^-$ (**A**) is added to a neutrally buffered aqueous solution in the absence of CO_2, it protonates and decomposes according to Reactions (4.1) and (4.2). (Peroxynitrious acid decomposition represents "R1" from the formalism of Section 4.1.4; there is no separate species **B** in this system.) In the presence of a solute bearing a thiol moiety [**C**: in the present work, cysteine (Cys) or glutathione (Glt)], two further reaction mechanisms occur. In the first mechanism, peroxynitrous acid and deprotonated thiolate (RS^-, either $Cys\text{-}S^-$ or $Glt\text{-}S^-$) react with second-order kinetics to form the corresponding sulfenic acid and nitrite (Trujillo and Radi, 2002):

$$\mathrm{ONOOH} + \mathrm{RS}^- \xrightarrow{k_3} \mathrm{RSOH} + \mathrm{NO}_2^- . \tag{4.5}$$

The sulfenic acid reacts with another molecule of thiolate to form a disulfide and hydroxide ion:

$$\mathrm{RSOH} + \mathrm{RS}^- \xrightarrow{fast} \mathrm{RSSR} + \mathrm{OH}^- . \tag{4.6}$$

Reaction (4.6) is sufficiently fast that Reaction (4.5) is rate-limiting, and thus the rate constant of Reaction (4.6) is difficult to measure accurately. (Ashby and Nagy (2007) estimate that its value for cysteine must be at least 10^5 M^{-1} s^{-1}, and it is reasonable to expect that the corresponding value for Glt is comparable.) Thus, Reaction (4.6) was considered to be instantaneous for both sulfhydryl species studied and the sum of Reactions (4.5) and (4.6) was used:

$$2\,\mathrm{RS}^- + \mathrm{ONOOH} \xrightarrow{k_3} \mathrm{RSSR} + \mathrm{NO}_2^- + \mathrm{OH}^- . \tag{4.7}$$

The rate expression for Reaction (4.7) is first order in both thiolate and ONOOH, with $R_{thiol} = 2R_{Per} = -2k_3 C_{\mathrm{RS}^-} C_{\mathrm{ONOOH}}$. The concentrations of the ionic subspecies in this expression can also be written in terms of the total species (protonated plus deprotonated forms) as

$$R_{thiol} = 2R_{Per} = -2\,k_3\, f_{Per}\left(1 - f_{thiol}\right) C_{thiol} C_{Per} , \tag{4.8}$$

where $f_j = \left(1 + 10^{\mathrm{pH} - \mathrm{pK}_{a,j}}\right)^{-1}$ is the fraction of species *j* in the protonated state.

The second mechanism is quite complex and comprises reactions of the thiol-bearing substrate with the radical products of ONOOH decomposition, as discussed in Ford et al. (2002), Goldstein et al. (2004a), Hoffman and Hayon (1973), Karoui et al.

(1996), Mezyk (1996a; 1996b), Wardman (1998), Wardman and von Sonntag (1995), and Zhao et al. (1994). However, the scaling estimates described below indicate that this mechanism can be neglected in the present experiments. The significant contamination of nitrite in the peroxynitrite preparation (see Section 4.3.1) likely scavenged the HO generated by Per decomposition (forming NO_2 and OH^-) before it could react appreciably with the thiol. Nitrogen dioxide, derived both from nitrite scavenging of HO and from decomposition of Per, reacts considerably more slowly with thiols than does HO and likely competed inefficiently with Per for both Cys and Glt.

Hydroxyl radical reacts with both NO_2^- and Cys:

$$HO + NO_2^- \xrightarrow{k_{HO-NO_2^-}} OH^- + NO_2 . \quad (4.9)$$

$$HO + Cys\text{–}S^-(H^+) \xrightarrow{k_{HO-Cys}} OH^-(H^+) + Cys\text{–}S . \quad (4.10)$$

The rate constants $k_{HO-NO_2^-}$ and $k_{HO\text{-}Cys}$ have values of 5×10^9 M^{-1} s^{-1} (Merényi et al., 1999) and 2×10^{10} M^{-1} s^{-1} (Nucifora et al., 1972), respectively. The value of $k_{HO\text{-}Cys}$ is independent of the thiol protonation state, and the rate constant $k_{HO\text{-}Glt}$ for the reaction of HO and Glt is presumably comparable to $k_{HO\text{-}Cys}$. At the concentrations of nitrite (~ 70 mM) and thiol (500 μM) present in the experiments of Section 4.2.6, the pseudo-first-order rate constants for these reactions of HO are 3.5×10^8 s^{-1} and 1×10^7 s^{-1}, respectively. Hydroxyl radical should thus react approximately 35 times faster with nitrite than with thiol, and thus the majority of HO formed from Per decomposition should be converted to NO_2. (To note, the nitrite impurity will be rapidly diluted as the bolus volume mixes with the target solution volume (see Section 4.2.6.2), and the HO scavenging efficiency of nitrite will decrease accordingly. If the mixing is sufficiently

fast, most of the Per initially present in the bolus will react before the nitrite concentration has fallen significantly and the HO reaction with thiol can still be neglected.)

An expression for the quasi-steady-state (QSS) concentration of NO_2 resulting from Per decomposition in the presence of nitrite can be obtained by solving the following quadratic equation:

$$0 = 2 \cdot (0.3k_2) f_{Per} C_{Per} - \frac{2 K_{1N} k_{2N}}{1 + k_{2N}/k_{-1N}} C_{NO_2}^2 - k_{thiol} C_{thiol} C_{NO_2} . \quad (4.11)$$

The three terms represent formation of NO_2 from decomposition of Per, dimerization and hydrolysis of NO_2, and reaction of NO_2 with thiol, respectively. It is assumed that all HO is converted to NO_2 and that the concentration of N_2O_4 obeys quasi-equilibrium behavior (see Section 3.2.5.3). The constants K_{1N} and k_{2N} in the dimerization/hydrolysis term correspond to K_1 and k_2 from Table 3.1, respectively, and the quantity k_{2N}/k_{-1N} equals 0.145 (Graetzel et al., 1969). The constant k_{thiol} describes the rate at pH 7.4 of the apparent reaction of NO_2 with total thiol and has values of 5×10^7 M^{-1} s^{-1} and 2×10^7 M^{-1} s^{-1} for cysteine and glutathione, respectively (Ford et al., 2002). Assuming that Reaction (4.6) is not affected by NO_2, the fraction of thiol consumption attributable to reaction with NO_2 is

$$f_{NO_2} = \frac{k_{thiol} C_{NO_2}}{k_{thiol} C_{NO_2} + 2 k_3 f_{Per} (1 - f_{thiol}) C_{Per}} \quad (4.12)$$

where C_{NO_2} is the QSS concentration of NO_2 calculated from Eq. (4.11). For thiol concentrations of at least 200 μM, f_{NO_2} has a maximum value of 0.055, independent of

the peroxynitrite concentration. In all experiments performed the residual thiol concentration was no less than approximately 300 μM, and thus the radical-thiol reaction mechanism was assumed to be negligible.

4.2.2.2 Diazenyl dye formation from 1-naphthol and diazotized sulfanilic acid

Addition of diazotized sulfanilic acid (**A**: diazo-SAA or dSAA) to a solution of excess 1-naphthol (**C**: 1-NA) results in the formation of three diazenyl dye species via two parallel reaction pathways (Wenger et al., 1992):

$$1\text{–NA} + \text{diazo–SAA} \xrightarrow{k_{5p}} \text{p–R}\,. \tag{4.13}$$

$$1\text{–NA} + \text{diazo–SAA} \xrightarrow{k_{5o}} \text{o–R}\,. \tag{4.14}$$

$$\text{p–R} + \text{diazo–SAA} \xrightarrow{k_{6o}} \text{S}\,. \tag{4.15}$$

$$\text{o–R} + \text{diazo–SAA} \xrightarrow{k_{6p}} \text{S}\,. \tag{4.16}$$

Chemical structures for all five species are given in Figure 4.1. The para- and ortho-substituted mono-diazenyl dye products are denoted as p-R (**B**) and o-R, respectively, and S is the bis-diazenyl product. Rate constants for Reactions (4.13) through (4.16) have been determined by Bourne et al. (1990) and are reported in Table 4.1. The subscripts of these rate constants indicate the site of the diazenyl substitution in each reaction: for example, k_{ip} is the rate constant for para-diazenylation in reaction *i*. This system will be referred to as either the 'diazenyl dye' or the 'dye' system.

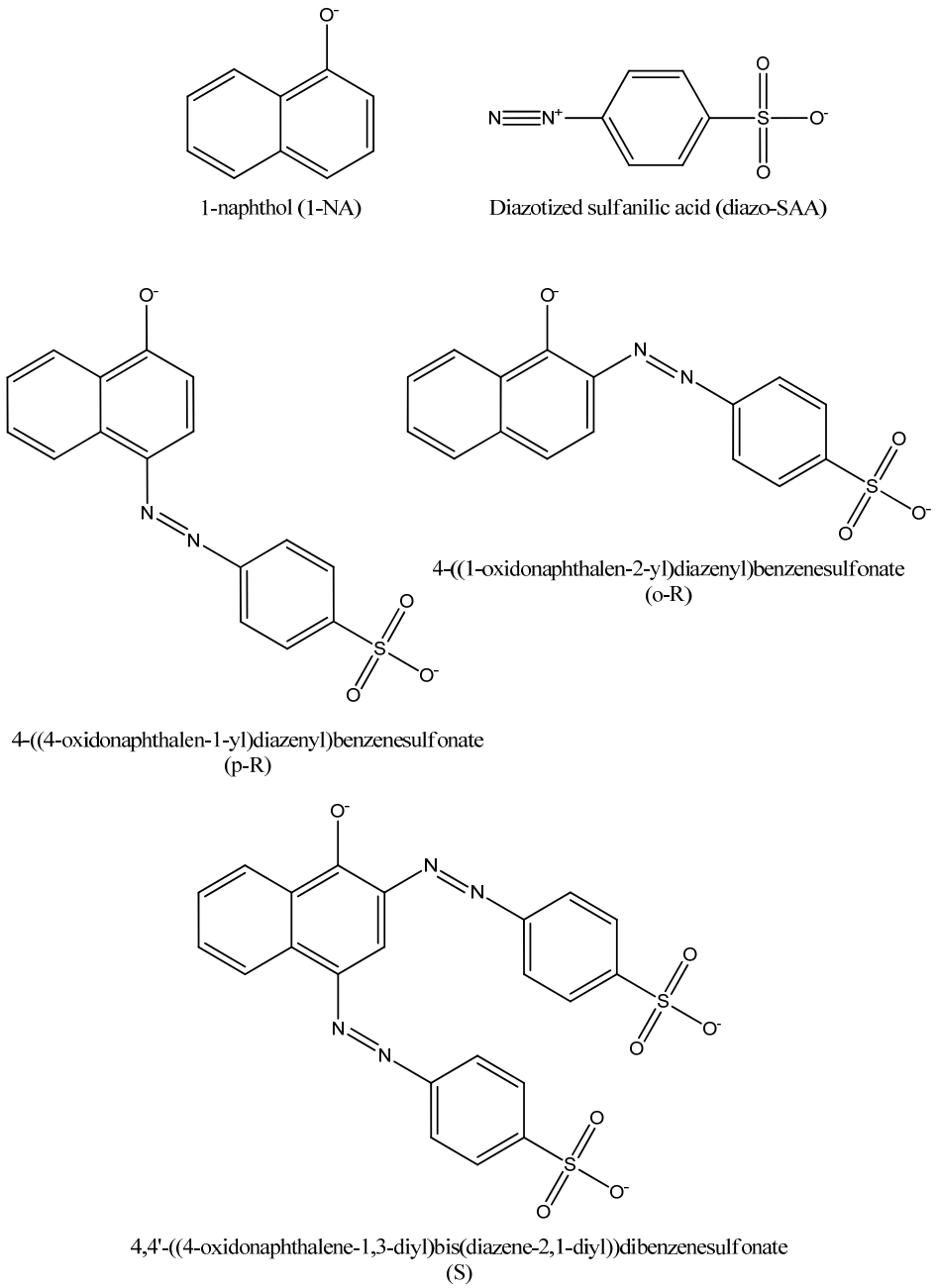

Figure 4.1. Molecular structures of species in the diazenyl dye reaction system.

Structures (at alkaline pH) and systematic names generated by ChemBioDraw Ultra 12 (CambridgeSoft, Cambridge, MA).

4.2.2.3 Copper(II) salt precipitation and alkaline hydrolysis of ethyl chloroacetate

Addition of concentrated NaOH (**A**) to a stirred solution of $CuSO_4$ (**C**) and the organic ester ethyl chloroacetate (**B**: ECA) results in three competing reactions. The first two are the rapid precipitation of copper(II) hydroxide salts, one the simple hydroxide and the other a mixed sulfate-hydroxide (Brucato et al., 2000; Marani et al., 1995; Yoder et al., 2007):

$$Cu^{2+}(aq) + 2OH^{-}(aq) \xrightarrow{fast} Cu(OH)_2(s). \quad (4.17)$$

$$4Cu^{2+}(aq) + SO_4^{2-}(aq) + 6OH^{-}(aq) \xrightarrow{fast} CuSO_4 \cdot 3Cu(OH)_2(s). \quad (4.18)$$

According to Brucato et al. (2000) only Reaction (4.17) should be operative. However, as will be discussed (Section 4.3.2), both reactions were apparently occurring. The third reaction of interest is the alkaline hydrolysis of ECA to form chloroacetate anion and ethanol:

$$OH^{-} + \underbrace{ClCH_2C(O)OCH_2CH_3}_{\text{ECA}} \xrightarrow{k_4} ClCH_2C(O)O^{-} + CH_3CH_2OH. \quad (4.19)$$

At the ECA concentrations used (Section 4.2.6.1), the time scale of Reaction (4.19) is moderate, with a value of approximately 2 s. Conversely, Reactions (4.17) and (4.18), which are essentially encounter-limited, have time scales on the order of nanoseconds and thus are functionally instantaneous (Brucato et al., 2000). This system will be referred to as the "Cu^{2+}/ECA" system.

Table 4.1. Rate constants for chemical mechanisms used to test the delivery model.

System	Parameter	Value	Units	Reference
Per/Thiol	K_1	1.58×10^{-7}	M	Pryor and Squadrito, 1995 ($pK_a = 6.8$)
	k_2	1.25	s^{-1}	Goldstein et al., 2005
	$k_{3,Cys}$	2.7×10^{5} [a]	$M^{-1}\ s^{-1}$	Radi et al., 1991
	$k_{3,Glt}$	2.4×10^{5}	$M^{-1}\ s^{-1}$	Trujillo and Radi, 2002
	$pK_{a,Cys}$	8.3	–	Trujillo and Radi, 2002
	$pK_{a,Glt}$	8.8	–	Trujillo and Radi, 2002
Cu^{2+}/ECA	k_4	2.3×10^{1}	$M^{-1}\ s^{-1}$	Kirby, 1972
Dye	k_{5p}	1.2×10^{7}	$M^{-1}\ s^{-1}$	Bourne et al., 1990
	k_{5o}	9.2×10^{5}	$M^{-1}\ s^{-1}$	Bourne et al., 1990
	k_{6p}	2.2×10^{4}	$M^{-1}\ s^{-1}$	Bourne et al., 1990
	k_{6o}	1.8×10^{3}	$M^{-1}\ s^{-1}$	Bourne et al., 1990

All values except those for k_3 are for 20–25 °C and were used without correction. Values of k_3 are for the reaction of the thiolate (RS^-) with ONOOH at 37 °C and were also used without correction.

[a] Value recalculated from published result of Radi et al. (1991).

4.2.3 Concentration measurements

Peroxynitrite stock solutions were diluted 800-fold in 0.1 N NaOH and assayed at 302 nm (ε_{302} = 1705 M^{-1} cm^{-1}; Bohle et al., 1996) against a blank of 0.1 N NaOH. Hydrogen peroxide concentrations were determined by a procedure modified from that of Artiss et al. (1981), as follows (concentrations given are for the stock solutions). For each assay, a cuvette was charged with 400 µl each of 3,5-dichloro-2-hydroxybenzene-sulfonate (10 mM) and 4-aminoantipyrine (7.5 mM). To this was added 100 µl of the sample (pre-diluted to 30-300 µM H_2O_2), after which A_{510} was read as a blank. The assay reaction was initiated by addition of 100 µl horseradish peroxidase (0.1 U ml^{-1}, prepared each day and stored on wet ice), and A_{510} was read after a 10-min incubation in the dark. The assay signal was taken as the difference between the final and the blank A_{510} values. Hydrogen peroxide concentrations were determined by comparison with a calibration curve obtained from dilution of a solution of 30% H_2O_2. Due to the instability of hydrogen peroxide, the concentration of H_2O_2 in the stock solution (stored at 4 °C) was periodically quantitated by titration with $KMnO_4$, per the method of Kolthoff and Sandell (1952). Nitrite concentrations were determined by Griess assay. A detailed description of this method can be found in Section 3.2.4.

Free thiols were assayed using Ellman's reagent, 5,5′-dithiobis-2-nitrobenzoic acid (DTNB; Ellman, 1959), as follows. Excess DTNB reacts with free sulfhydryls, releasing the strongly colored 5-thio-2-nitrobenzoic acid dianion (TNB; ε_{412} = 14.2×10^3 M^{-1} cm^{-1} at 25 °C; Eyer et al., 2003). For each sample, a 2-ml cuvette was charged with 1.5 ml of sodium phosphate ($Na\text{-}PO_4$) buffer (100 mM, pH 7.3) containing 500-800 µM of the metal ion chelator diethylene-triamine-pentaacetic acid (DTPA). To

this was added 50 µl of 4 mM DTNB (in Na-PO_4 buffer, 100 mM, pH 7.3). The absorbance of the solution at 412 nm (A_{412}) was measured both before and after addition of the DTNB (as 'blank' and 'reference' readings, respectively), as the latter absorbs weakly at 412 nm. The sample (50 µL; diluted to 50-500 µM thiol) was added and A_{412} was read after a 5-min incubation period (BioSpec-1601, Shimadzu Scientific Instruments, Columbia, MD). The reading for each sample was calculated as

$$A_{reading} = \left[A_{sample} - A_{blank} \right] - \rho \left[A_{reference} - A_{blank} \right] \tag{4.20}$$

to account for the absorbance of DTNB. The factor ρ equals 0.9688 and corrects for the dilution of the DTNB due to addition of the sample volume. Unknown sample concentrations were determined by comparison with a calibration curve generated from prepared thiol solutions of known concentration.

A three-point spectrophotometric measurement was used for simultaneous determination of the three diazenyl dyes of Section 4.2.2.2, with measurements at 390, 510, and 630 nm using the extinction coefficients listed in Table 4.2. In the experiments described in Section 4.2.6, samples were typically diluted two-, four-, and twenty-fold before reading at 630, 390, and 510 nm, respectively.

Samples containing Cu^{2+} were diluted as appropriate and assayed at 800 nm (ε_{800} = 11.7 M^{-1} cm^{-1}, determined from a calibration curve) against a blank of Cu^{2+}-free buffer. Samples containing insoluble copper salts were centrifuged at 7000 ×*g* for 10 min before assay of the supernatant.

Table 4.2. Extinction coefficients for the diazenyl dye products of the 1-NA/diazo-SAA chemical system.

Species	Extinction coefficient (M^{-1} cm^{-1})		
	390 nm	510 nm	630 nm
p-R	2.78×10^3	3.17×10^4	7.73×10^1
o-R	4.01×10^3	2.38×10^4	6.46×10^1
S	6.55×10^3	1.88×10^4	7.76×10^3

Extinction coefficients at 390 nm are those of Bourne et al. (1990); those at 510 and 630 nm are those of Wenger et al. (1992). The values of Bourne et al. were used initially for all three wavelengths; the values of Wenger et al. were substituted for the two highest wavelengths due to the increased accuracy of their determination. The Bourne et al. values at 390 nm were retained because Wenger et al. did not report extinction coefficients for wavelengths shorter than 400 nm. In any subsequent experiments it is recommended to use the Wenger et al. values at 400 nm instead of the Bourne et al. values at 390 nm.

4.2.4 Peroxynitrite synthesis

Peroxynitrite is available commercially (Cayman Chemical, Ann Arbor, MI), but numerous synthesis methods have been published in the literature and it can be more efficient and cost-effective to synthesize it, especially if large quantities are required. A number of chemistries can be used to synthesize peroxynitrite, including reaction of NO gas with superoxide salts in the solid phase (Koppenol et al., 1996) or in anhydrous ammonia (Bohle et al., 1996); combination of solutions of acidified hydrogen peroxide and nitrite followed by quenching with alkali (Robinson and Beckman, 2005; Saha et al., 1998); reaction of azide and ozone (Pryor et al., 1995); and autoxidation of hydroxylamine (Hughes et al., 1971). Given the necessity of storing peroxynitrite in strongly basic solution, alkali is inevitably present in any aqueous preparation. Most methods produce solutions with additional contaminants, including nitrite, nitrate, azide, and salts such as sodium chloride. In general, significant experimental effort must be expended to eliminate these contaminants and, depending on the desired application and the likelihood of interference, such effort may not be worthwhile. The synthesis used in this study was that of Robinson and Beckman (2005), as described below.

In acid solution, nitrite protonates to form nitrous acid, which reacts with hydrogen peroxide to form peroxynitrous acid:

$$HNO_2 + H_2O_2 \longrightarrow ONOOH + H_2O\,. \qquad (4.21)$$

The ONOOH thus formed immediately begins to decompose by Reaction (4.2), but slowly enough that quenching the reaction mixture with strong base yields a solution of alkali-stabilized $ONOO^-$ at concentrations typically in the range of 100-200 mM. The

synthesis reaction was carried out using the apparatus schematized in Figure 4.2. Solutions of acidified H_2O_2 (0.6 M in both H_2O_2 and HCl), sodium nitrite (0.6 M), and sodium hydroxide (3 N) were prepared in DI H_2O. Five 30-ml syringes were filled with these solutions: two with H_2O_2/HCl, two with $NaNO_2$, and one with NaOH. The syringes were mounted on a syringe pump and connected to the appropriate feed lines of the tubing network. The outlet tube was directed to a waste beaker and the syringe pump was engaged at its maximum pumping rate (~15 ml min^{-1} for this size syringe). Once the effluent stream had turned the bright yellow color indicative of $ONOO^-$ the solution (final pH 13.6) was collected on ice in a poly(tetrafluoroethylene) (PTFE) beaker. The peroxynitrite solution was treated with high-purity MnO_2 [synthesized as described in Robinson and Beckman (2005)] to destroy residual H_2O_2, after which the particulate MnO_2 was removed by vacuum filtration. Aliquots of the product solution before and after MnO_2 treatment were assayed for peroxynitrite, H_2O_2, and nitrite. Aliquots of the peroxynitrite product (1.5 ml) were flash-frozen in perfluoroalkoxy (PFA) vials (Elemental Scientific, Inc., Omaha, NE) by immersion in liquid nitrogen. The frozen aliquots were stored at –80 °C and individually thawed on wet ice as needed. The thawed aliquots were immediately assayed as described above (Section 4.2.3), diluted to the desired concentration with 0.1 N NaOH, and stored on wet ice. Aliquots were assayed again at the end of each day's experiments to determine the extent of decomposition (typically 5-15%) and the Per concentration for each experiment was adjusted assuming linear decomposition over time.

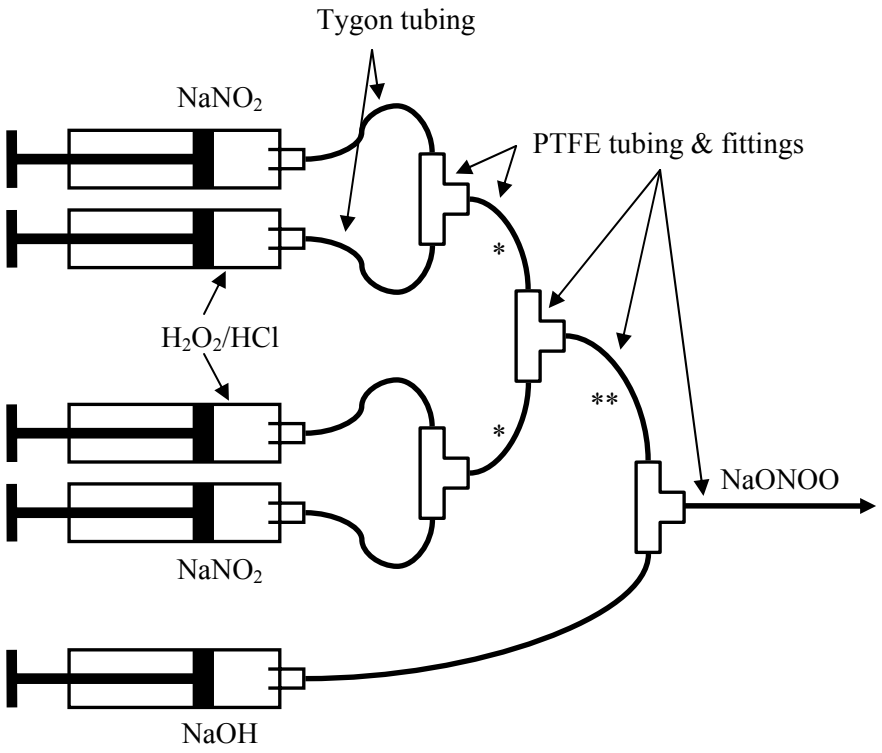

Figure 4.2. Schematic of peroxynitrite synthesis apparatus.

Most tubing and fittings were PTFE, except for the inlet lines (connected to the syringes) which were Tygon. All tubing was approximately 1/8″ in outer diameter. The tubing sections marked "*" were approximately 4 cm in length; the section marked "**" was varied from 2 cm to 8 cm in an attempt to optimize the yield of peroxynitrite. The entire tubing apparatus was placed in a plastic bin to contain any leaks of the corrosive acid and base streams and/or the corrosive and toxic $ONOO^-$.

4.2.5 Bolus delivery model

The bolus delivery model is conceived as follows. Consider a liquid volume $V_{N,o}$ in an agitated vessel initially containing one or more solutes at concentrations $\hat{C}_j$, to which has been added a much smaller volume $V_{R,o}$ of the same liquid (the bolus) containing one or more solutes at initial concentrations $C_{j,o}$. Figure 4.3(a) portrays the first instant after the addition of $V_{R,o}$, before the two volumes have begun to mix. As time advances, assume that the V_R engulfs a portion of V_N at an instantaneous rate proportional to V_N [Figure 4.3(b)]. (Since the total liquid volume is constant ($V_T = V_R + V_N$ at all times), the instantaneous V_N can just be written as $V_T - V_R$, where $V_T = V_{N,o} + V_{R,o}$). As the exchange of fluid between V_R and V_N progresses, it is assumed that the solute concentrations within V_N are uniform and remain constant at $\hat{C}_j$ at all times. Concentrations within V_R are assumed uniform, but are modeled as time-variant due both to the reactions occurring and to the dilution of V_R by V_N. The central hypotheses of the model are the partitioning of the liquid into V_R and V_N and the assumption that agitation is vigorous enough that V_R can be considered well-mixed.

A mass balance written around V_R for each solute *j* takes the form

$$\frac{d}{dt}\left(C_j V_R\right) = \hat{C}_j \frac{dV_R}{dt} + R_j V_R \,. \tag{4.22}$$

The term on the left-hand side of Eq. (4.22) is the accumulation term, and the terms on the right-hand side represent transport of species *j* into V_R via the engulfment of V_N and reaction within V_R, respectively. Expanding the left-hand side of Eq. (4.22) gives

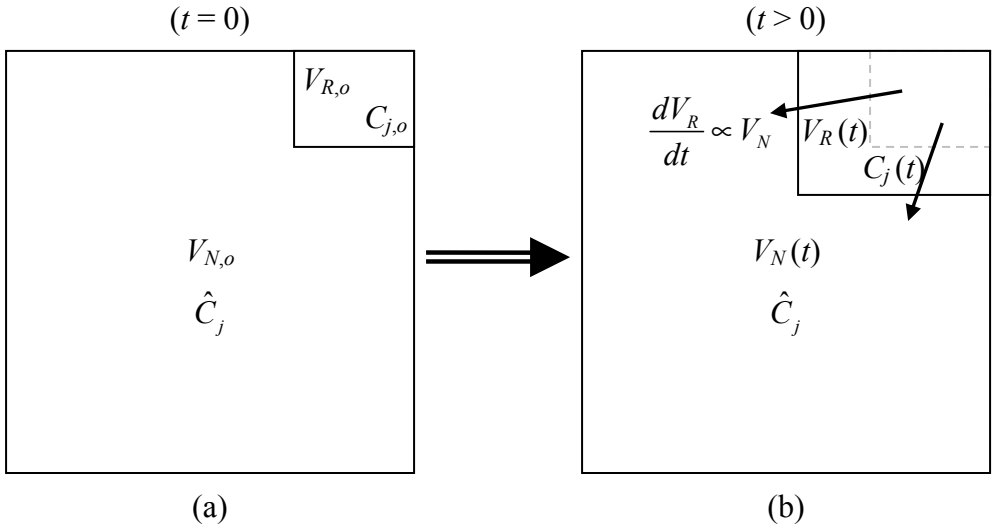

Figure 4.3. Schematic representation of proposed reactive mixing model.

At time $t = 0$, the volume $V_{R,o}$ is added to the larger volume $V_{N,o}$. As time advances, V_R is assumed to engulf the liquid of V_N at a rate dV_R/dt that is proportional to the remaining V_N at each instant in time. The solute concentrations within V_N are assumed to remain constant at $\hat{C}_j$, whereas those within V_R are assumed to be uniform but time-variant.

$$V_R \frac{dC_j}{dt} + C_j \frac{dV_R}{dt} = \hat{C}_j \frac{dV_R}{dt} + R_j V_R \,. \tag{4.23}$$

Rearrangement of Eq. (4.23) yields an expression for dC_j/dt in terms of both C_j and V_R:

$$\frac{dC_j}{dt} = \frac{\hat{C}_j - C_j}{V_R} \frac{dV_R}{dt} + R_j \,. \tag{4.24}$$

Defining the proportionality constant between dV_R/dt and V_N as τ^{-1}, where τ is the 'mixing time,' and invoking the constant liquid volume in the system gives:

$$\frac{dV_R}{dt} = \frac{1}{\tau} V_N = \frac{1}{\tau}\left(V_T - V_R\right). \tag{4.25}$$

Eqs. (4.24) and (4.25), along with the initial conditions $C_j(0) = C_{j,o}$ and $V_R(0) = V_{R,o}$, fully define the model. Eq. (4.25) can be solved explicitly as

$$V_R(t) = V_T - \left(V_T - V_{R,o}\right) \cdot \exp\left[-t/\tau\right]. \tag{4.26}$$

The set of differential equations governing each chemical system, comprising Eq. (4.24) written for each species and Eq. (4.25), was solved numerically in either MATLAB (Mathworks, Natick, MA) or in MAPLE (Maplesoft, Waterloo, ON, Canada). The full set of equations solved for each chemical system is provided in Table 4.3. In the Per/thiol system, since the reactive volume is initially strongly alkaline and the non-reactive volume is neutrally buffered, the pH of V_R changed rapidly over the course of each simulated bolus addition. It was necessary in this system to capture this time-dependent pH behavior in order to accurately capture the peroxynitrite decomposition kinetics. This was achieved by imposing on the system of differential equations algebraic constraints derived from the various protonation equilibria; the mass balances for Per,

thiol, and buffer; and electroneutrality. In order to specify the initial pH of the reactive volume and to close the charge balance, it was necessary to define the quantity

$$I(t) \equiv \sum_{\text{spectator}} z_j C_j(t) \ , \tag{4.27}$$

which is the charge-weighted sum of the concentrations of spectator ions, *excluding hydrogen* (H^+) *and hydroxyl* (OH^-) *ions*, at time *t*. (The presence of the negatively-charged chloride ion in a 1 M solution of hydrochloric acid, for example, would result in a value of *I* for that solution very near to –1.0 M.) A differential equation written for *I* was included in the system of equations solved. Nitrite ion was assumed to exist in the deprotonated state at all times, and the contributions of RS^- and NO_3^- to the charge balance were assumed to be negligible.

The kinetics of the diazenyl dye system are not dependent on the protonation state of the reactants at the pH used, so equilibrium constraints were not included in simulations of the dye system. Despite the dramatic pH changes within the reactive volume in bolus addition of concentrated NaOH to Cu^{2+}/ECA solutions, treatment of OH^- as a non-equilibrium species was found to introduce negligible error in the simulation results. Accordingly, no protonation equilibria were simulated in this system either.

When simulating the addition of more than one bolus, the reactive volume concentrations at the end of the simulation of a given bolus were used as the initial non-reactive volume concentrations ($\hat{C}_j$) in simulating the addition of the subsequent bolus. The endpoint of all simulations was selected to be no less than ten times the mixing time, which was sufficient for all reactions to go to completion. For each set of experimental data, the best-fit value of τ was determined as that which minimized the root-mean-

Table 4.3. Differential equations and algebraic constraints used in model simulations

Chemical System	Equation	Description
(All)	$\frac{dV_R}{dt} = \frac{1}{\tau}(V_T - V_R);\ V_R(0) = V_{R,o}$	Reactive volume DE
	$\delta_j = \frac{\hat{C}_j - C_j}{V_R}\frac{dV_R}{dt}$ [a]	Generic dilution term
Per/Thiol	$\frac{dC_{Per}}{dt} = -k_2 C_{\mathrm{ONOOH}} - k_3 C_{\mathrm{ONOOH}} C_{\mathrm{RS^-}} + \delta_{Per}$ [b]	Reactant DEs
	$\frac{dC_{thiol}}{dt} = -2k_3 C_{\mathrm{ONOOH}} C_{\mathrm{RS^-}} + \delta_{thiol}$ [c]	
	$\frac{dC_{\mathrm{P_i}}}{dt} = \delta_{\mathrm{P_i}}$ [c]	Phosphate buffer DE
	$\frac{dC_I}{dt} = \delta_I$ [d]	Spectator ion DE
	$K_{\mathrm{P2}} = \frac{C_{\mathrm{HPO_4^{2-}}} C_{\mathrm{H^+}}}{C_{\mathrm{H_2PO_4^-}}};\ K_{\mathrm{P3}} = \frac{C_{\mathrm{PO_4^{3-}}} C_{\mathrm{H^+}}}{C_{\mathrm{HPO_4^{2-}}}}$	Buffer equilibria
	$C_{\mathrm{P_i}} = C_{\mathrm{H_2PO_4^-}} + C_{\mathrm{HPO_4^{2-}}} + C_{\mathrm{PO_4^{3-}}}$	Buffer mass balance
	$K_1 = \frac{C_{\mathrm{ONOO^-}} C_{\mathrm{H^+}}}{C_{\mathrm{ONOOH}}};\ C_{Per} = C_{\mathrm{ONOO^-}} + C_{\mathrm{ONOOH}}$	Reactant mass balances and equilibria
	$K_{a,thiol} = \frac{C_{RS^-} C_{H^+}}{C_{RSH}};\ C_{thiol} = C_{RS^-} + C_{RSH}$	
	$K_w = C_{\mathrm{H^+}} C_{\mathrm{OH^-}}$	Water dissociation
	$C_{\mathrm{H^+}} + C_I - C_{\mathrm{ONOO^-}} - C_{\mathrm{NO_2^-}} - C_{\mathrm{OH^-}} - C_{\mathrm{H_2PO_4^-}} - 2C_{\mathrm{HPO_4^{2-}}} - 3C_{\mathrm{PO_4^{3-}}} = 0$	Charge balance
Cu^{2+}/ECA	$\frac{dC_{\mathrm{OH^-}}}{dt} = -k_{ppt} C_{\mathrm{Cu^{2+}}} C_{\mathrm{OH^-}} - k_4 C_{\mathrm{ECA}} C_{\mathrm{OH^-}} + \delta_{\mathrm{OH^-}}$ [b]	Reactant DEs
	$\frac{dC_{\mathrm{Cu^{2+}}}}{dt} = -\left[\frac{1}{2} f_{\mathrm{Cu(OH)_2}} + \frac{2}{3}\left(1 - f_{\mathrm{Cu(OH)_2}}\right)\right] k_{ppt} C_{\mathrm{Cu^{2+}}} C_{\mathrm{OH^-}} + \delta_{\mathrm{Cu^{2+}}}$ [c,e]	
	$\frac{dC_{\mathrm{ECA}}}{dt} = -k_4 C_{\mathrm{ECA}} C_{\mathrm{OH^-}} + \delta_{\mathrm{ECA}}$ [c]	

Table 4.3. Differential equations and algebraic constraints used in model simulations (cont.)

Chemical System	Equation	Description
Diazenyl Dye	$\frac{dC_{\text{dSAA}}}{dt} = -\left[\left(k_{5o}+k_{5p}\right)C_{\text{1-NA}} + k_{6o}C_{\text{p-R}} + k_{6p}C_{\text{o-R}}\right]C_{\text{dSAA}} + \delta_{\text{dSAA}}$ [b]	Reactant DEs
	$\frac{dC_{\text{1-NA}}}{dt} = -\left(k_{5o}+k_{5p}\right)C_{\text{1-NA}}C_{\text{diazo-SAA}} + \delta_{\text{1-NA}}$ [c]	
	$\frac{dC_{\text{o-R}}}{dt} = \left(k_{5o}C_{\text{1-NA}} - k_{6p}C_{\text{o-R}}\right)C_{\text{dSAA}} + \delta_{\text{o-R}}$ [f]	Dye DEs
	$\frac{dC_{\text{p-R}}}{dt} = \left(k_{5p}C_{\text{1-NA}} - k_{6o}C_{\text{p-R}}\right)C_{\text{dSAA}} + \delta_{\text{p-R}}$ [f]	
	$\frac{dC_{\text{S}}}{dt} = \left(k_{6p}C_{\text{o-R}} + k_{6o}C_{\text{p-R}}\right)C_{\text{dSAA}} + \delta_{\text{S}}$ [f]	

[a] δ_j represents the first term on the right-hand side of Eq. (4.24)

[b] $\hat{C}_j = 0$ and $C_j(0) = C_{j,o}$ before addition of the first bolus

[c] $\hat{C}_j \neq 0$ and $C_j(0) = 0$ before addition of the first bolus

[d] Charge-weighted spectator ion concentration, see Eq. (4.27); $\hat{C}_I \neq 0$, $C_I(0) \neq 0$

[e] The precipitation reactions were assumed to follow elementary second-order kinetics in both Cu^{2+} and OH^-, where $-R_{OH^-} = k_{ppt}C_{Cu^{2+}}C_{OH^-}$. The actual kinetics are relatively unimportant given the extremely rapid rate of reaction. The fractions 1/2 and 2/3 derive from the stoichiometry of Eqs. (4.17) and (4.18). The distribution of products is described by the parameter $f_{Cu(OH)_2}$, which represents the fraction of consumed OH^- that forms the simple copper(II) hydroxide.

[f] $\hat{C}_j = C_j(0) = 0$ before addition of the first bolus

squared-error between the model predictions and the experimentally measured concentrations.

4.2.6 Bolus delivery experiments

4.2.6.1 Preparation of reactant solutions

In delivery of peroxynitrite to thiol-containing solutions, the peroxynitrite stock was thawed and typically diluted to 30 mM in 0.1 N NaOH. Solutions containing thiols (both Cys and Glt) were typically prepared at 500 μM in Na-PO_4 buffer (100 mM, pH 7.3) in the presence of 500-800 μM DTPA.

The reactant solutions in the dye system required more careful preparation, as both 1-NA and diazo-SAA are unstable in solution (decay rates of approximately 5%/6 h and 1%/5 h, respectively). Both solutions were prepared using methods adapted from those of Wenger et al. (1992). The 1-NA solution was prepared daily by dissolving a 14-mg quantity of the solid in 50 ml of 0.1 N NaOH, yielding a concentration of 1.9 mM. A 1-ml portion of this intermediate solution was then diluted into 14 ml of sodium bicarbonate buffer (215 mM, pH 9.9) to give a final concentration of 130 μM. The diazotization of SAA was carried out twice daily using a slight excess of acidified $NaNO_2$, as follows. A 50-mM solution of SAA was prepared by adding 104 mg of the solid to 12 ml of DI H_2O kept on ice. To this was added 310 μl of 2 M HCl and 625 μl of 1 M $NaNO_2$, with stirring. This mixture was incubated for 10 minutes, after which the remaining nitrite was destroyed by addition of 0.1 M urea (120 μl). The solution was diluted to a final concentration of 30 mM diazo-SAA by addition of 6.95 ml DI H_2O and was kept on ice.

In competition studies between alkaline precipitation of Cu^{2+} salts and ECA hydrolysis, solutions of $CuSO_4$ (typically 5.25 mM) were prepared either in the presence or absence of 28 mM ECA. (The ECA is sparingly soluble and thus dissolves rather slowly in the $CuSO_4$ solution, often requiring ten minutes or more of vigorous mixing for complete dispersal.) Solutions of NaOH between 1 N and 3 N were prepared in DI H_2O.

4.2.6.2 Delivery experiments

In most experiments the same manner of addition was used: small volumes (typically 25 μl) of concentrated 'bolus solutions' of Per, NaOH, or diazo-SAA were added by a pipettor to larger volumes (typically 15 ml) of more dilute 'target solutions' of thiol, $CuSO_4$/ECA, or 1-NA, respectively. In certain preliminary experiments, agitation of the target solutions was effected by manual swirling in a beaker. More rigorous control of this swirling style of mixing was achieved by placing the beaker on an orbital mixer (laboratory shaker) whose cyclic rate (90-240 rpm) was measured by a strobe tachometer. For cyclic rates above 190 rpm it was necessary to affix the beaker to the mixer platform with laboratory tape. In tests with DI H_2O, agitation was sufficiently intense at cyclic rates greater than 240 rpm that liquid splashed out of the beaker. Agitation by vortexing was achieved by placing 15 ml of target solution in a 50-ml centrifuge tube and bringing the laboratory vortexer up to steady motion at various settings (1-9 on the arbitrary scale of the vortexer; the cyclic rate was not quantified). The bolus solution was introduced by pipetting through a small hole cut in the tube cap.

The time scales of the three chemical systems of Section 4.2.2, analyzed using the scaling formalism of Section 4.1.4, are summarized in Table 4.4.

Table 4.4. Reaction time scales for the test chemical systems.

Chemical System	Per/RSH	Diazenyl Dye [a]	Cu^{2+}/ECA
Species **A**	Per	Diazo-SAA	OH^-
Species **B**	*(decomposition)* [b]	p-R	ECA
k_{R1}	$0.25\ s^{-1}$ $(f_{Per}k_2)$	$1.8 \times 10^3\ M^{-1}\ s^{-1}$	$2.3 \times 10^1\ M^{-1}\ s^{-1}$
C_B	–	80 μM [c]	28 mM
τ_{R1}	4.0 s	6.9 s	1.6 s
Species **C**	Cys [d]	1-NA	Cu^{2+}
k_{R2}	$6.1 \times 10^3\ M^{-1}\ s^{-1}$ $(f_{Per}\left[1-f_{Cys}\right]k_{3,Cys})$	$1.2 \times 10^7\ M^{-1}\ s^{-1}$	$> 10^8\ M^{-1}\ s^{-1}$ [e]
C_C	500 μM	130 μM	5.3 mM
τ_{R2}	0.33 s	0.64 ms	< 1.9 μs

[a] The diazenyl system was simplified in this analysis by neglecting the formation of o-R

[b] The first-order decomposition of ONOOH is the slower of the two competing reactions in this system

[c] Scaling estimate for the p-R concentration after addition of the first bolus of diazo-SAA; see, e.g., Figure 4.7

[d] Values for Glt are similar to those for Cys

[e] Assumed

4.3 Results and Discussion

The results of the peroxynitrite synthesis are described first (Section 4.3.1), followed by discussion of initial tests performed on the three chemical systems (Section 4.3.2). The thiol/peroxynitrite and diazenyl dye systems were found to work as expected, but the Cu^{2+}/ECA system proved to be unsatisfactory. The remainder of the section describes the reproducibility of the bolus delivery experiments (Section 4.3.3) and evaluates the performance of the model as it pertains to experiments with agitation by orbital mixing and by vortexing (Sections 4.3.4 and 4.3.5, respectively).

4.3.1 Peroxynitrite synthesis

The peroxynitrite synthesis successfully generated stock solutions at a concentration sufficient for the experiments performed: concentrations of peroxynitrite, hydrogen peroxide, and nitrite in samples withdrawn both before and after the MnO_2 treatment were 90 mM, 1 mM, and 70 mM, respectively. The relative absence of H_2O_2 prior to the MnO_2 treatment indicated that most of the H_2O_2 fed into the tubing network had been consumed. It proved difficult to produce peroxynitrite at a concentration greater than approximately 100 mM, despite the Per concentrations as high as 170-190 mM obtained by Robinson and Beckman (2005). The significant nitrite impurity observed in the product, amounting to nearly 80% of the final peroxynitrite concentration, combined with the comparatively miniscule (~ 1%) residual H_2O_2 concentration implies that much less H_2O_2 reached the reaction zone in the tubing network than was intended. Presumably either an error was made in the titrimetric assays of the 30% H_2O_2 stock

solution or significant decomposition of the H_2O_2 occurred at some point in the synthesis protocol.

4.3.2 Preliminary tests of the chemical systems

Preliminary tests of the three chemical systems of Section 4.2.2 were performed to confirm that they were functioning in accordance with expectations. Peroxynitrite was added to vigorously stirred solutions of Cys and Glt in borate buffer at pH 9, where less than 1% of Per is present as ONOOH. Under these conditions the decomposition of ONOOH is negligible and all of the added Per is expected to consume the thiol. In all such experiments performed, the data conformed to the 2:1 stoichiometry expected from Reaction (4.7) within a few percent.

Combination of equimolar amounts of diazo-SAA and 1-NA under vigorous stirring resulted in quantitative formation of p-R and o-R in approximately the 10:1 ratio predicted from the values of k_{5o} and k_{5p} (Table 4.1) with negligible formation of S. Addition of diazo-SAA to 1-NA in a molar ratio of 2:1 yielded results that were difficult to interpret, likely due to decomposition of S (Bourne et al., 1990; Wenger et al., 1992). In agreement with the conclusions of Bourne et al. (1990), it was estimated that decomposition could be neglected as long as less than 40% of the initial 1-NA was converted to S.

NaOH was added to solutions of $CuSO_4$ in the absence of ECA; with no competing reactions, all alkali added should react with Cu^{2+} to form insoluble salts as per Reactions (4.17) and (4.18). Despite the claim of Brucato et al. (2000) that Reaction (4.17) is the only precipitation reaction expected to occur, the observed

stoichiometry was observed to vary between the 1:2 ratio of moles Cu^{2+} consumed per mole of OH^- added predicted by Reaction (4.17) and the 2:3 ratio predicted by Reaction (4.18). This uncertainty in the stoichiometry of the precipitation reaction translates to a corresponding uncertainty in any mixing times fitted to the experimental results. Accordingly, the Cu^{2+}/ECA system was abandoned, and the remainder of this section will focus on the results from the Per/thiol and dye systems.

4.3.3 Reproducibility of bolus delivery

In general, the experiments were highly reproducible, with data from repetitions of a particular experiment typically matching within 5-10%. In all experiments with the Per/thiol system the consumption of thiol was a linear function of the respective mole quantity of Per added, independent of agitation method and intensity. Figure 4.4 plots representative data for delivery of Per to Cys with agitation by orbital mixing.

Since the diazenyl dye system is composed of a pair of parallel, two-step reaction pathways, the product generation curves are not expected to be a linear function of added diazo-SAA. The data were still quite reproducible however: Figure 4.5 plots the measured concentrations of the three diazenyl dyes (mean ± s.d. of three experiments) in bolus delivery of diazo-SAA to 1-NA with orbital mixer agitation at 120 and 155 rpm. The concentrations of all three dye products were repeatable within approximately 20% after addition of each aliquot of diazo-SAA. The amount of p-R present initially increases with added diazo-SAA, due to its much faster rate of formation from 1-NA (Reaction (4.13), Table 4.1) compared to the other products. It then decreases on

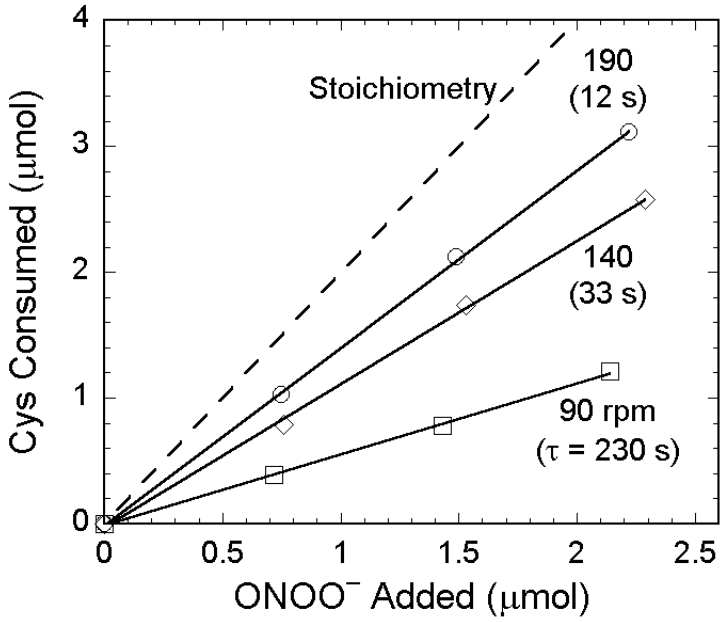

Figure 4.4. Consumption of cysteine in bolus delivery of alkaline peroxynitrite during agitation by orbital mixing.

Samples were assayed for Cys at least in duplicate after addition of each bolus of alkaline peroxynitrite; the mean difference from assays of the original stock solution $\left[\left(C_{stock} - C_{sample}\right) \cdot V_{target}\right]$ is reported. The error bars for both Cys and $ONOO^-$ are smaller than the symbols. The solid lines are linear fits of the data points at each agitation rate and closely match the model results at the best-fit values of the mixing time (indicated in parentheses for each dataset). The dashed line indicates the curve predicted by stoichiometry if all Per reacts with Cys. The Cys concentration in all experiments was 500 μM; Per concentrations varied slightly between runs but were all approximately 30 mM. The target solution volume was 15 ml; the bolus volume was 25 μl.

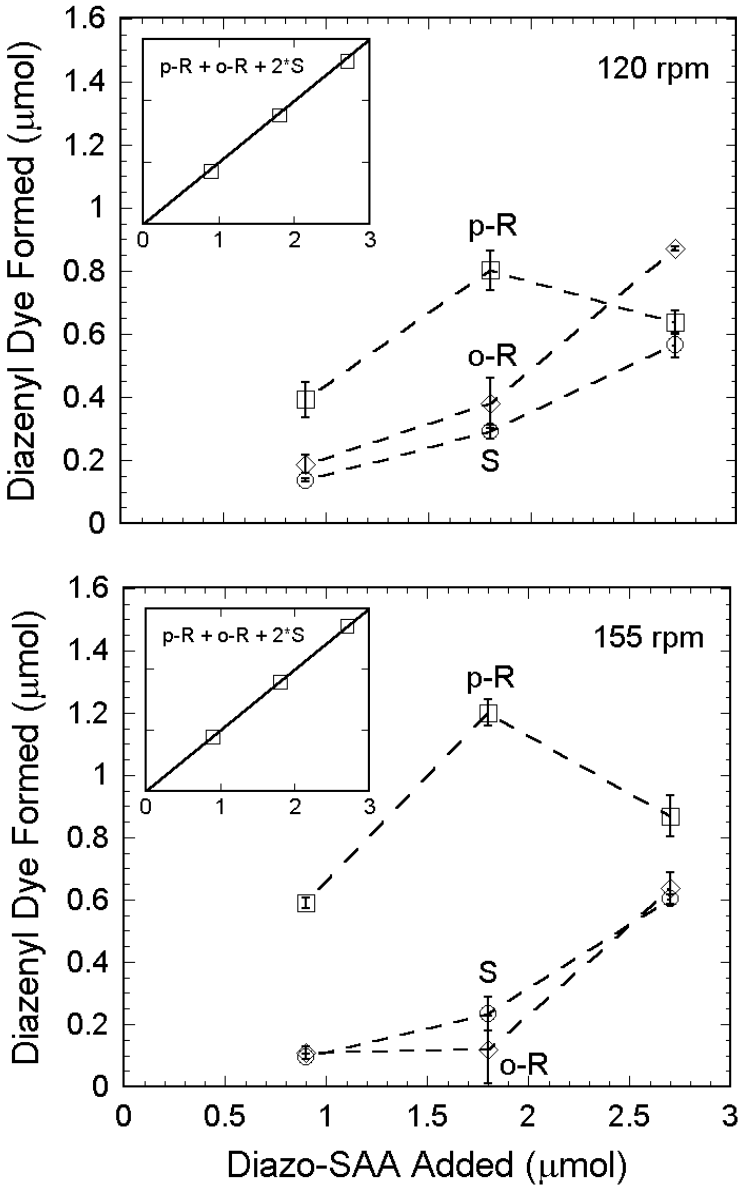

Figure 4.5. Diazenyl dye formation from addition of diazo-SAA to 1-NA during agitation by orbital mixing.

Data are mean ± s.d. for three experimental runs at each agitation rate. Three boluses of diazo-SAA were added and samples were assayed after each addition. Dashed lines are included as a visual aid. Concentrations (volumes) for diazo-SAA and 1-NA were 30 mM (30 μl) and 128 μM (15 ml), respectively. See text for discussion of figure insets.

addition of the third bolus of diazo-SAA because 1-NA is nearly depleted and there is a net conversion of p-R to S.

The apparent increase in o-R on addition of the third bolus is somewhat perplexing given the depletion of 1-NA, but presumably it is a consequence of the non-ideal mixing in the system. Another possibility is that a side product other than o-R with similar spectroscopic properties is actually being formed. (Given that the three-point assay used here is not over-specified for measurements of three species, it is possible that these results are confounded by, e.g., a decomposition product of S. Use of a four-point assay would permit determination of whether this is the case.) Regardless, the mass balance on diazenyl groups (assuming accurate measurement of the three dyes) was maintained for sufficiently low conversion to S: the moles of diazo-SAA added consistently equaled the measured quantity (o-R + p-R + 2×S) within 5%, as shown by the close fit of the data points to the identity line in the insets of Figure 4.5.

4.3.4 Evaluation of bolus mixing model for orbital mixer agitation

Visual observation of experiments with the dye system indicated that agitation by orbital mixing is not a suitable experimental model for the proposed mixing model. As noted in Section 4.2.5, a key assumption of the model is that the composition of the reactive volume is uniform at all times during the delivery process. Given the reaction time scales involved, this means that the local length scale at all points in the reaction zone must be no greater than a few microns. However, at even the fastest orbital mixer agitation rate used, 240 rpm, the reaction zone did not rapidly disperse but remained relatively coherent, with an irregular shape of linear dimension on the order of 1-2 cm.

Unfortunately, observation of this crucial feature of the orbital mixing system was only made after extensive investigation had already been performed.

While the mixing model was typically able to identify best-fit values of τ for the orbital mixing data, it proved impossible to reconcile them given that the mixing behavior should have been independent of the chemical system under study. As an example, a subset of the fitted values of τ for the Cys/Per and dye systems are presented in Figure 4.6 (data are mean ± s.d. for at least two experiments). While the expected trend of decreasing τ with increasing intensity of agitation was observed within each chemical system, the values of τ are not consistent between the two systems for a given agitation rate.

Interestingly, despite the mismatch in the fitted mixing times, the model predictions of species concentrations were relatively good in both the thiol-peroxynitrite and diazenyl dye systems. The mixing model accurately reproduced the linear consumption curves in the thiol-peroxynitrite system (Figure 4.4), and the predictions of the dye concentration profiles also matched moderately well. Figure 4.7 presents the same data from the dye system as in Figure 4.5, but adds the simulated dye concentrations at the best-fit value of τ. The predicted concentrations of p-R and S are in relatively good agreement with the observed concentrations, whereas the predictions of the o-R dye concentration are poor.

Further incompatibility of results from different chemistries can be seen by comparing delivery of Per to the two thiol-bearing substrates, Cys and Glt. Figure 4.8 plots experimental data for orbital mixer experiments at 90 and 190 rpm for the two substrates along with the corresponding best-fit values of τ. As can be seen, the

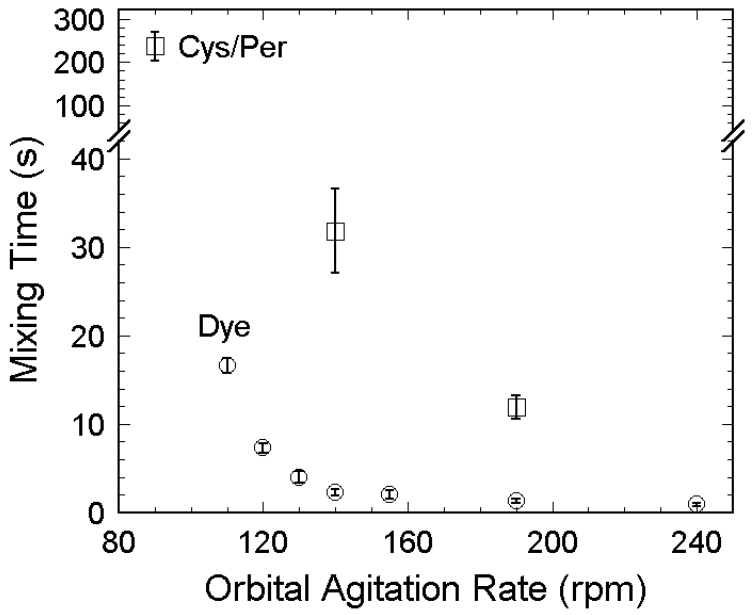

Figure 4.6. Comparison of best-fit mixing times in Cys/Per and diazenyl dye systems with orbital mixing agitation.

Data are mean ± s.d. for at least two experiments. If the mixing model of Section 4.2.5 were accurately capturing the fluid dynamical behavior of bolus delivery with agitation by orbital mixing, the fitted mixing times should be equal for both chemical systems at a given agitation rate.

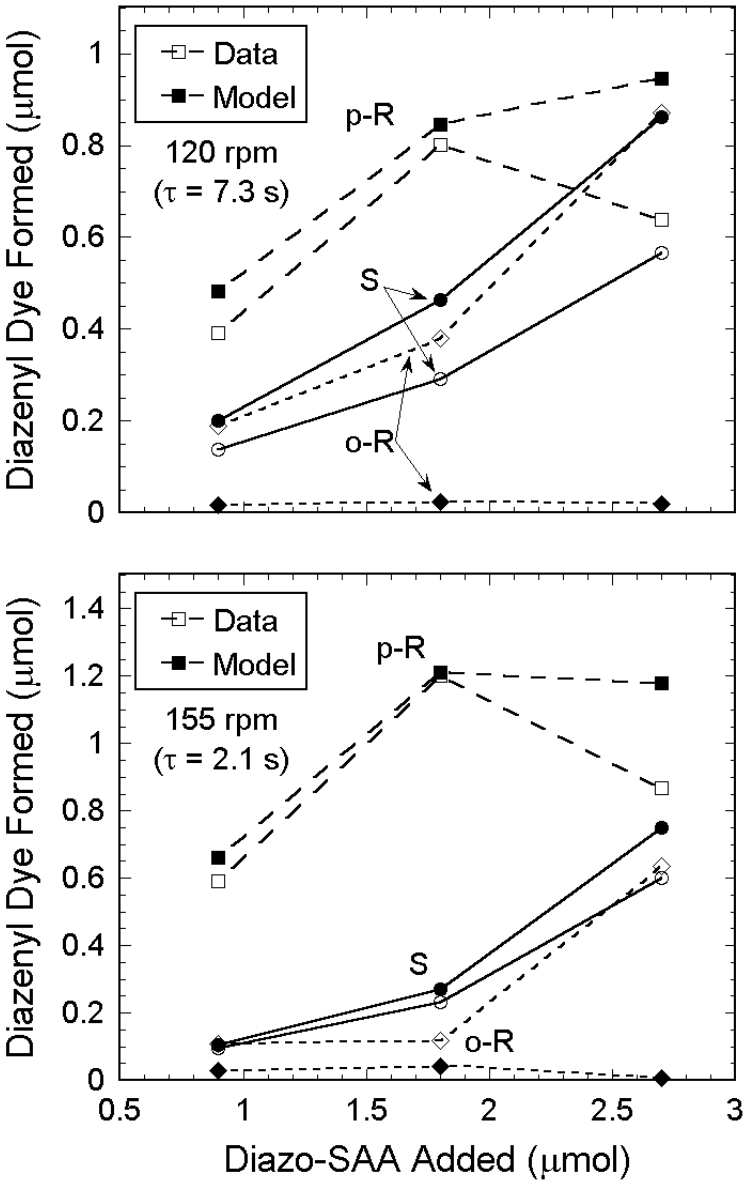

Figure 4.7. Comparison between observed and predicted diazenyl dye concentrations with orbital mixing agitation.

The data (open symbols) are the same as in Figure 4.5; error bars are omitted for clarity. The filled symbols are the model predictions for each species. Lines are included to aid in visual association of each paired set of experimental and simulated data points. The best-fit values of τ are provided in parentheses below each agitation rate. The target solution volume was 15 ml.

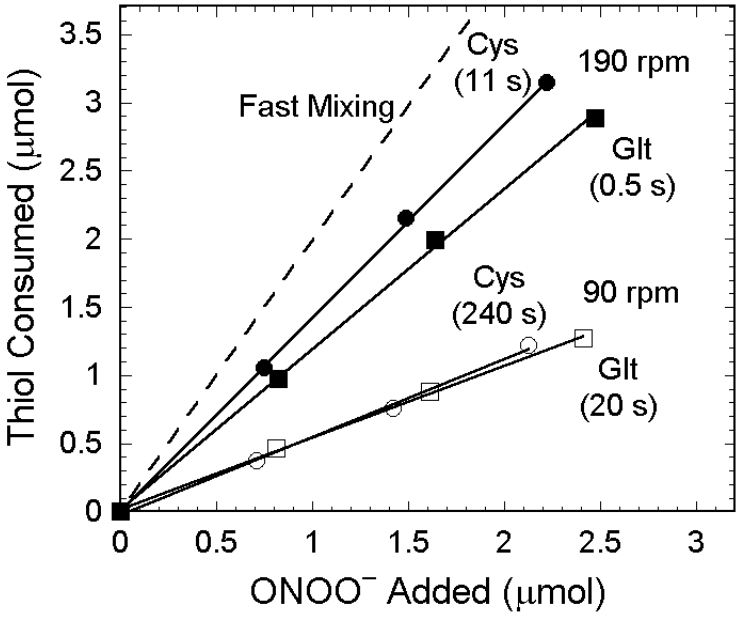

Figure 4.8. Comparison of thiol consumption in delivery of peroxynitrite with orbital mixing agitation.

Data are for single runs; error bars for both $ONOO^-$ and thiol are smaller than the symbols. Initial thiol concentrations were 500 μM; peroxynitrite concentrations varied slightly between runs but were all approximately 30 mM. Liquid volumes were 15 ml (thiol) and 25 μl ($ONOO^-$). Solid lines are linear best-fit functions for each dataset. The thiol concentrations and pH are both sufficiently high that the predicted stoichiometry in the limit of fast mixing (dashed line) deviates negligibly from the 2:1 ratio obtained if only Reaction (4.7) is assumed to occur. Fitted mixing times are provided in parentheses under the label for each curve.

agreement in the best-fit τ values is poor, despite somewhat similar consumption profiles. Interestingly, while at 90 rpm the Cys and Glt data fall nearly in line, at 190 rpm the profiles diverge somewhat. Accounting for the protonation states of Per and RSH [as in Eq. (4.8)], the time scale for the pseudo-first-order thiol reaction of Per (at 500 μM thiol) is approximately 4 s. At 190 rpm, the regressed values of τ are both on the order of this reaction time scale, whereas at 90 rpm the fitted mixing time scales are significantly greater than the reaction scale, especially for Cys. It is reasonable to conclude that at 90 rpm the mixing is sufficiently slow that the thiol reaction is fast with respect to the mixing behavior (which in the real system is identical for both species despite the difference in the fitted mixing times), thus resulting in identical consumption profiles for both species. At 190 rpm, however, the mixing is rapid enough that kinetic differences between the two substrates begin to play a role and the observed consumption profiles differ.

4.3.5 Evaluation of bolus mixing model for vortexer agitation

Most of the experimental effort expended in attempting to validate the mixing model of Section 4.2.5 was focused on the unsuitable orbital mixing agitation method. The data gathered with agitation by vortexing showed quality and repeatability similar to that of the orbital mixing data and, unlike the latter, gave preliminary indications of insensitivity to the chemical system used, as required by the assumptions of the model. More extensive work is required, however, to ascertain whether the model describes vortexing quantitatively.

Figure 4.9 summarizes fitted values of τ obtained for vortexing experiments with the cysteine/peroxynitrite and diazenyl dye chemical systems at various vortexer settings. As part of this investigation, the effects of changes in the 1-NA concentration and in the bolus volume on the fitted mixing times were examined. The dye system data denoted "1x [1-NA]" is for the baseline conditions of Section 4.2.6.1. In experiments marked "5x [1-NA]", the 1-NA concentration in the target solution was increased five-fold but the diazo-SAA concentration in the bolus solution was kept unchanged. The quantity of diazo-SAA added was increased five-fold as follows: for the "5x V_{bolus}" data, the bolus volume was increased five-fold to 150 µl, whereas for the "5x n_{bolus}" data the bolus volume was left unchanged but the number of boluses was increased five-fold. In the latter case, the solution was sampled for assay only after addition of every fifth bolus.

As can be seen in Figure 4.9, the fitted values of τ fell within a relatively close range for all configurations examined, near a value of 1 s. One possible explanation for this consistency is that the mixing within the centrifuge tube is primarily limited by the rate of exchange of fluid elements in the axial direction along the inside of the tube wall. If this is the case, the cyclic rate may not be nearly as important in determining τ as other factors such as the tube geometry or the volume of target solution charged to the tube. This insensitivity to agitation rate would be favorable in performing quantified delivery experiments, as precise calibration of the cyclic rate of the vortexer would not be required. No experiments were attempted that varied any hydrodynamically-relevant system parameters other than the vortexer cyclic rate and the bolus volume, however, so the details of this possible behavior remain unexplored.

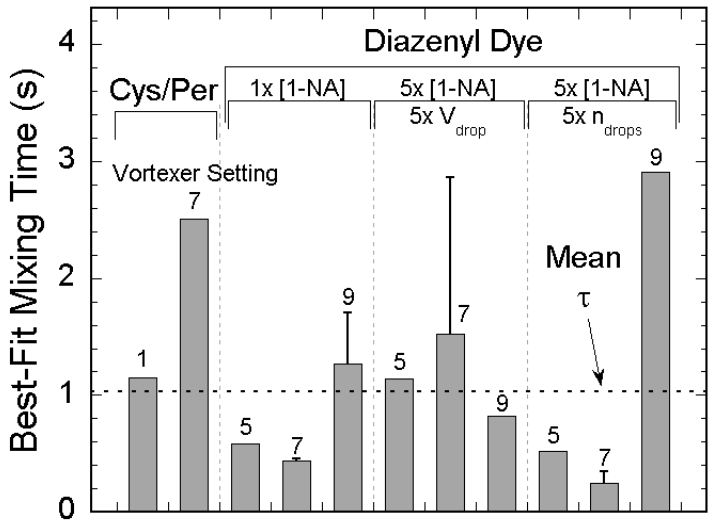

Figure 4.9. Best-fit mixing times for bolus delivery with vortexing agitation.

Data are mean ± s.d. for at least two experiments where error bars are reported; otherwise data are for single experiments. Vortexer speed setting is indicated for each data point. The horizontal dotted line is the mean mixing time for all data shown. See text for experimental details of the various cases of the diazenyl dye data.

The predictions of the model for the dye system with vortexing agitation were quite good, representing a marked improvement over those for experiments with orbital mixing agitation. Plots comparing experimental data and model predictions for vortexing delivery at speed setting "7" are provided in Figure 4.10; the "1x [1-NA]" and "5x [1-NA] / 5x V_{bolus}" conditions are as described above (p 212). The predictions are extremely good for both conditions, and the minimal formation of o-R is well reproduced by the simulations. The results of Figures 4.9 and 4.10 are encouraging in terms of the potential for the proposed model to provide a quantitative description of bolus addition with agitation by vortexing, suitable for study of the toxicologically relevant reactions of peroxynitrite.

4.4 Conclusion

Though not conclusively demonstrating the quantitative utility of the proposed model, these preliminary tests of bolus delivery with agitation by vortex mixing are encouraging. The arguments in favor of the model would be strengthened if other vortexing configurations could be identified that yielded best-fit mixing times other than the 1 s observed in the data of Figure 4.9. If the resulting values of τ were consistent across chemical systems and independent of the reactant concentrations, the model would be validated.

The thiol/peroxynitrite and diazenyl dye systems on the whole seem well suited for the work. The main constraints seem to be use of thiol and nitrite concentrations large enough to keep radical chemistry negligible, and keeping formation of S sufficiently low to avoid problematic decomposition. Assaying nitrite and nitrate in

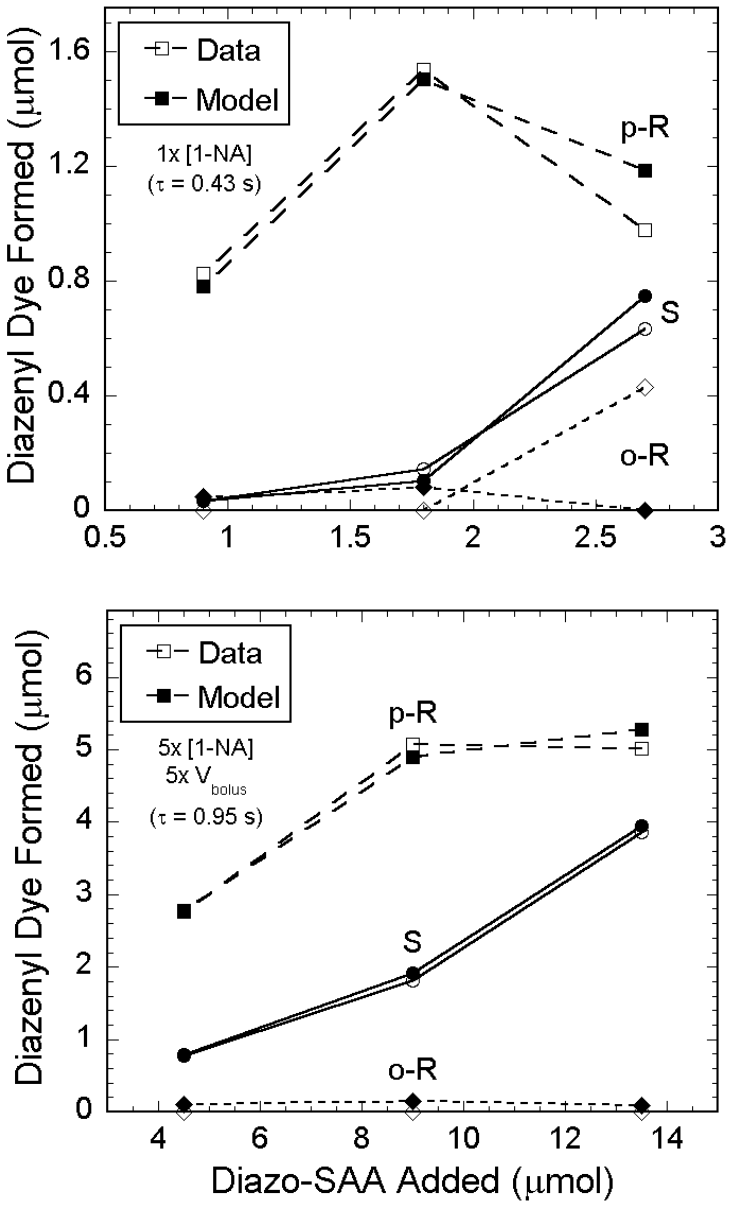

Figure 4.10. Comparison between observed and predicted diazenyl dye concentrations with vortexing agitation.

The open symbols are data gathered with agitation at vortexer setting 7. The filled symbols are the corresponding model predictions. The labels for the experiments (e.g., "1x [1-NA]") are explained on page 212. Lines are included to aid in visual association of each pair of experimental and simulated data points. The best-fit mixing times are given in parentheses. The target solution volume was 15 ml.

addition to residual thiol would at least partly close the mass balance in the RSH/Per system and help to confirm the behavior of that chemistry. If another chemical test system involving peroxynitrite is needed, use of ebselen [2-phenyl-1,2-benzisoselenazol-3(*2H*)-one] may be suitable. Ebselen reacts directly with $ONOO^-$ but appears not to participate in reactions with the radical decomposition products of peroxynitrite (Masumoto and Sies, 1996). Ebselen and its peroxynitrite oxidation product (a selenoxide) at present must be assayed using HPLC techniques, however, which are substantially more complicated than the DTNB assay for thiols.

One possible application of a validated bolus delivery model is elucidation of the nature of the reactions between peroxynitrite and folate. Folate has been shown to have an antioxidant activity which is possibly of physiological relevance (Gliszczynska-Swiglo, 2007; Joshi et al., 2001; Rezk et al., 2003). Nakamura et al. (2002) postulate a site-specific mechanism of folate nitration by peroxynitrite, where direct two-electron oxidation results in nitration at C-12 but multi-step, radical-mediated nitration yields N-10 nitro-folate. Whether applied to this or any other system of interest, however, the development of a simple, quantitative method and model for delivery of pre-formed peroxynitrite would greatly facilitate study of this important molecule.

Appendix A

Experimental Data from Nitric Oxide Delivery System

The complete dataset for the experiments reported in Chapter 2 is provided in this appendix. The date on which each experiment was performed is indicated in each figure.

- O_2 depletion experiments, porous PTFE membrane

  Figure A.1, Section 2.3.1

- O_2 depletion experiments, PDMS tubing

  Figure A.2, Section 2.3.1

- 10% NO delivery without O_2 replenishment, no Mor

  Figure A.3, Section 2.3.2

- 10% NO delivery without O_2 replenishment, with Mor

  Figure A.4, Section 2.3.2

- Simultaneous NO and O_2 delivery

  Figure A.5, Section 2.3.3

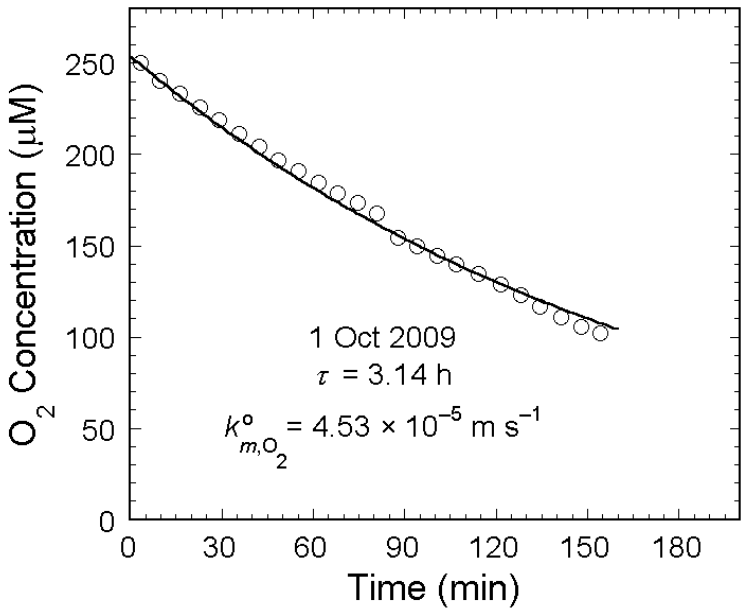
250
200
150
100
50
0
O_2 Concentration (μM)
0
30
60
90
120
150
180
Time (min)
1 Oct 2009
τ = 3.14 h
k^o_{m,O_2} = 4.53 × 10^{-5} m s^{-1}

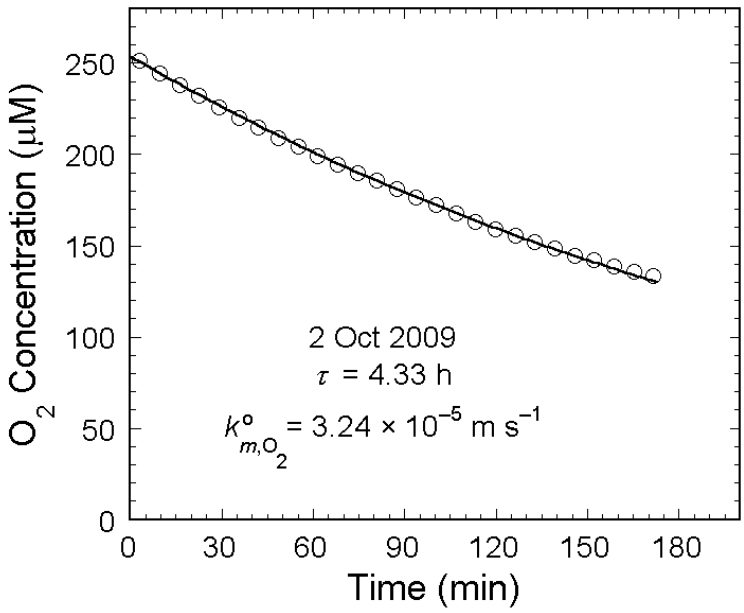
250
200
150
100
50
0
O_2 Concentration (μM)
0
30
60
90
120
150
180
Time (min)
2 Oct 2009
τ = 4.33 h
k^o_{m,O_2} = 3.24 × 10^{-5} m s^{-1}

(Figure A.1)

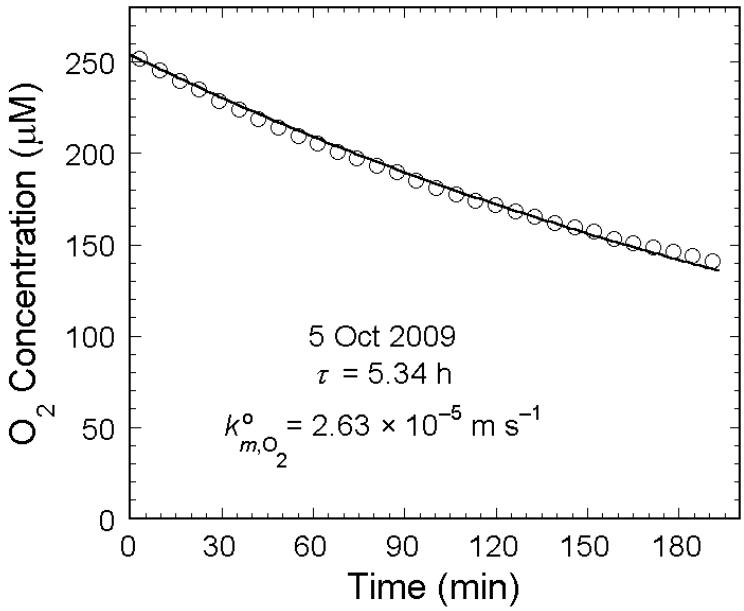
250
200
150
100
50
0
O2 Concentration (μM)
0
30
60
90
120
150
180
Time (min)
5 Oct 2009
τ = 5.34 h
k°m,O2 = 2.63 × 10−5 m s−1

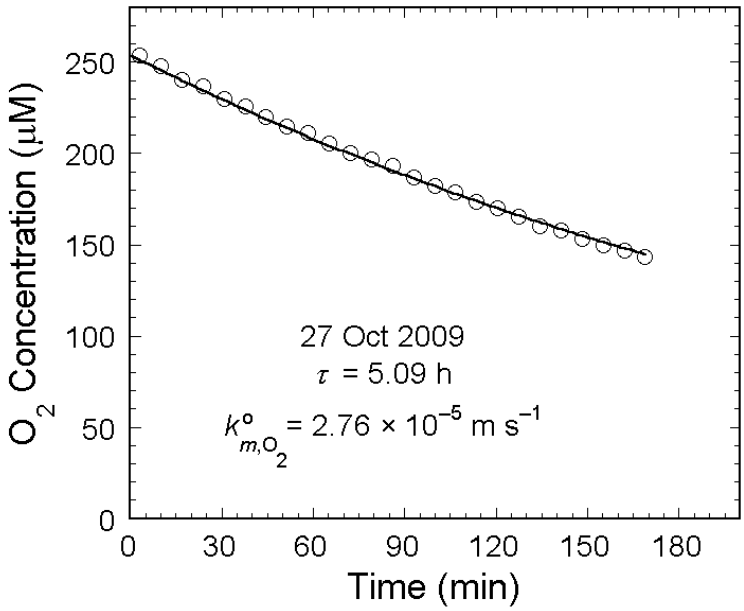
250
200
150
100
50
0
O2 Concentration (μM)
0
30
60
90
120
150
180
Time (min)
27 Oct 2009
τ = 5.09 h
k°m,O2 = 2.76 × 10−5 m s−1

(Figure A.1)

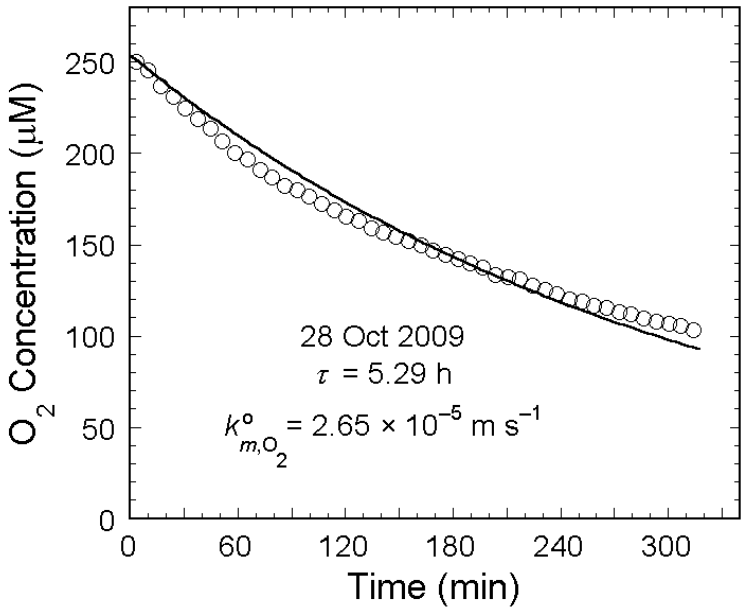
250
200
150
100
50
0
O2 Concentration (μM)
28 Oct 2009
τ = 5.29 h
k°m,O2 = 2.65 × 10−5 m s−1
0
60
120
180
240
300
Time (min)

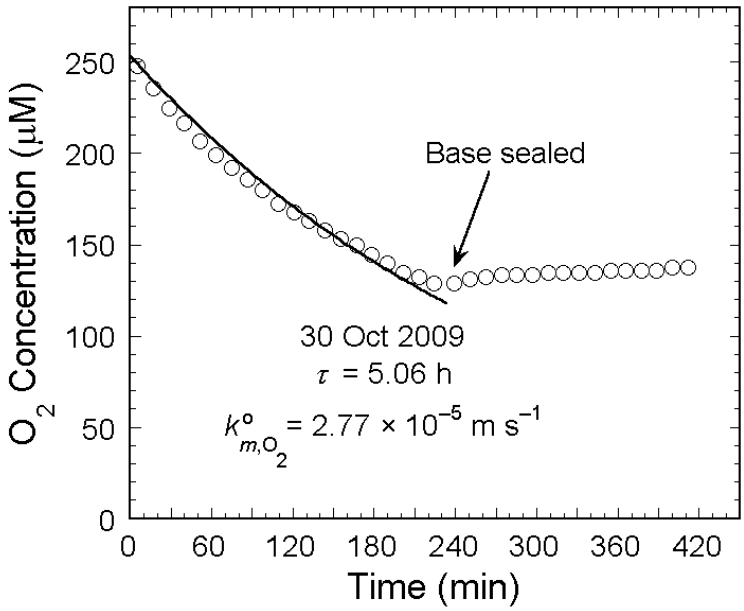
250
200
150
100
50
0
O2 Concentration (μM)
Base sealed
30 Oct 2009
τ = 5.06 h
k°m,O2 = 2.77 × 10−5 m s−1
0
60
120
180
240
300
360
420
Time (min)

(Figure A.1)

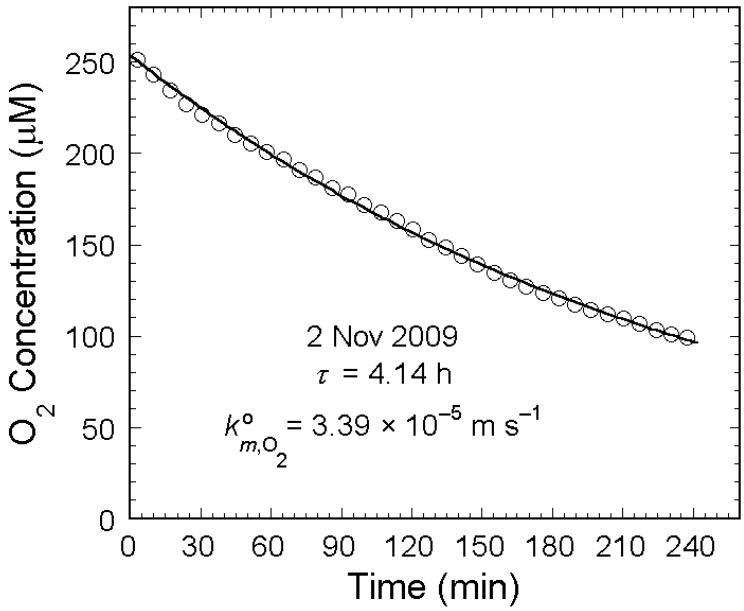

Figure A.1. O_2 depletion experiments for PTFE base membrane.

Open symbols are subsets of the measured O_2 concentrations. Solid lines are the fits of Eq. (2.20). Best-fit values of τ and k°_{m,O_2} are shown. The plot for 30 Oct 2009 shows concentration data after discontinuing N_2 flow and sealing the inlet and outlet ports of the base. The sub-ambient asymptotic concentration indicates that the reactor was gas-tight.

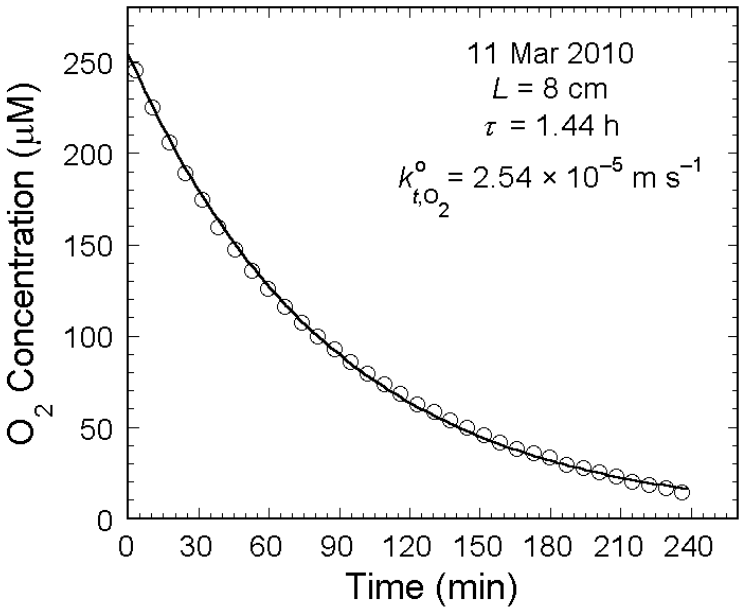
11 Mar 2010
L = 8 cm
τ = 1.44 h
k^{o}_{t,O_2} = 2.54 × 10^{-5} m s^{-1}
O$_2$ Concentration (μM)
Time (min)
0
50
100
150
200
250
0
30
60
90
120
150
180
210
240

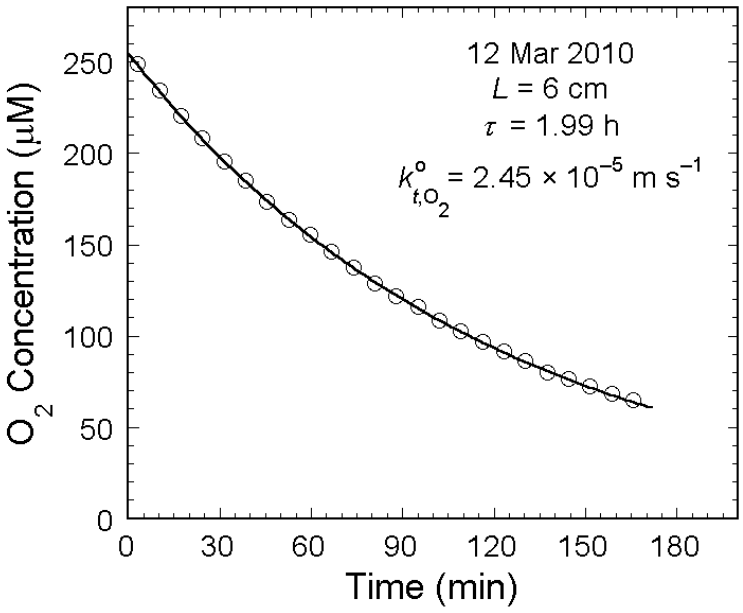
12 Mar 2010
L = 6 cm
τ = 1.99 h
k^{o}_{t,O_2} = 2.45 × 10^{-5} m s^{-1}
O$_2$ Concentration (μM)
Time (min)
0
50
100
150
200
250
0
30
60
90
120
150
180

(Figure A.2)

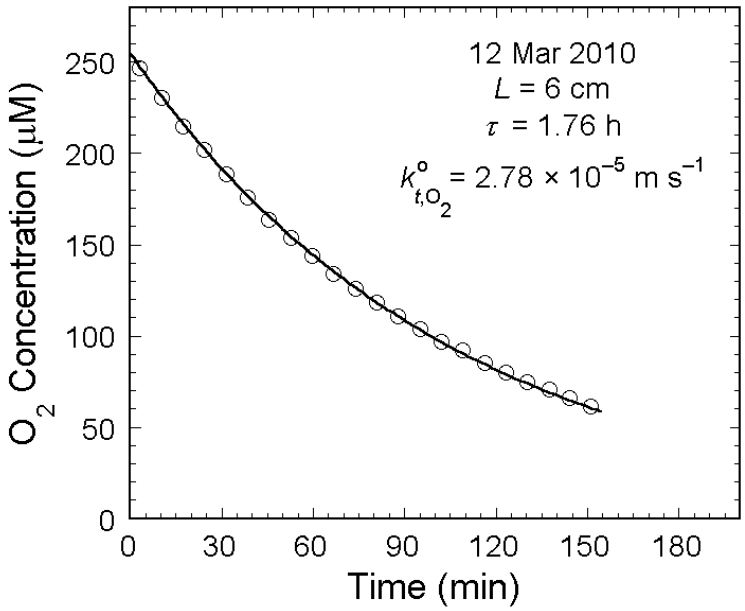
12 Mar 2010
L = 6 cm
τ = 1.76 h
k^{o}_{t,O_2} = 2.78 × 10^{-5} m s^{-1}
O$_2$ Concentration (μM)
Time (min)
0
50
100
150
200
250
0
30
60
90
120
150
180

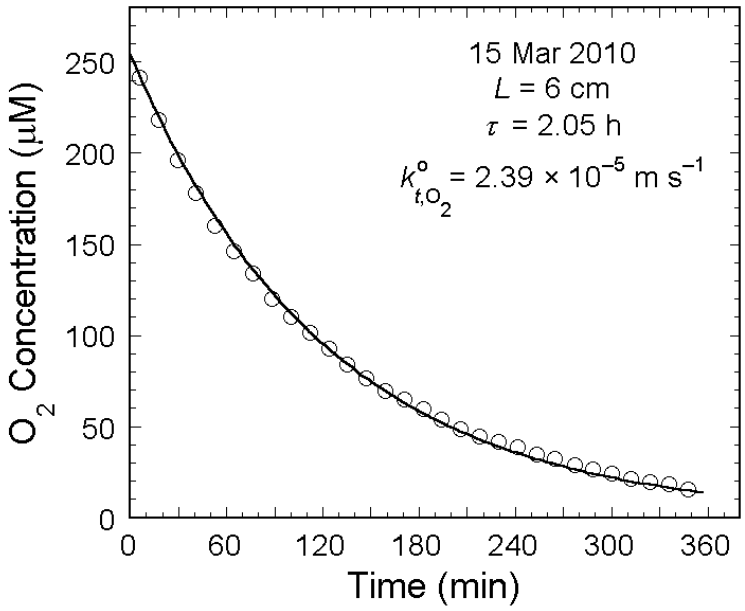
15 Mar 2010
L = 6 cm
τ = 2.05 h
k^{o}_{t,O_2} = 2.39 × 10^{-5} m s^{-1}
O$_2$ Concentration (μM)
Time (min)
0
50
100
150
200
250
0
60
120
180
240
300
360

(Figure A.2)

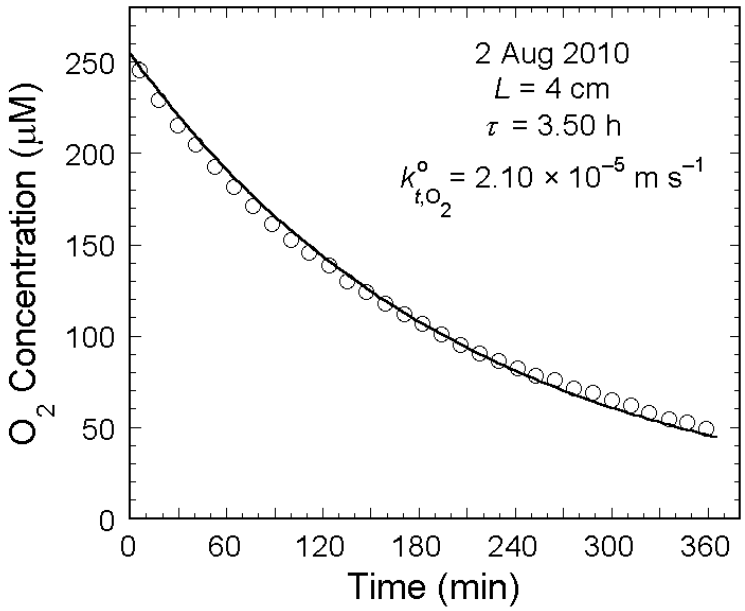

Figure A.2. O_2 depletion experiments for PDMS tubing.

Open symbols are subsets of the measured O_2 concentrations. Solid lines are the fits of Eq. (2.20). Best-fit values of τ and k^{o}_{t,O_2} are shown. The tubing length used in each experiment is shown on the individual figures.

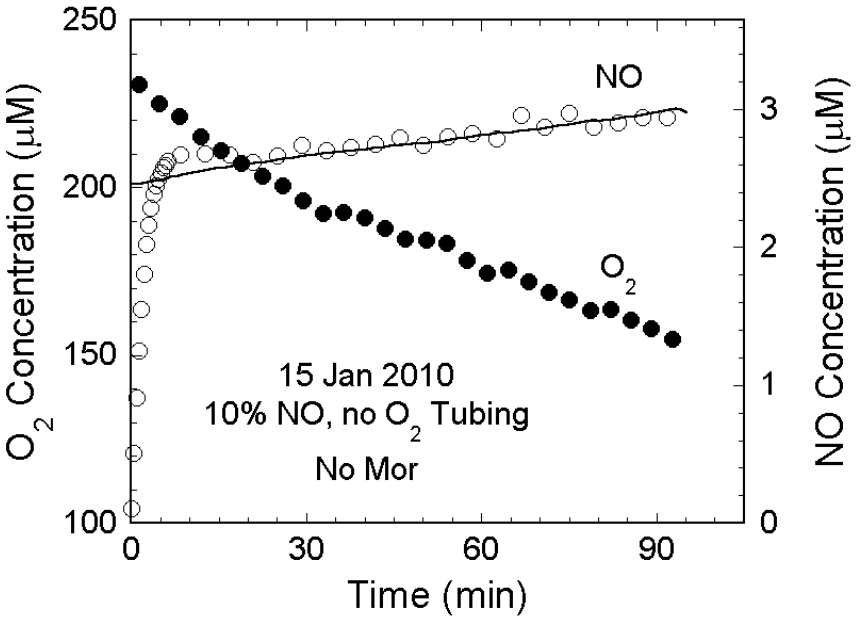
250
200
150
100
0
30
60
90
Time (min)
O2 Concentration (μM)
NO Concentration (μM)
3
2
1
0
NO
O2
15 Jan 2010
10% NO, no O2 Tubing
No Mor

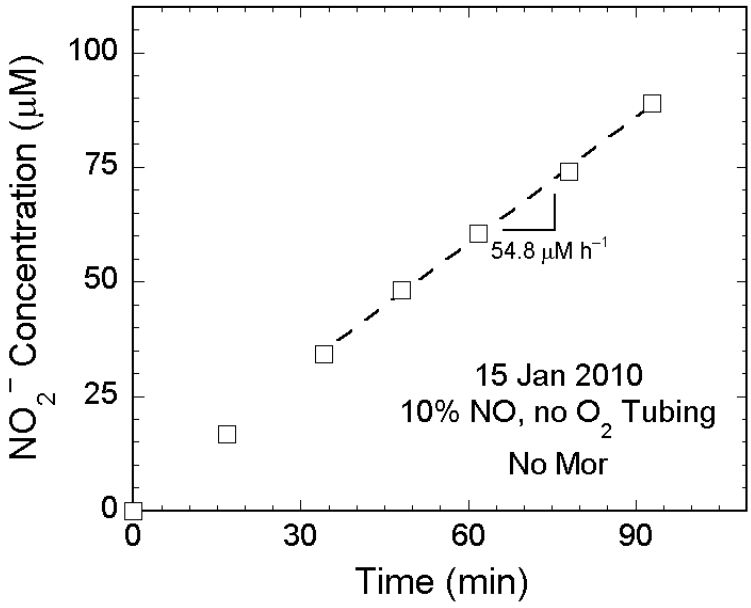
100
75
50
25
0
0
30
60
90
Time (min)
NO2− Concentration (μM)
54.8 μM h−1
15 Jan 2010
10% NO, no O2 Tubing
No Mor

(Figure A.3)

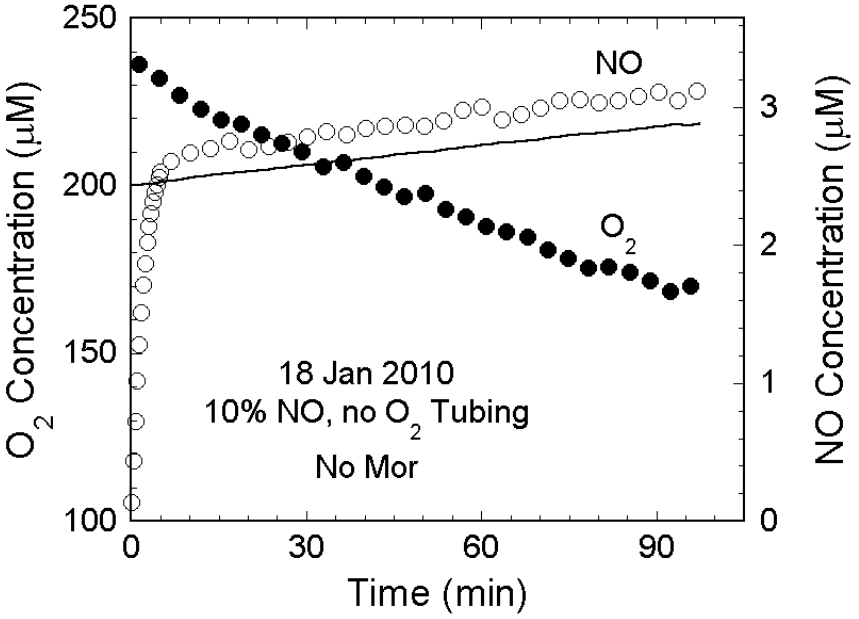
250
200
150
100
0
30
60
90
Time (min)
O2 Concentration (μM)
NO Concentration (μM)
3
2
1
0
NO
O2
18 Jan 2010
10% NO, no O2 Tubing
No Mor

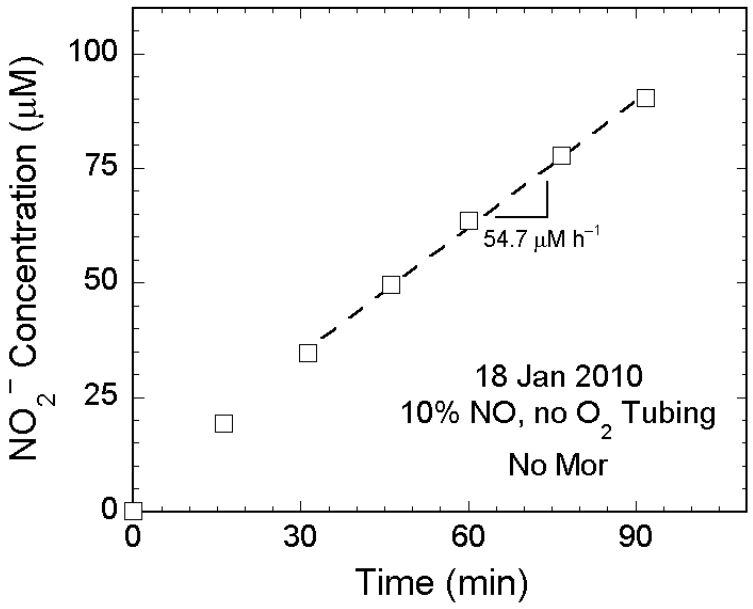
100
75
50
25
0
0
30
60
90
Time (min)
NO2− Concentration (μM)
54.7 μM h−1
18 Jan 2010
10% NO, no O2 Tubing
No Mor

(Figure A.3)

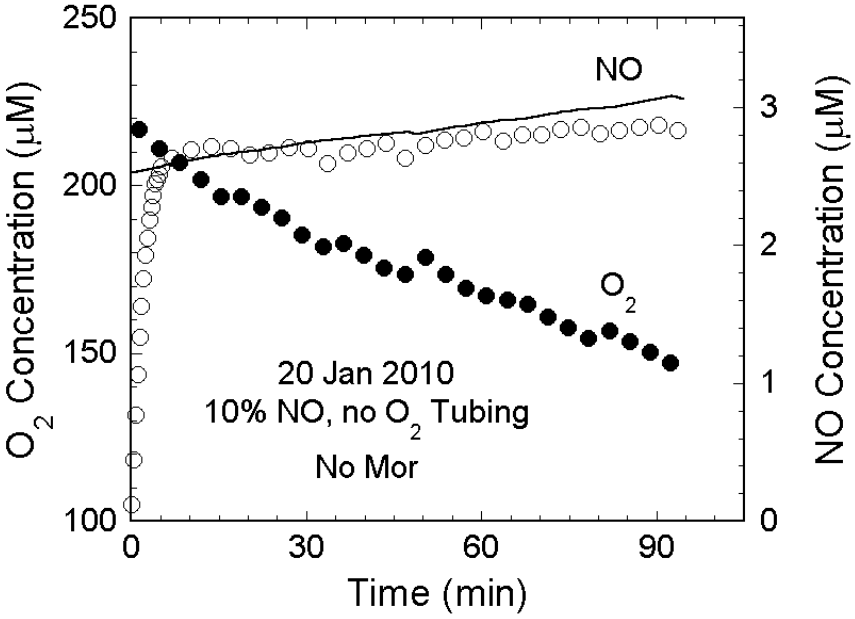
250
200
150
100
0
30
60
90
Time (min)
O2 Concentration (μM)
NO Concentration (μM)
3
2
1
0
NO
O2
20 Jan 2010
10% NO, no O2 Tubing
No Mor

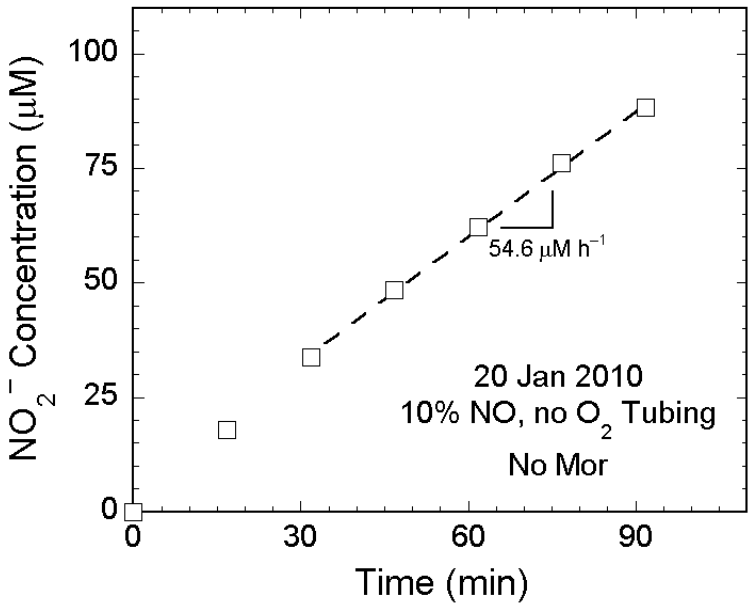
100
75
50
25
0
0
30
60
90
Time (min)
NO2− Concentration (μM)
54.6 μM h−1
20 Jan 2010
10% NO, no O2 Tubing
No Mor

(Figure A.3)

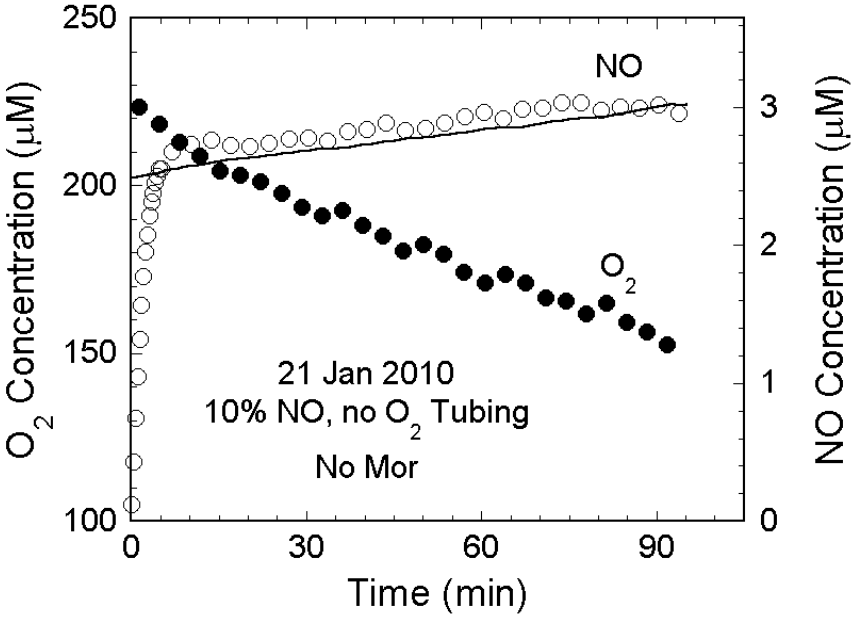
250
200
150
100
0
30
60
90
Time (min)
O2 Concentration (μM)
NO Concentration (μM)
3
2
1
0
NO
O2
21 Jan 2010
10% NO, no O2 Tubing
No Mor

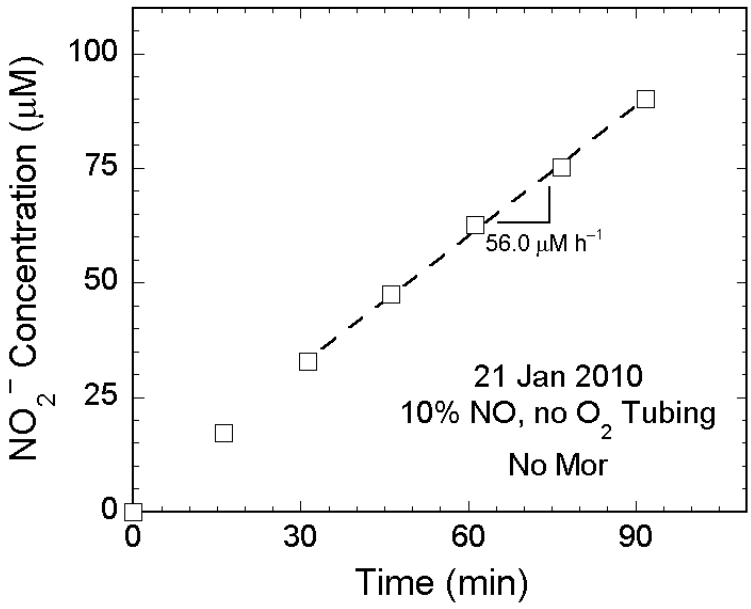
100
75
50
25
0
0
30
60
90
Time (min)
NO2− Concentration (μM)
56.0 μM h−1
21 Jan 2010
10% NO, no O2 Tubing
No Mor

(Figure A.3)

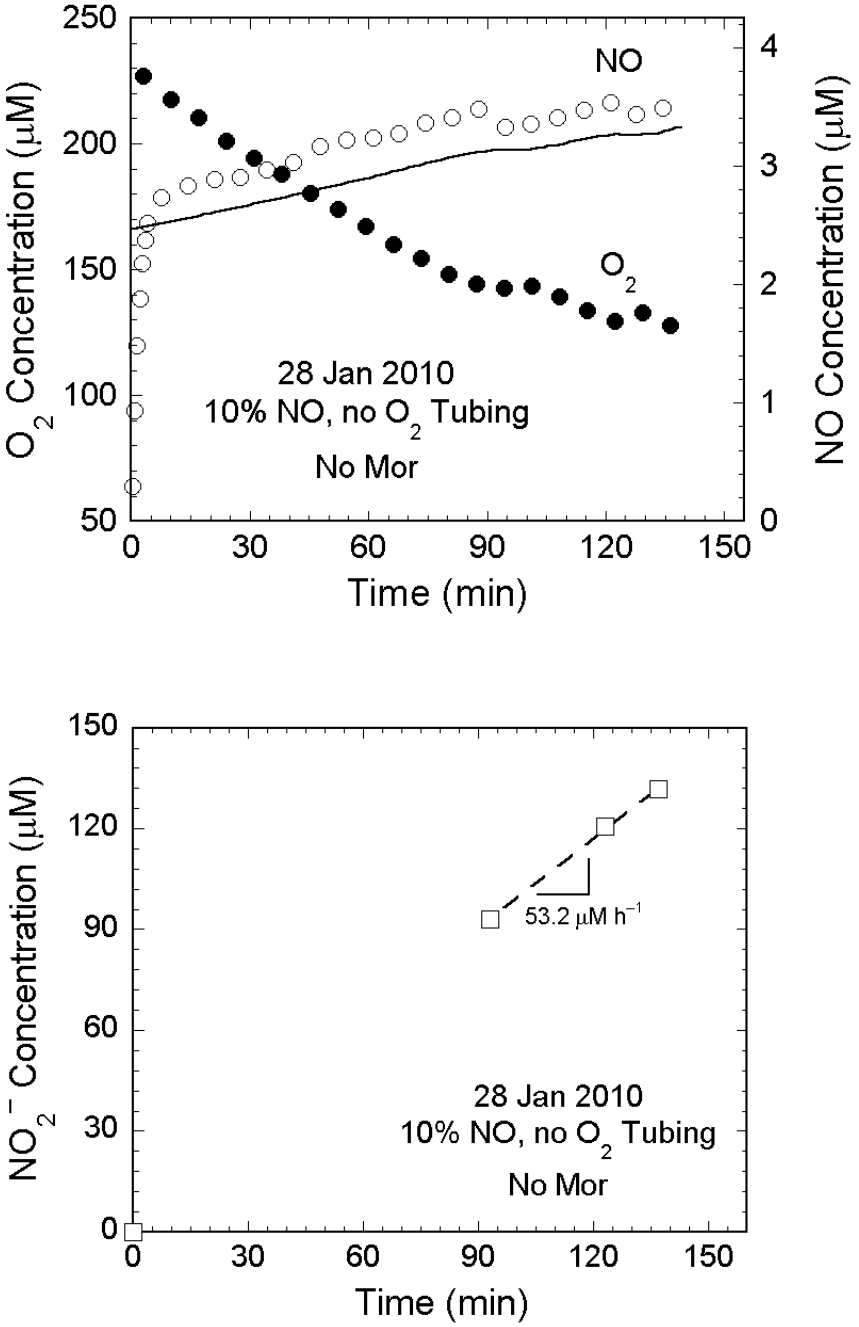
NO
O_2
28 Jan 2010
10% NO, no O_2 Tubing
No Mor
O_2 Concentration (μM)
NO Concentration (μM)
Time (min)
53.2 μM h^{-1}
NO_2^- Concentration (μM)

(Figure A.3)

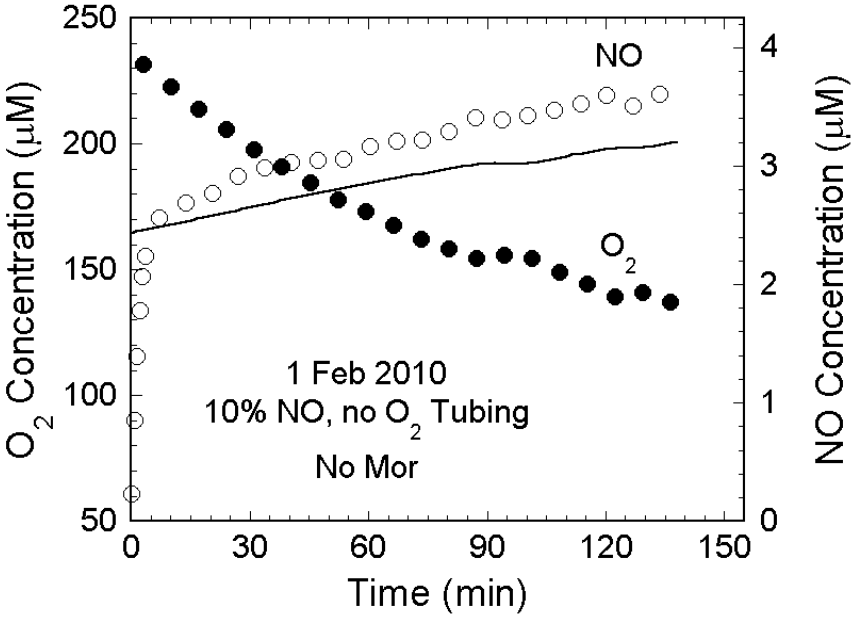
NO
O_2
1 Feb 2010
10% NO, no O_2 Tubing
No Mor
O_2 Concentration (μM)
NO Concentration (μM)
Time (min)
250
200
150
100
50
4
3
2
1
0
0
30
60
90
120
150

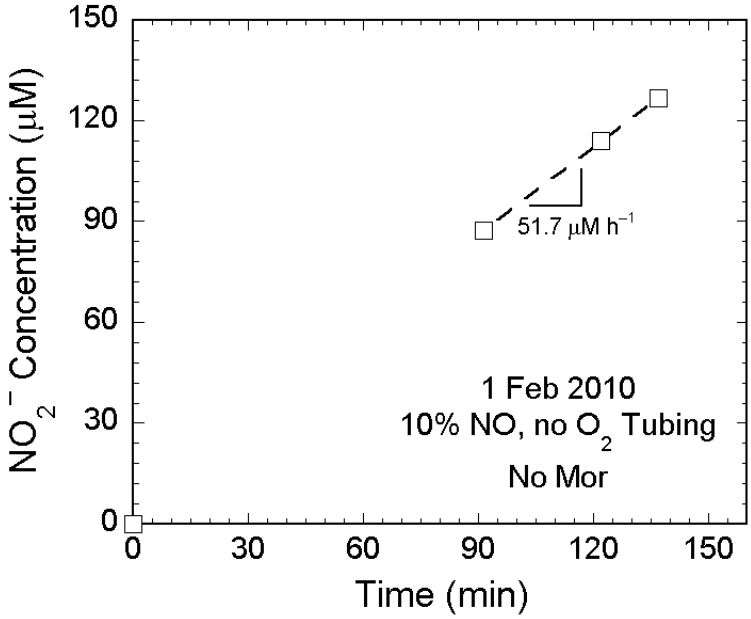
51.7 μM h^{-1}
1 Feb 2010
10% NO, no O_2 Tubing
No Mor
NO_2^- Concentration (μM)
Time (min)
150
120
90
60
30
0
0
30
60
90
120
150

(Figure A.3)

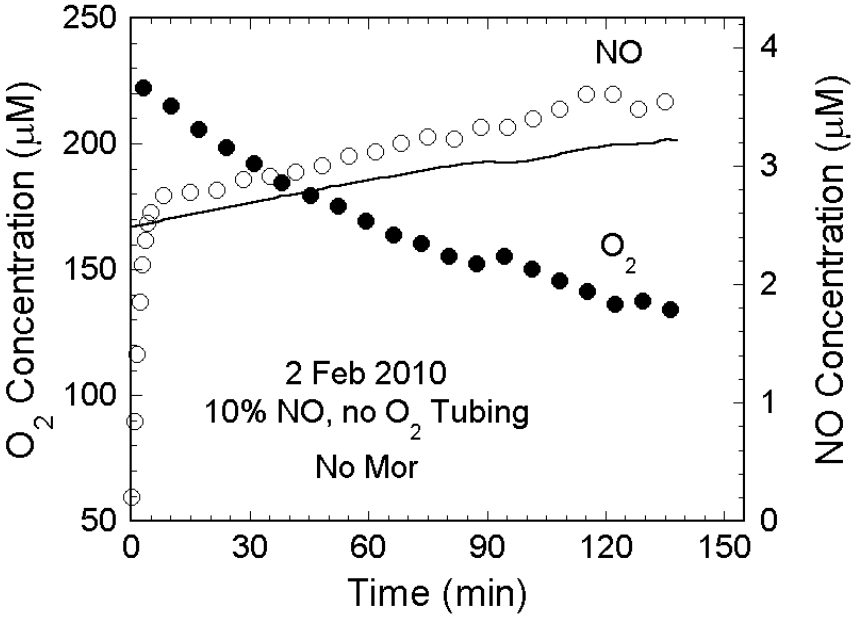
NO
O_2
2 Feb 2010
10% NO, no O_2 Tubing
No Mor
O_2 Concentration (μM)
NO Concentration (μM)
Time (min)
250
200
150
100
50
4
3
2
1
0
0
30
60
90
120
150

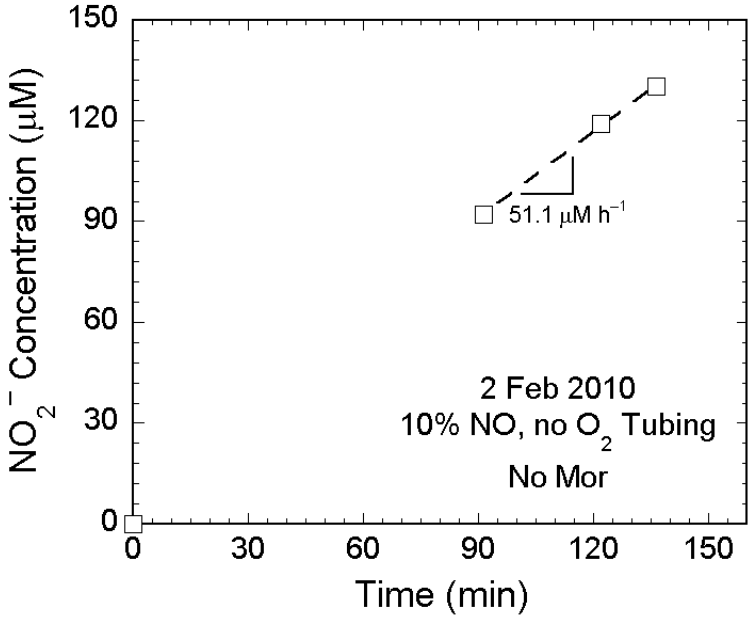
51.1 μM h^{-1}
2 Feb 2010
10% NO, no O_2 Tubing
No Mor
NO_2^- Concentration (μM)
Time (min)
150
120
90
60
30
0
0
30
60
90
120
150

(Figure A.3)

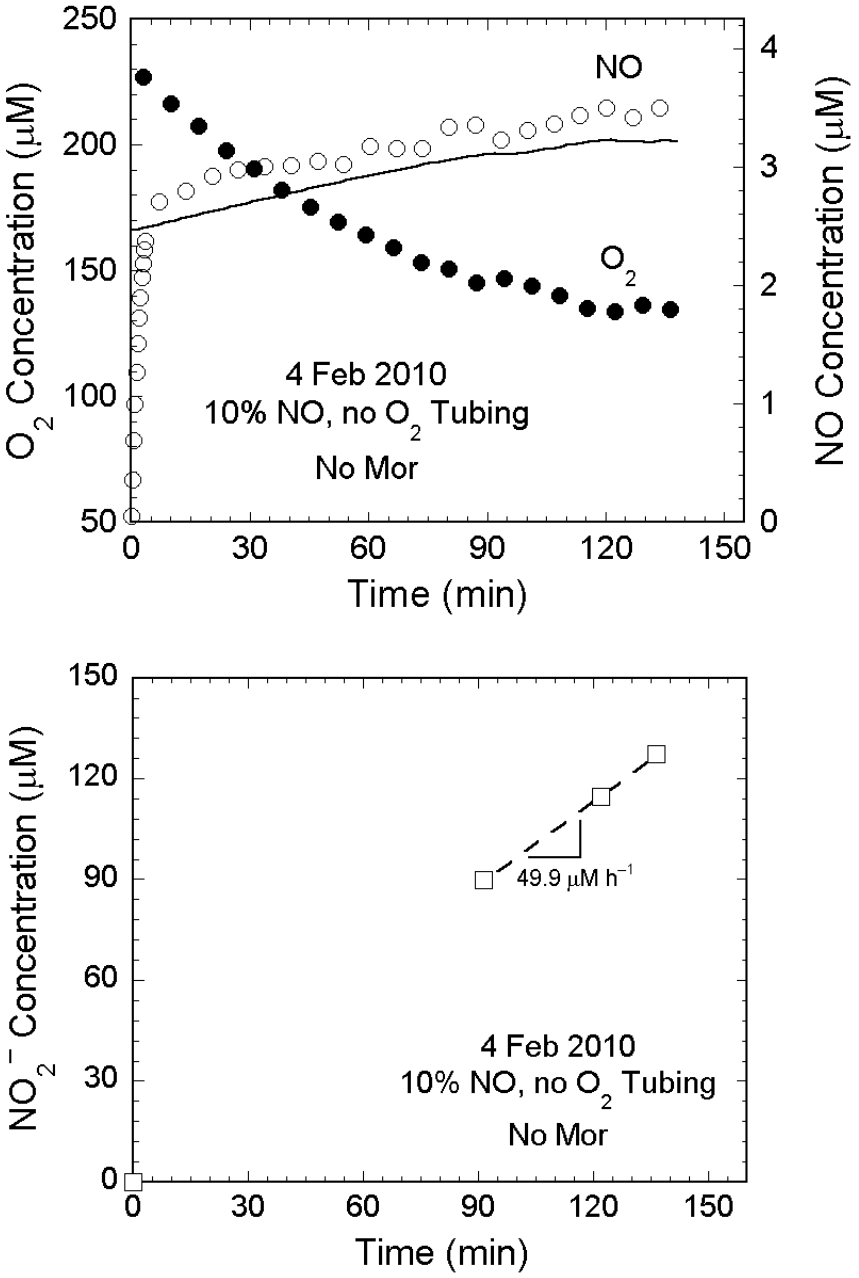

Figure A.3. Measured NO, O_2 and NO_2^- concentrations in delivery of 10% NO in the absence of Mor without O_2 replenishment.

The data for NO and O_2 are subsets of the data collected. The initial O_2 concentrations varied depending on the duration of the initial N_2 purge. The solid lines are the pseudo-steady state predictions of Eq. (2.25). The dashed lines are linear fits for $t \geq 30$ min.

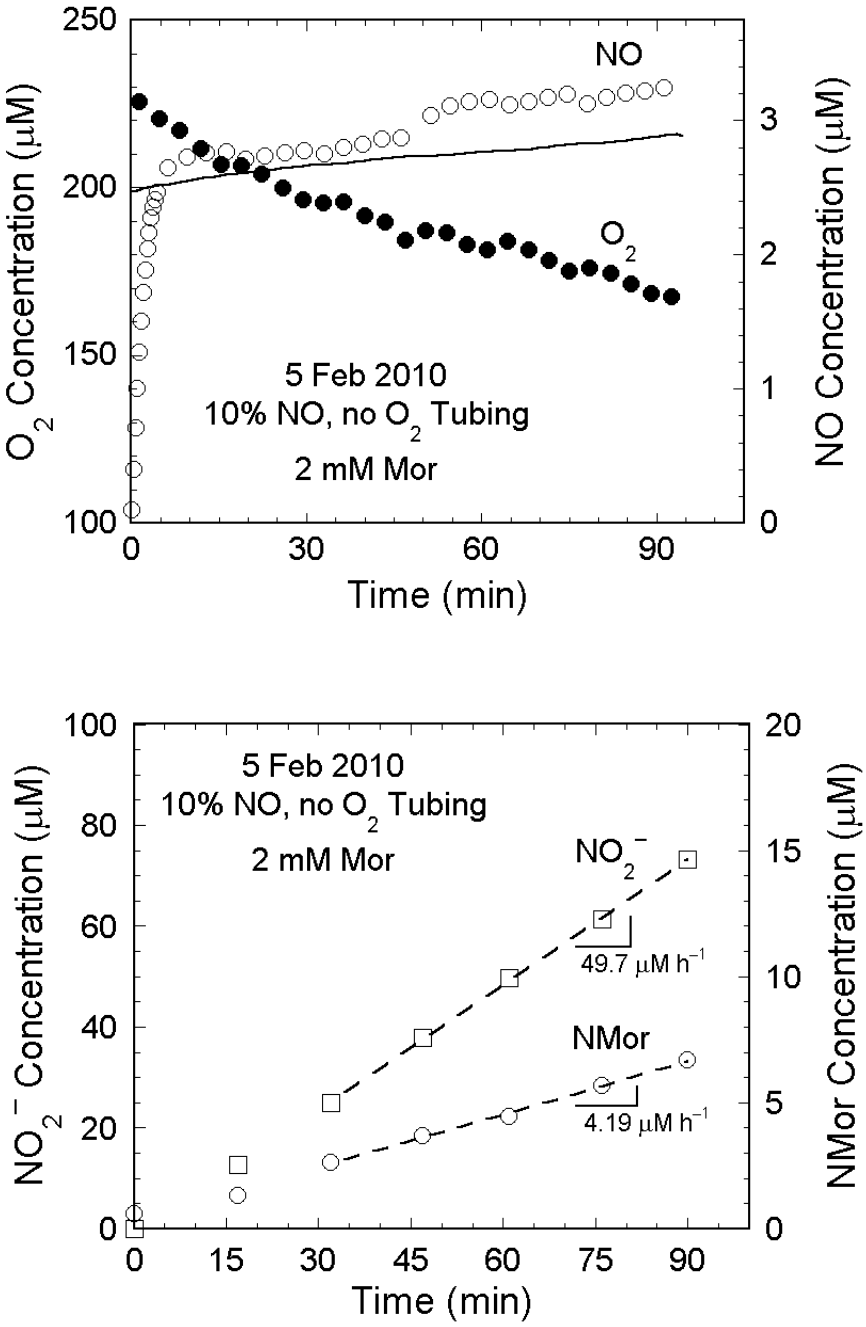
NO
O2
5 Feb 2010
10% NO, no O2 Tubing
2 mM Mor
O2 Concentration (μM)
NO Concentration (μM)
Time (min)
NO2− Concentration (μM)
NMor Concentration (μM)
NO2−
49.7 μM h−1
NMor
4.19 μM h−1

(Figure A.4)

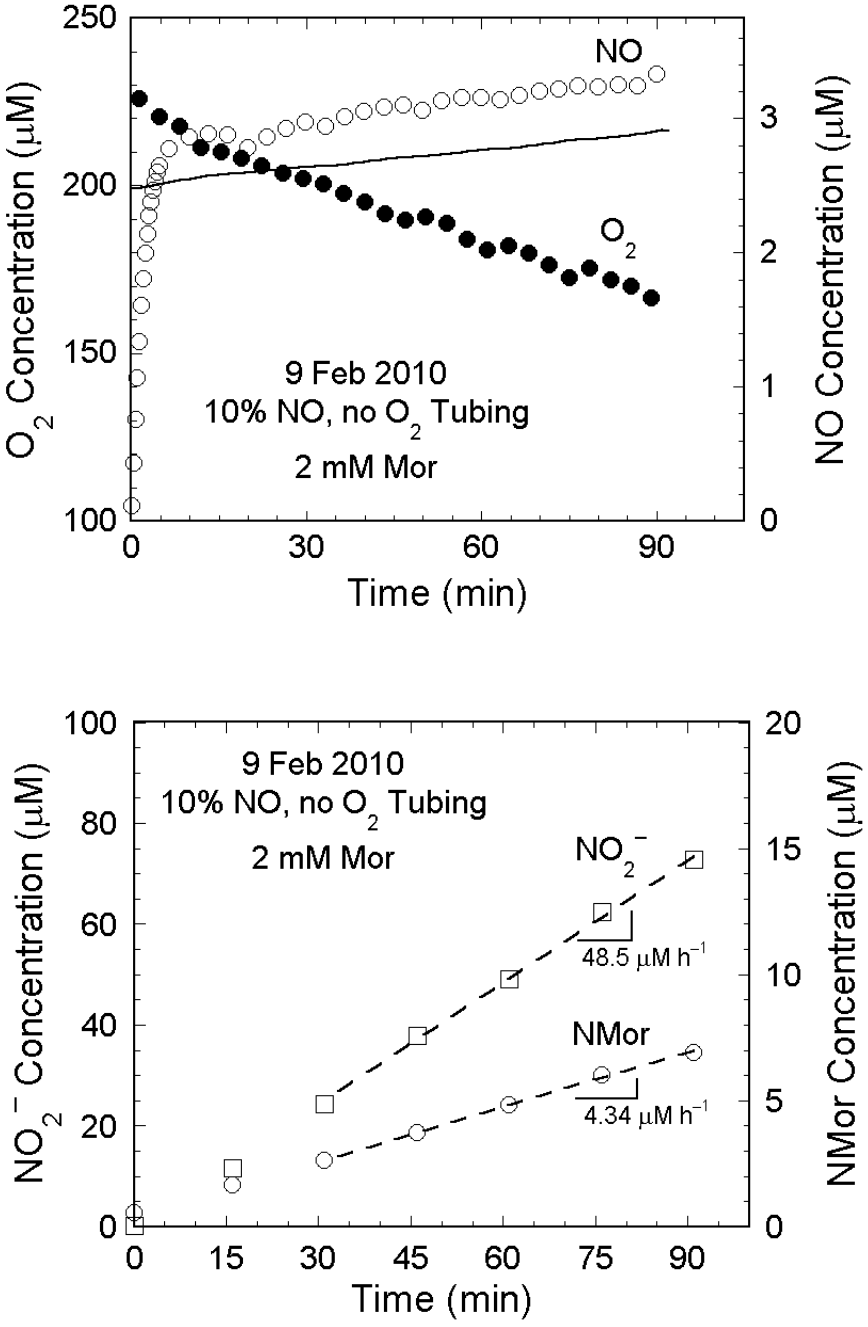
250
200
150
100
O_2 Concentration (μM)
NO
O_2
9 Feb 2010
10% NO, no O_2 Tubing
2 mM Mor
0
30
60
90
Time (min)
3
2
1
0
NO Concentration (μM)
100
80
60
40
20
0
NO_2^- Concentration (μM)
9 Feb 2010
10% NO, no O_2 Tubing
2 mM Mor
NO_2^-
48.5 μM h^{-1}
NMor
4.34 μM h^{-1}
0
15
30
45
60
75
90
Time (min)
20
15
10
5
0
NMor Concentration (μM)

(Figure A.4)

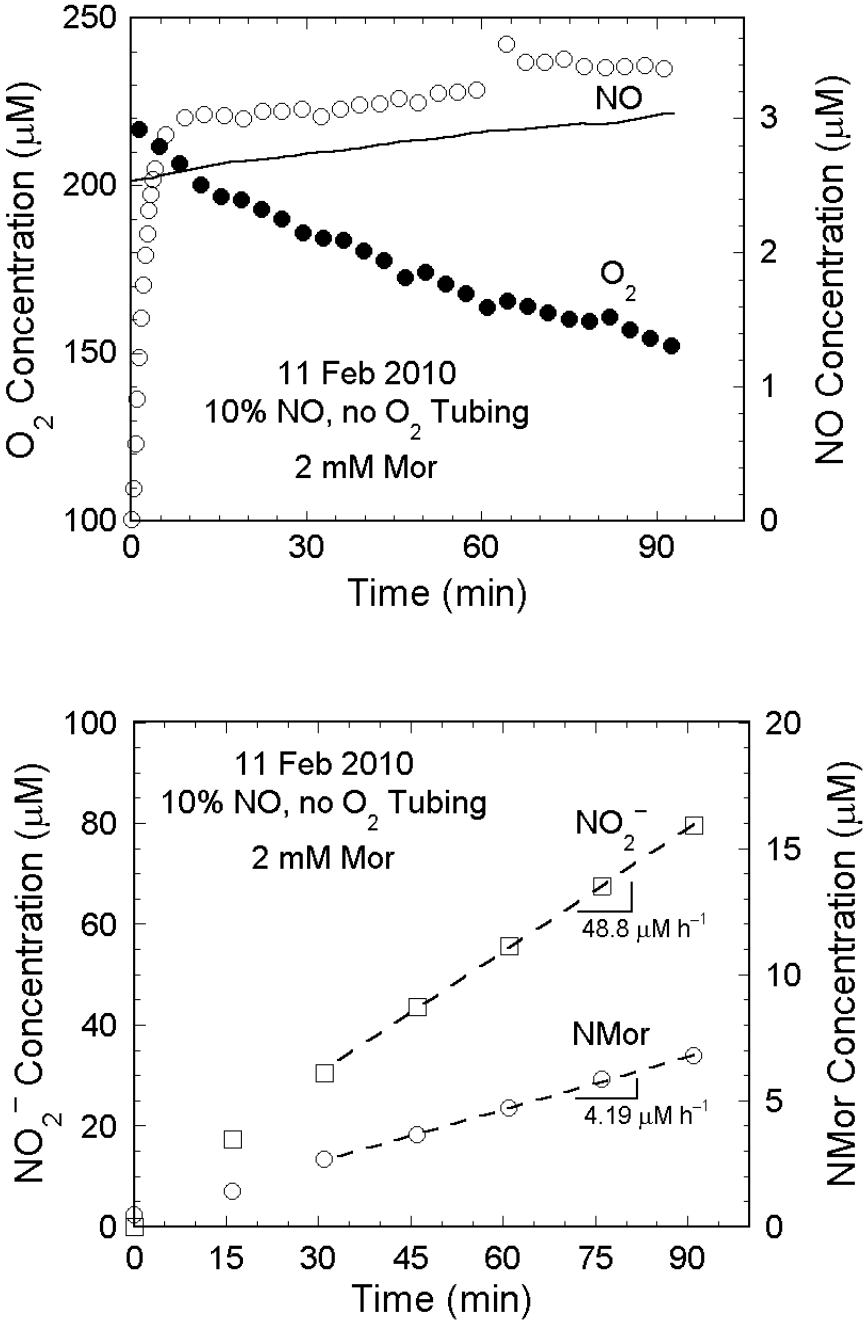
250
200
150
100
O_2 Concentration (μM)
NO
O_2
11 Feb 2010
10% NO, no O_2 Tubing
2 mM Mor
0
30
60
90
Time (min)
3
2
1
0
NO Concentration (μM)
100
80
60
40
20
0
NO_2^- Concentration (μM)
11 Feb 2010
10% NO, no O_2 Tubing
2 mM Mor
NO_2^-
48.8 μM h^{-1}
NMor
4.19 μM h^{-1}
0
15
30
45
60
75
90
Time (min)
20
15
10
5
0
NMor Concentration (μM)

(Figure A.4)

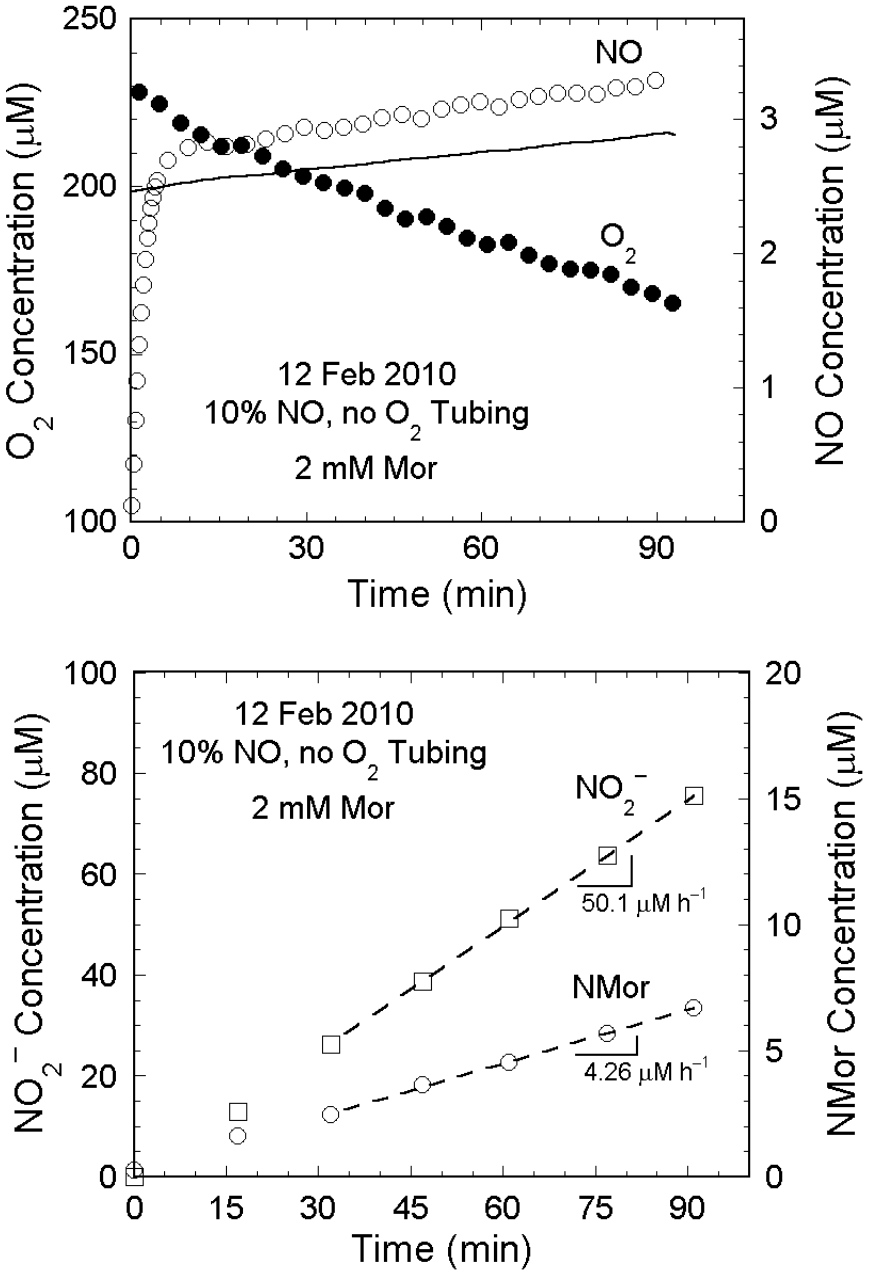

Figure A.4. Measured NO, O_2, NO_2^-, and NMor concentrations in delivery of 10% NO in the presence of 2 mM Mor without O_2 replenishment.

The data for NO and O_2 are subsets of the data collected. The initial O_2 concentrations varied depending on the duration of the initial N_2 purge. The solid lines are the pseudo-steady state predictions of Eq. (2.25). The dashed lines are linear fits for $t \geq 30$ min.

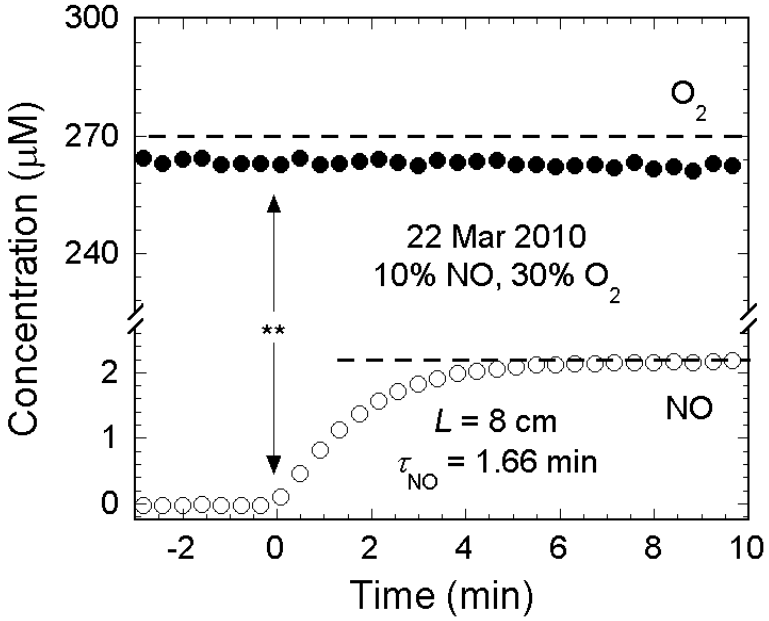
300
270
240
2
1
0
Concentration (μM)
O2
22 Mar 2010
10% NO, 30% O2
**
NO
L = 8 cm
τNO = 1.66 min
-2
0
2
4
6
8
10
Time (min)

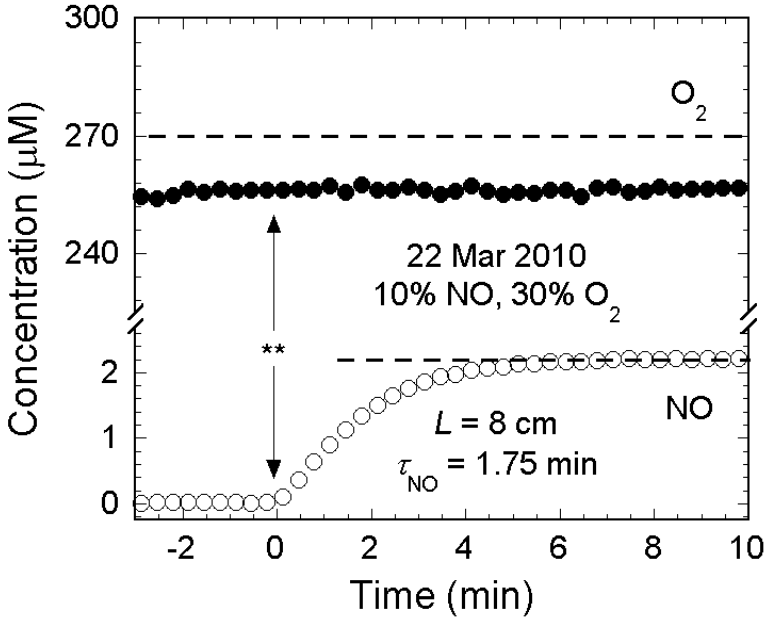
300
270
240
2
1
0
Concentration (μM)
O2
22 Mar 2010
10% NO, 30% O2
**
NO
L = 8 cm
τNO = 1.75 min
-2
0
2
4
6
8
10
Time (min)

(Figure A.5)

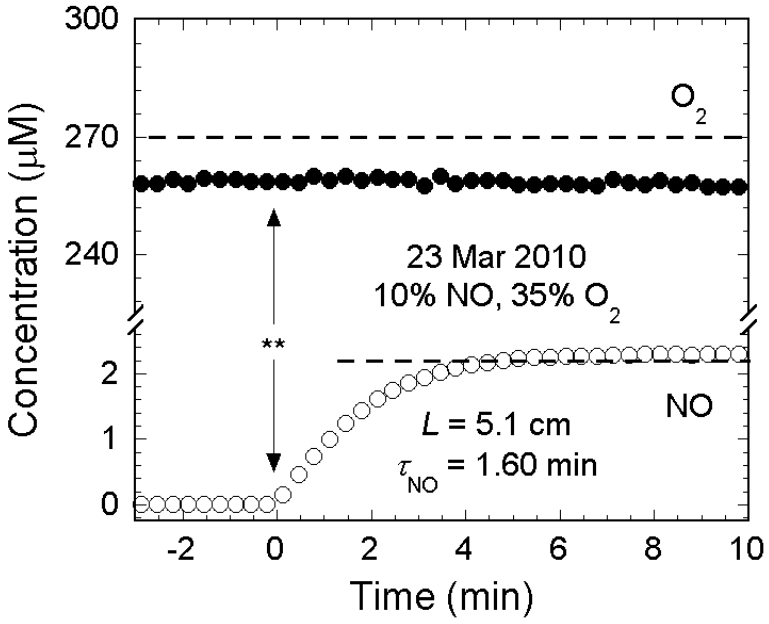
300
270
240
2
1
0
Concentration (μM)
O2
23 Mar 2010
10% NO, 35% O2
**
NO
L = 5.1 cm
τNO = 1.60 min
-2
0
2
4
6
8
10
Time (min)

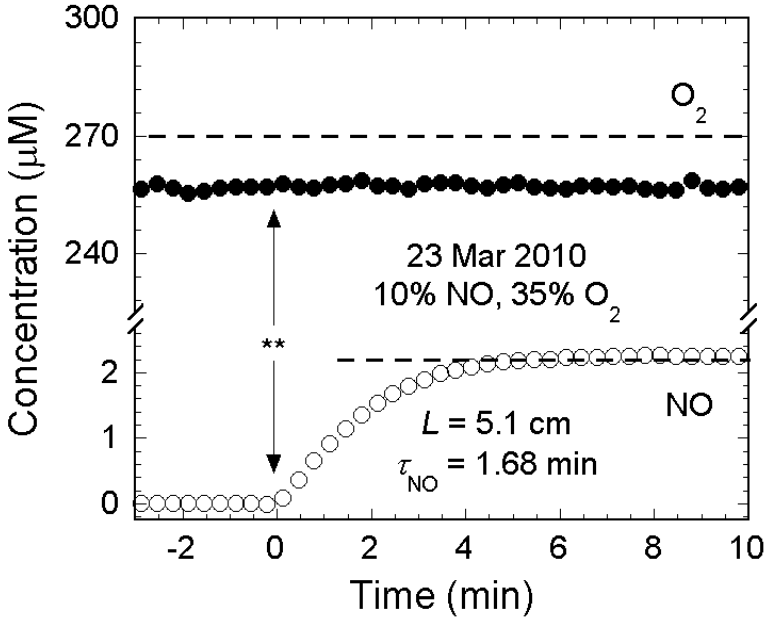
300
270
240
2
1
0
Concentration (μM)
O2
23 Mar 2010
10% NO, 35% O2
**
NO
L = 5.1 cm
τNO = 1.68 min
-2
0
2
4
6
8
10
Time (min)

(Figure A.5)

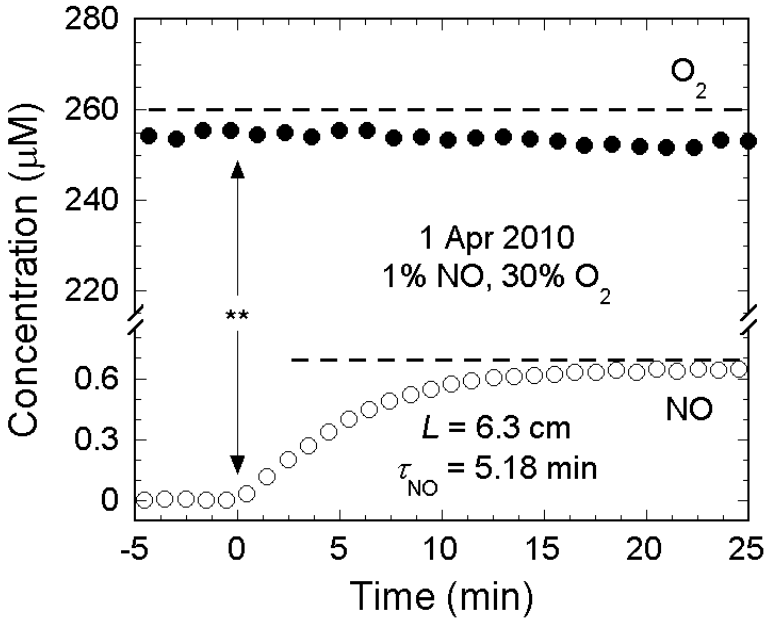
280
260
240
220
0.6
0.3
0
Concentration (μM)
O2
1 Apr 2010
1% NO, 30% O2
**
NO
L = 6.3 cm
τNO = 5.18 min
-5
0
5
10
15
20
25
Time (min)

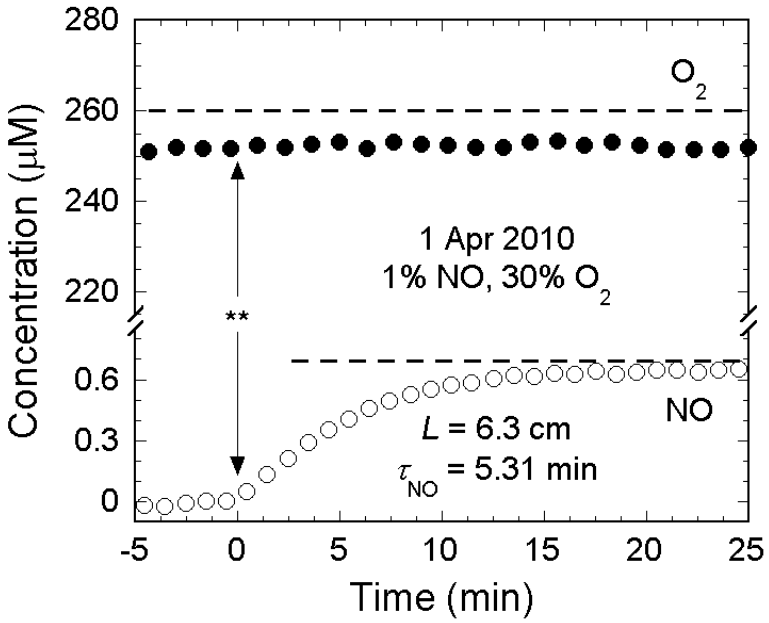
280
260
240
220
0.6
0.3
0
Concentration (μM)
O2
1 Apr 2010
1% NO, 30% O2
**
NO
L = 6.3 cm
τNO = 5.31 min
-5
0
5
10
15
20
25
Time (min)

(Figure A.5)

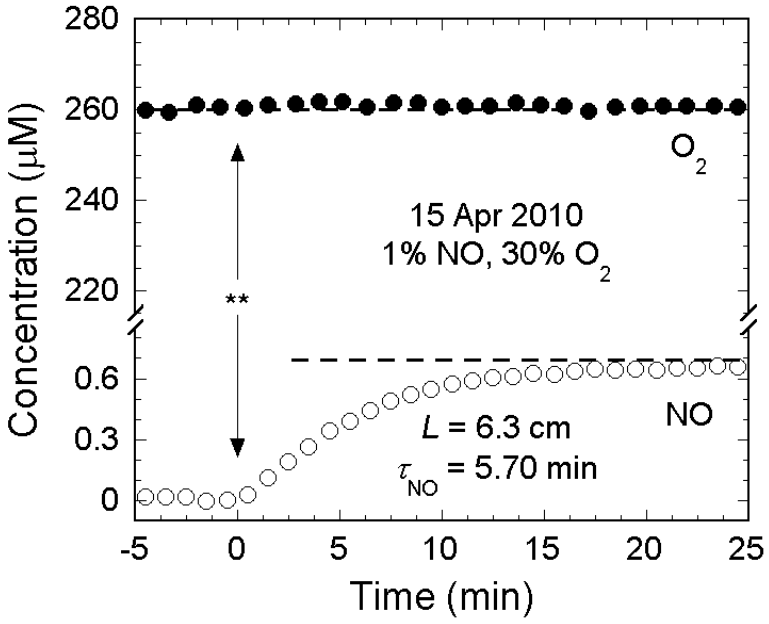
280
260
240
220
0.6
0.3
0
Concentration (μM)
O2
15 Apr 2010
1% NO, 30% O2
**
NO
L = 6.3 cm
τNO = 5.70 min
-5
0
5
10
15
20
25
Time (min)

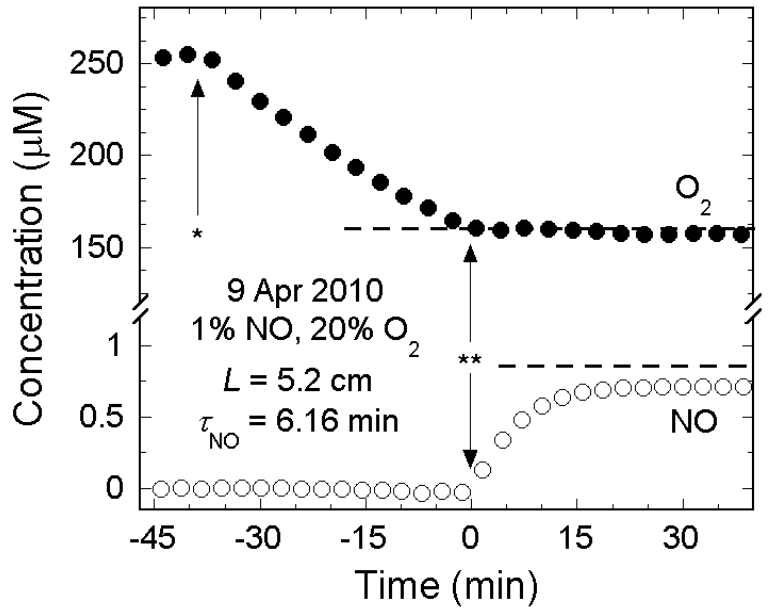
250
200
150
1
0.5
0
Concentration (μM)
O2
*
9 Apr 2010
1% NO, 20% O2
L = 5.2 cm
τNO = 6.16 min
**
NO
-45
-30
-15
0
15
30
Time (min)

(Figure A.5)

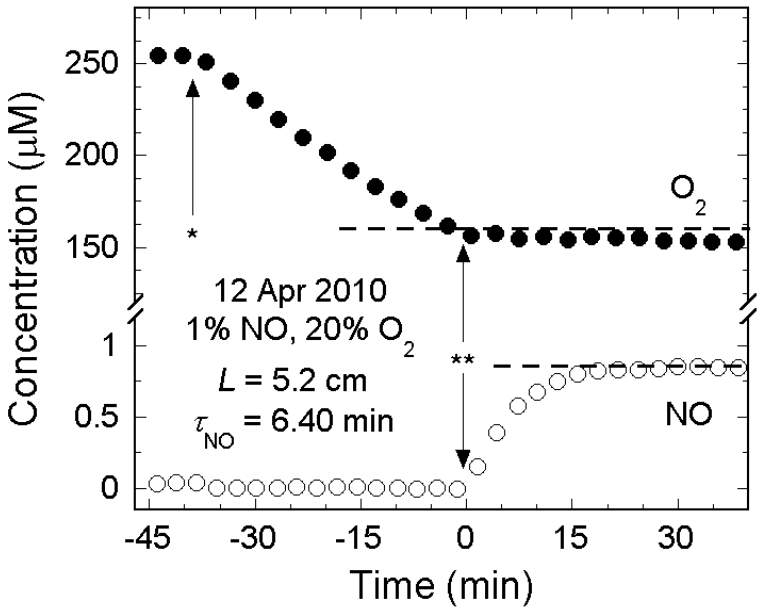
Concentration (μM)
250
200
150
1
0.5
0
O2
NO
*
**
12 Apr 2010
1% NO, 20% O2
L = 5.2 cm
τNO = 6.40 min
-45
-30
-15
0
15
30
Time (min)

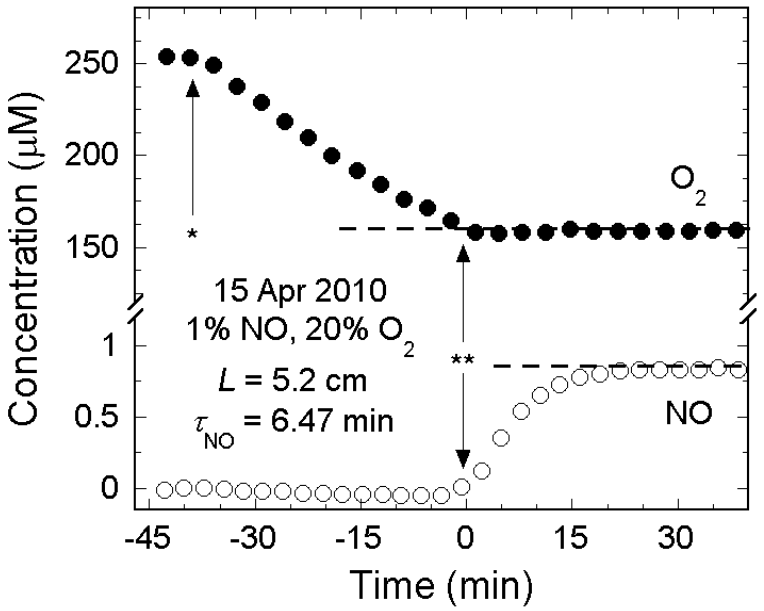
Concentration (μM)
250
200
150
1
0.5
0
O2
NO
*
**
15 Apr 2010
1% NO, 20% O2
L = 5.2 cm
τNO = 6.47 min
-45
-30
-15
0
15
30
Time (min)

(Figure A.5)

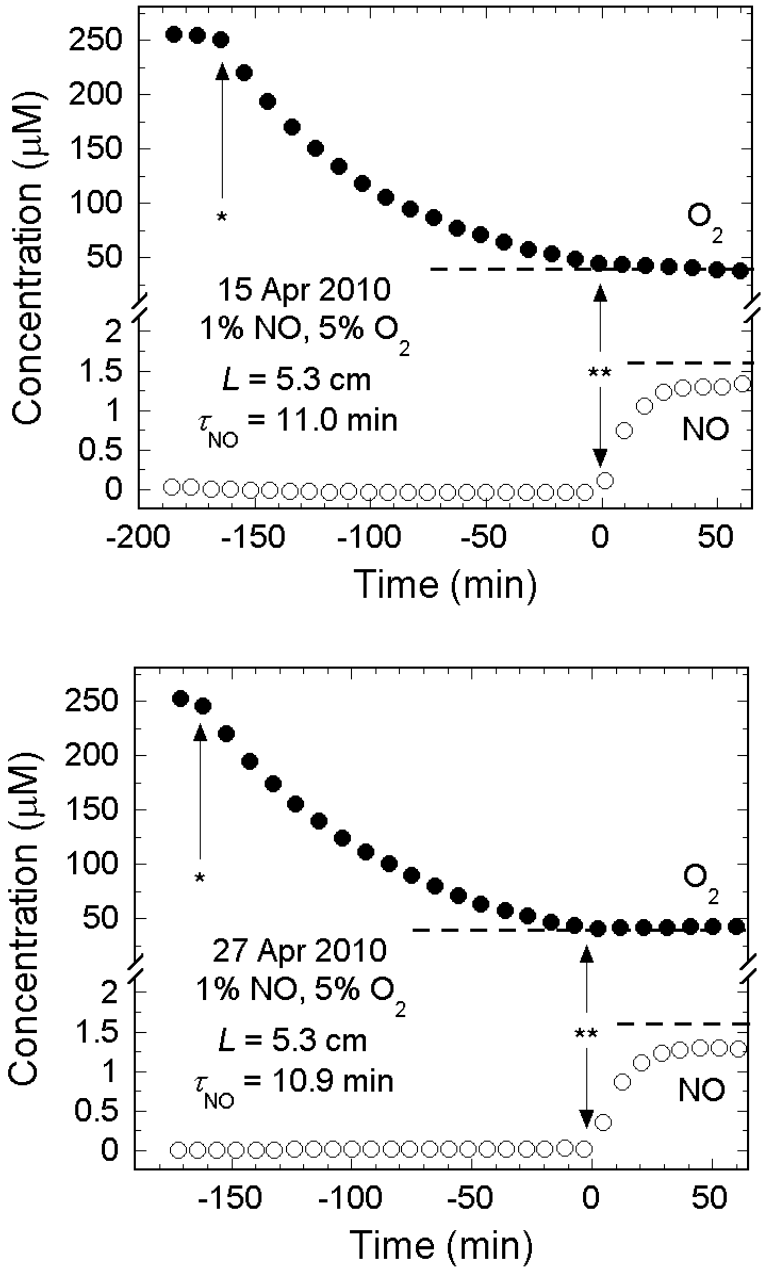

Figure A.5. Measured NO and O_2 concentrations in simultaneous delivery of NO and O_2 in the absence of Mor.

The gas mixtures and tubing lengths used are indicated on each figure along with the fitted NO rise times (τ_{NO}). The dashed lines are the predictions of Table 2.3. The markings "*" and "**" are as in Figure 2.6.

Appendix B

Experimental Data from Nitrogen Dioxide Delivery System

The complete dataset for the experiments reported in Chapter 3 is provided in this appendix. The date on which each experiment was performed is indicated in each figure.

- O_2 depletion-repletion experiments, Figure B.1, Section 3.3.1
- H_2O evaporation experiments, Figure B.2, Section 3.3.1
- NO_2 delivery experiments (Q = 365 sccm except where specified):
    - Direct gas-liquid contacting, no ABTS, Section 3.3.2
        - 1% NO_2: 250 sccm, Figure B.3; 365 sccm, Figure B.4
        - 0.1% NO_2, Figure B.5
        - 0.01% NO_2, Figure B.6
        - 0.001% NO_2, Figure B.7
    - Direct gas-liquid contacting, with ABTS, Section 3.3.2
        - 0.01% NO_2, Figure B.8
        - 0.001% NO_2, Figure B.9
    - Apparatus of Wang and Deen (2003), no ABTS

      Figure B.10, Section 3.3.2
    - Apparatus of Wang and Deen (2003), with ABTS

      Figure B.11, Section 3.3.2
    - Apparatus of Skinn et al. (2011), no ABTS

      Figure B.12, Section 3.3.2

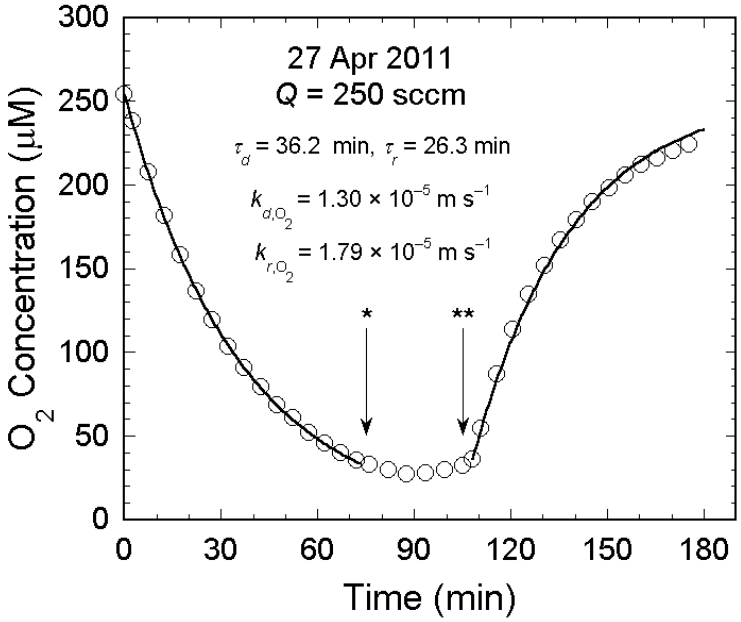
27 Apr 2011
Q = 250 sccm
τd = 36.2 min, τr = 26.3 min
kd,O2 = 1.30 × 10−5 m s−1
kr,O2 = 1.79 × 10−5 m s−1
*
**
O2 Concentration (μM)
Time (min)
0
50
100
150
200
250
300
0
30
60
90
120
150
180

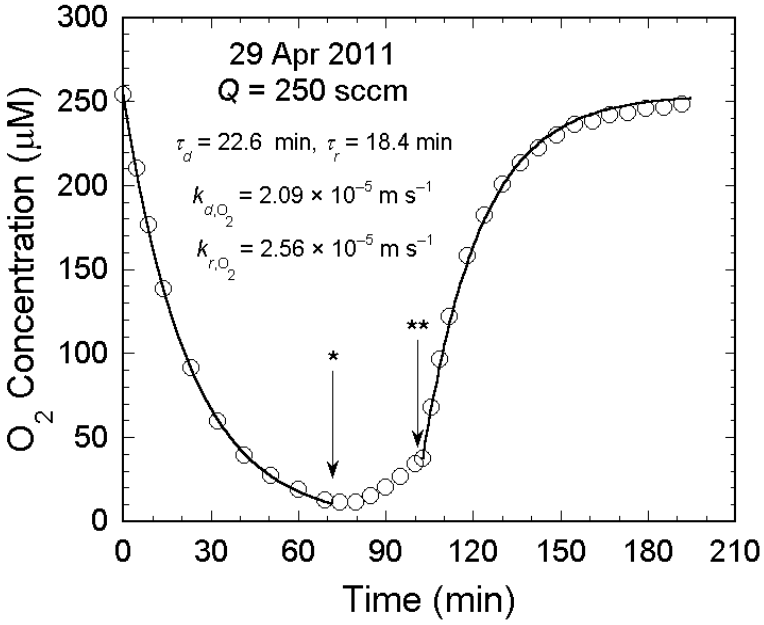
29 Apr 2011
Q = 250 sccm
τd = 22.6 min, τr = 18.4 min
kd,O2 = 2.09 × 10−5 m s−1
kr,O2 = 2.56 × 10−5 m s−1
*
**
O2 Concentration (μM)
Time (min)
0
50
100
150
200
250
300
0
30
60
90
120
150
180
210

(Figure B.1)

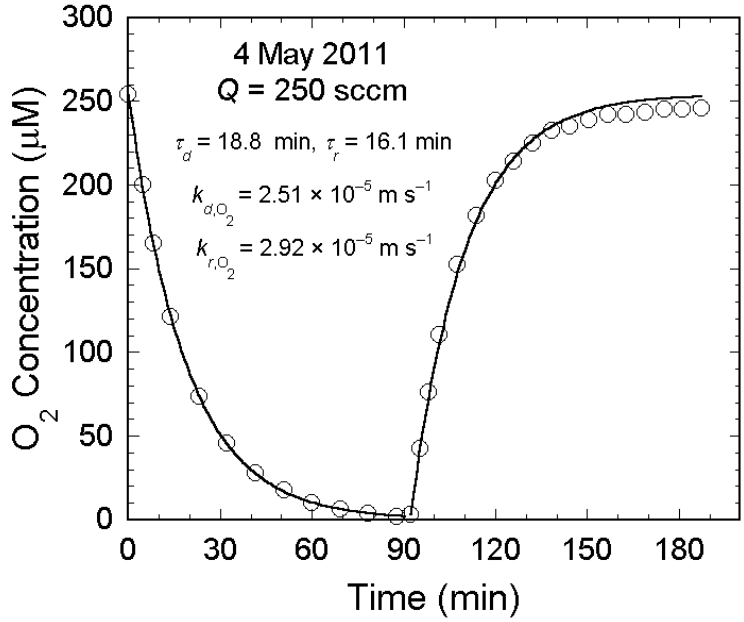
4 May 2011
Q = 250 sccm
τ_d = 18.8 min, τ_r = 16.1 min
k_{d,O_2} = 2.51 × 10^{-5} m s^{-1}
k_{r,O_2} = 2.92 × 10^{-5} m s^{-1}
O$_2$ Concentration (μM)
Time (min)
0
50
100
150
200
250
300
0
30
60
90
120
150
180

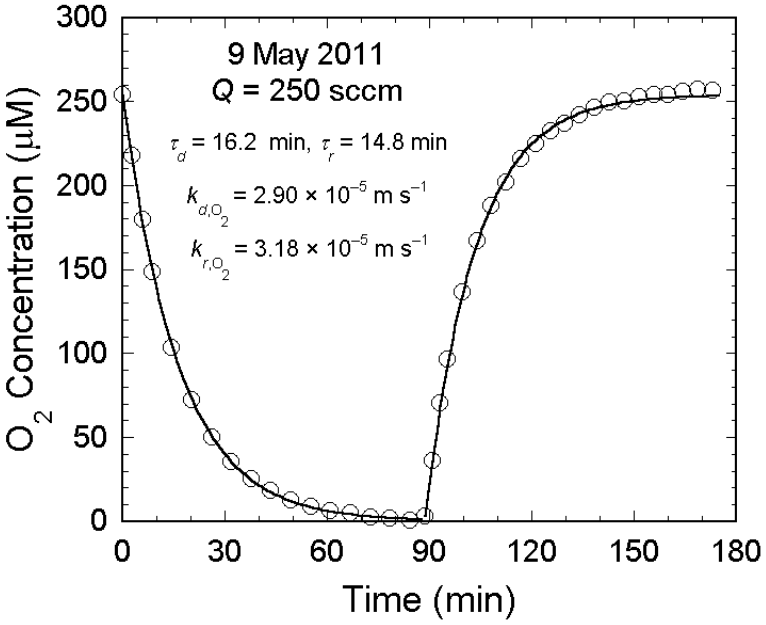
9 May 2011
Q = 250 sccm
τ_d = 16.2 min, τ_r = 14.8 min
k_{d,O_2} = 2.90 × 10^{-5} m s^{-1}
k_{r,O_2} = 3.18 × 10^{-5} m s^{-1}
O$_2$ Concentration (μM)
Time (min)
0
50
100
150
200
250
300
0
30
60
90
120
150
180

(Figure B.1)

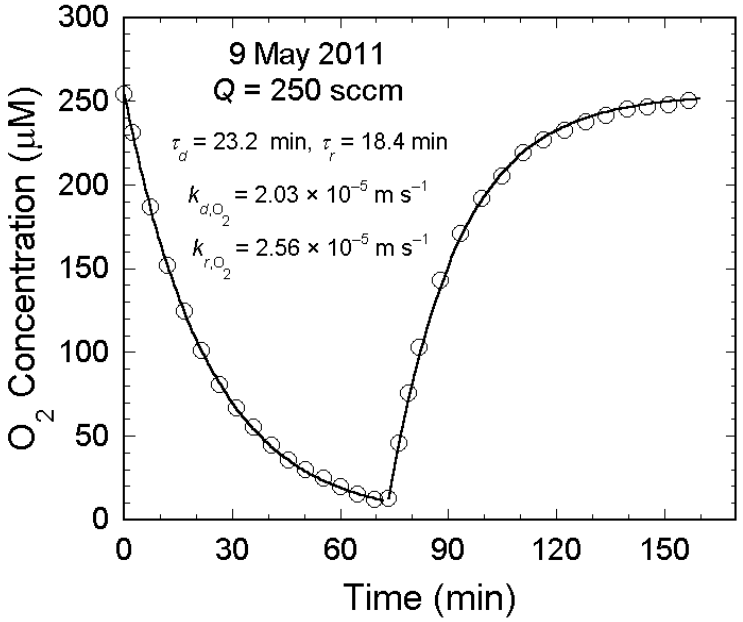
9 May 2011
Q = 250 sccm
τd = 23.2 min, τr = 18.4 min
kd,O2 = 2.03 × 10−5 m s−1
kr,O2 = 2.56 × 10−5 m s−1
O2 Concentration (μM)
Time (min)
0
50
100
150
200
250
300
0
30
60
90
120
150

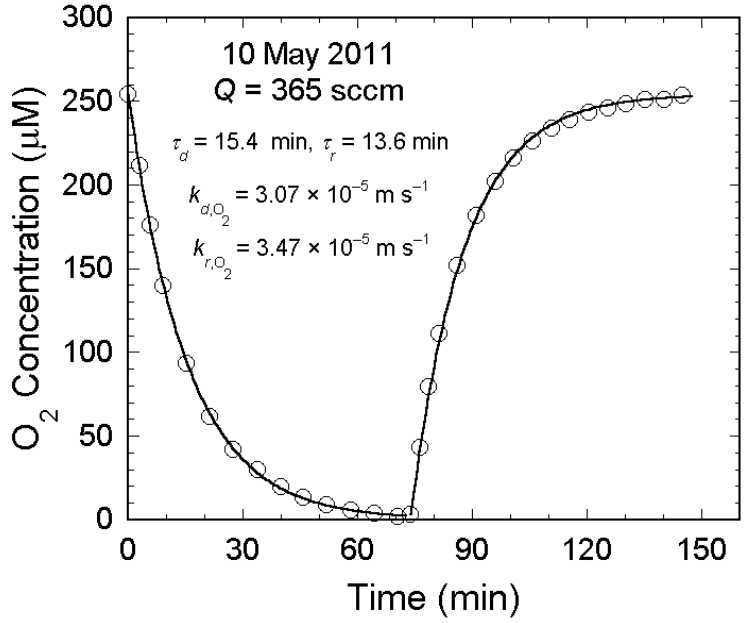
10 May 2011
Q = 365 sccm
τd = 15.4 min, τr = 13.6 min
kd,O2 = 3.07 × 10−5 m s−1
kr,O2 = 3.47 × 10−5 m s−1
O2 Concentration (μM)
Time (min)
0
50
100
150
200
250
300
0
30
60
90
120
150

(Figure B.1)

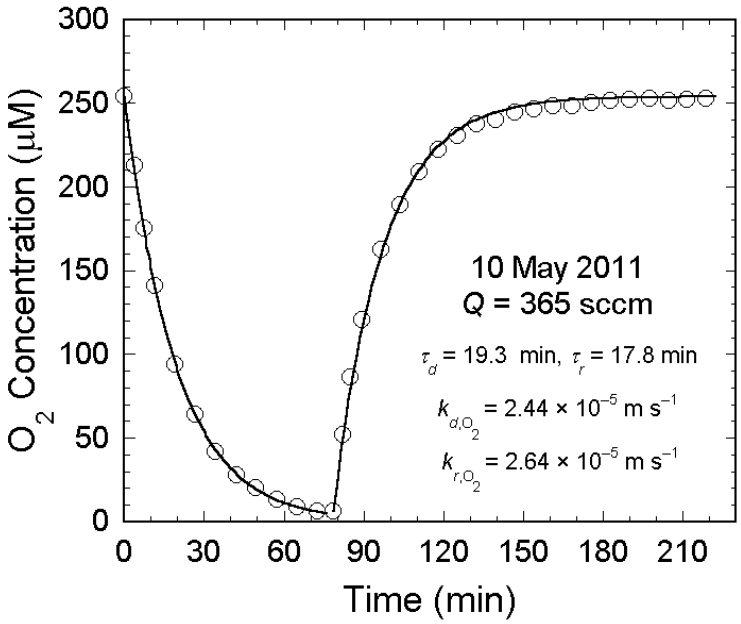

Figure B.1. O_2 depletion-repletion experiments.

The open symbols are subsets of the measured O_2 concentrations. The solid lines are the fits of Eq. (3.14). Best-fit values of τ and k_{O_2} are shown; the subscripts "*d*" and "*r*" correspond to the 'depletion' and 'repletion' phases, respectively. Data from 27 Apr and 29 Apr include a brief leak-check phase: the gas lines were disconnected and the reactor ports were capped at the times marked "*", and the gas lines were reconnected and lab air flow initiated at the times marked "**". The increase in O_2 concentration during these intervals indicates the reactor was not gas-tight in this configuration, presumably due to imperfect sealing of the O_2 probe. The leak is sufficiently slow that it is not expected to influence the measured values of τ. In all other experiments, the O_2 probe was not used and the probe mount was replaced with a closed plug. Thus, this leakage should not significantly affect any of the experimental data collected.

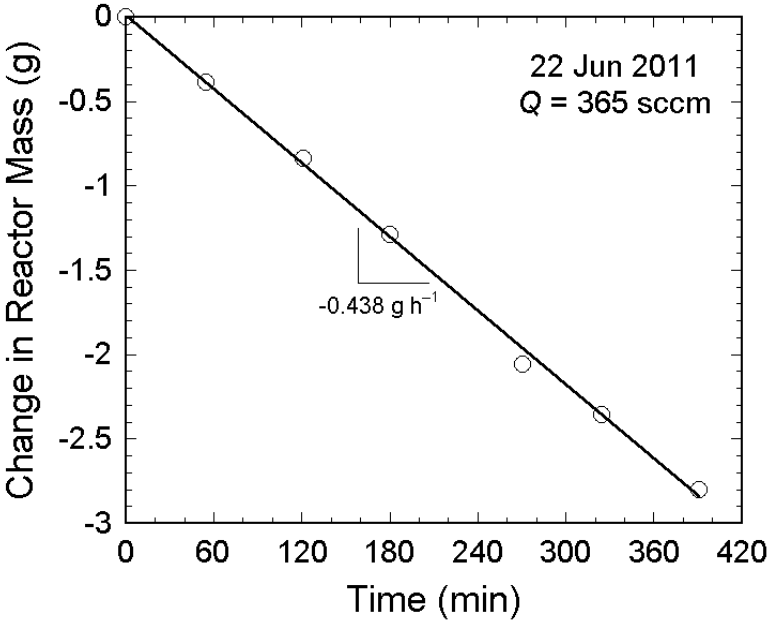
22 Jun 2011
Q = 365 sccm
-0.438 g h−1
Change in Reactor Mass (g)
Time (min)
0
-0.5
-1
-1.5
-2
-2.5
-3
0
60
120
180
240
300
360
420

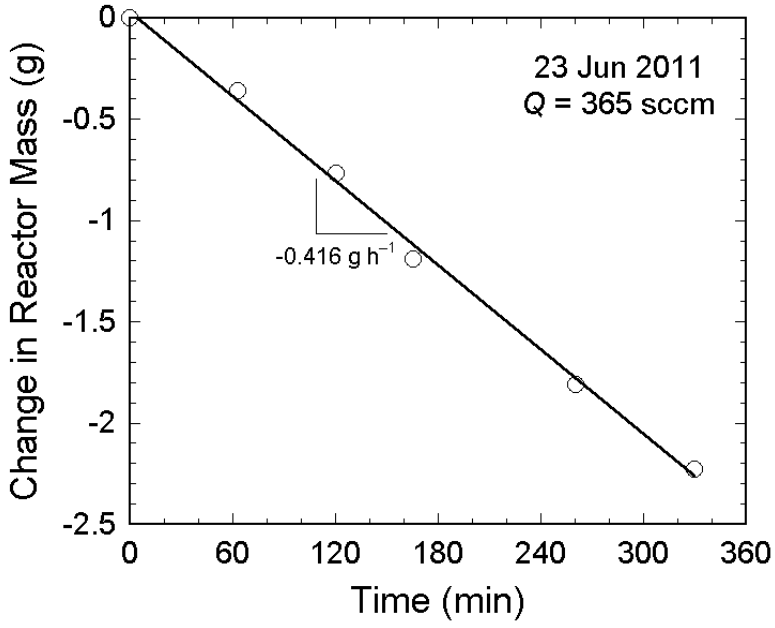
23 Jun 2011
Q = 365 sccm
-0.416 g h−1
Change in Reactor Mass (g)
Time (min)
0
-0.5
-1
-1.5
-2
-2.5
0
60
120
180
240
300
360

(Figure B.2)

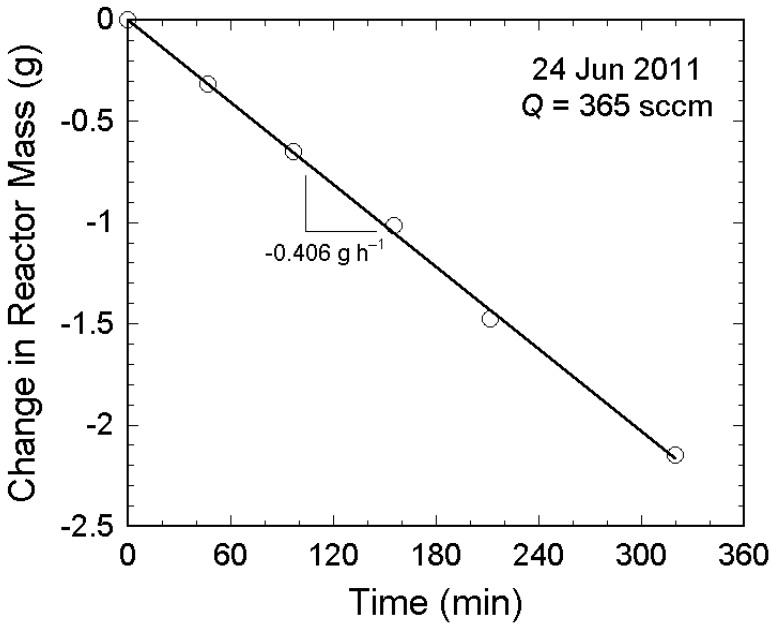

Figure B.2. H_2O evaporation during flow of N_2 through reactor headspace.

The open symbols are the differences between reactor mass at the start of the experiment and at times indicated. Error bars based on the precision of the mass balance are smaller than the symbols. The solid lines are linear best-fits of the data, with slopes as indicated. Gas flow rate was 365 sccm for all three experiments. The sampling times were corrected for the brief intervals that the reactor was disconnected from the gas flow for weighing.

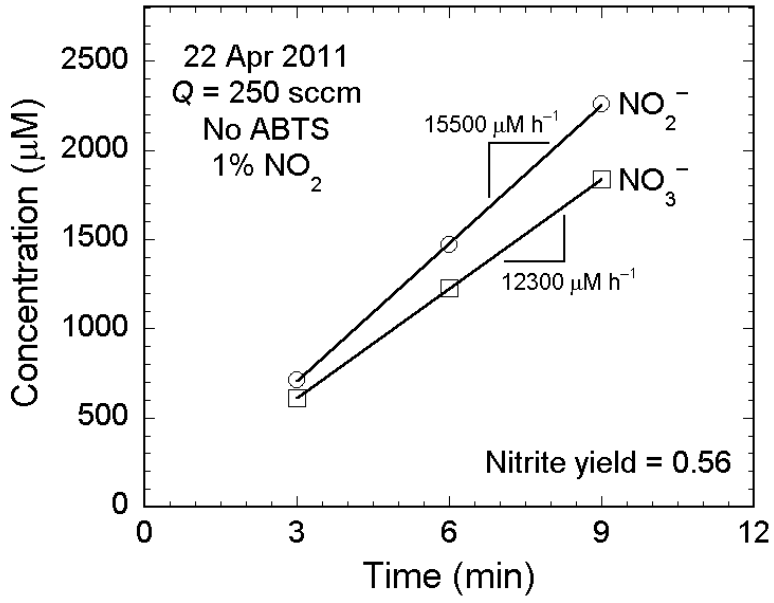
22 Apr 2011
Q = 250 sccm
No ABTS
1% NO2
15500 μM h−1
NO2−
NO3−
12300 μM h−1
Nitrite yield = 0.56
Concentration (μM)
Time (min)
0
500
1000
1500
2000
2500
0
3
6
9
12

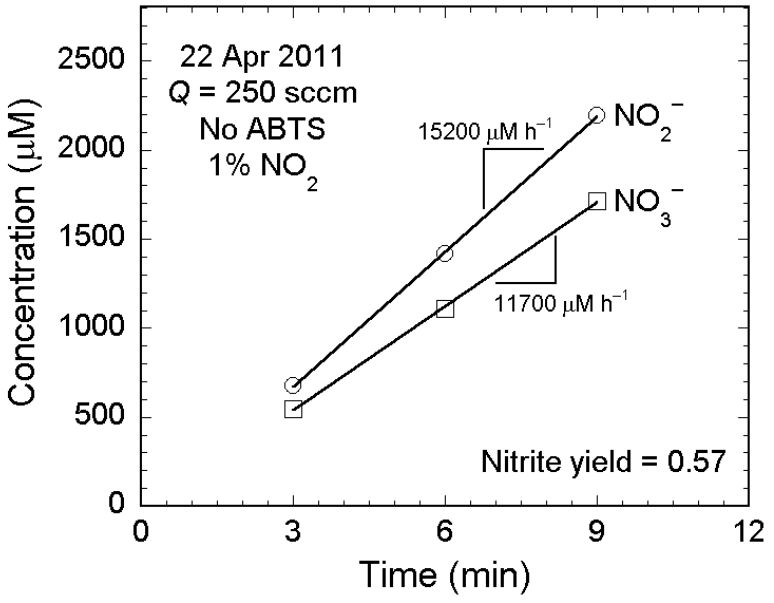
22 Apr 2011
Q = 250 sccm
No ABTS
1% NO2
15200 μM h−1
NO2−
NO3−
11700 μM h−1
Nitrite yield = 0.57
Concentration (μM)
Time (min)
0
500
1000
1500
2000
2500
0
3
6
9
12

(Figure B.3)

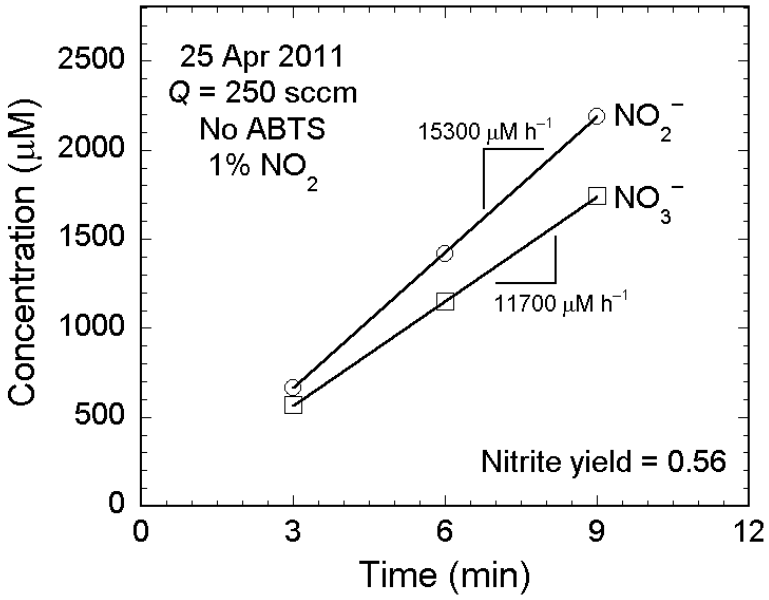
25 Apr 2011
Q = 250 sccm
No ABTS
1% NO2
15300 μM h−1
NO2−
NO3−
11700 μM h−1
Nitrite yield = 0.56
Concentration (μM)
Time (min)
0
500
1000
1500
2000
2500
0
3
6
9
12

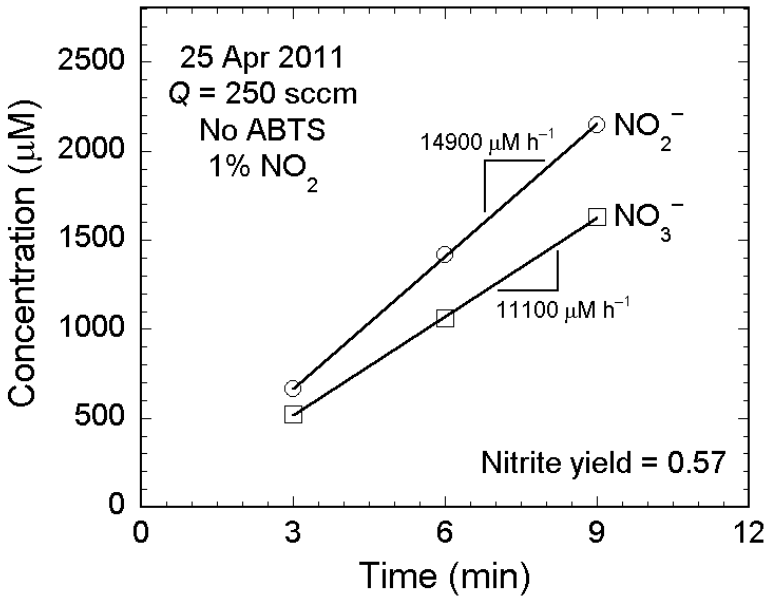
25 Apr 2011
Q = 250 sccm
No ABTS
1% NO2
14900 μM h−1
NO2−
NO3−
11100 μM h−1
Nitrite yield = 0.57
Concentration (μM)
Time (min)
0
500
1000
1500
2000
2500
0
3
6
9
12

(Figure B.3)

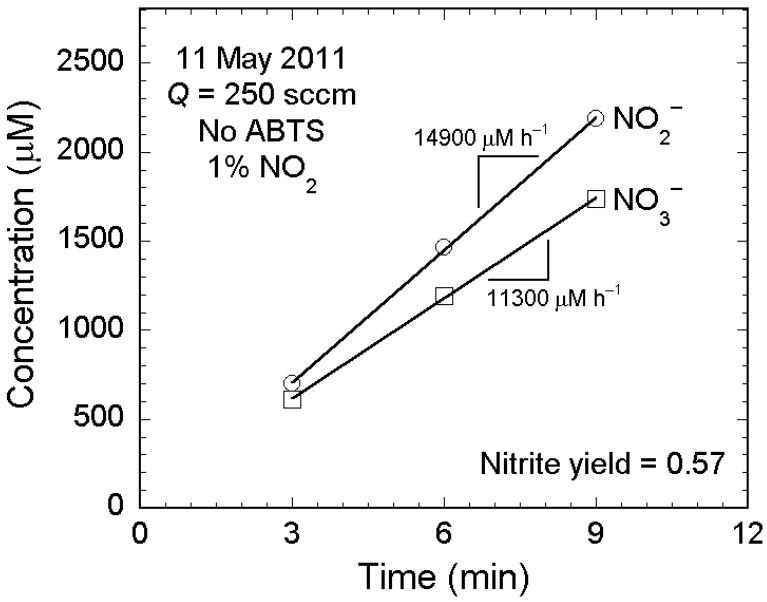

Figure B.3. Delivery of 1% NO_2 by direct gas-liquid contacting in the absence of ABTS (Q = 250 sccm).

The open symbols are the measured concentrations at the times indicated. All samples were assayed in duplicate. Error bars are smaller than the symbols. The solid lines are linear best-fits of the data shown, with slopes as indicated. The nitrite yield for each dataset is given on the respective figures.

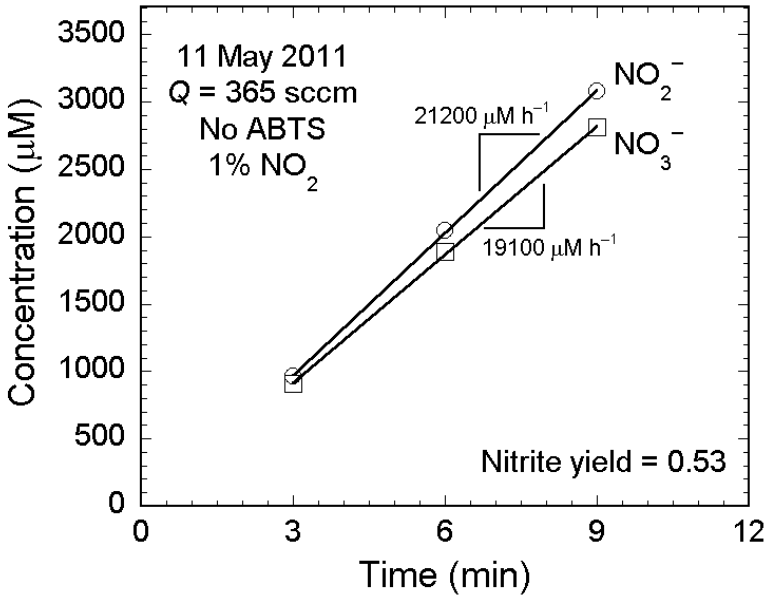
11 May 2011
Q = 365 sccm
No ABTS
1% NO2
NO2−
NO3−
21200 μM h−1
19100 μM h−1
Nitrite yield = 0.53
Concentration (μM)
Time (min)
0
500
1000
1500
2000
2500
3000
3500
0
3
6
9
12

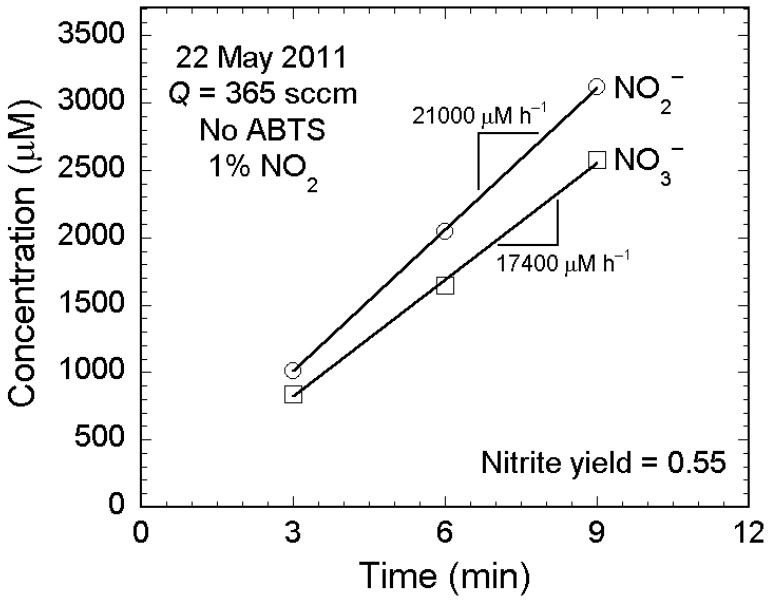
22 May 2011
Q = 365 sccm
No ABTS
1% NO2
NO2−
NO3−
21000 μM h−1
17400 μM h−1
Nitrite yield = 0.55
Concentration (μM)
Time (min)
0
500
1000
1500
2000
2500
3000
3500
0
3
6
9
12

(Figure B.4)

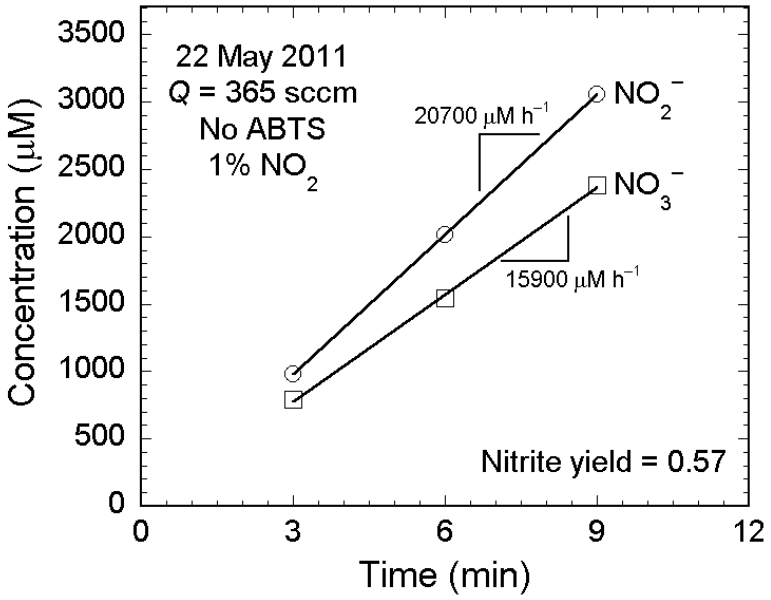

Figure B.4. Delivery of 1% NO_2 by direct gas-liquid contacting in the absence of ABTS (Q = 365 sccm).

The open symbols are the measured concentrations at the times indicated. All samples were assayed in duplicate. Error bars are smaller than the symbols. The solid lines are linear best-fits of the data shown, with slopes as indicated. The nitrite yield for each dataset is given on the respective figures.

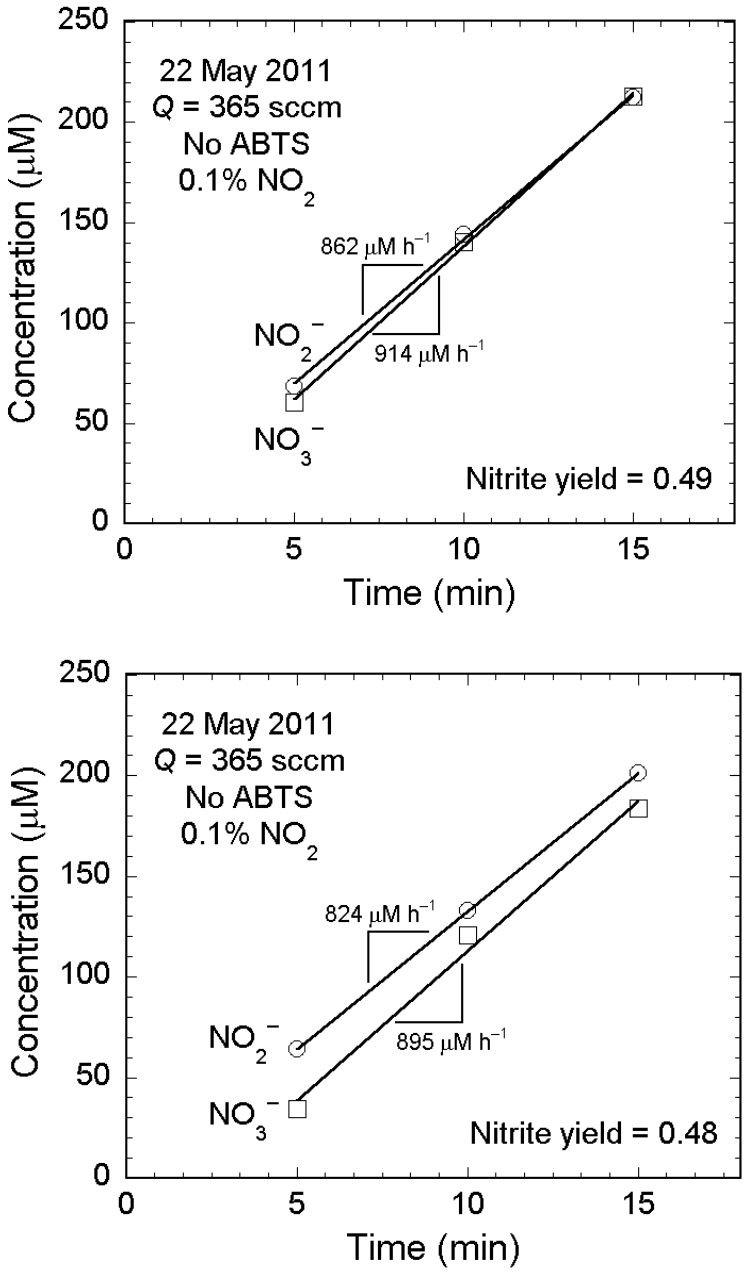

Figure B.5. Delivery of 0.1% NO_2 by direct gas-liquid contacting in the absence of ABTS.

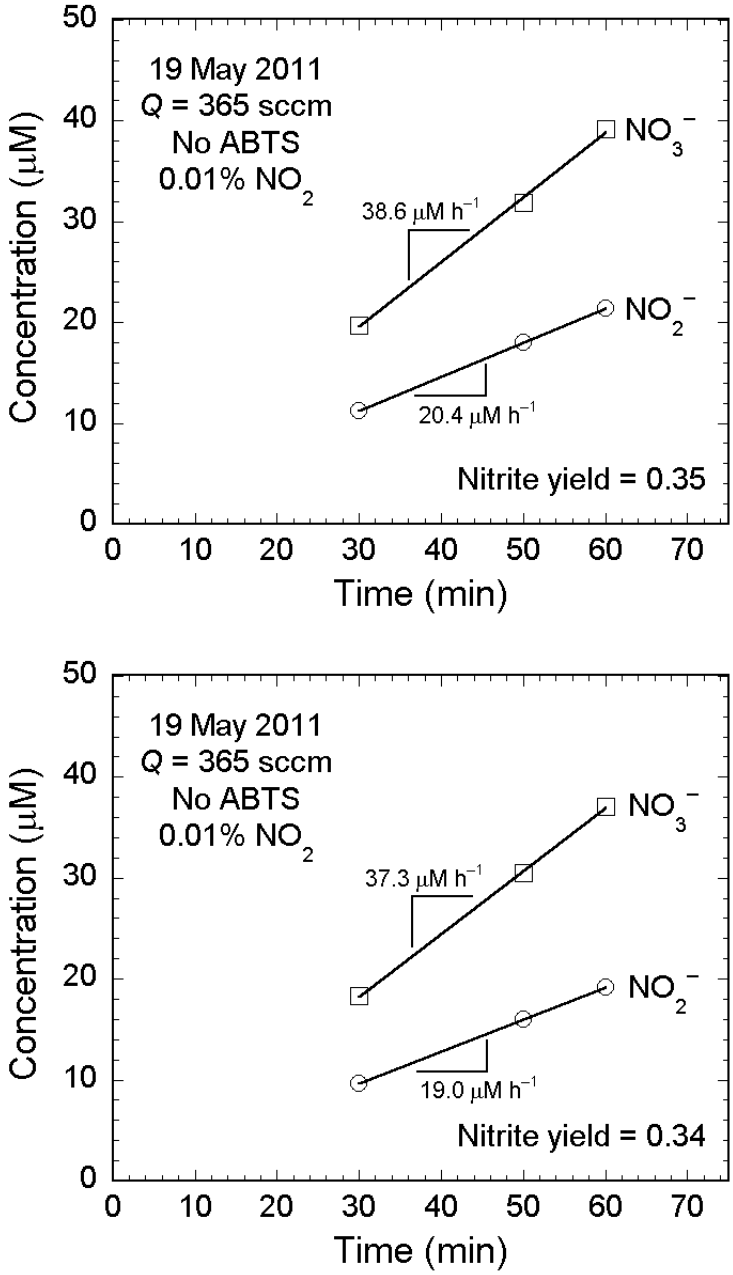

Figure B.6. Delivery of 0.01% NO_2 by direct gas-liquid contacting in the absence of ABTS.

The open symbols are the measured concentrations at the times indicated. All samples were assayed in duplicate. Error bars are smaller than the symbols. The solid lines are linear best-fits of the data shown, with slopes as indicated. The nitrite yield for each dataset is given on the respective figures.

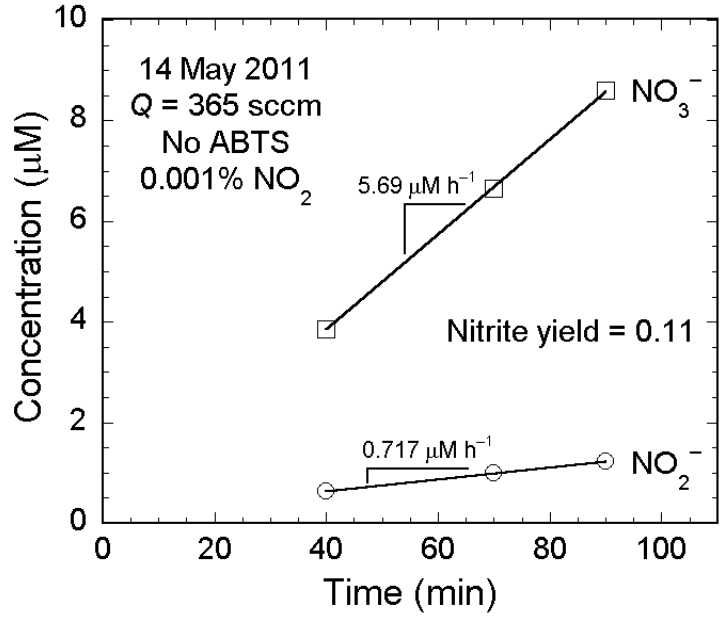
14 May 2011
Q = 365 sccm
No ABTS
0.001% NO2
5.69 μM h−1
NO3−
Nitrite yield = 0.11
0.717 μM h−1
NO2−
Concentration (μM)
Time (min)
0
2
4
6
8
10
0
20
40
60
80
100

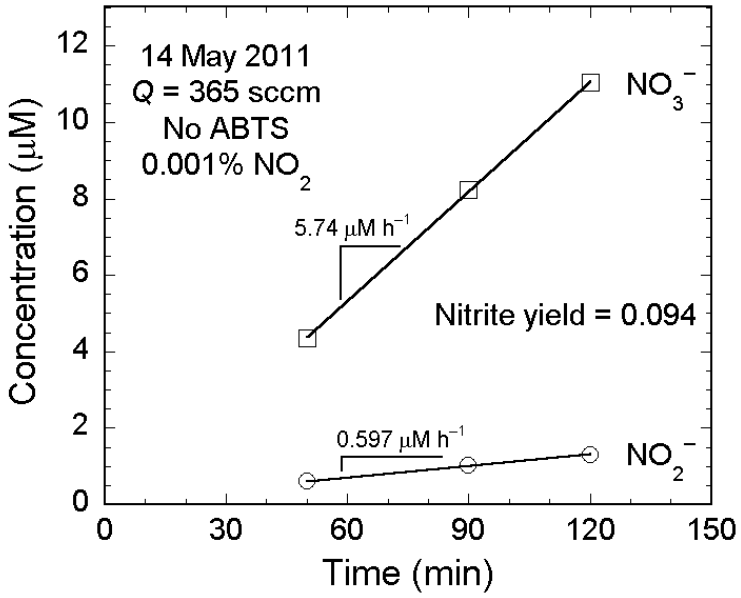
14 May 2011
Q = 365 sccm
No ABTS
0.001% NO2
5.74 μM h−1
NO3−
Nitrite yield = 0.094
0.597 μM h−1
NO2−
Concentration (μM)
Time (min)
0
2
4
6
8
10
12
0
30
60
90
120
150

(Figure B.7)

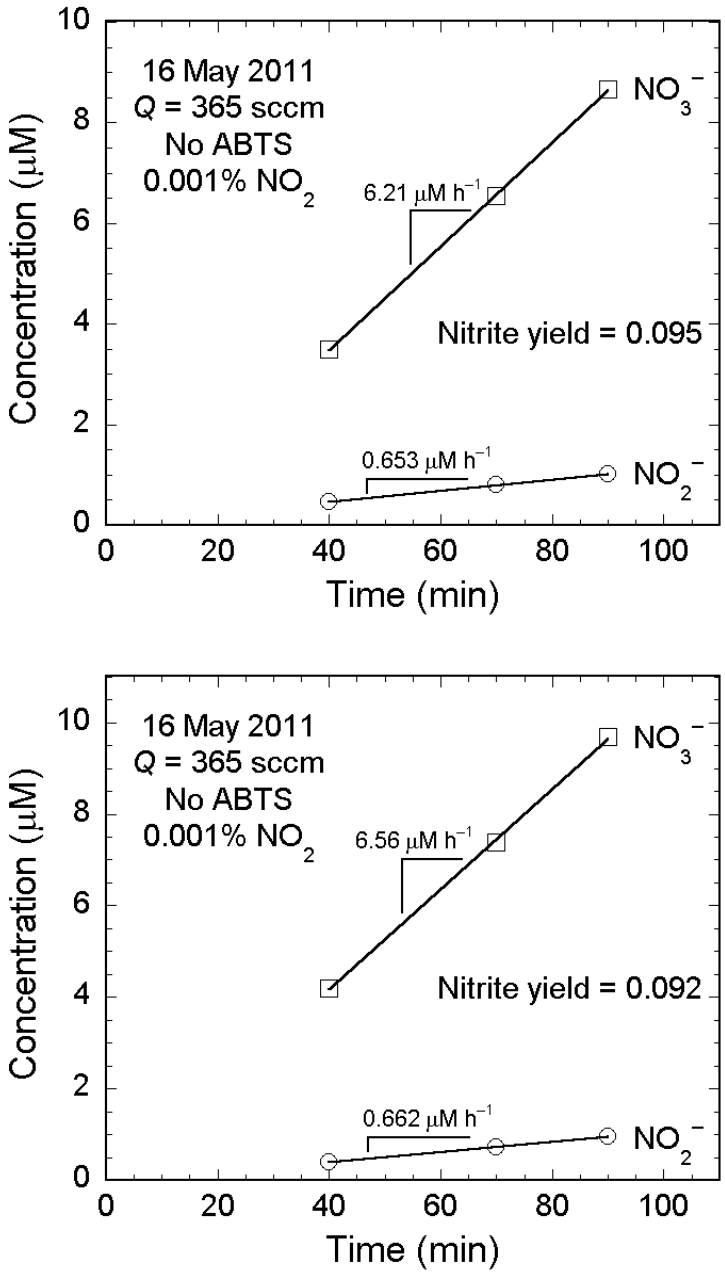

Figure B.7. Delivery of 0.001% NO_2 by direct gas-liquid contacting in the absence of ABTS.

The open symbols are the measured concentrations at the times indicated. All samples were assayed in duplicate. Error bars are smaller than the symbols. The solid lines are linear best-fits of the data shown, with slopes as indicated. The nitrite yield for each dataset is given on the respective figures.

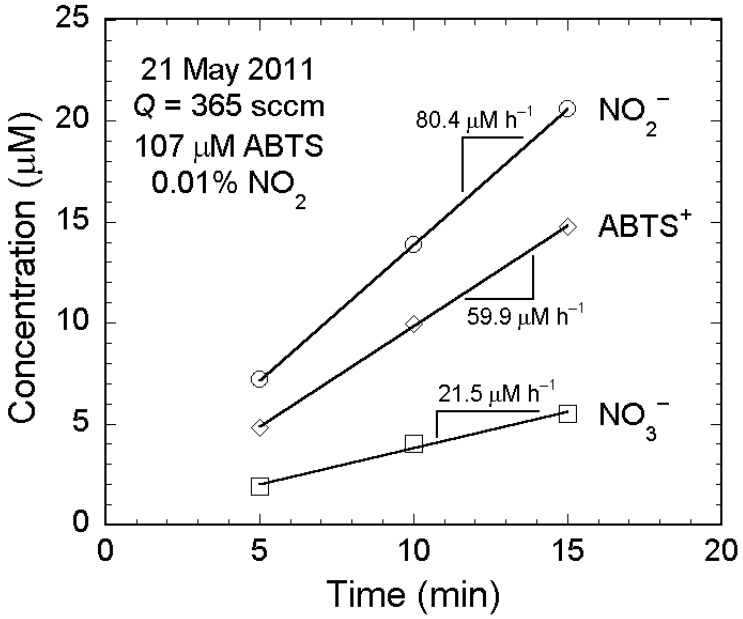
21 May 2011
Q = 365 sccm
107 μM ABTS
0.01% NO2
80.4 μM h−1
NO2−
ABTS+
59.9 μM h−1
21.5 μM h−1
NO3−
Concentration (μM)
Time (min)
0
5
10
15
20
25

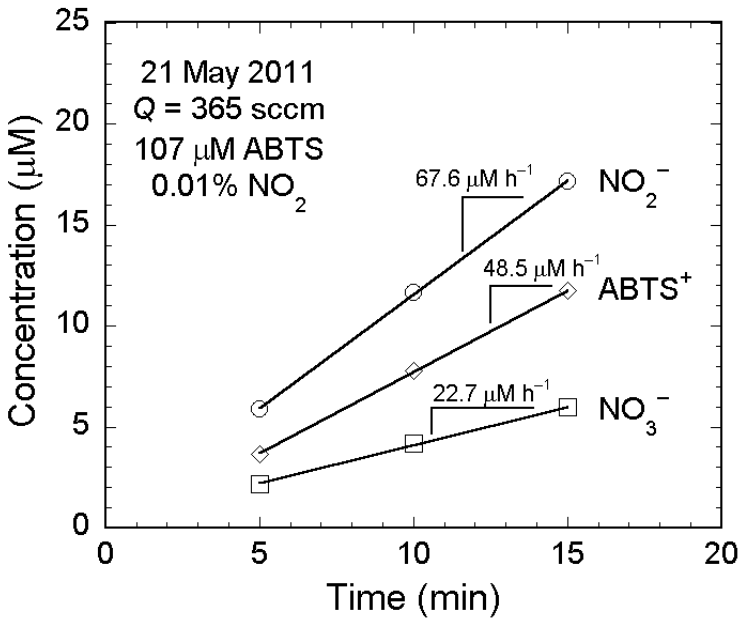
21 May 2011
Q = 365 sccm
107 μM ABTS
0.01% NO2
67.6 μM h−1
NO2−
48.5 μM h−1
ABTS+
22.7 μM h−1
NO3−
Concentration (μM)
Time (min)
0
5
10
15
20
25

(Figure B.8)

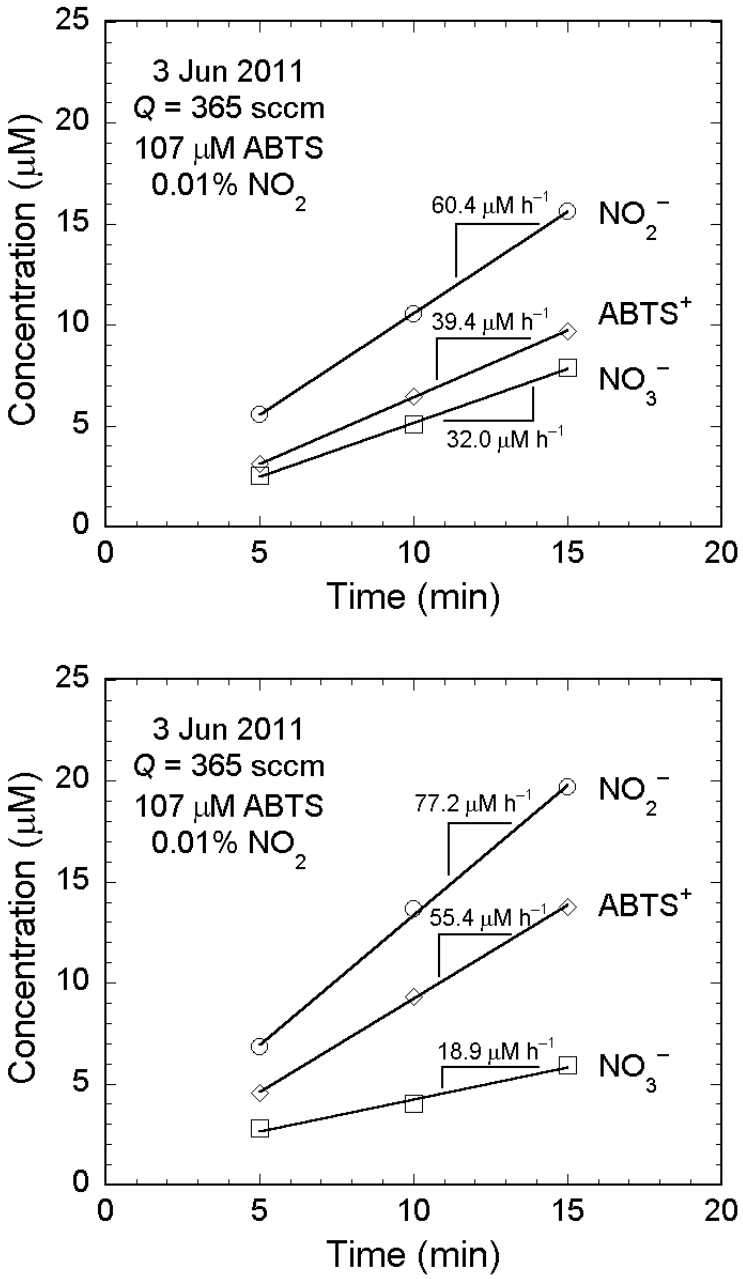

Figure B.8. Delivery of 0.01% NO_2 by direct gas-liquid contacting in the presence of ABTS.

The open symbols are the measured concentrations at the times indicated. All samples were assayed in duplicate. Error bars are smaller than the symbols. The solid lines are linear best-fits of the data shown, with slopes as indicated.

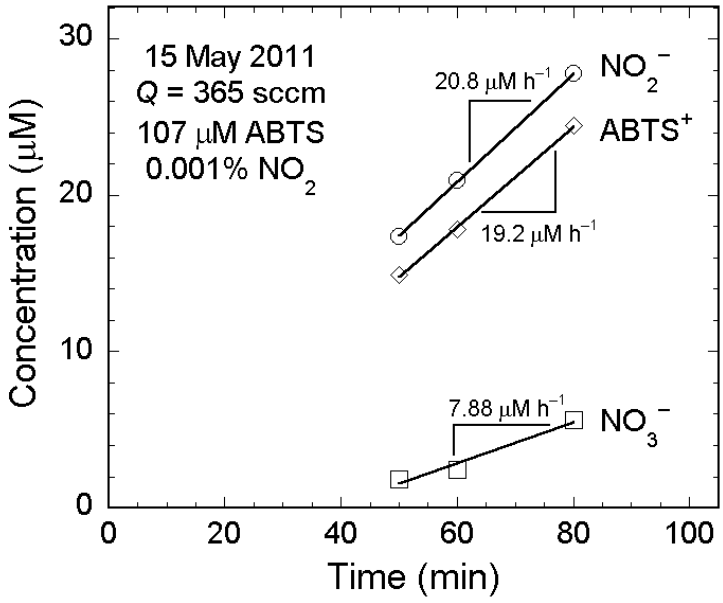
15 May 2011
Q = 365 sccm
107 μM ABTS
0.001% NO2
20.8 μM h−1
NO2−
ABTS+
19.2 μM h−1
7.88 μM h−1
NO3−
Concentration (μM)
Time (min)
0
10
20
30
0
20
40
60
80
100

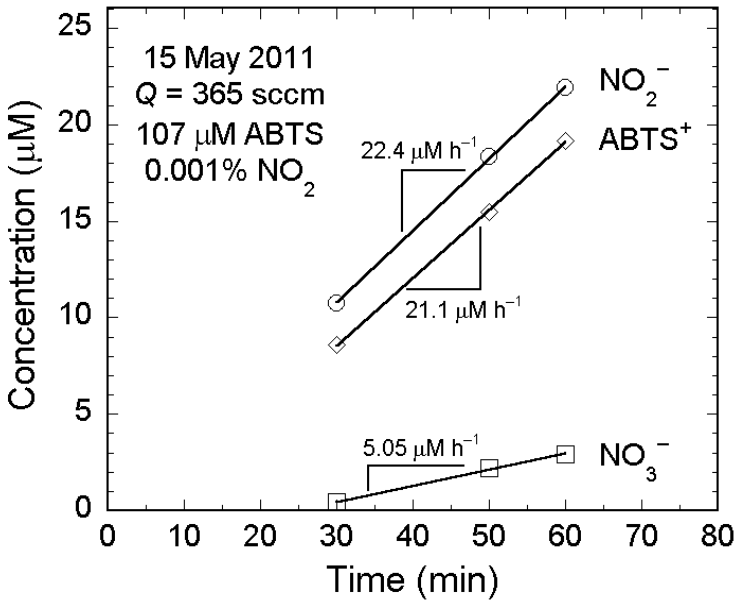
15 May 2011
Q = 365 sccm
107 μM ABTS
0.001% NO2
22.4 μM h−1
NO2−
ABTS+
21.1 μM h−1
5.05 μM h−1
NO3−
Concentration (μM)
Time (min)
0
5
10
15
20
25
0
10
20
30
40
50
60
70
80

(Figure B.9)

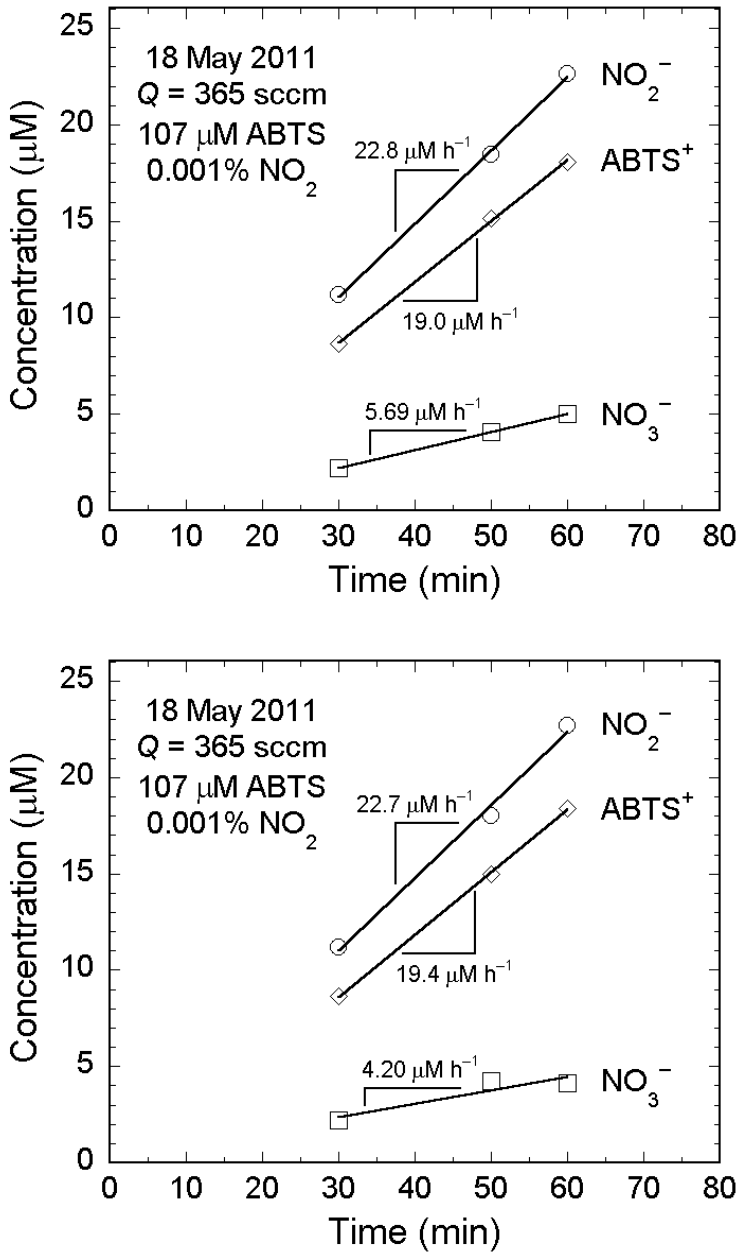

Figure B.9. Delivery of 0.001% NO_2 by direct gas-liquid contacting in the presence of ABTS.

The open symbols are the measured concentrations at the times indicated. All samples were assayed in duplicate. Error bars are smaller than the symbols. The solid lines are linear best-fits of the data shown, with slopes as indicated.

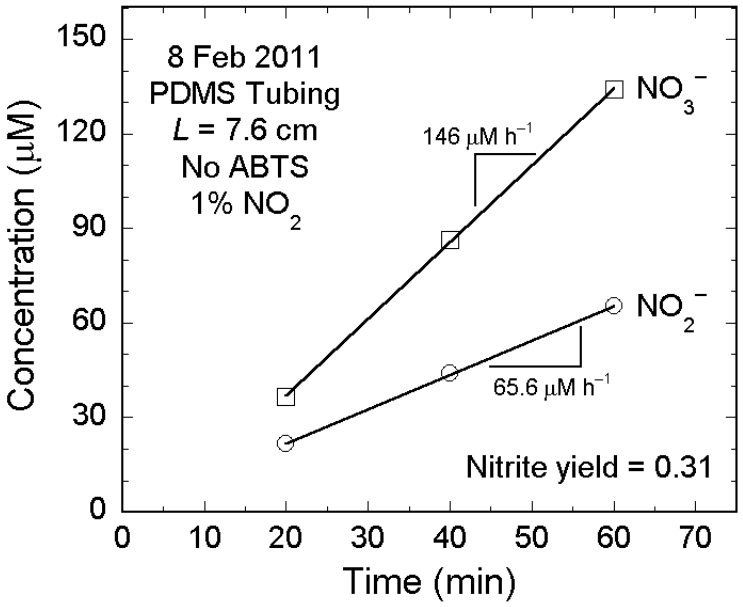
8 Feb 2011
PDMS Tubing
L = 7.6 cm
No ABTS
1% NO2
NO3−
146 μM h−1
NO2−
65.6 μM h−1
Nitrite yield = 0.31
Concentration (μM)
Time (min)
0
30
60
90
120
150
0
10
20
30
40
50
60
70

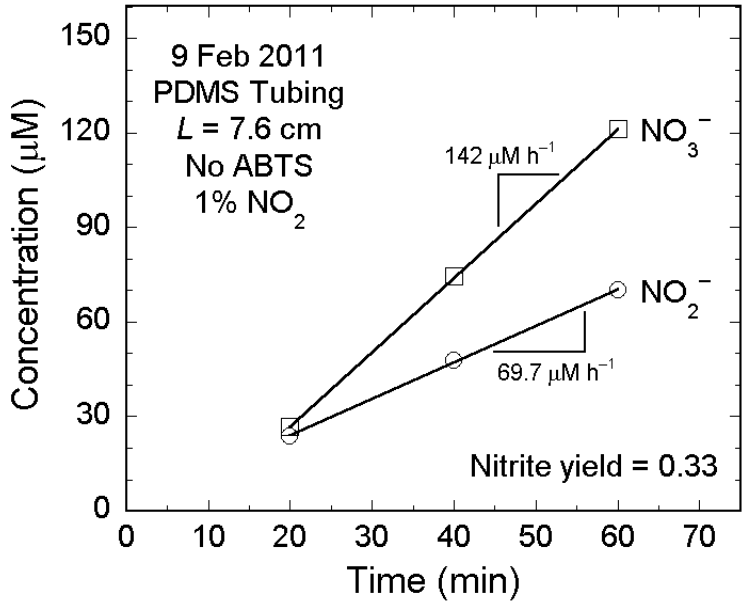
9 Feb 2011
PDMS Tubing
L = 7.6 cm
No ABTS
1% NO2
NO3−
142 μM h−1
NO2−
69.7 μM h−1
Nitrite yield = 0.33
Concentration (μM)
Time (min)
0
30
60
90
120
150
0
10
20
30
40
50
60
70

(Figure B.10)

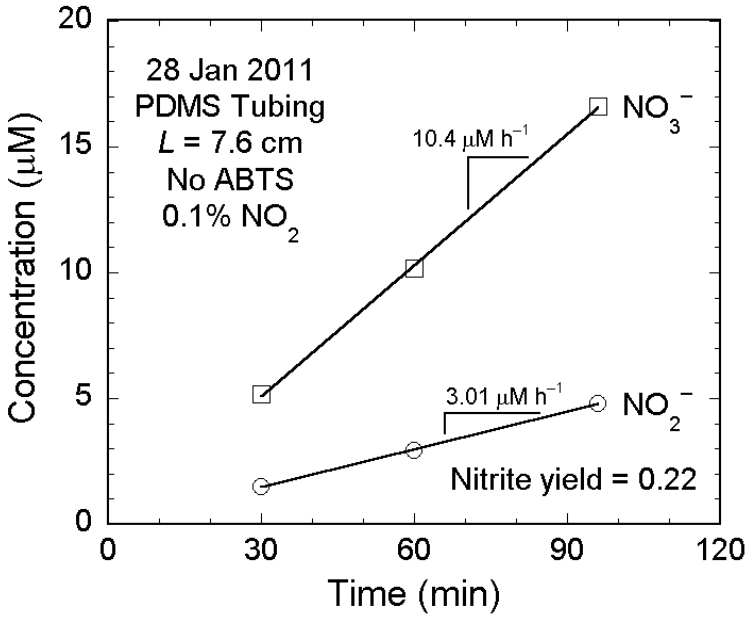
28 Jan 2011
PDMS Tubing
L = 7.6 cm
No ABTS
0.1% NO2
10.4 μM h−1
NO3−
3.01 μM h−1
NO2−
Nitrite yield = 0.22
Concentration (μM)
Time (min)
0
5
10
15
20
0
30
60
90
120

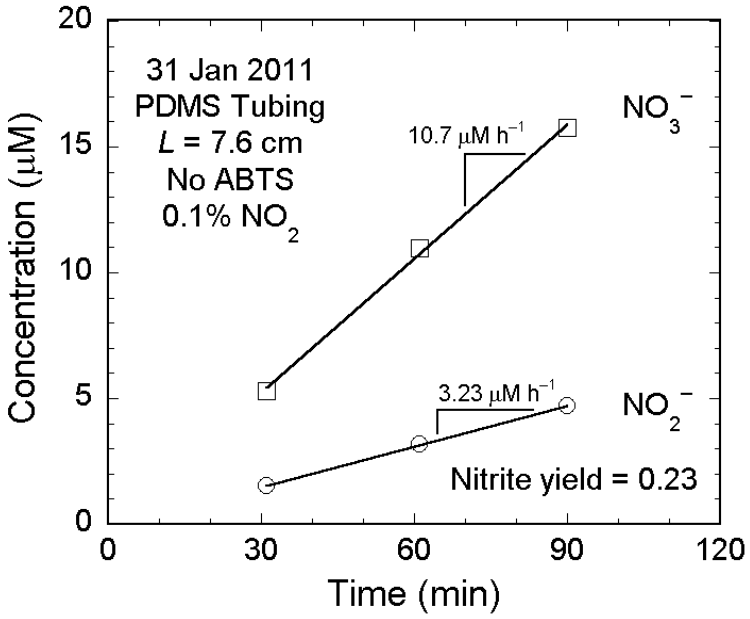
31 Jan 2011
PDMS Tubing
L = 7.6 cm
No ABTS
0.1% NO2
10.7 μM h−1
NO3−
3.23 μM h−1
NO2−
Nitrite yield = 0.23
Concentration (μM)
Time (min)
0
5
10
15
20
0
30
60
90
120

(Figure B.10)

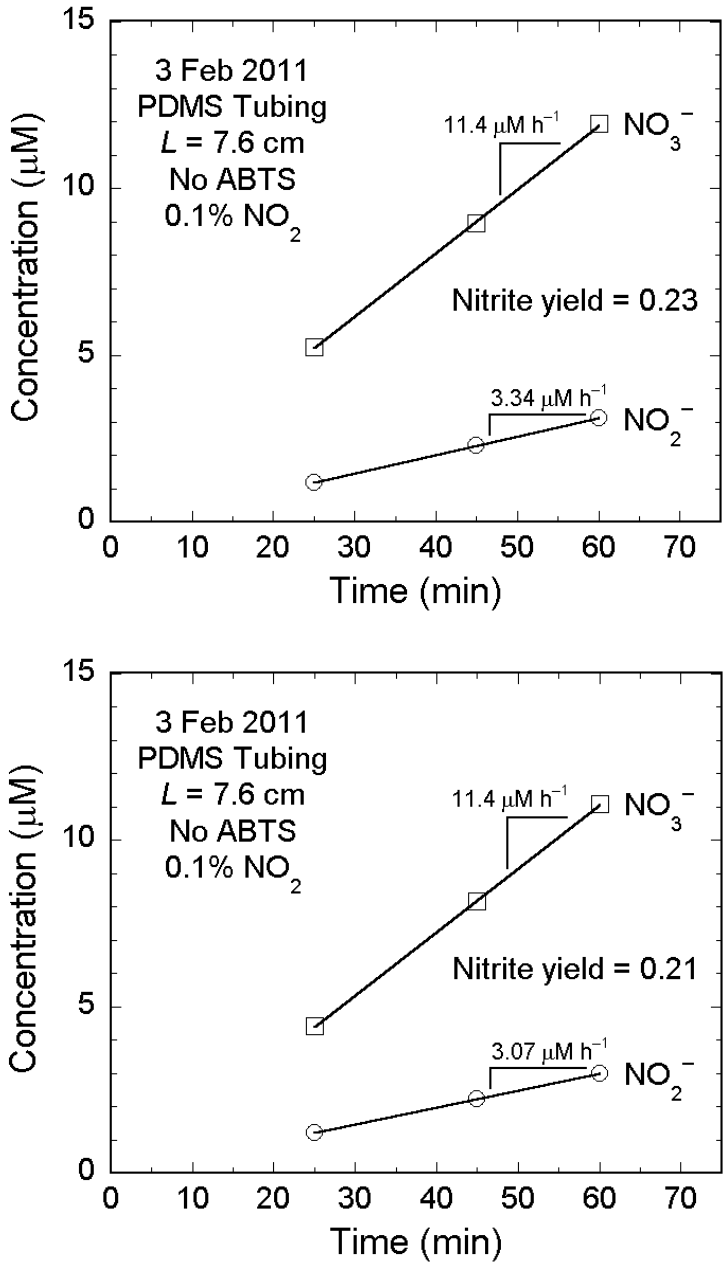

Figure B.10. Delivery of NO_2 by diffusion through PDMS tubing in the absence of ABTS.

The open symbols are the measured concentrations at the times indicated. All samples were assayed in duplicate. Error bars are smaller than the symbols. The solid lines are linear best-fits of the data shown, with slopes as indicated. The nitrite yield for each dataset is given on the respective figures. The data for 8 Feb and 9 Feb are for 1% NO_2; the remainder are for 0.1% NO_2.

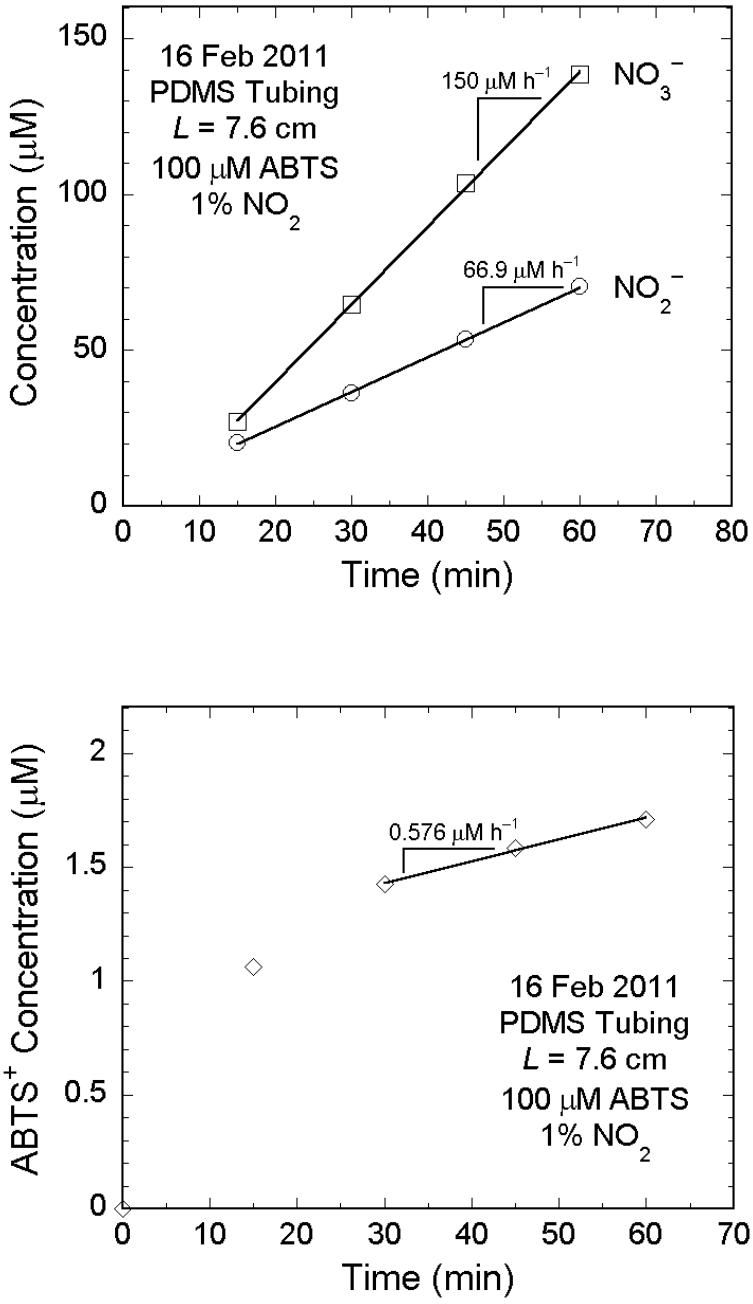
16 Feb 2011
PDMS Tubing
L = 7.6 cm
100 μM ABTS
1% NO2
150 μM h−1
NO3−
66.9 μM h−1
NO2−
Concentration (μM)
Time (min)
0.576 μM h−1
ABTS+ Concentration (μM)
16 Feb 2011
PDMS Tubing
L = 7.6 cm
100 μM ABTS
1% NO2
Time (min)

(Figure B.11)

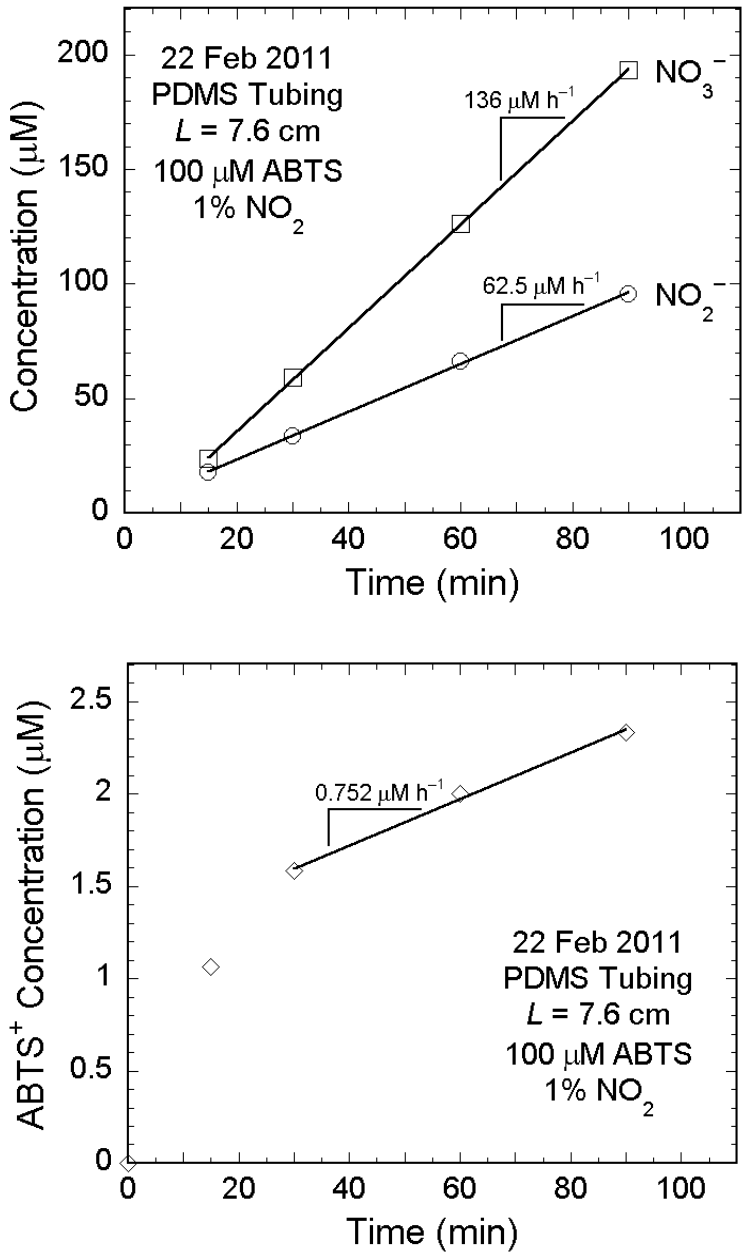

Figure B.11. Delivery of NO_2 by diffusion through PDMS tubing in the presence of ABTS.

The open symbols are the measured concentrations at the times indicated. All samples were assayed in duplicate. Error bars are smaller than the symbols. The solid lines are linear best-fits of the data shown, with slopes as indicated. Two datasets are shown; in both cases the $ABTS^+$ concentration initially rose quickly, and then settled to a slower rate of accumulation. In both experiments the nitrite and nitrate accumulation rates were similar to those observed in the absence of ABTS (1% experiments in Figure B.10).

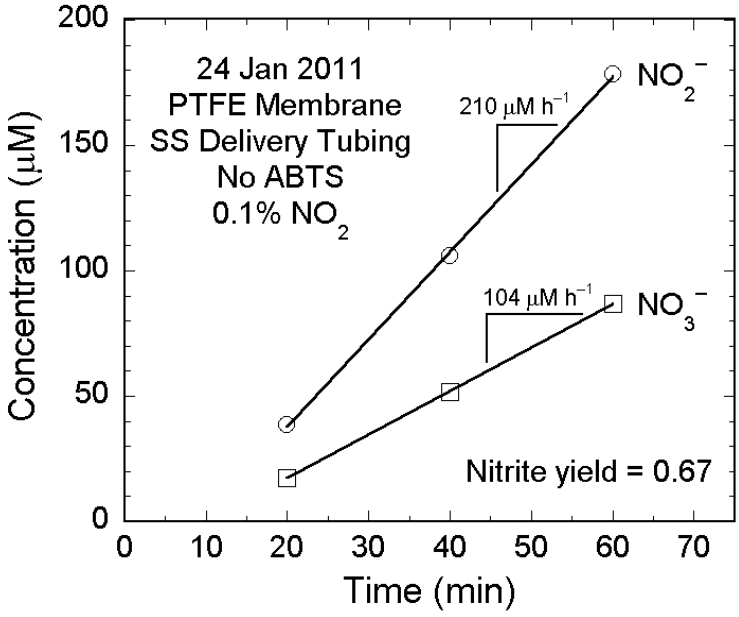
24 Jan 2011
PTFE Membrane
SS Delivery Tubing
No ABTS
0.1% NO2
210 μM h−1
NO2−
104 μM h−1
NO3−
Nitrite yield = 0.67
Concentration (μM)
Time (min)
0
50
100
150
200
0
10
20
30
40
50
60
70

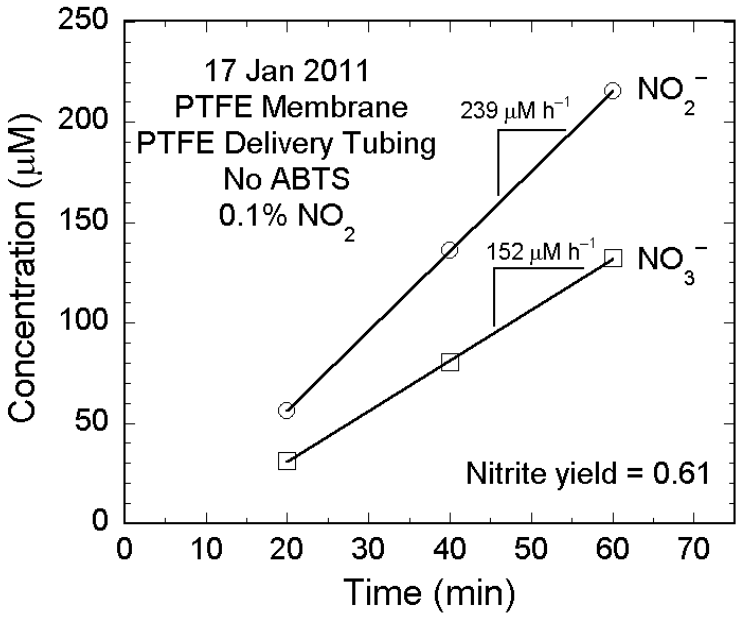
17 Jan 2011
PTFE Membrane
PTFE Delivery Tubing
No ABTS
0.1% NO2
239 μM h−1
NO2−
152 μM h−1
NO3−
Nitrite yield = 0.61
Concentration (μM)
Time (min)
0
50
100
150
200
250
0
10
20
30
40
50
60
70

(Figure B.12)

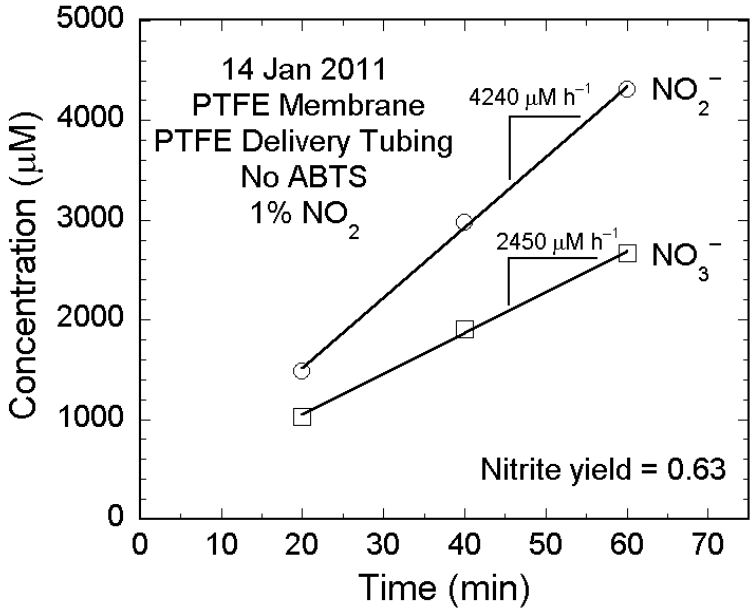

Figure B.12. Delivery of NO_2 by diffusion through a porous PTFE membrane in the absence of ABTS.

The open symbols are the measured concentrations at the times indicated. All samples were assayed in duplicate. Error bars are smaller than the symbols. The solid lines are linear best-fits of the data shown, with slopes as indicated. The nitrite yield for each dataset is given on the respective figures.

Appendix C

Thermodynamic Constraints for Aqueous N_2O_3 and N_2O_4 Solubilities

Introduction

The rapid hydrolysis of the dinitrogen oxides (N_2O_3 and N_2O_4) complicates accurate determination of their aqueous solubilities, denoted by α_j. However, thermodynamic constraints impose relationships between the gas- and liquid-phase equilibrium constants and the solubilities of the various species involved that permit estimation of these quantities from more readily measurable quantities.

In the analyses below, a hypothetical closed, equilibrated gaseous-aqueous system is postulated in which the rapid hydrolysis of N_2O_3 or N_2O_4, as appropriate, proceeds negligibly. The partial pressures of all species must be uniform in such a system, imposing constraints on the species concentrations in each phase that can be solved for the desired solubility parameter.

N_2O_4 Solubility

Consider the system as postulated above that has been charged with NO_2 and N_2O_4. As noted, the partial pressures of both species must be uniform throughout the system:

$$\tilde{P}_{NO_2} = P_{NO_2}, \quad \tilde{P}_{N_2O_4} = P_{N_2O_4}. \tag{C.1}$$

The symbols $\tilde{P}_j$ and P_j here refer to the partial pressure of species *j* in the gas and aqueous phases, respectively. The liquid-phase partial pressures of Eq. (C.1) can be written in terms of aqueous-phase concentrations and solubilities, giving

$$\tilde{P}_{NO_2} = \frac{1}{\alpha_{NO_2}} C_{NO_2}, \quad \tilde{P}_{N_2O_4} = \frac{1}{\alpha_{N_2O_4}} C_{N_2O_4}. \tag{C.2}$$

The equilibrium constants as reported in Table 3.1 are defined as

$$\tilde{K}_1 = \frac{\tilde{P}_{N_2O_4}}{\tilde{P}^2_{NO_2}}, \quad K_1 = \frac{C_{N_2O_4}}{C^2_{NO_2}}. \tag{C.3}$$

Dividing the N_2O_4 expression from Eq. (C.2) by the square of that for NO_2 permits substitution of both expressions of Eq. (C.3). Algebraic rearrangement yields the constraint for $\alpha_{N_2O_4}$ as

$$\alpha_{N_2O_4} = \frac{K_1}{\tilde{K}_1} \left(\alpha_{NO_2} \right)^2. \tag{C.4}$$

N_2O_3 Solubility

Consider the system as postulated above that has been charged with NO, NO_2, and N_2O_3. The partial pressure constraints are

$$\tilde{P}_{NO} = P_{NO}, \quad \tilde{P}_{NO_2} = P_{NO_2}, \quad \tilde{P}_{N_2O_3} = P_{N_2O_3}. \tag{C.5}$$

Rewriting the liquid-phase partial pressures in terms of concentrations and solubilities, the relations of Eq. (C.5) become

$$\tilde{P}_{NO} = \frac{1}{\alpha_{NO}} C_{NO}, \quad \tilde{P}_{NO_2} = \frac{1}{\alpha_{NO_2}} C_{NO_2}, \quad \tilde{P}_{N_2O_3} = \frac{1}{\alpha_{N_2O_3}} C_{N_2O_3}. \tag{C.6}$$

The gas- and aqueous-phase equilibrium constants are defined as

$$\tilde{K} = \frac{\tilde{P}_{N_2O_3}}{\tilde{P}_{NO}\tilde{P}_{NO_2}}, \quad K = \frac{C_{N_2O_3}}{C_{NO}C_{NO_2}}, \tag{C.7}$$

where $K = k_2/k_{-2}$ (rate constants from Table 2.1) and $\tilde{K}$ = 0.525 atm^{-1} (Wiberg and Aylett, 2001). Dividing the N_2O_3 expression from Eq. (C.6) by those for NO and NO_2 permits substitution of both expressions of Eq. (C.7). Algebraic rearrangement yields the desired expression for the N_2O_3 solubility as

$$\alpha_{N_2O_3} = \frac{K}{\tilde{K}}\alpha_{NO}\alpha_{NO_2}. \tag{C.8}$$

To note, dimerization of NO_2 to N_2O_4 was assumed to be negligible in this calculation. In a real system, in the presence of a sufficient amount of NO_2 the simultaneous equilibration of NO and NO_2 with N_2O_3 and N_2O_4 must be considered.

Appendix D

Base Well and Membrane Scaling Arguments for Delivery of NO

D.1 Introduction

The success of the custom reactor for NO delivery described in Chapter 2 can be explained in terms of various scaling arguments. Numerical simulations including a specified level of NO_2 impurity at the surface of the porous membrane facing the liquid indicate that NO_2 must be present at an abundance of less than 0.55 ppm in a 10% NO gas mixture in order for the perturbation of the nitrite accumulation rate to be less than 5% (Section D.2). The scaling arguments presented in Section D.3 indicate that the corresponding upper bound on the NO_2 abundance in delivery of 1% NO is 0.17 ppm. In Section D.4, a model is presented that characterizes the transport in the well and the membrane. This model is subsequently used to generate estimates of the concentration scales for NO, O_2 and NO_2 (Section D.4.4). The potential effects of NO oxidation on NO_2 transport (Section D.4.5) and on the NO_2 concentration scale (Section D.4.6) are also discussed. Finally, scaling arguments are presented (Section D.5) that support the experimental observations that masking of the porous membrane was vital to the proper functioning of the reactor. All of the analysis presented here assumes a temperature of 298 K (25 °C).

D.2 Numerical estimation of threshold NO_2 abundance

The microscopic model of Section 2.2.6.2 was revised to permit simulation of NO_2 as a non-quasi-equilibrium species. That is, Eq. (2.13) was solved for NO, O_2 and NO_2, instead of just for NO and O_2. Quasi-equilibrium behavior was assumed for N_2O_3, and N_2O_3 was assumed to contribute negligibly to the overall transport of nitrogen. The latter assumption should be reasonable for the relatively small NO_2 impurities under consideration here. The solubility of NO_2 was taken as the adjusted value from Chapter 3, 9 mM/atm. All other system parameters are as in Table 2.1.

The system of equations solved was the following:

$$0 = D_{\mathrm{NO}} \frac{d^2 \hat{C}_{\mathrm{NO}}}{dx^2} - 2k_1 \hat{C}_{\mathrm{NO}}^2 \hat{C}_{\mathrm{O_2}} - \frac{k_2 k_P'}{k_P' + k_{-2}} \hat{C}_{\mathrm{NO}} \hat{C}_{\mathrm{NO_2}} . \tag{D.1}$$

$$0 = D_{\mathrm{O_2}} \frac{d^2 \hat{C}_{\mathrm{O_2}}}{dx^2} - k_1 \hat{C}_{\mathrm{NO}}^2 \hat{C}_{\mathrm{O_2}} . \tag{D.2}$$

$$0 = D_{\mathrm{NO_2}} \frac{d^2 \hat{C}_{\mathrm{NO_2}}}{dx^2} + 2k_1 \hat{C}_{\mathrm{NO}}^2 \hat{C}_{\mathrm{O_2}} - \frac{k_2 k_P'}{k_P' + k_{-2}} \hat{C}_{\mathrm{NO}} \hat{C}_{\mathrm{NO_2}} . \tag{D.3}$$

$$\hat{C}_j(0) = \alpha_j P_{m,j}; \ \hat{C}_j(\delta) = C_{w,j} . \tag{D.4}$$

The definition of k_P' is the same as that of Eq. (2.16). While a precise value for the well-mixed NO_2 concentration could have been calculated assuming quasi-steady-state behavior, it was found that negligible error was introduced by simply setting $C_{w,\mathrm{NO_2}}$ equal to zero. As in the Appendix of Wang and Deen (2003), the NO_2 concentration was found to fall rapidly to zero within a few microns of the membrane surface.

The correction factor γ for the reaction term was calculated using an expression similar to Eq. (2.17):

$$\gamma = 1 + \frac{A_m}{4k_1 C_{w,\mathrm{NO}}^2 C_{w,\mathrm{O_2}} V} \int_0^{\delta} \frac{2k_2 k_P'}{k_P' + k_{-2}} \hat{C}_{\mathrm{NO}} \hat{C}_{\mathrm{NO_2}} dx \,. \tag{D.5}$$

The reaction term within the integral was expressed in terms of the quasi-equilibrium expression for the N_2O_3 concentration, whereas that in the denominator was left in terms of the overall kinetics of NO oxidation in the well-mixed region. Use of the latter form was permissible because the NO_2 concentration is not expected to deviate significantly from its quasi-steady-state value far from the membrane. Figure D.1 plots the value of γ as a function of the NO_2 abundance within the membrane, $\tilde{x}_{\mathrm{NO_2}}$. For the relatively low levels of NO_2 shown, γ is linearly dependent on $\tilde{x}_{\mathrm{NO_2}}$.

The confidence interval on the nitrite accumulation rate reported in Section 2.3.2 is approximately 5%. Based upon the linear best-fit to the simulation results in Figure D.1, the NO_2 abundance must be no greater than about 0.55 ppm in order for it to have an experimentally indistinguishable effect on the rate of nitrite accumulation. The magnitude of this threshold is remarkable: a 0.00055% relative impurity of NO_2 in a 10% mixture of NO is predicted to cause a 5% change in the observed nitrite formation rate.

D.3 Scaling arguments for NO_2 enhancement of nitrite accumulation

The enhancement of NO uptake due to the presence of a small amount of contaminating NO_2 can be estimated using a scaling argument as follows. The diffusion of NO_2 away from the porous PTFE membrane into the liquid will be balanced by reaction with NO and the hydrolysis of the resulting N_2O_3:

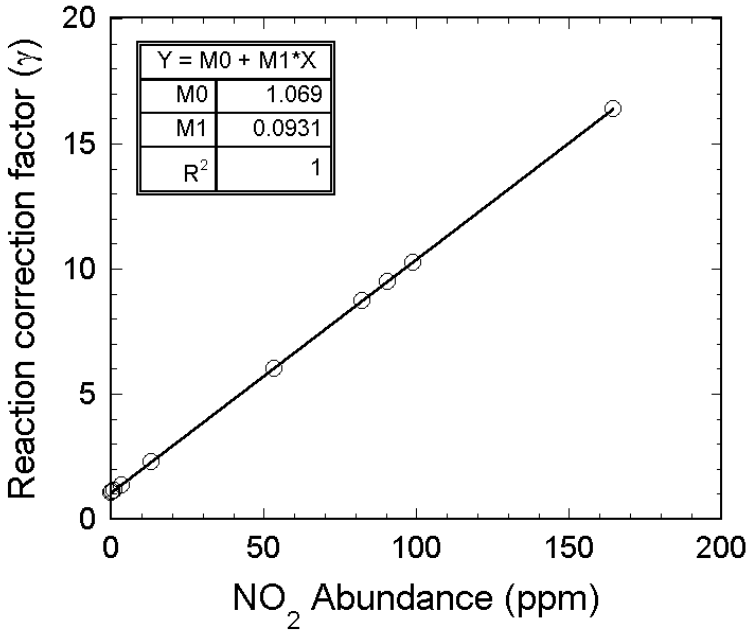

Figure D.1. Predicted reaction correction factor (γ) as a function of NO_2 abundance.

The open symbols are individual values of γ determined by simulation. The solid line is a linear fit of these results, with best-fit parameters as shown. The simulations were performed using Eqs. (D.1)-(D.4) assuming a 10% NO gas mixture. The correction factor γ was calculated using Eq. (D.5).

$$D_{NO_2} \frac{d^2 C_{NO_2}}{dx^2} \sim \frac{k_2 k'_P}{k'_P + k_{-2}} C^*_{NO} C^*_{NO_2} . \quad \text{(D.6)}$$

Since all of the NO_2 is expected to be rapidly consumed within a short distance of the membrane, the scales for the NO_2 concentration and for the change in the NO_2 concentration are equal. Eq. (D.6) thus reduces to

$$\frac{D_{NO_2}}{L^2_{NO_2}} \sim k'' C^*_{NO} , \quad \text{(D.7)}$$

where L_{NO_2} is the length scale over which the NO_2 is consumed and $k'' = k_2 k'_P \left(k'_P + k_{-2}\right)^{-1}$. The value of k'' was calculated as 3.55×10^7 M^{-1} s^{-1} for the 50 mM Na-PO_4 buffer used. Rearranging Eq. (D.7) gives an expression for L_{NO_2}:

$$L_{NO_2} = \left(\frac{D_{NO_2}}{k'' C^*_{NO}} \right)^{1/2} . \quad \text{(D.8)}$$

For a 10% NO mixture, L_{NO_2} = 0.52 μm. The flux of NO_2 into the liquid can be estimated as

$$N_{NO_2} = -D_{NO_2} \frac{dC_{NO_2}}{dx} \sim \frac{D_{NO_2} C^*_{NO_2}}{L_{NO_2}} \sim \left(D_{NO_2} k'' C^*_{NO} \right)^{1/2} C^*_{NO_2} . \quad \text{(D.9)}$$

The combined stoichiometry of Reactions (2.2) and (2.3) indicates that one molecule of NO must be consumed along with each molecule of NO_2 that enters the liquid. As with NO_2, the rapid chemistry is expected to impose a kinetically-defined length scale on the change in the NO concentration. Since NO and NO_2 will be

consumed in a 1:1 ratio, an appropriate scale for ΔC_{NO} is $C^*_{NO_2}$. The balance between the scales for diffusion and reaction of NO thus takes the form

$$D_{NO}\frac{d^2C_{NO}}{dx^2} \sim \frac{D_{NO}C^*_{NO_2}}{L^2_{NO}} \sim k''C^*_{NO}C^*_{NO_2}. \tag{D.10}$$

The factors of $C^*_{NO_2}$ cancel, and the resulting expression for L_{NO} is

$$L_{NO} = \left(\frac{D_{NO}}{k''C^*_{NO}}\right)^{1/2}. \tag{D.11}$$

Comparison of Eqs. (D.8) and (D.11) reveals that the length scales over which NO and NO_2 will be consumed are nearly equal, differing only by the square root of the ratio of their respective diffusivities. Accordingly, the subsequent analysis will be simplified by assuming $L_{NO_2} \approx L_{NO}$. The flux of NO into the liquid in the presence of NO_2 can be estimated [in a manner analogous to Eq. (D.9)] as

$$N_{NO} \sim \left(D_{NO}k''C^*_{NO}\right)^{1/2} C^*_{NO_2}. \tag{D.12}$$

Summing Eqs. (D.9) and (D.12) yields an estimate of the total flux of NO and NO_2 (NO_x) into the liquid:

$$N_{NO_x} \sim 2\left(D_{NO}k''C^*_{NO}\right)^{1/2} C^*_{NO_2}. \tag{D.13}$$

In the absence of a gas-phase NO_2 impurity, the flux of NO into the liquid can be estimated from the NO mass transfer coefficient $k_{m,NO}$ (Table 2.2). Given that $\alpha_{NO}P_{m,NO} \gg C_{w,NO}$, it follows that

$$N^o_{NO} \sim k_{m,NO}\alpha_{NO}P_{m,NO} = k_{m,NO}C^*_{NO}. \tag{D.14}$$

An estimate of the magnitude of the enhancement of NO_x entry due to the NO_2 impurity is given by the ratio

$$\frac{N_{NO_x}}{N^o_{NO}} \sim \frac{2\left(D_{NO}k''C^*_{NO}\right)^{1/2}C^*_{NO_2}}{k_{m,NO}C^*_{NO}} = \frac{2C^*_{NO_2}}{k_{m,NO}}\left(\frac{D_{NO}k''}{C^*_{NO}}\right)^{1/2}. \tag{D.15}$$

Considering the ~ 5% experimental uncertainty in the nitrite accumulation rate, any enhancement in NO_x entry that is less than 5% of the nominal rate should be experimentally undetectable. The constraint on the NO_2 impurity derived from Eq. (D.15) is thus

$$C^*_{NO_2} \le 0.025\, k_{m,NO}\left(\frac{C^*_{NO}}{D_{NO}k''}\right)^{1/2}. \tag{D.16}$$

The upper-limit values of $C^*_{NO_2}$ for 10% and 1% mixtures are 40 nM and 13 nM, respectively. These correspond to NO_2 impurities in the base well of 4.5 ppm and 1.4 ppm, respectively. It is worthwhile to note that this 4.5-ppm estimate calculated for a 10% NO gas mixture is approximately one order of magnitude greater than that obtained from the simulations of Section D.2. Accordingly, the estimate of 1.4 ppm for a 1% NO mixture is likely also too high by about an order of magnitude. The scaling relationship captured within Eq. (D.16), that $C^*_{NO_2} \propto \left(C^*_{NO}\right)^{1/2}$, remains valid, however. A safe upper estimate of the allowable NO_2 impurity in delivery of 1% NO mixtures calculated from this scaling relationship and the simulation results of Section D.2 is 0.17 ppm.

D.4 Microscopic model of base well and membrane

D.4.1 Model description

In an effort to obtain estimates of the species concentrations within the porous membrane and the base well during steady delivery of NO to oxygenated solutions, the following mass balance was used for each species *j*:

$$0 = Q\left(\tilde{C}_{f,j} - \tilde{C}_j\right) - \tilde{k}A\left(\tilde{C}_j - \tilde{C}_{g,j}\right) + \tilde{V}\tilde{R}_j . \qquad \text{(D.17)}$$

The well was considered to be a well-mixed region with volume $\tilde{V}$ = 0.77 cm^3. The inlet and outlet gas flow rates were assumed equal at Q = 350 sccm. The concentration of species *j* within the well, at the inlet (feed point), and at the surface of the porous membrane was denoted respectively as $\tilde{C}_j$, $\tilde{C}_{f,j}$ and $\tilde{C}_{g,j}$. The rate of mass transfer from the well-mixed region to the lower surface of the membrane was described with the mass transfer coefficient $\tilde{k}$, assumed to be the same for all species, across the membrane open area A = 1.27 cm^3. The volumetric rate of reaction of each species is $\tilde{R}_j$.

The mass transfer of each species through the porous membrane (porosity and thickness of ε = 0.83 and δ_m = 75 μm, respectively) was assumed to be purely diffusive. The gas-phase diffusivities of NO, O_2, and NO_2 were estimated using the Chapman-Enskog correlation as described in Green and Maloney (1997) and the critical property data of Horstmann et al. (2005). The diffusivity estimates for all three species were nearly equal, so a common value of $\tilde{D}$ = 1.6 × 10^{-5} m^2 s^{-1} was used. According to Tomadakis and Sotirchos (1993), the apparent diffusivity perpendicular to a bed of fibers randomly oriented in two dimensions can be expressed as

$$\tilde{D}' = \frac{\varepsilon}{\eta}\tilde{D}, \tag{D.18}$$

where the tortuosity η represents an empirical correction for the indirect path a molecule must take in traversing the bed. [Data for a bed of randomly oriented fibers was selected as the most appropriate for the membranes used based upon inspection of a micrograph published on the manufacturer's web page (http://advantecmfs.com/filtration/membranes/mb_ptfeunsup.shtml, accessed 15 Nov 2011).] Figure 11 of Tomadakis and Sotirchos indicates that for a membrane of porosity $\varepsilon = 0.83$ as in the present case, the tortuosity should be at most approximately $\eta = 2.5$. The apparent diffusivity of the three species of interest within the membrane should thus be no less than $\tilde{D}' = 5.3 \times 10^{-6}$ m^2 s^{-1}. The diffusive flux of each species upward across the membrane was written as

$$-\frac{\tilde{D}'}{\delta_m}\left(\tilde{C}_{g,j} - \tilde{C}_{\ell,j}\right), \tag{D.19}$$

where $\tilde{C}_{g,j}$ and $\tilde{C}_{\ell,j}$ are the concentration of species j at the gas-facing and liquid-facing surfaces of the membrane, respectively.

The magnitude of the NO_2 impurity was assumed to be sufficiently small that the transport of NO and O_2 from the porous membrane into the liquid was unaffected by reactions. Accordingly, the mass transfer coefficients $k_{m,j}$ of Table 2.2 were used without modification. The scaling estimate of Eq. (D.9) for the NO_2 flux into the liquid can be used to estimate the mass transfer coefficient for NO_2 at the porous membrane:

$$k_{m,\mathrm{NO_2}} = \left(D_{\mathrm{NO_2}} k'' C^*_{\mathrm{NO}}\right)^{1/2}. \tag{D.20}$$

D.4.2 Estimation of the base well mass transfer coefficient

A lower-bound estimate for the mass transfer coefficient for transport from the well-mixed region of the base well to the underside of the porous membrane can be obtained as follows. Conservation of mass dictates that the mean volumetric flow rate across any plane perpendicular to the net volumetric flow within the well must be equal to Q. The mean velocity across such a plane is $U = Q/A$, where A is the area of intersection of the plane and the open volume of the well. Since it is desirable to argue that mass-transfer limitations within the well and membrane are negligible, a lower-bound estimate of $\tilde{k}$ is needed. Such an estimate can be obtained by considering the largest possible A, which in this case is a rectangle with width and height equal to the diameter and depth of the well, respectively. The upper-bound area so calculated is $A = 0.77$ cm^2, which corresponds to a gas velocity of $U = 7.92$ cm s^{-1}.

Boundary-layer theory [Case 1, Table 10-3 of Deen (1998)] predicts that in mass transfer between a fluid and solid surface the average Sherwood number is related to the Reynolds and Schmidt numbers as

$$\mathrm{Sh} \sim B(\mathrm{Sc})\,\mathrm{Re}^{1/2}, \tag{D.21}$$

where $\mathrm{Sh} = \tilde{k}L/\tilde{D}$, $\mathrm{Re} = UL/\tilde{\nu}$, and $\mathrm{Sc} = \tilde{\nu}/\tilde{D}$. The gas-phase kinematic viscosity $\tilde{\nu} = \tilde{\mu}/\tilde{\rho}$ (units of m^2 s^{-1}), where $\tilde{\mu}$ and $\tilde{\rho}$ are the gas-phase dynamic viscosity and density (units of Pa-s and g l^{-1}, respectively). The most appropriate length scale to use here is the depth of the well, $L = 0.605$ cm, both because it is smaller than the well diameter (1.27 cm) and because it is the dimension of the system parallel to the direction of the transport processes of interest. Using as a reasonable estimate the properties of

pure N_2 at 20 °C, $\tilde{\mu}$ = 1.76 × 10^{-5} Pa-s [Table 1-4 of Deen (1998)] and $\tilde{\rho}$ = 1.16 g l^{-1} (ideal gas law), the kinematic viscosity can be estimated as $\tilde{\nu}$ = 1.50 × 10^{-5} m^2 s^{-1}. This yields a value for the Schmidt number of 0.94, which is nearly indistinguishable from unity.

Substitution of the definitions of Sh and Re into Eq. (D.21), assuming a value of $B(\mathrm{Sc}) \approx 1$, and rearranging gives

$$\tilde{k} = \tilde{D}\left(\frac{U}{L\tilde{\nu}}\right)^{1/2}. \qquad \text{(D.22)}$$

The mass transfer coefficient calculated using the above estimates of U and $\tilde{\nu}$, along with the value of $\tilde{D}$ (not $\tilde{D}'$) from Section D.4.1, is $\tilde{k}$ = 1.5 cm s^{-1}.

Note that the above estimate of U is a lower bound, since most of the well has a smaller cross-sectional area than the value of A used here. Further, any recirculation within the well will increase the actual value of U. Correspondingly, per the form of Eq. (D.22), this value of $\tilde{k}$ is also a lower bound.

D.4.3 Series resistances analysis

The exchange of the species of interest between the well-mixed gaseous and liquid regions is governed by the resistances to mass transfer represented by the liquid- and gas-phase boundary layers and the porous membrane. Using an analysis similar to that of Section 3.2.5, the overall mass transfer into the liquid from the base well can be expressed as

$$N_j = k_{T,j}\left(K_j \tilde{C}_j - C_{w,j}\right);\ k_{T,j} = \left[\frac{1}{k_{m,j}} + \frac{K_j \delta_m}{\tilde{D}'} + \frac{K_j}{\tilde{k}}\right]^{-1}, \qquad \text{(D.23)}$$

where $K_j = \alpha_j RT$ is the partition coefficient for species j as defined in Section 3.2.5. Estimates of the three mass transfer resistances represented in the definition of $k_{T,j}$ and of values of $k_{T,j}$ itself for all three species are given in Table D.1, for both 10% and 1% gas mixtures. As can be seen, the liquid-phase boundary layer resistance dominates for all three species.

D.4.4 Estimation of base well concentration scales

All of the results from this section are summarized in Table D.3.

D.4.4.1 Oxygen

An estimate of the gas-phase concentration of O_2 within the well can be obtained as follows. Assuming that the feed gas stream has been rigorously scrubbed of O_2, substitution of the overall flux expression of Eq. (D.23) into Eq. (D.17) and rearranging yields

$$\tilde{C}_{O_2} = \frac{k_{T,O_2} A C_{w,O_2}}{Q + k_{T,O_2} A K_{O_2} + \tilde{k}_5 \tilde{V} \tilde{C}_{NO}^2}, \qquad \text{(D.24)}$$

where $\tilde{k}_5$ = 7.3 × 10^3 M^{-2} s^{-1} (Atkinson et al., 2004) is the rate constant for the gas-phase oxidation of NO by O_2 [Reaction (E.14)]. Assuming the concentration of NO in the well is nearly identical to that in the gas feed, $\tilde{C}_{NO}$ equals 4.1 and 0.41 mM for 10% and 1% NO mixtures, respectively. It is worthwhile to examine the magnitudes of the second and third terms in the denominator of Eq. (D.24) relative to the first term (Q = 350 ml min^{-1}).

Table D.1. Mass transfer resistances and overall mass transfer coefficients for base well and membrane boundary layers.

Gas Mixture	Species	$\frac{1}{k_{m,j}}$	$\frac{K_j \delta_m}{\tilde{D}'}$	$\frac{K_j}{\tilde{k}}$	$k_{T,j}$
10% NO	O_2	32,000	0.42	2.0	3.1×10^{-5}
	NO	31,000	0.66	3.1	3.2×10^{-5}
	NO_2	280	3.1	15	3.4×10^{-3}
1% NO	O_2	32,000	0.42	2.0	3.1×10^{-5}
	NO	31,000	0.66	3.1	3.2×10^{-5}
	NO_2	900	3.1	15	1.1×10^{-3}

Units for the mass transfer resistances are s m^{-1}; those for $k_{T,j}$ are m s^{-1}. Values for the liquid-phase boundary layer resistance of NO_2 were calculated from Eq. (D.20).

The second term has a value of 6.9×10^{-3} ml min^{-1}, and the third term has values of 5.7 and 0.057 ml min^{-1} for 10% and 1% NO gas mixtures, respectively. Eq. (D.24) can thus be simplified to

$$\tilde{C}_{O_2} = \frac{k_{T,O_2} A C_{w,O_2}}{Q}. \qquad \text{(D.25)}$$

For air-equilibrated buffer, the well-mixed liquid concentration of O_2 is 254 μM. The base well gas-phase concentration for O_2 calculated from Eq. (D.25) is $\tilde{C}_{O_2}$ = 170 nM for both 10% and 1% NO mixtures.

D.4.4.2 Nitric oxide

Writing Eq. (D.17) for NO and moving all terms containing $\tilde{C}_{NO}$ to the left-hand side [again substituting in the overall flux expression of Eq. (D.23)], gives

$$\tilde{C}_{NO}\left(Q + K_{NO} k_{T,NO} A + 2\tilde{k}_5 \tilde{V} \tilde{C}_{NO} \tilde{C}_{O_2}\right) = Q\tilde{C}_{f,NO} + k_{T,NO} A C_{w,NO}. \qquad \text{(D.26)}$$

The greatest $C_{w,NO}$ observed experimentally (Section 2.3.3) was less than 4 μM. Using this as an upper bound, for a 1% NO gas mixture the two terms on the right-hand side of Eq. (D.26) have values of 2.5 μmol s^{-1} and 1.6×10^{-5} μmol s^{-1}, respectively. Thus, the $C_{w,NO}$ term can be neglected for both 1% and 10% NO mixtures, since the first term will be ten times larger with the latter mixture.

Simplification of the left-hand side is facilitated by making the initial assumption that $\tilde{C}_{NO} \approx \tilde{C}_{f,NO}$. Making use of the estimate of $\tilde{C}_{O_2}$ from Section D.4.4.1, the values of the three terms within the parentheses on the left-hand side of Eq. (D.26) are calculated as 350, 1.1×10^{-2}, and 4.7×10^{-4} ml min^{-1}, respectively, for a 10% NO mixture. The

second two terms are thus negligible for both 10% and 1% NO mixtures, since the magnitude of the third term will be ten times smaller with 1% NO than with 10% NO. Eq. (D.26) thus reduces to $\tilde{C}_{\mathrm{NO}} \approx \tilde{C}_{f,\mathrm{NO}}$, as assumed.

D.4.4.3 Nitrogen dioxide

Estimation of the gas-phase NO_2 concentration proceeds in essentially the same manner as for NO and O_2. Writing Eq. (D.17) for NO_2, bringing all terms containing $\tilde{C}_{\mathrm{NO_2}}$ to the left-hand side of the equation, and substituting the overall flux expression of Eq. (D.23) gives

$$\tilde{C}_{\mathrm{NO_2}}\left(Q + k_{T,\mathrm{NO_2}} A K_{\mathrm{NO_2}}\right) = k_{T,\mathrm{NO_2}} A C_{w,\mathrm{NO_2}} + 2\tilde{k}_5 \tilde{V} \tilde{C}_{\mathrm{NO}}^2 \tilde{C}_{\mathrm{O_2}} . \qquad \text{(D.27)}$$

As with O_2, it is assumed that the feed stream has been completely scrubbed of NO_2 and thus $\tilde{C}_{f,\mathrm{NO_2}} = 0$. Eq. (D.27) can be simplified by separately comparing the two terms on the right-hand side and the two terms within the parentheses on the left-hand side. The magnitudes of these terms are reported in Table D.2.

Briefly, the quasi-steady concentration of NO_2 in the well-mixed liquid region ($C_{w,\mathrm{NO_2}}$) can be estimated from Eq. (2.14) using the values of $\overline{C}_{\mathrm{NO}}$ from Table 2.3 and assuming $C_{w,\mathrm{O_2}} = 254$ μM. These estimates of $C_{w,\mathrm{NO_2}}$ permit evaluation of the first term on the right-hand side of Eq. (D.27). The reaction term on the right-hand side of Eq. (D.27) and the mass transfer term within the parentheses on the left-hand side can be evaluated directly from previously computed quantities. Based upon the values reported in Table D.2, the mass balance for NO_2 from Eq. (D.27) can be reduced to

Table D.2. Quantities used to estimate the gas-phase NO_2 concentration scale.

Quantity	Units	10% NO	1% NO
$C_{w,\mathrm{NO_2}}$	pM	5.2 pM	1.6 pM
$k_{T,\mathrm{NO_2}} A C_{w,\mathrm{NO_2}}$	pmol s^{-1}	2.2×10^{-3}	2.2×10^{-4}
$2\tilde{k}_5 \tilde{V} \tilde{C}_{\mathrm{NO}}^2 \tilde{C}_{\mathrm{O_2}}$	pmol s^{-1}	32	0.32
Q	ml min^{-1}	350	350
$k_{T,\mathrm{NO_2}} A K_{\mathrm{NO_2}}$	ml min^{-1}	5.7	1.8

$$\tilde{C}_{NO_2} = \frac{2\tilde{k}_5 \tilde{V} \tilde{C}_{NO}^2 \tilde{C}_{O_2}}{Q}. \quad \text{(D.28)}$$

Eq. (D.28) gives estimates for $\tilde{C}_{NO_2}$ of 5.3 and 5.3×10^{-2} nM with 10% and 1% NO gas mixtures, respectively, which are included in Table D.3. These concentrations correspond to gas-phase NO_2 abundances of 0.13 ppm and 1.3×10^{-3} ppm, respectively, both of which are below the thresholds identified in Sections D.2 and D.3, respectively. It is thus reasonable to argue that no NO_2-mediated enhancement of NO_x uptake should be observed, in line with the experimental observations.

D.4.5 Effect of reactions on membrane and gas-phase boundary layer transport

If the reaction between NO and O_2 proceeds quickly enough, it has the potential to influence the rate of mass transfer across the porous membrane and the gas-phase boundary layer. The magnitude of both of these effects can be estimated using scaling arguments and the various concentration scales and mass transfer resistances calculated above.

D.4.5.1 Porous membrane

The effect of reactions on transport across the PTFE membrane can be estimated using the Damkohler number derived from the reaction-diffusion equation:

$$\mathrm{Da}_{m,j} = \frac{\left|\nu_j\right| \tilde{k}_5 \tilde{C}_{NO}^2 \tilde{C}_{O_2} \delta_m^2}{\tilde{D}' \left(\Delta \tilde{C}_j\right)_m^*}. \quad \text{(D.29)}$$

The v_j term is the stoichiometric coefficient for species j. The $\left(\Delta\tilde{C}_j\right)_m^*$ term is the scale for the concentration difference across the membrane, which can be calculated from the series resistances information in Table D.1 as

$$\left(\Delta\tilde{C}_j\right)_m^* = k_{T,j}\frac{K_j\delta_m}{\tilde{D}'}\cdot\left(\Delta\tilde{C}_j\right)^*, \tag{D.30}$$

where $\left(\Delta\tilde{C}_j\right)^*$ is the scale for the overall gas-phase-equivalent concentration difference between the well-mixed regions of the liquid and gas phases. For NO and NO_2, $\left(\Delta\tilde{C}_j\right)^* \sim \tilde{C}_j$, whereas for O_2 $\left(\Delta\tilde{C}_{O_2}\right)^* \sim C_{w,O_2}K_{O_2}^{-1}$.

Relevant values of $\left(\Delta\tilde{C}_j\right)_m^*$ and $Da_{m,j}$ are summarized in Table D.3. As can be seen, NO oxidation is anticipated to negligibly influence transport of NO and O_2, whereas the moderate values of Da_{m,NO_2} imply that formation of NO_2 will perturb the NO_2 concentration profile within the membrane somewhat. These values of Da_{m,NO_2} are not so large as to invalidate the conclusions of Section D.4.4.3, however, since a modestly increased mass transfer resistance of the membrane will still be negligible compared to that of the liquid-phase boundary layer.

D.4.5.2 Gas-phase boundary layer

The effect of reactions on transport across the gas-phase boundary layer can be estimated in a similar fashion as for the porous membrane. Modeling the boundary layer as a stagnant film of thickness $\delta_g = \tilde{D}/\tilde{k}$ permits definition of the Damkohler number

Table D.3. Estimation of the significance of NO oxidation on gas-phase boundary layer and porous membrane transport.

Parameter	10% NO			1% NO		
	O_2	NO	NO_2	O_2	NO	NO_2
$\tilde{C}_j$	170 nM	4.1 mM	5.3 nM	170 nM	0.41 mM	53 pM
$\tilde{x}_{NO_2}$	–	–	0.13 ppm	–	–	1.3 ppb
$\tilde{x}_{NO_2,max}$ [a]	–	–	0.55 ppm	–	–	0.17 ppm
$\left(\Delta\tilde{C}_j\right)^*$	8.7 mM	4.1 mM	5.3 nM	8.7 mM	0.41 mM	53 pM
$\left(\Delta\tilde{C}_j\right)^*_m$	120 nM	84 nM	56 pM	120 nM	8.4 nM	0.18 pM
$Da_{m,j}$	2×10^{-4}	5×10^{-4}	0.79	2×10^{-6}	5×10^{-5}	2.5
$\left(\Delta\tilde{C}_j\right)^*_g$	540 nM	390 nM	0.27 nM	540 nM	39 nM	0.85 pM
$Da_{g,j}$	4×10^{-3}	9×10^{-3}	11	4×10^{-5}	9×10^{-4}	34
Da'_{m,NO_2}	–	–	8×10^{-3}	–	–	8×10^{-3}
Da'_{g,NO_2}	–	–	0.58	–	–	0.55

[a] Thresholds for $\tilde{x}_{NO_2}$ at 10% and 1% NO are as calculated in Sections D.2 and D.3, respectively.

$$\mathrm{Da}_{g,j} = \frac{|\nu_j| \tilde{k}_5 \tilde{C}_{\mathrm{NO}}^2 \tilde{C}_{\mathrm{O_2}} \delta_g^2}{\tilde{D}\left(\Delta \tilde{C}_j\right)_g^*} = \frac{|\nu_j| \tilde{k}_5 \tilde{C}_{\mathrm{NO}}^2 \tilde{C}_{\mathrm{O_2}} \tilde{D}}{\tilde{k}^2 \left(\Delta \tilde{C}_j\right)_g^*}. \tag{D.31}$$

The value of $\left(\Delta \tilde{C}_j\right)_g^*$ can be calculated in a fashion analogous to that of $\left(\Delta \tilde{C}_j\right)_m^*$:

$$\left(\Delta \tilde{C}_j\right)_g^* = k_{T,j} \frac{K_j}{\tilde{k}} \left(\Delta \tilde{C}_j\right)^*. \tag{D.32}$$

Again, relevant values of $\left(\Delta \tilde{C}_j\right)_g^*$ and $\mathrm{Da}_{g,j}$ are summarized in Table D.3. As with the porous membrane, NO oxidation is expected to negligibly influence transport of NO and O_2 across the gas-phase boundary layer. Unlike in the porous membrane, the formation of NO_2 by NO oxidation will likely have some effect on the NO_2 concentration profile within the boundary layer for both 1% and 0.1% NO, as evidenced by the magnitudes of the values of $\mathrm{Da}_{g,\mathrm{NO_2}}$. These values are still small enough that any resulting augmentation or diminution of the mass transfer resistance of the gas-phase boundary layer should have a negligible effect on the overall transport from the well to the liquid, however, given the relative magnitudes of the respective resistances in Table D.1.

D.4.6 Effect of reactions on NO_2 concentration scales

Significant excess formation of NO_2 within either the porous membrane or the gas-phase boundary layer could cause the actual scales for the gas-phase NO_2 concentration to be greater than those listed in Table D.3. This is less of a concern for the boundary layer because its volume was implicitly included in the derivation of Eq. (D.28), but is still worthwhile to compute an estimate. The significance of the formation of NO_2 within a particular volume in terms of its capacity to influence the total amount of NO_2

present can be estimated by comparing the time scale of NO_2 formation to the time scale of transport of NO_2 through (alternatively, out of) that volume. The appropriate parameter $\mathrm{Da}'_{i,\mathrm{NO}_2}$ for each volume is similar to the $\mathrm{Da}_{m,\mathrm{NO}_2}$ and $\mathrm{Da}_{g,\mathrm{NO}_2}$ of Eqs. (D.29) and (D.31), respectively, but with the $\left(\Delta\tilde{C}_{\mathrm{NO}_2}\right)_i^*$ term in the denominator replaced by $\tilde{C}_{\mathrm{NO}_2}$:

$$\mathrm{Da}'_{m,\mathrm{NO}_2} = \frac{\left|\nu_{\mathrm{NO}_2}\right| \tilde{k}_5 \tilde{C}_{\mathrm{NO}}^2 \tilde{C}_{\mathrm{O}_2} \delta_m^2}{\tilde{D}' \tilde{C}_{\mathrm{NO}_2}}. \tag{D.33}$$

$$\mathrm{Da}'_{g,\mathrm{NO}_2} = \frac{\left|\nu_{\mathrm{NO}_2}\right| \tilde{k}_5 \tilde{C}_{\mathrm{NO}}^2 \tilde{C}_{\mathrm{O}_2} \tilde{D}}{\tilde{k}^2 \tilde{C}_{\mathrm{NO}_2}}. \tag{D.34}$$

The values of both $\mathrm{Da}'_{i,\mathrm{NO}_2}$ for gas mixtures of 1% and 10% NO less than unity, as shown in Table D.3. Accordingly, NO_2 formation by NO oxidation is not expected to significantly affect the NO_2 concentration scale in either of the two volumes.

D.5 Scaling analysis of radial intramembrane transport

As noted in Section 2.4.1, preliminary NO delivery experiments conducted with an unmasked membrane yielded unexpectedly high nitrite accumulation rates. It was hypothesized that radial diffusion within the porous membrane caused the effective mass transfer area to be much greater than the nominal 0.5-in diameter open well area. This effect was rationalized with the following scaling argument.

Neglecting reactions, the transport of a gas within the region of an unmasked membrane outside of the 0.5-in open area of the base well can be described by the following conservation equation:

$$0 = \tilde{D}' \left[\frac{1}{r} \frac{\partial}{\partial r} \left(r \frac{\partial C_j'}{\partial r} \right) + \frac{\partial^2 C_j'}{\partial z^2} \right], \tag{D.35}$$

with boundary conditions

$$C_j'(r = r_i, z) = \tilde{C}_j . \tag{D.36}$$

$$\frac{\partial C_j'}{\partial r}(r = r_o, z) = 0 . \tag{D.37}$$

$$\frac{\partial C_j}{\partial z}(r, z = 0) = 0 . \tag{D.38}$$

$$-\tilde{D}' \frac{\partial C_j'}{\partial z}(r, z = \delta_m) = K_j k_{m,j} \left[C_j'(r, z = \delta_m) - \frac{C_{w,j}}{K_j} \right]. \tag{D.39}$$

The positive z-axis points into the liquid from the membrane. Based upon the negligible resistance to axial mass transfer posed by the membrane relative to the liquid-phase boundary layer (Table D.1), the concentration for all $r < r_i$ (where $2 \cdot r_i$ is the diameter of the well) is essentially uniform and equal to $\tilde{C}_j$ [Eq. (D.36)]. It is assumed that the membrane is sealed from the atmosphere at $r = r_o$ by an impregnated grease barrier [Eq. (D.37)] and that the solid body of the PTFE insert represents an impermeable barrier at $z = 0$ [Eq. (D.38)]. The final boundary condition matches the intramembrane flux in the positive z-direction with the convective transport in the liquid. For simplicity, a uniform mass transfer coefficient is assumed.

A useful simplification of Eq. (D.35) can be obtained by defining the *z*-averaged concentration of species *j*:

$$\bar{C}'_j(r) \equiv \frac{1}{\delta_m}\int_0^{\delta_m} C'_j(r,z)\,dz\,. \tag{D.40}$$

Application of this same *z*-averaging to the differential equation of Eq. (D.35) and canceling the intramembrane diffusivity yields

$$0 = \frac{1}{r}\frac{\partial}{\partial r}\left(r\frac{\partial \bar{C}'_j}{\partial r}\right) + \frac{1}{\delta_m}\int_0^{\delta_m}\frac{\partial^2 C'_j}{\partial z^2}\partial z\,. \tag{D.41}$$

The integral term can be evaluated by using the boundary conditions of Eqs. (D.38) and (D.39):

$$\int_0^{\delta_m}\frac{\partial^2 C'_j}{\partial z^2}\partial z = \left.\frac{\partial C'_j}{\partial z}\right|_0^{\delta_m} = -\frac{K_j k_{m,j}}{\tilde{D}'}\left(C'_j - \frac{C_{w,j}}{K_j}\right). \tag{D.42}$$

Due to the extremely small aspect ration of the porous membrane (ratio of thickness to diameter of approximately 0.0035), the variation of C'_j in the *z*-direction is expected to be negligible, and thus $C'_j = \bar{C}'_j$ to good approximation. Eq. (D.41) can thus be written as

$$0 = \frac{1}{r}\frac{d}{dr}\left(r\frac{d\bar{C}'_j}{dr}\right) - \frac{K_j k_{m,j}}{\delta_m \tilde{D}'}\left(\bar{C}'_j(r) - \frac{C_{w,j}}{K_j}\right), \tag{D.43}$$

where the derivatives have been written with total differentials to indicate that $\bar{C}'_j$ is a function of a single independent variable. The boundary conditions of Eqs. (D.36) become

$$\bar{C}'_j(r_i) = \tilde{C}_j\,. \tag{D.44}$$

$$\frac{d\bar{C}_j'}{dr} = 0 . \tag{D.45}$$

To permit more ready examination of the significance of the axial transport term in Eq. (D.43), non-dimensionalize the problem with

$$\Theta_j = \frac{\bar{C}_j' - C_{w,j}/K_j}{\tilde{C}_j - C_{w,j}/K_j} ; \ \eta = \frac{r}{r_o} ; \ \eta_i = \frac{r_i}{r_o} . \tag{D.46}$$

The non-dimensional forms of Eqs. (D.43)-(D.45) are

$$0 = \frac{1}{\eta}\frac{d}{d\eta}\left(\eta \frac{d\Theta_j}{d\eta}\right) - \kappa_j \Theta_j ; \ \kappa_j = \frac{K_j k_{m,j} r_o^2}{\delta_m \tilde{D}'} . \tag{D.47}$$

$$\Theta_j(\eta_i) = 1 ; \ \frac{d\Theta_j}{d\eta}(1) = 0 . \tag{D.48}$$

The coefficients of the axial transport terms of Eq. (D.47) are similar for NO and O_2: $\kappa_{NO} = 2.1$ and $\kappa_{O_2} = 1.3$. Thus, the concentrations of both species will be non-uniform throughout the membrane, with Θ_{NO} and Θ_{O_2} both varying between zero and one. Nitric oxide and oxygen thus coexist within the unmasked membrane, presumably resulting in significant formation of NO_2 and corresponding adventitious formation of nitrite. Masking the membrane via thermal lamination, as mentioned in Section 2.4.1 and described in detail in Section F.2, was thus crucial to the proper functioning of the NO delivery system.

Appendix E

Gas-Phase Scaling Arguments for Delivery of NO_2

E.1 Introduction

The primary question to be addressed in this analysis is whether the gas-phase reactions (Section E.3) have the capability to influence the distribution of nitrogen-containing species entering the liquid. If N_2O_4 hydrolysis is significant, then some fraction of the entering NO_2/N_2O_4 will be converted to nitrous and nitric acids (together, 'oxyacids') which are essentially unreactive in the buffered liquid. Further, if the entire mechanism of Reactions (E.10) through (E.14) is operative, net conversion of nitrous acid to nitric acid is possible. To see this, consider the stoichiometry of the overall mechanism assuming all reactions go forward to completion, represented by the sum of 4×(E.10) + 4×(E.11) + 2×(E.12) + 2×(E.13) + 1×(E.14):

$$4\,NO_2 + 2\,H_2O + O_2 \longrightarrow 4\,HNO_3\,. \qquad \text{(E.1)}$$

The gas-phase chemistry thus has the capability to skew the nitrite yield Eq. (3.47) to an extent that varies directly with the extent to which the overall mechanism described by Reaction (E.1) goes to completion.

The discussion of scaling in the headspace begins with an analysis of the transient behavior there (Section E.2). The remainder is then an examination of various scaling arguments describing significant features of the gas-phase chemistry under delivery conditions. It will be shown that the only reaction capable of proceeding at a rate

sufficient to influence the distribution of nitrogen-oxygen species reaching the liquid is N_2O_4 hydrolysis [forward Reaction (E.11)]. [To note, a sensitivity study performed on the various model parameters (Section 3.4.3.2) demonstrated that under simulated delivery conditions even the hydrolysis reaction could be neglected.] The effects of gas-phase chemistry on mass transfer across the gaseous boundary layer are also shown to be negligible.

E.2 Relaxation time scale for transient phenomena

The complete mass balance for species *j* in the headspace is [Eq. (3.4)].

$$\tilde{V}\frac{d\tilde{C}_j}{dt} = Q\left(\tilde{C}_{j,f} - \tilde{C}_j\right) - \tilde{k}_j A\left(\tilde{C}_j - \tilde{C}_{j,i}\right) + \tilde{V}\tilde{R}_j . \tag{E.2}$$

For the purposes of illustration, assume the reaction term represents a first-order decomposition of *j*, where $\tilde{R}_j = -\tilde{k}_R \tilde{C}_j$. Non-dimensionalizing with

$$\theta = \frac{\tilde{C}_j}{\tilde{C}_{j,f}};\ \theta_i = \frac{\tilde{C}_{j,i}}{\tilde{C}_{j,f}};\ \tau = \frac{t}{t^*} \tag{E.3}$$

yields

$$\frac{d\theta}{d\tau} = \frac{Qt^*}{\tilde{V}}(1-\theta) - \frac{\tilde{k}_j A t^*}{\tilde{V}}(\theta - \theta_i) - \tilde{k}_R t^* \theta . \tag{E.4}$$

Collecting together all of the θ terms in Eq. (E.4) yields

$$\frac{d\theta}{d\tau} = \frac{Q}{\tilde{V}}t^* + \frac{\tilde{k}_j A}{\tilde{V}}t^*\theta_i - t^*\left[\frac{Q}{\tilde{V}} + \frac{\tilde{k}_j A}{\tilde{V}} + \tilde{k}_R\right]\theta . \tag{E.5}$$

Given the form of the θ term on the right hand side of Eq. (E.5), it is natural to choose the time scale such that

$$t^* = \left[\frac{Q}{\tilde{V}} + \frac{\tilde{k}_j A}{\tilde{V}} + \tilde{k}_R \right]^{-1}. \tag{E.6}$$

Eq. (E.5) becomes

$$\frac{d\theta}{d\tau} = \alpha_r + \alpha_e \theta_i - \theta \,;\; \alpha_r = \left[1 + \frac{\tilde{k}_j A}{Q} + \frac{\tilde{k}_R \tilde{V}}{Q} \right]^{-1} \,;\; \alpha_e = \left[1 + \frac{Q}{\tilde{k}_j A} + \frac{\tilde{k}_R \tilde{V}}{\tilde{k}_j A} \right]^{-1}. \tag{E.7}$$

Assuming an arbitrary initial concentration $\theta(0) = \theta_o$, the solution to Eq. (E.7) is

$$\theta(\tau) = (\alpha_r + \alpha_e \theta_i) - (\alpha_r + \alpha_e \theta_i - \theta_o) \cdot \exp[-\tau]. \tag{E.8}$$

Of primary interest in the result of Eq. (E.8) is the argument to the exponential, where the scaling of τ controls the time scale of approach of θ to its steady value. Examining Eq. (E.6), the scale of $1/t^*$ will always be determined by the term(s) of greatest magnitude. That is, the fastest of the three processes (inflow/outflow, transport to the gas-liquid interface, and homogeneous gas-phase reaction) will always determine the scale of the overall relaxation time constant of the headspace dynamics. An implication of this result is that a known value of any of these time scales represents an upper limit on the relaxation time scale, since any process with a greater time scale would contribute negligibly in Eq. (E.6).

In the case of the present system the residence times are directly known, with values of 5 s and 7 s for gas flow rates of 365 sccm and 250 sccm, respectively. These residence times are negligible compared to the elapsed interval before the first samples

were withdrawn in all experiments. Thus, given that the calculated residence times are an upper limit on the headspace relaxation time, it is appropriate to disregard transient phenomena in the gas phase. The resulting mass balance is

$$0 = Q\left(\tilde{C}_{j,f} - \tilde{C}_j\right) - \tilde{k}_j A\left(\tilde{C}_j - \tilde{C}_{j,i}\right) + \tilde{V}\tilde{R}_j, \tag{E.9}$$

which is Eq. (3.6) in the text. As in the text, it will be assumed that all $\tilde{k}_j \approx \tilde{k}_{H_2O}$, with $\tilde{k}_{H_2O}$ as in Table 3.1.

E.3 Chemical mechanism

The gas-phase chemistry of NO_2 in the presence of O_2 and H_2O comprises the following set of reactions.

$$2\,NO_2 \underset{}{\overset{\tilde{K}_1}{\rightleftharpoons}} N_2O_4\,. \tag{E.10}$$

$$N_2O_4 + H_2O \underset{\tilde{k}_{-2}}{\overset{\tilde{k}_2}{\rightleftharpoons}} HNO_2 + HNO_3\,. \tag{E.11}$$

$$2\,HNO_2 \underset{\tilde{k}_{-3}}{\overset{\tilde{k}_3}{\rightleftharpoons}} N_2O_3 + H_2O\,. \tag{E.12}$$

$$N_2O_3 \underset{}{\overset{\tilde{K}_4}{\rightleftharpoons}} NO + NO_2\,. \tag{E.13}$$

$$2\,NO + O_2 \xrightarrow{\tilde{k}_5} 2\,NO_2\,. \tag{E.14}$$

Note that $\tilde{k}_3$ here refers to a different reaction than does k_3 in the text: namely, the gas-phase condensation of two molecules of nitrous acid, as opposed to the aqueous-phase reaction of NO_2 with ABTS. Also, although estimates are available for the reverse rate constant of Reaction (E.14) (Rosser, 1956), only the forward reaction is fast enough to

potentially be relevant. Reactions (E.10) and (E.13) are assumed to be fast enough that equilibria characterized respectively by the constants $\tilde{K}_1$ and $\tilde{K}_4$ will hold at every point within the gas phase. The above mechanism is adapted from the literature (from, for example, Denbigh and Prince, 1947). Numerical values for the rate and equilibrium constants are provided in Table E.1.

E.4 Scales for interfacial concentrations

The scale for the driving force for transport through the gas-phase boundary layer (gas-BL) must be defined with care, because if $\tilde{C}_j \sim \tilde{C}_{j,i}$ then it is possible that $\left(\tilde{C}_j - \tilde{C}_{j,i}\right)^* \Big/ \tilde{C}_j^* \ll 1$. For convenience, define $\left(\Delta\tilde{C}_j\right)^* \equiv \left(\tilde{C}_j - \tilde{C}_{j,i}\right)^*$.

E.4.1 HNO_2 and HNO_3

HNO_2 and HNO_3 are both strong acids, and as such are expected to rapidly and completely deprotonate upon entering the liquid. Thus, even though the concentrations of the conjugate bases NO_2^- and NO_3^- will be appreciable, the interfacial concentrations of the protonated acids are expected to be essentially zero. The relations $\tilde{C}_{\mathrm{HNO_x},i} \approx 0$ and $\left(\Delta\tilde{C}_{\mathrm{HNO_x}}\right)^* \Big/ \tilde{C}_{\mathrm{HNO_x}}^* \approx 1$ should thus hold for both species.

E.4.2 NO_2 and N_2O_4

The non-linearity of the mass balance equations for NO_2 and N_2O_4 (together 'RN'; see Section 3.2.5.4) prevents straightforward *a priori* derivation of analytical expressions for $\tilde{C}_{j,i} \big/ \tilde{C}_j$. However, in general it is expected that the resistance to mass

Table E.1. Gas-phase rate and equilibrium constants for NO_2/N_2O_4 mechanism.

Constants reported in the literature in terms of partial pressure units are converted to concentration units assuming ideal gas behavior.

Parameter	Value	Units	Reference
$\tilde{K}_1$	168	M^{-1}	Schwartz and White, 1981
$\tilde{k}_2$	328	$M^{-1}\ s^{-1}$	England and Corcoran, 1974
$\tilde{k}_{-2}$	5.85×10^3	$M^{-1}\ s^{-1}$	England and Corcoran, 1974
$\tilde{k}_3$	570	$M^{-1}\ s^{-1}$	Chan et al., 1976
$\tilde{k}_{-3}$	1.70×10^3 [a]	$M^{-1}\ s^{-1}$	Chan et al., 1976
$\tilde{K}_4$	7.77×10^{-2}	M	Wiberg and Aylett, 2001
$\tilde{k}_5$	7.3×10^3	$M^{-2}\ s^{-1}$	Atkinson et al., 2004

[a] The rate constant k_1 of Chan et al. after conversion to concentration units is equal to $\tilde{k}_{-3}/\tilde{K}_4$; the value reported here makes use of the $\tilde{K}_4$ of Wiberg.

transfer imposed by the liquid-phase boundary layer (liq-BL) will be comparable to or greater than that imposed by the gas-BL. At minimum, it is expected that $\left(\Delta\tilde{C}_j\right)^* \lesssim \tilde{C}_j^*$; if the resistance of the gas-BL is sufficiently small relative to that of the liq-BL, then $\left(\Delta\tilde{C}_j\right)^* \ll \tilde{C}_j^*$ will hold. In either case, it is not appropriate to make the simplifying assumption that $\left(\Delta\tilde{C}_j\right)^* \sim \tilde{C}_j^*$ for NO_2 and N_2O_4. Any scaling estimates for interfacial transport of RN must therefore carefully consider the distinction between these two scales.

It is possible to make use of the experimentally observed product accumulation rates to develop an estimate for $\left(\Delta\tilde{C}_{NO_2}\right)^*$. For all NO_2 mixtures studied, the majority of RN in the gas phase is predicted to be present as NO_2 ($\tilde{\varphi} > 0.9$). Accordingly, to first order it is reasonable to assign substantially all of the entry of RN into the liquid, as detected by the accumulation of nitrite and nitrate, to transport of NO_2 across the gas-BL. In order for NO_2 transport to explain the observed product accumulation rates, the total mole accumulation rate of stable products must be on the same order of magnitude as the mole rate of transport of NO_2 across the gas-BL.

$$2 \cdot d\overline{C}_{NO_2^-} V \sim \tilde{k} A \left(\Delta\tilde{C}_{NO_2}\right)^* . \tag{E.15}$$

Twice the nitrite rate was used in Eq. (E.15) instead of the sum of the nitrite and nitrate rates because the putative HNO_3 impurity in the feed gas (see Section 3.4.2.1) makes the nitrate accumulation rate a less useful metric for transport of specifically RN, as opposed to nitrogen-oxygen species generally. Rearrangement of Eq. (E.15) provides estimates for $\left(\Delta\tilde{C}_{NO_2}\right)^*$, which are reported in Table E.2.

E.5 Scales for well-mixed concentrations

E.5.1 NO_2 and N_2O_4

The NO_2/N_2O_4 composition of the feed gas is specified, and the only other processes operative in the headspace are sinks for these species. As all of the chemistry of interest involves second order reactions, upper bounds for concentration scales are a useful starting point for analysis. As such, *a priori* assignment of the NO_2 and N_2O_4 concentration scales to their respective feed concentrations is warranted, as $\tilde{C}_j^* = \tilde{C}_{j,f}$. Since the scale $\tilde{C}_{NO_2}^*$ is not used in any subsequent calculations, only values for $\tilde{C}_{N_2O_4}^*$ are provided in Table E.2.

E.5.2 H_2O

Given that the entering gas stream is dry, an upper limit estimate of the H_2O concentration can be constructed by assuming that consumption by either hydrolysis reaction is negligible. Eq. (E.9) thus reduces to

$$\tilde{C}_{H_2O}^* = \tilde{C}_{H_2O,sat}\left(\frac{\tilde{\kappa}_{H_2O}}{1+\tilde{\kappa}_{H_2O}}\right);\ \tilde{\kappa}_{H_2O} = \frac{\tilde{k}_{H_2O}A}{Q}, \tag{E.16}$$

which is directly analogous to the form of Eq. (3.9). This estimate represents an upper bound on the H_2O concentration scale; if N_2O_4 hydrolysis is sufficiently rapid, the actual H_2O concentration will be lower.

E.5.3 HNO_2

As no nitrous acid impurity in the feed gas is expected, the nitrous acid concentration will be dynamically determined by a balance between formation by N_2O_4 hydrolysis and loss/consumption by one of three processes: outflow, loss to the liquid, and self-condensation [Reaction (E.12)]. Neglecting self-condensation for the moment, which can only decrease $\tilde{C}_{\mathrm{HNO_2}}$, a nitrous acid concentration scale can be obtained from Eq. (E.9) as

$$\tilde{C}^*_{\mathrm{HNO_2}} = \frac{\tilde{k}_2 \tilde{C}^*_{\mathrm{H_2O}} \tilde{C}^*_{\mathrm{N_2O_4}} \tilde{V}}{\tilde{k}_{\mathrm{HNO_2}} A + Q}. \tag{E.17}$$

Implicit in Eq. (E.17) is an assumption that $\left(\Delta\tilde{C}_{\mathrm{HNO_2}}\right)^* \sim \tilde{C}^*_{\mathrm{HNO_2}}$ (or, alternatively, that $\tilde{C}_{\mathrm{HNO_2}} \gg \tilde{C}_{\mathrm{HNO_2},i}$). This assumption will be justified below for both HNO_2 and HNO_3. The HNO_2 concentration scales obtained from Eq. (E.17) for the various f_N are then valid upper-bound estimates that can be used to evaluate the significance of HNO_2 self-condensation.

E.5.4 HNO_3

As with HNO_2, the primary mechanism for formation of nitric acid in the gas phase is N_2O_4 hydrolysis. Unlike HNO_2, there is reason to believe the feed gas contains a significant HNO_3 impurity (Section 3.4.2.1); accordingly, the concentration scale derived from Eq. (E.9) is

$$\tilde{C}^*_{\mathrm{HNO_3}} = \frac{\tilde{C}_{\mathrm{HNO_3},f}}{1+\tilde{\kappa}_{\mathrm{HNO_3}}} + \frac{\tilde{k}_2 \tilde{C}^*_{\mathrm{H_2O}} \tilde{C}^*_{\mathrm{N_2O_4}} \tilde{V}}{\tilde{k}_{\mathrm{HNO_3}} A + Q}. \tag{E.18}$$

The definition of $\tilde{\kappa}_{\mathrm{HNO_3}}$ is directly analogous to that of $\tilde{\kappa}_{\mathrm{H_2O}}$ in Eq. (E.16). As above, $\tilde{C}_{\mathrm{HNO_3}} \gg \tilde{C}_{\mathrm{HNO_3},i}$ is assumed.

Since the magnitude of the HNO_3 impurity is estimated from the difference ΔdC between the observed HNO_3 and HNO_2 accumulation rates for each f_N (see Section 3.4.2.1), it is more convenient to rewrite the first term on the right hand side of Eq. (E.18) in terms of this quantity. The quantity $\tilde{C}_{\mathrm{HNO_3},f} \Big/ \left(1+\tilde{\kappa}_{\mathrm{HNO_3}}\right)$ represents the portion of the HNO_3 concentration in the headspace due to the impurity (after accounting for the headspace dynamics), with the remainder attributed to N_2O_4 hydrolysis. Since $\tilde{C}_{\mathrm{HNO_3},i} \approx 0$ (Section E.4), the following expression for $\delta_{\mathrm{HNO_x}}$ can be derived.

$$\delta_{\mathrm{HNO_x}} = \frac{\tilde{k}_{\mathrm{HNO_3}} A}{V} \frac{\tilde{C}_{\mathrm{HNO_3},f}}{1+\tilde{\kappa}_{\mathrm{HNO_3}}}. \tag{E.19}$$

Substitution of Eq. (E.19) into Eq. (E.18) yields

$$\tilde{C}^*_{\mathrm{HNO_3}} = \frac{\delta_{\mathrm{HNO_x}} V}{\tilde{k}_{\mathrm{HNO_3}} A} + \frac{\tilde{k}_2 \tilde{C}^*_{\mathrm{H_2O}} \tilde{C}^*_{\mathrm{N_2O_4}} \tilde{V}}{\tilde{k}_{\mathrm{HNO_3}} A + Q}. \tag{E.20}$$

E.5.5 N_2O_3, NO and O_2

It is shown below (Section E.6) that the effect of HNO_2 self-condensation on the final distribution of stable products is negligible. Therefore, concentration scales for N_2O_3 and NO are not required for this analysis. As O_2 only participates in Reaction (E.14) and formation of NO is negligible, the concentration scale for O_2 is unnecessary as well.

E.6 Scales for reaction velocities

Define the reaction velocity $\tilde{\xi}_n$ of each reaction *n* as the contribution $\tilde{\mu}_{j,n}$ of reaction *n* to the mole rate of formation of species *j*, divided by the stoichiometric coefficient $\tilde{\nu}_{j,n}$ of species *j* in reaction *n*. The $\tilde{\nu}_{j,n}$ for reactant and product species in each reaction are taken as strictly negative and positive, respectively. By this definition, $\tilde{\xi}_n$ for a given reaction is independent of the species whose $\tilde{\mu}_{j,n}$ and $\tilde{\nu}_{j,n}$ are used to construct it. The quantity $\tilde{\xi}_n / V$ then becomes a scaling estimate of the effect of gas-phase reaction *n* on the product accumulation rates in the liquid. This quantity can be directly compared with the magnitude of the observed product accumulation rates as an upper limit for the relative significance of reaction *n*.

The reaction velocity scale for N_2O_4 hydrolysis is $\tilde{\xi}_2 = \tilde{k}_2 \tilde{C}^*_{N_2O_4} \tilde{C}^*_{H_2O} \tilde{V}$, and that for HNO_2 self-condensation is $\tilde{\xi}_3 = \tilde{k}_3 \left(\tilde{C}^*_{HNO_2} \right)^2 \tilde{V}$. The values of $\tilde{\xi}_n / V$ for these two reactions are reported in Table E.2 along with the experimentally observed nitrite accumulation rates $\left(d\overline{C}_{NO_2^-} \right)$. (As before, the nitrite rates were used because they represent a criterion more specific to RN in arguing that the effect of the gas-phase reactions is small.) The relative magnitudes of $\tilde{\xi}_n / V$ with respect to $d\overline{C}_{NO_2^-}$ are also provided in Table E.2, in parentheses below each $\tilde{\xi}_n / V$ value. As can be seen, while it is reasonable to argue that HNO_2 self-condensation will proceed negligibly for all experimental purposes, it is not reasonable to argue the same for N_2O_4 hydrolysis, especially at higher f_N values. The negligibility of HNO_2 condensation permits

Reactions (E.12) through (E.14) to be ignored as well. It is worth re-stating that the estimate of $\tilde{\xi}_2/V$ in Table E.2 is an upper bound—the results presented below do not guarantee that N_2O_4 hydrolysis will be significant, they only prevent *a priori* elimination of the reaction from the governing equations. In particular, the assumption that $\tilde{C}_{N_2O_4,f}$ is a proper scale for the N_2O_4 concentration is questionable. Given the difficulty in generating more accurate scaling estimates, it was decided simply to retain the N_2O_4 hydrolysis term in the RN governing equation [Eq. (3.18)].

Reaction velocities are useful for ascertaining how close Reaction (E.11) is to equilibrium—that is, whether the HNO_2 and HNO_3 concentrations are sufficiently high that the mixed condensation reaction will appreciably diminish the net rate of hydrolysis of N_2O_4. A convenient metric to estimate the approach to equilibrium is $\tilde{\xi}_{-2}/\tilde{\xi}_2$, where $\tilde{\xi}_2$ is as above and $\tilde{\xi}_{-2} = \tilde{k}_{-2}\tilde{C}^*_{HNO_2}\tilde{C}^*_{HNO_3}\tilde{V}$. At equilibrium, and where each $\tilde{C}_j = \tilde{C}^*_j$, $\tilde{\xi}_{-2}/\tilde{\xi}_2 = 1$. Values of $\tilde{\xi}_{-2}/\tilde{\xi}_2$ are reported in Table E.2; as can be seen, all are sufficiently small to imply that buildup of the oxyacids will negligibly influence the kinetics. Consequently, explicit simulation of the gas-phase HNO_2 and HNO_3 concentrations is unnecessary. Incidentally, note that if not for the HNO_3 impurity the value of $\tilde{\xi}_{-2}/\tilde{\xi}_2$ at 0.001% NO_2 would be significantly smaller than the value reported in Table E.2, probably by at least one or two orders of magnitude.

E.7 Influence of reactions on H_2O concentration

Since N_2O_4 hydrolysis consumes water, if $\tilde{\xi}_2$ is sufficiently great the well-mixed concentration of H_2O may be affected. With a dry gas feed and aqueous solution

providing the source for evaporating water, the only sink other than N_2O_4 hydrolysis in Eq. (E.9) is outflow. Accordingly, if the quantity $f_{H_2O} = \tilde{\xi}_2 \cdot \left[Q\tilde{C}^*_{H_2O} \right]^{-1}$ is small then Eq. (E.16) remains a valid expression for $\tilde{C}^*_{H_2O}$ and, analogously, for $\tilde{C}_{H_2O}$. The values of f_{H_2O} reported in Table E.2 (calculated for Q = 365 sccm) indicate that N_2O_4 hydrolysis has a negligible effect on the gas-phase mass balance for water at NO_2 mixtures up to 0.1% and an appreciable but small effect at 1% NO_2.

E.8 Influence of N_2O_4 hydrolysis on boundary layer transport

Transport of the various species from the well-mixed region to the interface has the potential to be affected by reactions generally, and by N_2O_4 hydrolysis for this system in particular. The scaling argument that examines the strength of this potential effect can be developed as follows. Approximate the gas-BL as a stagnant film of thickness $x_g = \tilde{D}/\tilde{k}$, where $\tilde{D} = 10^{-5}\ \mathrm{m^2/s}$ and $\tilde{k} = 3\ \mathrm{cm/s}$ are representative estimates of the diffusivity and gas-phase mass transfer coefficient of the gas-phase species. Transport of species *j* across this film can be described by the differential equation

$$\tilde{D}\frac{d^2\tilde{C}_j}{dx^2} + \tilde{\nu}_{j,2}\tilde{k}_2\tilde{C}_{N_2O_4}\tilde{C}_{H_2O}, \tag{E.21}$$

where $\tilde{\nu}_{j,2}$ is defined as in Section E.6. The Damkohler number for species *j* derived from Eq. (E.21) is

$$\mathrm{Da}_j = \frac{\left|\tilde{\nu}_{j,2}\right| \tilde{k}_2 \tilde{C}^*_{N_2O_4} \tilde{C}^*_{H_2O} x_g^2}{\tilde{D}\left(\Delta\tilde{C}_j\right)^*}, \tag{E.22}$$

with $\left(\Delta\tilde{C}_j\right)^*$ defined as in Section E.4. Since NO_2 is in equilibrium with N_2O_4, the value of $\tilde{\nu}_{NO_2,2}$ equals –2 per the stoichiometry of Reaction (E.10).

Per the (fictitious) definition of x_g above, Eq. (E.22) can be rewritten as

$$\mathrm{Da}_j = \frac{\left|\tilde{\nu}_{j,2}\right| \tilde{k}_2 \tilde{C}^*_{N_2O_4} \tilde{C}^*_{H_2O} \tilde{D}}{\tilde{k}^2 \left(\Delta\tilde{C}_j\right)^*}. \qquad \text{(E.23)}$$

The Damkohler numbers of Eq. (E.23) represent the ratio between the rate of N_2O_4 hydrolysis in the gas-BL and the rate of transport of species *j* across the gas-BL. If Da_j is order unity or smaller, it can be assumed that N_2O_4 hydrolysis does not perturb $\tilde{k}$ from the unreactive $\tilde{k}_{H_2O}$ as experimentally determined.

Based on the analysis in Section E.7, an estimate for $\left(\Delta\tilde{C}_{H_2O}\right)^*$ derived from Eq. (E.16) should be appropriate; the value so calculated is reported in Table E.2. Per Section E.4.1, assumption of $\left(\Delta\tilde{C}_{HNO_x}\right)^* = \tilde{C}^*_{HNO_x}$ is warranted and the latter values have already been estimated (Sections E.5.3 and E.5.4). Values for $\left(\Delta\tilde{C}_{NO_2}\right)^*$ were computed previously (Section E.4.2). The values of Da_j for H_2O, HNO_2, HNO_3, and NO_2 are presented in Table E.2. As can be seen, N_2O_4 hydrolysis is predicted to have a negligible effect on the gas-BL transport of all species of interest.

Table E.2. Gas-phase chemistry scaling estimates for Q = 365 sccm.

Parameter	Units	f_N			
		0.001%	0.01%	0.1%	1%
$d\bar{C}_{NO_2^-}$	M s^{-1}	1.83×10^{-10}	5.47×10^{-9}	2.34×10^{-7}	5.83×10^{-6}
$\left(\Delta\tilde{C}_{NO_2}\right)^*$	M	3.44×10^{-10}	1.03×10^{-8}	4.42×10^{-7}	1.10×10^{-5}
$\tilde{C}^*_{N_2O_4}$	M	2.80×10^{-11}	2.80×10^{-9}	2.73×10^{-7}	2.23×10^{-5}
$\tilde{C}^*_{H_2O}$	M	1.06×10^{-3}			
$\left(\Delta\tilde{C}_{H_2O}\right)^*$	M	7.63×10^{-5}			
$\tilde{C}^*_{HNO_2}$	M	3.2×10^{-12}	3.2×10^{-10}	3.1×10^{-8}	2.6×10^{-6}
δ_{HNO_x}	M s^{-1}	1.5×10^{-9}	5.1×10^{-8}	1.7×10^{-8}	–
$\tilde{C}^*_{HNO_3}$	M	1.4×10^{-9}	5.1×10^{-9}	4.7×10^{-9}	2.6×10^{-6}
$\frac{\tilde{\xi}_2}{V}$ [a]	M s^{-1}	3.66×10^{-12} (0.020)	3.65×10^{-10} (0.067)	3.56×10^{-8} (0.15)	2.92×10^{-6} (0.49)
$\frac{\tilde{\xi}_3}{V}$ [a]	M s^{-1}	2.21×10^{-21} (1.2×10^{-11})	2.20×10^{-17} (4.0×10^{-9})	2.10×10^{-13} (9.0×10^{-7})	1.40×10^{-9} (2.4×10^{-4})
$\frac{\tilde{\xi}_{-2}}{\tilde{\xi}_2}$	–	2.7×10^{-6}	9.9×10^{-6}	9.2×10^{-5}	4.9×10^{-3}
f_{H_2O}	–	4.5×10^{-8}	4.5×10^{-6}	4.4×10^{-4}	3.6×10^{-2}
Da_{H_2O}	–	1.4×10^{-9}	1.4×10^{-7}	1.3×10^{-5}	1.1×10^{-3}
Da_{HNO_2}	–	3.4×10^{-2}			
Da_{HNO_3}	–	7.7×10^{-5}	2.1×10^{-3}	2.2×10^{-2}	3.4×10^{-2}
Da_{NO_2}	–	6.3×10^{-4}	2.1×10^{-3}	4.8×10^{-3}	1.6×10^{-2}

[a] Quantities in parentheses are the ratios $\tilde{\xi}_n \Big/ \left(V\, d\bar{C}_{NO_2^-}\right)$ for the corresponding $\tilde{\xi}_n / V$.

Appendix F

Fabrication and Assembly Instructions and Parts List for NO Delivery Apparatus

F.1 Introduction

The upgraded nitric oxide delivery reactor described in Chapter 2, which eliminates the 'hot spot' occurring in the prior design of Wang and Deen (2003), was constructed by modifying a Millipore (Billerica, MA) Amicon 8050 ultrafiltration cell (50 mL nominal volume, catalog #5122). NO is introduced into the stirred aqueous solution via transport from an NO-containing gas stream across a porous, hydrophobic poly(tetrafluoroethylene) (PTFE) membrane with a thermally-laminated poly(vinylidene fluoride) (PVDF) mask (½″-diameter active mass transfer area) at the base of the reactor (Section F.2). A custom baseplate insert with an open area matching the ½″-diam. unmasked area of the laminated membrane was fabricated from mechanical grade PTFE rod to provide a flow channel for the NO gas stream (Section F.3).

A new cap for the cell was also fabricated from polycarbonate (PC) rod (Section F.4). The 'basic' cap design contains inlet and outlet ports connected to a loop of poly(dimethylsiloxane) (PDMS) (Silastic®; Dow Corning, Midland, MI) tubing for O_2 delivery (purchased as #EW-96115-10, Cole-Parmer, Vernon Hills, IL) and a port for sample removal via hypodermic syringe. Mounts for a World Precision Instruments (Sarasota, FL) ISO-NOP nitric oxide probe and for either an Instech (Plymouth Meeting, PA) quenched-fluorescence oxygen sensor or an Orion (Thermo Fisher Scientific,

Waltham, MA) Clark-electrode oxygen probe were added to this 'minimal' cap design for experiments requiring measurement of NO and O_2 concentrations. This custom cap was used because of certain undesirable characteristics of the stock cap, which was designed for ultrafiltration. A large pressure-release valve is built into the stock cap, which limits the top surface area available for ports and probe mounts and introduces significant excess interior volume. Also, the positioning of the inlet for the positive-pressure line on the side of the cap introduces the potential for a significant headspace volume, potentially complicating the kinetic behavior within the reactor. Fabrication of the custom cap avoided these undesirable features and provides the further benefit of a dramatically reduced marginal cost of creating additional caps.

The cell baseplate was itself turned down slightly to accommodate the custom insert (Section F.5.1), and the bottom surface of the stirrer was sanded down to avoid collisions between the stirrer and the laminated membrane (Section F.5.2). A pair of Viton gaskets is proposed as a possible alternative to the grease seal for the membrane (Section F.5.3). The connection between the NO delivery line and the inlet of the base insert was achieved using a multi-part fitting assembly (Section F.6). To note, the NO delivery line *must* be constructed solely of stainless steel and glass to rigorously exclude O_2. Also provided in this appendix (Section F.7) are instructions for fabrication of a custom soda lime column to scrub any higher nitrogen oxide (NO_x) impurities from the NO mixture. It is assumed that the gas manifold connections to the soda lime column and the ports in the reactor base (Section F.6) are 1/8″ stainless steel tubing, pre-swaged with nut and ferrule sets from a standard 1/8″ stainless steel Swagelok (Solon, OH) compression fitting. Assembly instructions for the reactor are provided in Section F.8.

All part numbers with unspecified vendors are for McMaster-Carr Supply Company (Dayton, NJ). All circular pieces of plastic film were cut using an OLFA (Rosemont, IL) CMP-001 compass-style cutter.

F.2 Laminated porous PTFE Membrane

The laminated PTFE membrane was constructed from one hydrophobic PTFE membrane (Advantec MFS, Dublin, CA, #T300A025A; 3 μm pore size, 25 mm diameter, 75 μm thickness, 83% porosity) and two sheets of PVDF film (#8675K92). The PVDF sheets were cut into annuli of o.d. 1.872″ and i.d. 0.5″, the latter matching the diameter of the well in the PTFE insert for the reactor base. The membrane was centered between the PVDF annuli and clamped between two 4″-square glass plates ($^1/_8$″ thick; #8476K141) with binder clips (e.g., #12755T73). The membrane was placed in a lab oven pre-heated to 180 °C for 12 min to melt the PVDF ($T_m \approx 165$ °C; El-Hibri and Paul, 1986). The PTFE of the porous membrane, which has $T_m > 300$ °C (Brandrup et al., 2005), is expected to be essentially unchanged by this process. Figure F.1 presents photographs of various steps in the membrane fabrication procedure.

F.3 Reactor base insert

The schematic for the baseplate insert is shown in Figure F.2. This insert mates with the inset at the base of the cell body, and the drilled inlet/outlet channels in the insert align with the slots in the lower cell side wall. The ½″-diam. well in the obverse face of the insert aligns with the matching ½″-diam. open area of the masked PTFE membrane (Section F.2). The starting material for this part was 3″-diam. PTFE rod (#8803K22).

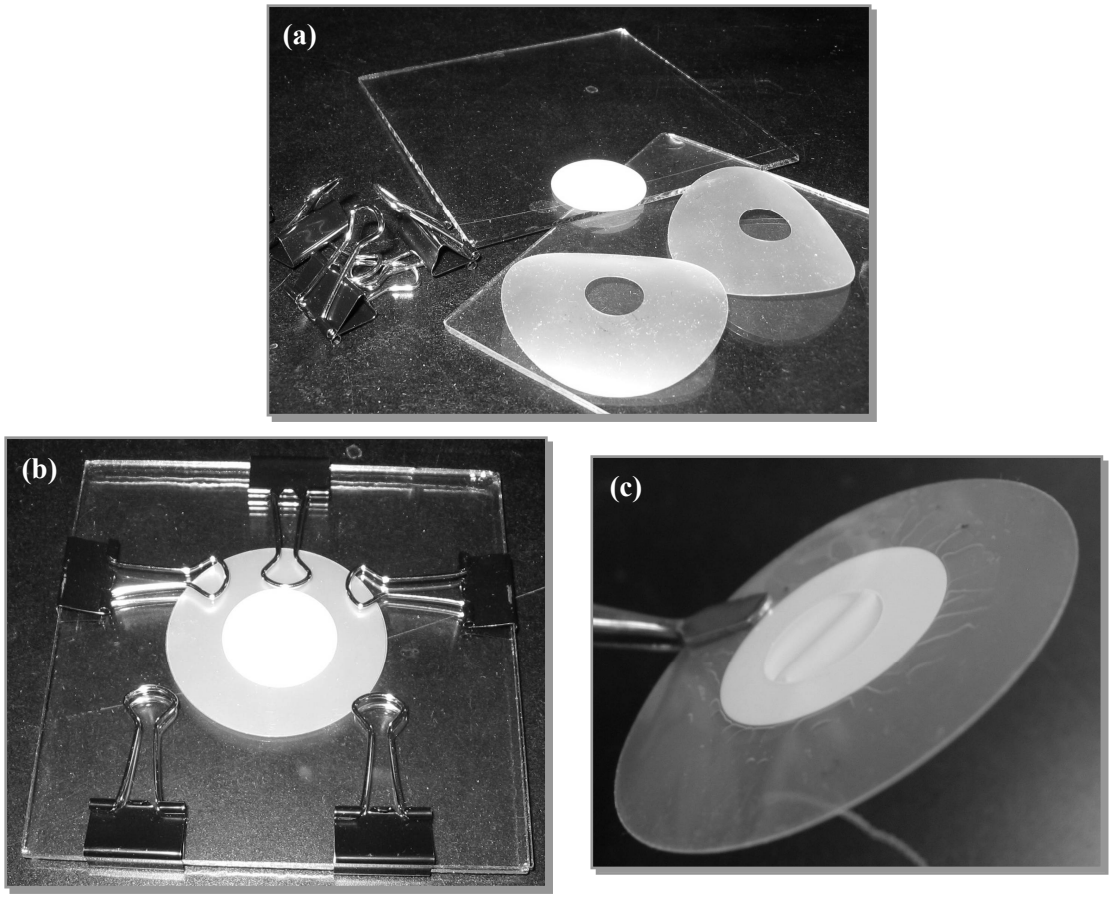

Figure F.1. Images of laminated membrane fabrication procedure.

Depicted are: (a) the individual components of the membrane; (b) the membrane and PVDF annuli clamped between glass plates, before heating; and (c) the final membrane, after heating and cooling.

Detailed fabrication instructions

0. Definitions:
   a. Obverse side: Side (axial-normal) out of which the NO flow channel is exposed
   b. Reverse side: Side (axial-normal) out of which protrudes the mating nub for the baseplate
   c. Outer edge: Radial-normal surface of the part
   d. Thickness: Axial dimension (linear)

1. Cold saw: cut a ~3/4″ long piece from 3″-diam. Teflon rod stock
   a. A smaller diameter of rod stock could be used; 3″-diam. stock permits plenty of leeway in the initial round-off of the outer surface in step (3.b)

2. Lathe, with spider as needed to leave ~¼″ of part in chuck jaws: Turn part to total thickness
   a. Face one side of part
   b. Flip part; face other side of part
   c. WITHOUT CHANGING Z-DISPLACEMENT, remove part, measure with calipers, and set lathe z-offset to measured thickness
   d. Return part to chuck; turn to total part thickness (0.540″ nominal)
   e. Before removing part from chuck after finishing (d), press tailstock center into part to form the anchor cavity (side with cavity becomes the reverse side)

3. Lathe, with tailstock center: Turn part to total diameter, turn base hub to diameter
   a. Remove part and spider; close chuck jaws such that radial extent of jaws is smaller than the final outer radius of the part; re-mount part, braced between the tailstock center and the partly closed jaws
   b. Turn part to ~ 2″ diameter (eliminates any eccentricity before diameter measurement and ensures that part fits in caliper jaws)
   c. WITHOUT CHANGING R-DISPLACEMENT, remove part from chuck and measure part diameter with calipers
   d. Return part to lathe; set r-offset to the diameter measured in (c)
   e. Turn full thickness of part to outer diameter (1.90″ nominal)
   f. Turn ~0.1″ thickness from the reverse side of the part down to the hub diameter (0.865″ nominal); DO NOT CHANGE Z-DISPLACEMENT
   g. Remove part from chuck; measure axial thickness of main section of part; set lathe z-offset to this thickness
   h. Turn main section of part to thickness (0.307″ nominal), exposing the remainder of the hub on the reverse side of the part
   i. Remove part from chuck; measure diameter of part and hub with calipers and compare to schematic; measure full thickness of part and thickness of main section and compare to schematic; turn part further if refinements are necessary

4. Lathe, with tailstock drill chuck and center-cutting ½″ end mill: Cut footspace well
   a. With end mill mounted in drill chuck, lock tailstock movement within reach of part surface

b. With lathe halted, lightly ground end mill against part; zero tailstock extension scale
c. Engage lathe; plunge a 0.238″ hole in the center of the obverse face of the part
    i. Note that this method tends to overshoot the depth of the plunge by ~0.01″, at minimum

5. Milling machine, with end mill long enough to mill full thickness of full-width section of part (probably 1/8″ end mill or larger): face two opposing edges
    a. Brace part on parallels (axial rotation irrelevant) with obverse side up and approximately ½″ of the part extending past the side of the vise
    b. With flutes of mill spanning the entire thickness of the full-diameter section of the part, edge a region approximately ½″ wide on the outer edge of the part
        i. Provides a flat surface against which the Luer fitting will rest
        ii. A very small amount of material is removed in this step
    c. Without removing part from vise, raise mill and translate to other side part not grasped by vise jaws; lower mill until flutes again span the entire thickness of the full-diameter section of the part
    d. Being careful not to contact the vise jaws or parallels with the end mill, again edge a region approximately ½″ wide on the edge of the part

6. Drill press, with center (#4) or spotting ($^{1}/_{8}$″ or $^{3}/_{16}$″) drill and #21 bit (for 10-32 tap)
    a. Using calipers and a center punch, mark the location for the center of one of the tapped holes for the Luer fittings (axial center location for the hole is 0.152″ from the obverse face)
    b. Mount part in vise clamp such that the drill hole slants slightly toward the obverse face, aiming to put the edge of the exit hole roughly 0.5 mm from the obverse face
    c. Start the hole with the center drill or spotting drill
    d. Finish the hole with the #21 bit
    e. Repeat (a) through (d) for the other Luer fitting hole

7. Tapping station, with 10-32 tap
    a. Tap the #21-drilled holes until the tap reaches ~½″ penetration

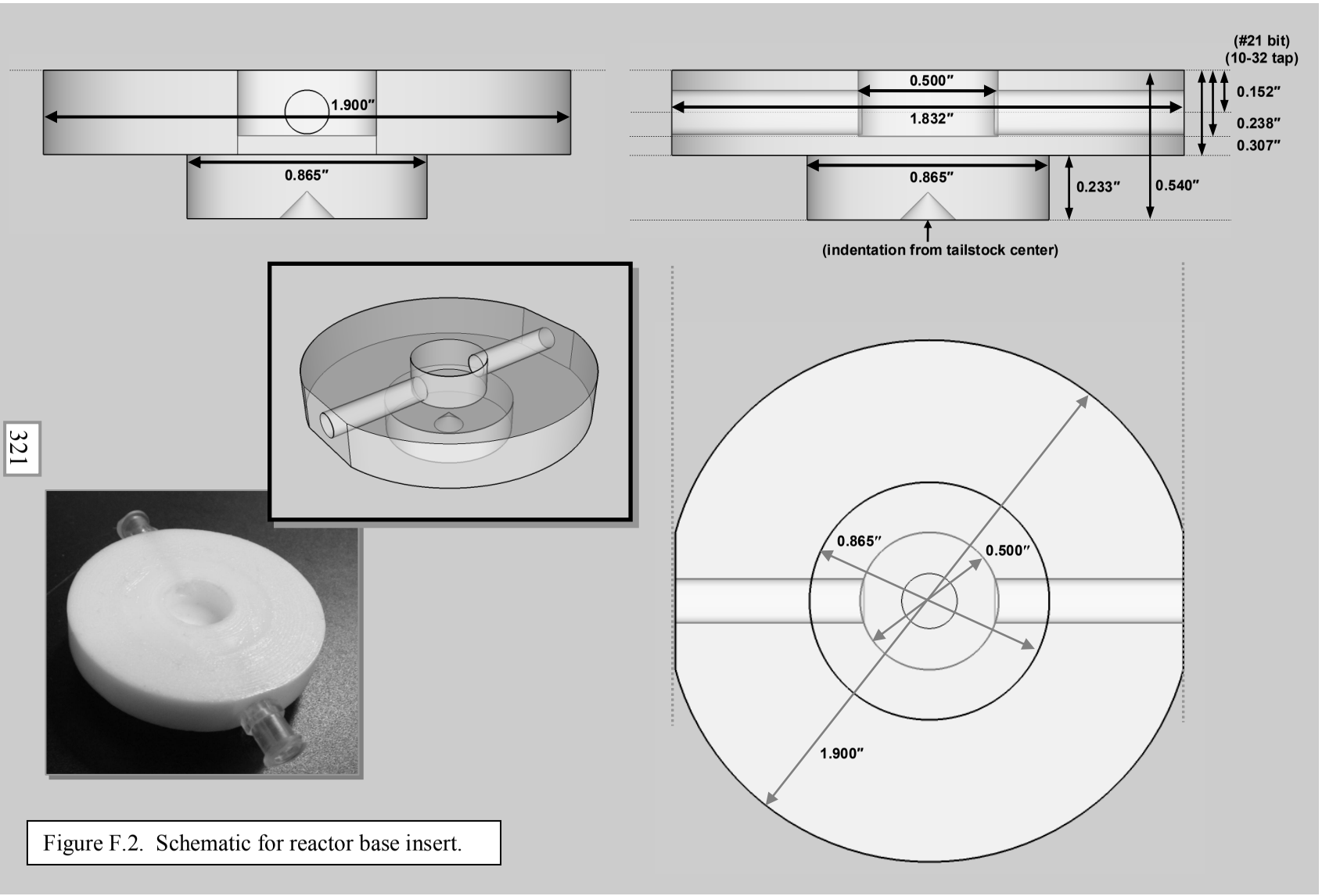

Figure F.2. Schematic for reactor base insert.

F.4 Reactor cap

The schematic for the final version of the reactor cap for the 50-mL Amicon cell is shown in Figure F.3. No modifications to the top surface of the cap are depicted here; depending on the particular application, different modifications will be required to accommodate the desired port configuration. (Detailed specifications for these modifications are provided in Section F.4.2.) The groove for the sealing O-ring (Viton, Dash 132; #9464K132) is located near the upper surface of the cap. This minimizes any potential unstirred liquid volume above the O-ring, between the outer surface of the cell body and the inner surface of the cap. Angled haemostatic forceps (e.g., #82027-424 from VWR, Inc., West Chester, PA) are helpful for extraction of this O-ring during reactor disassembly. Starting material for this part was 3″-diam. PC rod (#8571K23).

F.4.1 Detailed fabrication instructions

The following instructions make two (2) caps; if only one cap is needed, the unused half from step (3.b) can be finished at a later time, as needed.

0. Definitions:
   a. Obverse side: Side (axial-normal) facing the top of the finished part (‘external’ side, facing the air)
   b. Reverse side: Side (axial-normal) facing the bottom of the finished part (‘internal’ side, facing solution for NO delivery)
   c. Outer edge: Radial-normal surface of the part
   d. Thickness: Axial dimension (linear)

1. Cold saw: cut a ~1.8″ piece from 3″-diam. polycarbonate rod stock

2. Lathe, with spider chosen so that ~0.4″ of length of piece is held by three-jaw chuck: Turn outer contours of both parts
   a. Face one side of part; without moving stage, set zero of z-direction travel
   b. Turn diameter of part down a few mils, to about 0.4″ from end
   c. Measure diameter of turned section; set offset of r-direction travel

d. Turn main section of one end of part: to 0.45″ from end, 2.17″ diameter
e. Turn most of central section of part: to within 0.05″ of chuck, 2.37″ diameter
f. Remove part; swap to 15-mm spider; flip part and replace with un-turned side facing tailstock
g. Face end of part; without moving stage, set zero of z-direction travel
h. Turn main section of end of part: 0.45″ from end, 2.17″ diameter
i. Turn remainder of middle section of part: 2.37″ diameter

3. Band saw, with **broad-toothed blade** (PC will clog a fine-toothed blade): cut parts apart
   a. Mount part in clamp: turn clamp on its side and grasp the 2.17″-diam. section on one side with clamp jaws
   b. Being careful to maintain perpendicular orientation of blade to center axis of part (should be achieved naturally by mode of clamping), cut part in half, forming ~identical parts (part surfaces revealed by band saw cut become reverse sides for each part)
   c. Perform step (4) and following on each half obtained in (b)

4. Lathe, with three-jaw chuck and standard turning tool (no spider): face and turn rim-end (reverse side) of part
   a. Mount part with reverse side facing away from chuck and chuck jaws contacting only the smaller-diameter section of the part (obverse surface of rim should be flush against the chuck jaws)
   b. Face reverse side of part; measure rim thickness with calipers; set offset of z-direction travel to measured thickness
   c. Turn reverse side of part to match spec for rim thickness (0.2″ nominal)
   d. Check rim thickness with calipers; turn further as needed

5. Lathe, with three-jaw chuck, tailstock drill bit chuck, #5 center drill, ½″ drill bit, $^{5}/_{8}$″ center-cutting end mill, and boring bar: bore 1.78″ internal cavity of part
   a. Mount part in chuck with reverse side facing tailstock and rim flush against chuck jaws
   b. Mount #5 center drill in tailstock chuck; make starter hole, plunging drill to the depth of the full neck taper
   c. Drill ½″ starter hole
      i. Mount ½″ drill bit in tailstock
      ii. Move tailstock until tip of bit is just short of the reverse face of the part; lock tailstock movement
      iii. Zero tailstock extension scale; drill to 0.45″ depth
   d. Mill $^{5}/_{8}$″ starter bore hole
      i. Mount $^{5}/_{8}$″ center-cutting end mill in tailstock
      ii. Move tailstock until end mill lightly contacts part surface; lock tailstock movement
      iii. Zero tailstock extension scale; mill to 0.45″ depth
   e. Check/adjust depth of bore hole
      i. Mount boring bar

ii. Contact boring tool to inner part surface; zero z-direction travel
iii. Contact boring tool to reverse face of part; check against 0.45″ depth spec
iv. Mill hole further as needed to match spec

f. Finish bore hole
i. Bore away a small amount from hole edge
ii. WITHOUT moving stage in r-direction, measure hole diameter with calipers; set lathe r-direction offset
iii. Bore remainder of 1.78″-diam. hole
iv. Check fit of cap on Amicon cell; bore further as needed for smooth fit (free motion, but with minimal gap)
1. Typical final bore diameter is ~ 1.79″

6. Lathe, with three-jaw chuck and $^{1}/_{16}$″ groove tool: turn O-ring groove in internal cavity of part
a. NOTE: Actual groove dimensions differ from nominal specifications:
i. Width is 0.116″
1. Wider than initial 0.1″ spec
2. For $^{1}/_{16}$″ (0.0625″) groove tool; |Δz| of the stage for total span of groove is 0.0535″
ii. Depth (nominal) is 0.072″ (RADIUS mode)
1. Ultimately determined by fit of cap to cell with O-ring installed
iii. ~0.08″ separation between inner (reverse) face of cap and O-ring groove is okay
1. Greater separation might allow for easier O-ring removal and/or cell body insertion into cap
iv. The entire span between the groove and the inner cap surface is turned down 0.015″ (RADIUS mode)
1. Accommodates skew as cell is worked past O-ring during assembly
v. A 0.06″ span below (on the part-reverse side of) the O-ring groove is machined down 0.005″ (RADIUS mode)
1. Facilitates O-ring removal and provides additional volume for compressed O-ring in assembled reactor

b. Mount $^{1}/_{16}$″ groove tool in groove bar (with groove tool no more than ~2.5″ from the mount); mount groove bar on lathe stage
c. Align the outside edge of the groove tool with the reverse face of the cap rim; set z-position such that the z-zero will be at the obverse edge of the o-ring groove (i.e., such that z-zero is ~0.08″ from the inner reverse surface of the cap – nom. +0.37″)
i. This is a visual estimate; set r-offset such that no part of groove tool or support bar will contact rim, so as to avoid possibility of groove tool breakage
d. Move stage to z-zero; change to RADIUS mode
e. Start lathe; move r-position until the first glancing contact with the inner surface of the bore is achieved; set r-position to -0.01″
i. Glancing contact should be the furthest extent of the circular texturing of the surface (from prior machining) and not the actual surface of the part
f. Turn 0.072″ depth of groove (RADIUS); extract groove tool from part
g. Move stage the necessary offset to turn groove to full thickness (|Δz| for cap for 50-ml cell is 0.0535″); again, turn 0.072″ depth of groove

h. Clean the groove: at z-position 0.0535″, move to r-position (RADIUS) 0.072″, move to z-position 0″, move to negative r-position
i. Turn down 0.015″ thickness of 0.05″ between groove and cap
    i. z-position of -0.05″
j. Clean the rim of the groove: return to z-position 0″; move to r-position ~0.04″; return
k. Turn down 0.005″ thickness of 0.06″ span below groove (|Δz| for prototype part is 0.1135″)
l. Clean the rim of the groove: move to z-position 0.0535″ (nominal); move to r-position ~0.04″; return
m. Check fit of cell into cap, with O-ring; further turn **depth** of groove as needed, cleaning the groove each time, until assembly requires minimal stress on O-ring
n. Return radial-axis measurement to DIAM mode when finished

7. Drill press and tapping station, with #4 center drill, #21 drill bit, and 10-32 tap: Make tapped hole for sample extraction/fluid replacement
    a. Locate point on cap (off-center) where stirrer mount will not interfere with sample extraction
    b. With drill press, start hole with #4 center drill
    c. With drill press, finish hole with #21 drill bit
    d. At tapping station, tap full thickness of top of cap with 10-32 tap

8. Drill and tap other holes for ports/probe mounts as required (Section F.4.2)

F.4.2 Cap modifications

Depending on the intended application for a particular cap, different modifications are needed. Vendor part numbers are accurate as of the date of first submission of Skinn et al. (2011). 'Clearance' notations indicate the space around the fitting mount that must be left free to permit access during reactor assembly/operation. Material is stainless steel (SS), unless otherwise specified. Male Luer caps (polypropylene, PP), where needed, were #51525K371. Where noted, supplier abbreviations are: Cole-Parmer, Vernon Hills, IL (CP); and Swagelok, Solon, OH (SL).

- Gas delivery port (inlet or outlet) for PDMS tubing connection
    - Female Luer to $^{1}/_{16}$″ barbed connection; ¼-28 threaded mount, PP (CP #EW-45600-30)

- Seal: Dash 010 O-ring, Viton (#9464K15)
- Drill hole: #4 center drill, #3 bit
- Clearance: Male Luer cap or connector; finger-/wrench-tighten fitting

- Orion O_2 probe
  - Ultra-Torr ½″ i.d. to $^3/_8$″ Male NPT fitting (SL #SS-8-UT-1-6)
  - Seal: Teflon tape (e.g., #6802K12)
  - Drill hole: #4 center drill, ½″ bit (start with #3 bit, then step from J)
  - Clearance: Wrench-/ratchet-tighten of fitting base, plus finger-tighten of Ultra-Torr cap around probe
    - NOTE: Probe mount hole must be placed such that threads of Ultra-Torr mount does not impinge against stirrer or cell body
- Instech O_2 probe
  - Custom-modified probe body incorporating ¼-28 threaded sheath
    - Request this modification when placing order
  - Seal: Sealing washer, ¼″ screw size, $^5/_8$″ o.d., $^1/_{16}$″ thick, Viton (#93412A415)
  - Drill hole: #4 center drill, #3 bit
  - Clearance: Finger-tighten probe mount
- World Precision NO probe
  - Ultra-Torr $^1/_8$″ i.d. to $^1/_8$-27 NPT fitting (SL #SS-2-UT-1-2)
  - Seal: Teflon tape (e.g., #6802K12)
  - Drill hole: #4 center drill, Q bit (started with #3 bit, then stepped from J)
  - Clearance: Wrench-/ratchet-tighten fitting base; finger-tighten Ultra-Torr cap around probe
- Sampling/replacement port
  - Female Luer to 10-32 threaded mount, PP (#51525K235)
  - Seal: Dash 006 O-ring, Viton (#9464K11)
  - Drill hole: #4 center drill, #21 bit
  - Clearance: Male Luer cap; finger-tighten fitting

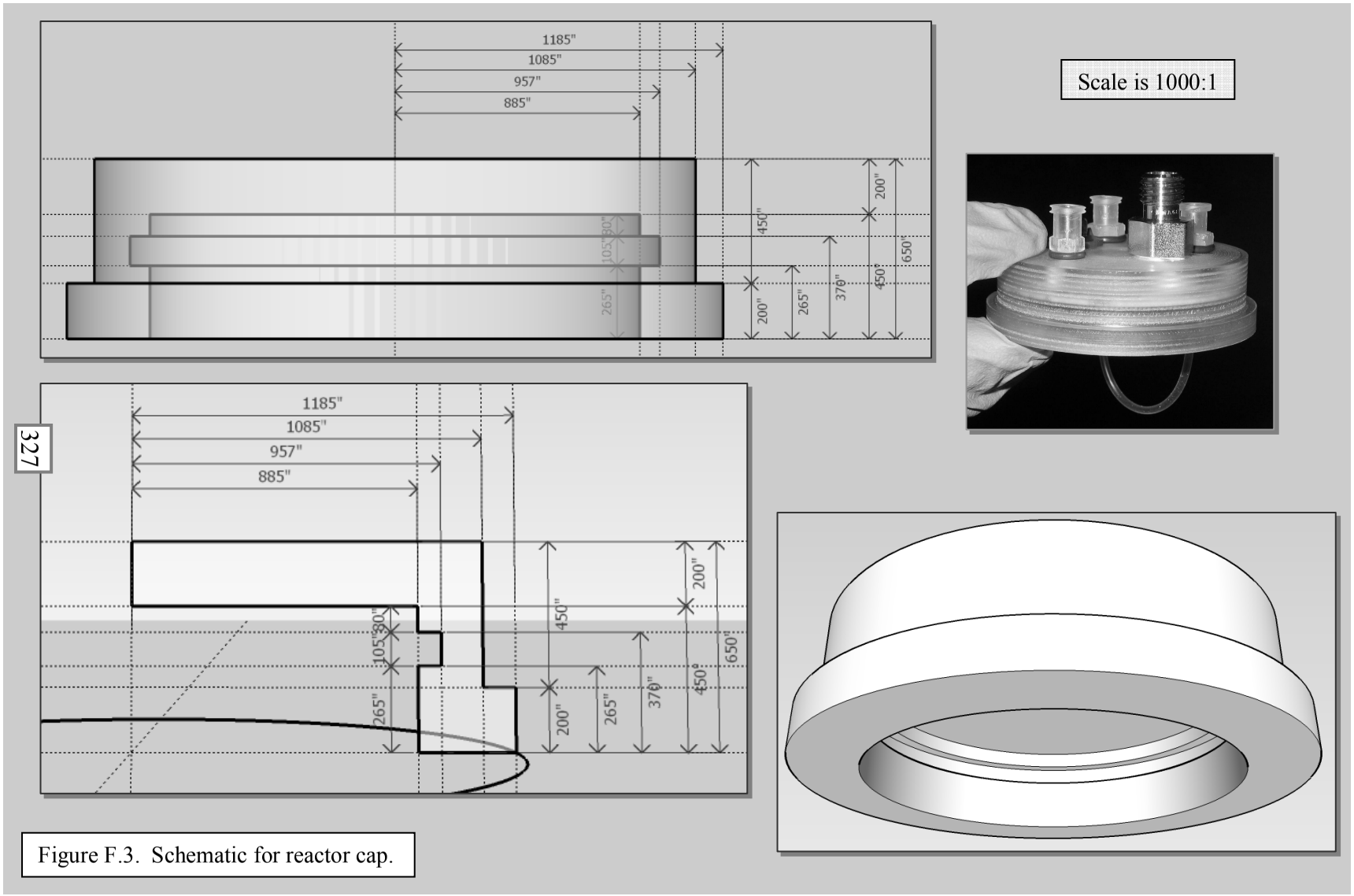

Figure F.3. Schematic for reactor cap.

F.5 Miscellaneous modifications

F.5.1 Ultrafiltration cell baseplate

The baseplate of the Amicon cell must be machined down slightly. In order to provide clearance for the Luer fittings through the slots in the cell body, the thickness of the upper (interior when assembled) surface of the baseplate must be machined down by approximately 0.05″, to a total thickness of 0.347″ at its thickest point.

F.5.2 Stirrer

The stirrer included with the Amicon cell is designed for a 'supported' (reinforced) membrane that is slightly recessed from the bottom of the main part of the cell. In the configuration as modified for NO delivery, the porous PTFE membrane is directly aligned with the bottom of the main part of the cell, introducing the risk of membrane damage due to impacts with the stirrer. As such, the stirrer height was reduced by approximately 1 mm by sanding with progressively finer grades of sandpaper, to a final height of 0.342″. The bulk of the material was removed with 220-grit sandpaper; the sanded surface was finished with 320- and 400-grit papers. A strip of the reflective tape from the strobe tachometer kit was applied to the upward-slanted face of the stirrer for later cyclic rate measurements.

This sanding method of resizing the stirrer is somewhat imprecise, and the mass transfer behavior at the porous membrane may vary depending on the exact stirrer-membrane separation distance. Re-determination of $k^{o}_{m,j}$ is recommended in order to eliminate uncertainty in the stirrer-membrane spacing as a source of error.

F.5.3 Viton gaskets as an alternative membrane seal

Preliminary experiments indicated that the laminated membrane of Section F.2 does not by itself provide an air-tight seal. Petrolatum grease was used in this study (see Section F.8) to seal the laminated membrane both to the cell body and to the PTFE insert of Section F.3 in order to achieve gas-tight operation. Oxygen depletion experiments with sealing gaskets of 0.005″-thick PTFE film in place of the grease seal have indicated that such gaskets can achieve a partial but not complete seal. Implementation of a grease-free seal would be desirable because any accidental transfer of grease to the porous membrane will inhibit mass transfer through the contaminated portion of the membrane.

The failure of the PTFE gaskets to provide a good seal is likely because PTFE is relatively incompressible. Similar gaskets fabricated from elastomer films might provide suitable sealing. The requirement for rigorous exclusion of O_2 from the NO flow space prevents use of an elastomer like PDMS, the gas permeability of which is far too high to be useful. It is hypothesized that gaskets cut from a thin film of a fluoroelastomer such as Viton might be sufficiently compressible and impermeable to enable grease-free sealing. One possible point of failure of these gaskets would be if it proved impossible to obtain a seal tight enough to prevent penetration of water past the gaskets by capillary action.

The proposed gaskets (two would be required, one each above and below the membrane) could be cut using an OLFA CMP-001 compass cutter from 0.016″-thick Viton sheet rubber (Manufacturer's Rubber, Brentwood, NH), which appears to be the thinnest sheet-form Viton commercially available. The proposed dimensions, which may require optimization, are 1.92″ o.d. and 1.36″ i.d.

F.6 Connection to gas handling system

Connection of the custom base insert of Section F.3 to the gas handling system was achieved as follows. The only fittings found to be small enough to fit into the slots on the side of the reactor body were polypropylene (PP) female Luer fittings with a male 10-32 threaded connection (#EW-45500-60, Cole-Parmer, Vernon Hills, IL). These fittings mate to the female 10-32 threaded holes in the insert, as shown in Figure F.2.

The Luer connection was adapted to the 1/8″ compression fittings of the gas handling system by a combination of fittings **(1)** and **(2)** from the 'Gas Inlet' of the NO_2 delivery system as depicted in Figure G.1 and described in Table G.1. These parts are #SS-200-7-2 (Swagelok, Solon, OH) and #EW-31507-44 (Cole-Parmer), respectively.

F.7 Soda lime column

The delivery system is very sensitive to the presence of NO_2 (and, by implication, of O_2) in the NO delivery line. Our experiments indicate that even freshly purchased NO gas mixtures often have levels of NO_x impurities sufficient to perturb the reactor chemistry. Inclusion of an in-line soda lime column to scrub the NO_x impurities (Ishibe et al., 1995; Lindberg and Rydgren, 1998) was sufficient to eliminate the undesired behavior. The permeability of oxygen through most polymeric materials is sufficiently great to preclude the use of plastics in any component of the NO delivery line, including the soda lime column. Stainless steel is a suitably inert and impermeable material (Wendt et al., 1994) for the majority of the line (tubing and fittings), though a transparent material is desired for the main body of the soda lime column as it permits direct

monitoring of the consumption of the indicating soda lime. Borosilicate glass was found to be a suitable material for this purpose.

One option for constructing a soda lime column of this type is to purchase a commercial glass/steel column (of whatever type) and repack it with soda lime. One such column is the indicating oxygen trap #202220 of Chromatography Research Supplies, Inc. (Louisville, KY), which comes equipped with $^1/_8$″ compression fittings. (**Warning**: The O_2-absorbing packing in this column rapidly releases heat on exposure to air, so the initial removal of the column packing must be performed with care.) The vendor appears not to offer an empty column of the appropriate type; a special order may be possible. One downside of these columns is the custom-designed compression fittings used in their manufacture. The fittings used are compatible with off-the-shelf Swagelok ferrules and nuts, but replacement fittings are not available commercially (again, a special order may be possible).

A second option is *de partibus* fabrication of a suitable column. The following are a parts list (Section F.7.1), procedure for construction/assembly (Section F.7.2) and schematic (Figure F.4) for a column meeting the necessary specifications. Figure F.5 is a photograph of the assembled soda lime column. **NOTE**: the Ultra-Torr fittings used in this design are only rated by the manufacturer for negative-pressure (vacuum) applications. Test each column for pressure-fastness before packing with soda lime and DO NOT exceed ~50 psig working pressure.

F.7.1 Parts/Equipment List

Column Parts

Parts for which a quantity is not indicated are sold in packs.

- 12″ borosilicate glass tube, o.d. ½″, 2.4mm wall thickness (#8729K35, 1pc)
- ½″ Ultra-Torr fitting with $^{3}/_{8}$″ M NPT (Swagelok #SS-8-UT-1-6, 2pc)
- Connector, $^{3}/_{8}$″ F NPT to ¼″ tube fitting (Swagelok #SS-400-7-6, 2pc)
- Reducer, ¼″ tube adapter to $^{1}/_{8}$″ tube fitting (Swagelok #SS-200-R-4, 2pc)
- Plugs, $^{1}/_{8}$″ tube size (Swagelok #SS-200-P, 2pc)
- PC shield, 1.5″ o.d., $^{1}/_{8}$″ thick (#8585K16, 1ft)
- Vinyl caps, fitting 1.5″ o.d. tubes, ¾″ inside ht (#9753K69)
- Spring, SS, 1.5″ length, $^{5}/_{16}$″ o.d. (#1986K8)
- O-ring, Dash 014, Viton; for Ultra-Torr grip seal (#9464K19)
- O-ring, Dash 012, Viton; cushion between end of tube & fitting (#9464K17)
- Cotton balls (#54845T16) or glass wool (VWR #82030-618)
- SS mesh, 70×70 mesh size, 12″×12″ piece (#85385T867)

Supplementary Equipment/Supplies

- Indicating soda lime (Sigma-Aldrich, St. Louis, MO; #72073)
- Knife-shape file, 6″ length, coarse cut; for scoring/frosting tubing (#4236A12)
- (Optional) Pliers-style chain glass tube cutter (#3655A13)
- Heavy-duty scissors (e.g., #3879A8)
- Utility knife (e.g., #4927A11)
- Straight pick (e.g., #3842A23)
- Heavy leather (e.g., #5354T15) or other cut-resistant (e.g., #6086T23) gloves
- Fractional wrenches, $^{7}/_{16}$″ through ¾″ (e.g., #5807A6)
- Adjustable wrench, approx. ¼″ through ½″ range (e.g., #5385A12)
- Glass stir rod (e.g., VWR #59060-080)
- Teflon tape (e.g., #6802K12)

- Plastic funnel (e.g., #1479T2)
- Large weigh boat (e.g., #17735T96)
- Pestle (e.g., #43095T62)

F.7.2 Construction/assembly procedure

Soda Lime Preparation

The indicating soda lime comes in the form of 2-4 mm pellets, which have a relatively small surface area-to-volume ratio. Much more efficient use can be made of the soda lime by pulverizing it. The pulverized lime cakes onto a ceramic mortar and pestle, so grinding against a plastic weigh boat with the ceramic pestle is recommended. The lime caked onto the pestle must be periodically scraped off into the weigh boat. The pulverized lime must be stored in an air-tight container, as it is slowly inactivated by ambient CO_2.

Preliminary Column Assembly

0. Performed once, before initial column use.

1. Cut 8″ length of glass tubing
   a. Use glass tube cutter, or
   b. Score full circumference of 12″ length of tubing at 8″ with file
   c. Deepen score line to a full circumferential groove of depth of about 0.5 mm
   d. Wearing heavy leather gloves, brace both thumbs at the score line and snap the tubing with a single quick, strong motion
      i. Under-application of force is much more likely to result in a poor break than over-application
   e. Smooth any sharp/rough edges at the break with the file

2. With the file, frost a ~1-cm span of the full circumference of both ends of the tube
   a. The roughness of the frosted surface is necessary for the Ultra-Torr fitting to maintain its grip when the column is pressurized

3. Assemble the fittings (perform 2x)
   a. Remove the nut, sleeve, and O-ring from the Ultra-Torr (SS-8-UT-1-6) fitting, discarding the O-ring
      i. A thin layer of vacuum grease is applied to the stock O-ring at the factory, preventing a tight grip on the glass tubing
   b. Wrap the $^{3}/_{8}$″ M NPT end of the Ultra-Torr fitting with three circumferences of Teflon tape
      i. For a proper seal, wrap clockwise as you look at the part with the NPT end facing you
   c. Join the Ultra-Torr fitting to the 'connector' (SS-400-7-6) fitting, tightening fully wrench-tight
   d. Swage the ¼″ tube adapter of the 'reducer' (SS-200-R-4) fitting onto the connector
      i. 1-¼ turns past finger-tight on initial assembly for this ¼″ fitting
      ii. Tighten only slightly past finger-tight on subsequent reassemblies
   e. Insert Dash 012 Viton O-ring into the lower seat of the Ultra-Torr fitting
   f. Insert Dash 014 Viton O-ring into the upper seat of the Ultra-Torr fitting
   g. Reassemble Ultra-Torr fitting sleeve & cap

4. Cut the stainless steel inserts (2x)
   a. Cut a ~½″-square piece of the stainless steel mesh
   b. Trim approximately into a circle, of diameter slightly greater than the glass tubing i.d.
   c. With pliers (or similar), bend the rim of the circle to 'cup' the mesh such that it fits into the tubing

5. Cut openings in vinyl end caps (2x)
   a. With utility knife, cut out a 5-mm-square piece from the center of the end cap
   b. With scissors, make 8-mm radial cuts in the cap from each of the four corners of the void made in (a)

Column Filling & Assembly

0. Performed before initial column use and at each re-pack after soda lime is exhausted.

1. Prepare bottom end of column
   a. Pack a quantity of cotton or glass wool into one end ('bottom') of the glass tubing, sufficient for a moderately packed plug of thickness 6-7 mm
   b. Position bottom-end mesh insert
      i. Drop one SS mesh insert into the other ('top') end of the tubing
      ii. Press insert down into contact with wool plug with stir rod, keeping insert perpendicular to the long axis of the tubing to the extent possible
   c. Insert spring ~2-3 mm into bottom end of tube with a slight clockwise twisting motion
   d. Mount bottom-end Swagelok fitting assembly
      i. Insert bottom end of tubing into Ultra-Torr end of one of the fitting assemblies

ii. Ensure that the tubing end is resting up against the lower (Dash 012) O-ring and the spring contacts the inside base of the 'connector' fitting
iii. Firmly finger-tighten the Ultra-Torr nut
    1. An inability to pull the tubing out of the fitting assembly by hand (exercise caution in the attempt) typically indicates sufficient frosting of the tubing ends

2. Fill column with pulverized soda lime
    a. Clamp column vertically in a lab stand
    b. Using plastic funnel, pour a small quantity of soda lime into the column
    c. Tamp the soda lime down firmly with a stirring rod
    d. Repeat (b) and (c) until ~1.5 cm open space remains at the top of the column

3. Prepare top end of column
    a. Position SS mesh insert flush against the soda lime packing and as perpendicular to the long axis of the column as possible
    b. Pack a small quantity of cotton or glass wool into the top of the column, again sufficient for a moderately packed plug of thickness 6-7 mm
    c. Insert spring ~2-3 mm into top end of column with the same clockwise twisting motion as in (1.c)
    d. Mount top-end Swagelok fitting assembly as in (1.d)

4. Assemble column and PC shield
    a. Attach modified vinyl cap to one end of PC tube
    b. Insert assembled column into other end of PC tube, pushing it just through the cuts in the cap
    c. Attach modified cap to other end of PC tube

5. If not installing column in gas flow manifold right away, seal fittings on both ends with plugs (Swagelok #SS-200-P) to avoid soda lime consumption by ambient CO_2

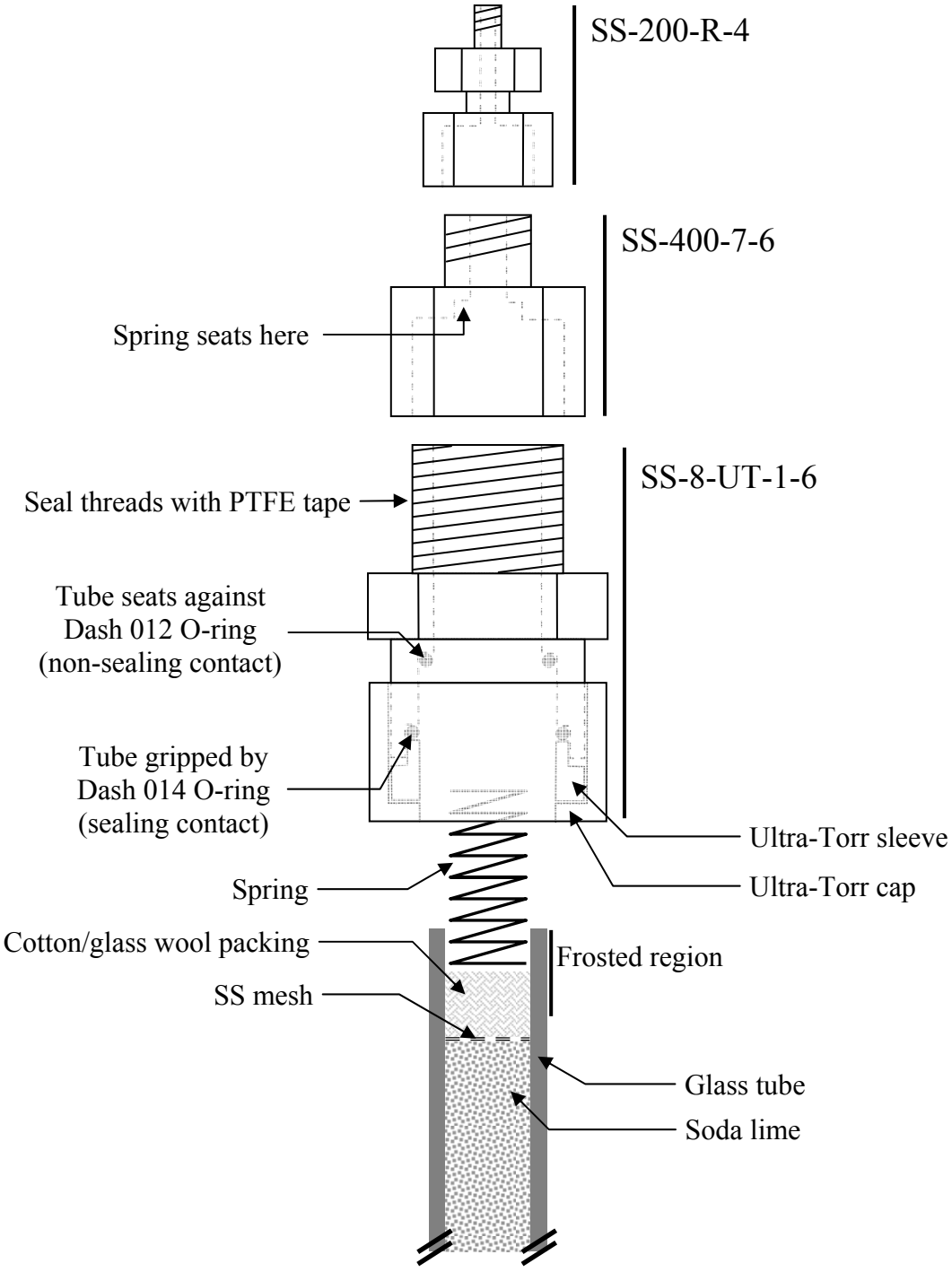

Figure F.4. Fitting assembly schematic for the custom soda lime column.

Component drawings are not to scale. The PC shield and vinyl end cap are not shown.

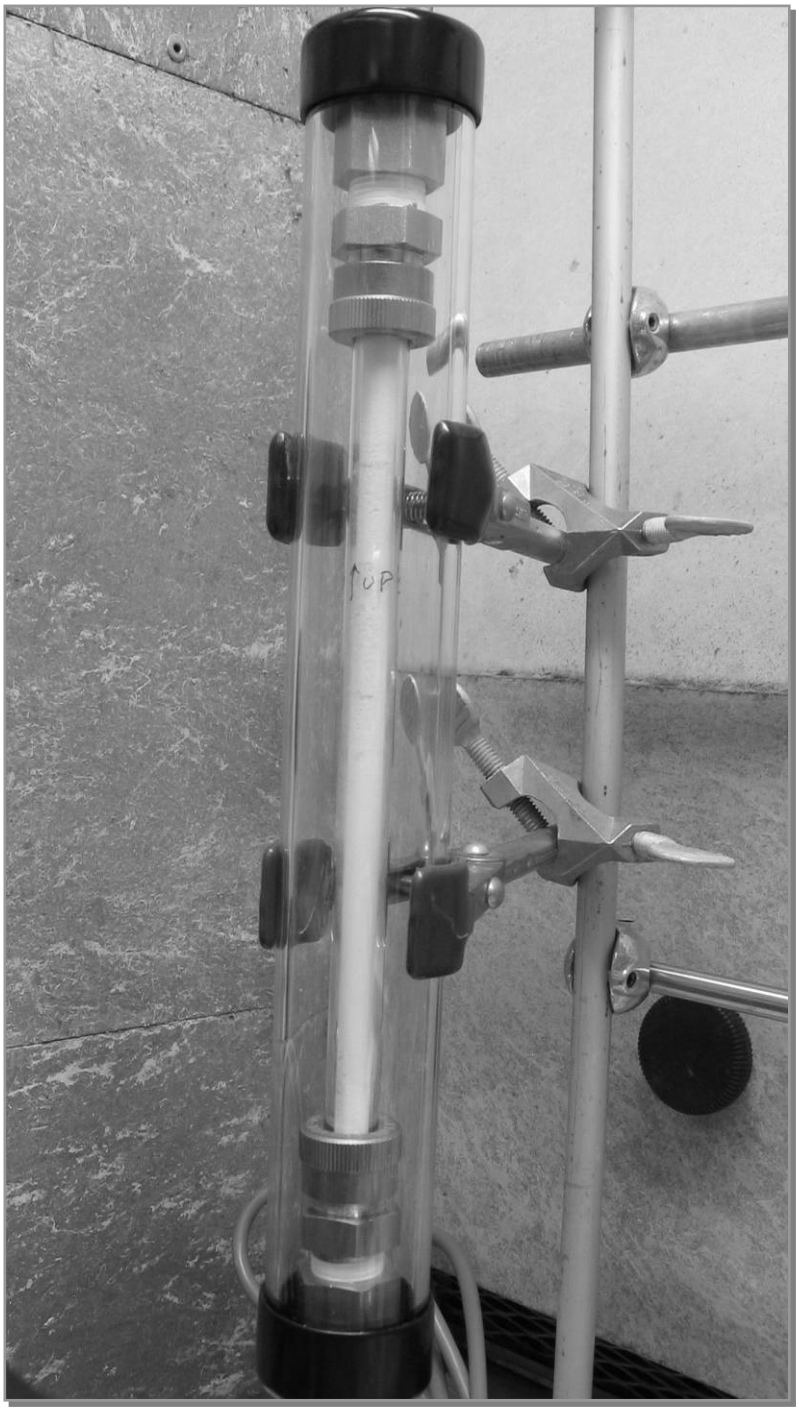

Figure F.5. Photograph of the assembled soda lime column.

F.8 Reactor assembly instructions

Figure F.6 is a photograph of the assembled reactor, minus the fitting for the O_2 probe and the stainless steel Luer/compression fitting assembly.

0. Parts required
   a. Petrolatum grease
   b. Custom Viton gaskets (optional; see Section F.5.3)
   c. Dash 132 Viton O-ring
   d. PP F Luer to M 10-32 fittings (2x), for base inlet & outlet
   e. Two-piece stainless steel fitting assembly, M Luer to 1/8″ compression fitting (Section F.6)
   f. PDMS tubing loop, cut to length
   g. Amicon cell body
   h. Modified Amicon cell baseplate (Section F.5.1) and stirrer (Section F.5.2)
   i. Laminated membrane (Section F.2)
   j. Custom insert (Section F.3)
   k. Custom cap (Section F.4), with *no fittings attached* except the Ultra-Torr fitting for the World Precision NO probe, if mounted (Section F.4.2)

1. Mount Luer fittings on base insert
   a. Apply a thin film of grease to the threads of each fitting
   b. Screw each fitting into insert, stopping at the first sign of resistance
   c. Turn each fitting ~ ¼ turn further
   d. These fittings can typically be left in place indefinitely

2. If using grease seals for the membrane, apply a layer of grease onto obverse face of insert
   a. There should be sufficient grease on the insert that all of the masked portion of the membrane is in contact with grease, but little enough that the pressure of reactor assembly does not expel grease from between the membrane and the insert
      i. If the insert and membrane are carefully handled, this grease layer typically only required refreshing about once in every five to ten times assembling the reactor

3. If using grease seals for the membrane, apply a layer of grease to the inner bottom surface of the cell body
   a. Spread an even layer of grease around the full circumference of the cell body
   b. Here, it was typically not problematic if a large enough amount of grease was used that a small bead formed along the seam between the cell body and the membrane

4. Assemble bottom portion of reactor:
   a. Hold the reactor upside down
   b. If using Viton gasket seals for the membrane, insert one Viton gasket
   c. Insert the laminated membrane and center it in the cell body

d. If using Viton gasket seals, insert the second Viton gasket
e. Fit the custom insert into the base of the cell, rotating the inlet/outlet fittings slightly as needed to fit them into the slots in the side of the cell
f. Screw on the cell baseplate by hand as tightly as possible

5. Assemble the cap
   a. Fit the Dash 132 Viton O-ring into the groove in the inner surface of the cap, pressing it uniformly into place
   b. Screw all fittings into the cap, using O-ring or other seals as appropriate
   c. Mount the PDMS tubing onto the barbed fittings, avoiding any kinks or creases

6. Fill and assemble the reactor
   a. Fill the reactor with the desired liquid medium to within ~ 2-3 mm of the rim
   b. Simultaneously insert the stirrer and assemble the cap
      i. The construction of the stirrer support together with the geometry of the PDMS tubing loop requires that the cap and stirrer be mounted at the same time
      ii. Place the central "leg" of the T-shaped stirrer support through the PDMS tubing loop
      iii. Lower the stirrer and cap together, until the stirrer support rests on the top rim of the reactor
      iv. Flex the stirrer support slightly until it slips into place at the top of the reactor
      v. Press the cap fully onto the reactor
   c. Using the sampling port, fill the remaining volume within the reactor with the liquid medium
   d. It was discovered that the cap, when tightly pressed against the cell body, partially impinged on a moving part of the stirrer. It was necessary to raise the cap by ~ ½ mm to avoid irregularities in the observed stirring rate

7. Mount the stainless steel Luer/compression fitting assembly on the inlet of the base insert

8. Connect the reactor inlet assembly to the terminus of the NO delivery line from the gas handling manifold

9. Mount NO and/or O_2 probes, as relevant

Disassembly of the reactor proceeds in substantially the reverse of the order described above. Care must be exercised to avoid smudging grease onto the active portion of the membrane when separating it from the base insert and from the cell body. All reactor components were thoroughly rinsed after disassembly to avoid contamination from one experiment to the next.

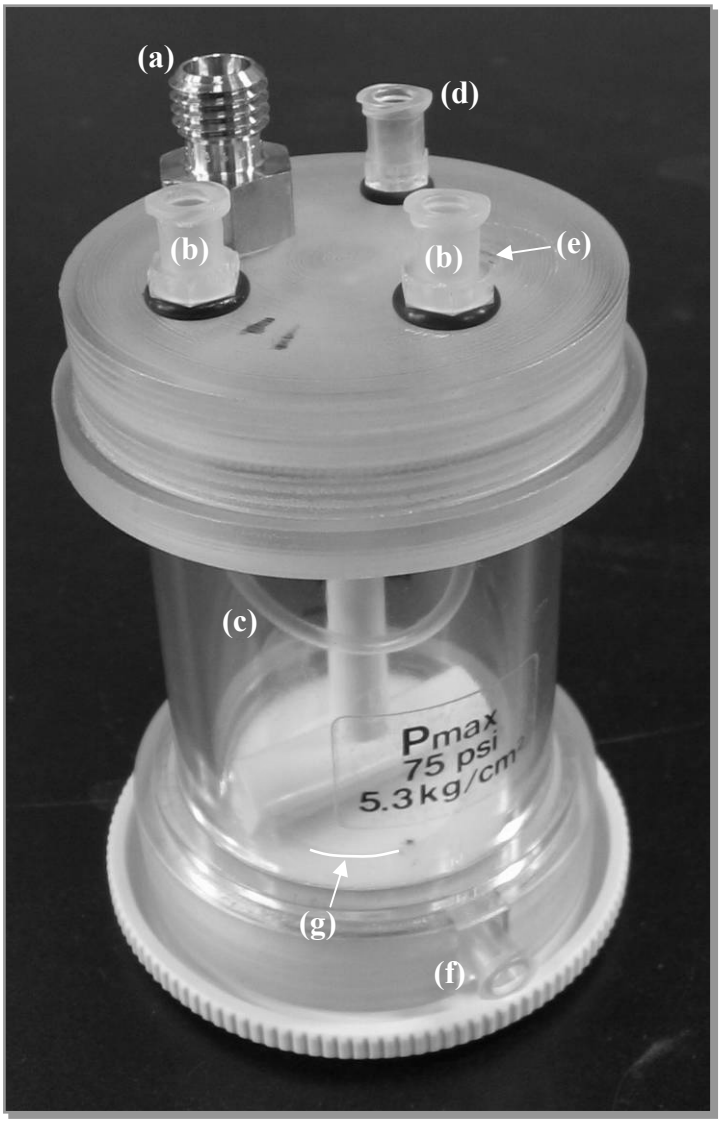

Figure F.6. Photograph of the assembled NO reactor.

Reactor is shown with (a) Ultra-Torr fitting for NO probe; (b) inlet and outlet for (c) PDMS tubing loop; and (d) sampling port. The empty threaded hole (e) would hold the mount for the O_2 probe. The reactor inlet (f) has the plastic Luer fitting installed but not the stainless steel assembly to adapt the Luer connection to a 1/8″ Swagelok compression fitting. It is just possible to make out the edge of the porous PTFE membrane (g) at the base of the reactor.

Appendix G

Parts List and Assembly Instructions for NO_2 Delivery Apparatus

The parts list below provides sufficient information for constructing the reactor used in the experiments of Chapter 3. It is assumed that a suitable stainless steel gas handling manifold has been constructed to deliver NO_2 gas mixtures at flow rates on the order of 250-365 standard cubic centimeters per minute, and that the terminal connection of this manifold is 1/8″ o.d. stainless steel tubing pre-swaged with a nut and ferrule set from a standard 1/8″ stainless steel Swagelok (Solon, OH) compression fitting.

Figure G.1 reproduces the reactor schematic of Figure 3.2 and adds representations of the parts comprising the various components. Figure G.2 is a photograph of the assembled device. Supplier abbreviations and part number information are given in Table G.1. Material abbreviations are: PTFE, poly(tetrafluoroethylene); PFA, perfluoroalkoxy; PCTFE, poly(chlorotrifluoroethylene); PVDF, poly(vinylidene fluoride); SS, stainless steel.

All fittings mated to the reactor cap have ¼-28 male threads, the tap for which (e.g., MC #2521A681; requires tap wrench, e.g., MC #25605A63) requires holes drilled to a final bit size of #3. The best syringe needles to use with this septum assembly were found to be 21-gauge, with length 1.5 in. This gauge of needle is narrow enough to traverse the bore of the Upchurch fitting while being wide enough to result in minimal backpressure during sample extraction. A 1.5-in needle is required in order to reach the liquid surface, and was found to be sufficient for withdrawal of volumes of at least 5 ml.

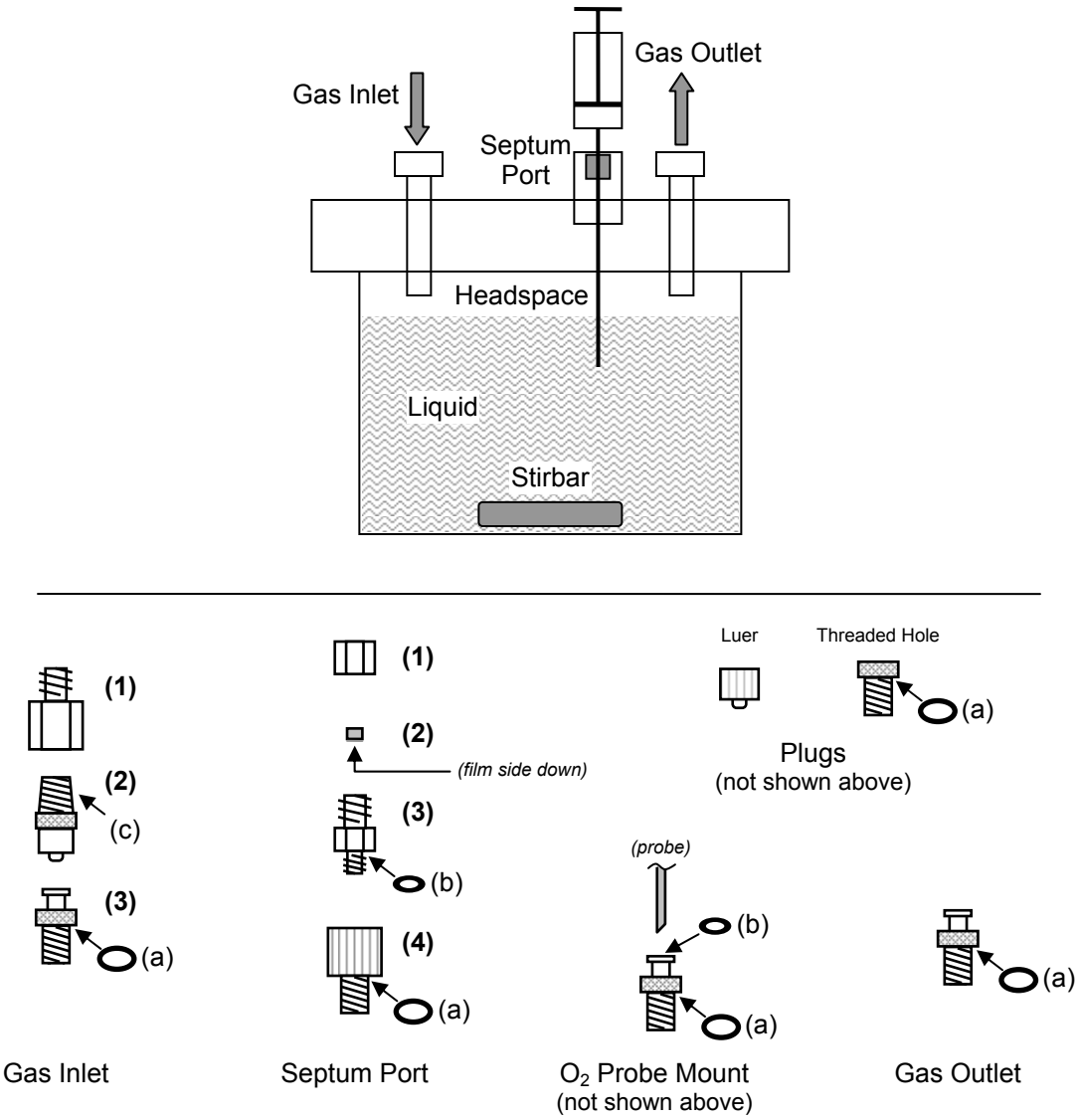

Figure G.1. Schematic of NO_2 reactor with small parts detail.

The upper portion of figure is reproduced from Figure 3.2. The lower portion provides more visual detail of the fitting assemblies indicated in the original figure. The bolded numerical notations refer to the individual fittings within a multi-part assembly, and the non-bolded alphabetical notations refer to components used for sealing purposes. The arrows point to the location of each seal when the reactor is assembled. The suppliers and part numbers for these components are listed in Table G.1.

Table G.1. Parts information for NO_2 reactor components.

Component	Fitting ID	Part No. (Supplier)	Description (Material)
Vessel	–	EW-06103-40 (CP)	Wide-Mouth Sample Jar, 120 ml (PFA)
Stirbar	–	58948-150 (VWR)	Stir Bar, Octagon, 5/16″ × 1 ½″ (PTFE coated)
Gas Inlet	(1)	SS-200-7-2 (SL)	1/8″ tube fitting to 1/8″ F NPT (SS)
	(2)	EW-31507-44 (CP)	M Luer Lock to 1/8″ M NPT (SS)
	(3)	EW-45512-66 (CP)	F Luer to ¼-28 Thread (PVDF)
Septum Port	(1)	T-202-1 (SL)	Nut for 1/8″ Tube Fitting (PTFE)
	(2)	EW-01994-20 (CP)	Puresep-T Septa, ¼″ diam. (PTFE film on silicone base)
	(3)	T-200-1-0157 (SL)	Straight – 10-32 M to 1/8″ Tube Fitting (PTFE)
	(4)	P-640-01 (UCS)	Adapter Body – F 10-32 to M ¼-28 (PCTFE)
Gas Outlet	–	EW-45512-66 (CP)	F Luer to ¼-28 Thread (PVDF)
O_2 Probe Mount	–	EW-45512-66 (CP)	F Luer to ¼-28 Thread (PVDF) (*must be drilled out to probe diameter*)
Threaded Hole Plug	–	EW-30706-31 (CP)	Pipe Plug, ¼-28, 3/8″ × 3/8″ (PVDF)
Luer Plug	–	EW-45513-56 (CP)	Male Luer Lock Plug (PVDF)
Seals	(a)	9464K15 (MC)	Dash 010 O-ring (Viton)
	(b)	93412A401 (MC)	Sealing Washer, 1/4″ o.d., 1/8″ i.d. (Viton)
	(c)	300008-840 (VWR)	Thread Sealing Tape (PTFE)

Supplier abbreviations: McMaster-Carr, Dayton, NJ (MC); Cole-Parmer, Vernon Hills, IL (CP); Upchurch Scientific, IDEX Health & Science, Oak Harbor, WA (UCS); VWR, Inc., Radnor, PA (VWR); Swagelok, Solon, OH (SL).

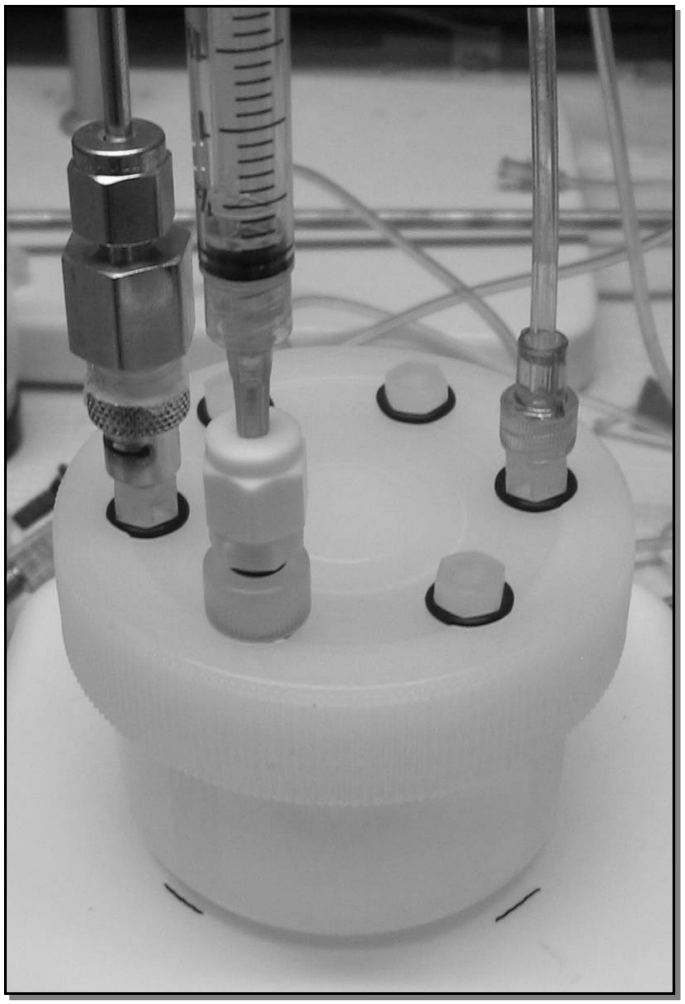

Figure G.2. Photograph of assembled NO_2 reactor.

From left to right, the ports depicted are the gas inlet, the septum port, and the gas outlet. Three additional threaded holes in the cap have been plugged with CP #EW-30706-31 and accompanying O-rings.

Bibliography

Abello, N., Kerstjens, H. A. M., Postma, D. S., and Bischoff, R. Protein tyrosine nitration: Selectivity, physicochemical and biological consequences, denitration, and proteomics methods for the identification of tyrosine-nitrated proteins. *Journal of Proteome Research* **8**: 3222-3238, 2009.

Abu-Reesh, I. and Kargi, F. Biological responses of hybridoma cells to defined hydrodynamic shear stress. *J. Biotechnol.* **9**: 167-178, 1989.

Afshari, A., Brok, J., Moller, A. M., and Wetterslev, J. Inhaled nitric oxide for acute respiratory distress syndrome and acute lung injury in adults and children: A systematic review with meta-analysis and trial sequential analysis. *Anesth. Analg.* **112**: 1411-1421, 2011.

Akinsheye, I. and Klings, E. S. Sickle cell anemia and vascular dysfunction: The nitric oxide connection. *J. Cell. Physiol.* **224**: 620-625, 2010.

Akiti, O. and Armenante, P. M. Experimentally-validated micromixing-based CFD model for fed-batch stirred-tank reactors. *AIChE J.* **50**: 566-577, 2004.

Alfassi, Z. B., Huie, R. E., Neta, P., and Shoute, L. C. T. Temperature dependence of the rate constants for reaction of inorganic radicals with organic reductants. *J. Phys. Chem.* **94**: 8800-8805, 1990.

Alican, I. and Kubes, P. A critical role for nitric oxide in intestinal barrier function and dysfunction. *Am. J. Physiol. Gastroint. Liver Physiol.* **270**: G225-G237, 1996.

Al-Sa'doni, H. and Ferro, A. S-nitrosothiols: A class of nitric oxide-donor drugs. *Clin. Sci.* **98**: 507-520, 2000.

Alvarez, B. and Radi, R. Peroxynitrite reactivity with amino acids and proteins. *Amino Acids* **25**: 295-311, 2003.

Amitai, Y. Physiologic role for "inducible" nitric oxide synthase: A new form of astrocytic-neuronal interface. *Glia* **58**: 1775-1781, 2010.

Appel, B. R., Wall, S. M., Tokiwa, Y., and Haik, M. Simultaneous nitric acid, particulate nitrate and acidity measurements in ambient air. *Atmos. Environ.* **14**: 549-554, 1980.

Artiss, J. D., Thibert, R. J., McIntosh, J. M., and Zak, B. Study of various substrates for peroxidase-coupled peroxide oxidations. *Microchem. J.* **26**: 487-505, 1981.

Ashby, M. T. and Nagy, P. Revisiting a proposed kinetic model for the reaction of cysteine and hydrogen peroxide via cysteine sulfenic acid. *Int. J. Chem. Kinet.* **39**: 32-38, 2007.

Atkinson, R., Baulch, D. L., Cox, R. A., Crowley, J. N., Hampson, R. F., Hynes, R. G., Jenkin, M. E., Rossi, M. J., and Troe, J. Evaluated kinetic and photochemical data for atmospheric chemistry: Volume I - gas phase reactions of O_x, HO_x, NO_x and SO_x species. *Atmos. Chem. Phys.* **4**: 1461-1738, 2004.

Atsukawa, M., Nishimoto, Y., and Takahashi, N. Removal of nitrogen oxide from effluent stack gases. *Technical Review - Mitsubishi Heavy Industries* **5**: 129-135, 1968.

Augusto, O., Bonini, M. G., Amanso, A. M., Linares, E., Santos, C. C. X., and De Menezes, S. L. Nitrogen dioxide and carbonate radical anion: Two emerging radicals in biology. *Free Radic. Biol. Med.* **32**: 841-859, 2002.

Ayyagari, V. N., Januszkiewicz, A., and Nath, J. Effects of nitrogen dioxide on the expression of intercellular adhesion molecule-1, neutrophil adhesion, and cytotoxicity: Studies in human bronchial epithelial cells. *Inhal. Toxicol.* **19**: 181-194, 2007.

Bakand, S., Winder, C., Khalil, C., and Hayes, A. An experimental in vitro model for dynamic direct exposure of human cells to airborne contaminants. *Toxicol. Lett.* **165**: 1-10, 2006.

Balazy, M. and Chemtob, S. Trans-arachidonic acids: New mediators of nitro-oxidative stress. *Pharmacol. Ther.* **119**: 275-290, 2008.

Balcerczyk, A., Sowa, K., and Bartosz, G. Metal chelators react also with reactive oxygen and nitrogen species. *Biochem. Biophys. Res. Commun.* **352**: 522-525, 2007.

Bambauer, A., Brantner, B., Paige, M., and Novakov, T. Laboratory study of NO_2 reaction with dispersed and bulk liquid water. *Atmos. Environ.* **28**: 3225-3232, 1994.

Bartesaghi, S., Ferrer-Sueta, G., Peluffo, G., Valez, V., Zhang, H., Kalyanaraman, B., and Radi, R. Protein tyrosine nitration in hydrophilic and hydrophobic environments. *Amino Acids* **32**: 501-515, 2007.

Bartesaghi, S., Trujillo, M., Denicola, A., Folkes, L., Wardman, P., and Radi, R. Reactions of desferrioxamine with peroxynitrite-derived carbonate and nitrogen dioxide radicals. *Free Radic. Biol. Med.* **36**: 471-483, 2004.

Beda, N. V. and Nedospasov, A. A. NO-dependent modifications of nucleic acids. *Russ. J. Bioorg. Chem.* **33**: 181-212, 2007.

Bhattacharya, M., Harold, M. P., and Balakotaiah, V. Low-dimensional models for homogeneous stirred tank reactors. *Chem. Eng. Sci.* **59**: 5587-5596, 2004.

Bielski, B. H. J. and Gebicki, J. M. Electron spin resonance studies of mechanism of interaction between nitrogen dioxide and olefinic solvents. *J. Phys. Chem.* **73**: 1402-&, 1969.

Bion, A., Fall, M., Gouriou, F., Le Prieur, E., Dionnet, F., and Morin, J. P. Biphasic culture of rat lung slices for pharmacotoxicological evaluation of complex atmospheres. *Cell Biol. Toxicol.* **18**: 301-314, 2002.

Blough, N. V. and Zafiriou, O. C. Reaction of superoxide with nitric oxide to form peroxonitrite in alkaline aqueous solution. *Inorg. Chem.* **24**: 3502-3504, 1985.

Bohle, D. S., Glassbrenner, P. A., and Hansert, B. Synthesis of pure tetramethylammonium peroxynitrite. *Methods Enzymol.* **269**: 302-311, 1996.

Bombick, D. W., Ayres, P. H., Putnam, K., Bombick, B. R., and Doolittle, D. J. Chemical and biological studies of a new cigarette that primarily heats tobacco. Part 3. In vitro toxicity of whole smoke. *Food Chem. Toxicol.* **36**: 191-197, 1998.

Bonnett, R. and Holleyhead, R. Reaction of tryptophan derivatives with nitrite. *J. Chem. Soc., Perkin Trans. 1* 962-964, 1974.

Bourne, J. R., Gholap, R. V., and Rewatkar, V. B. The influence of viscosity on the product distribution of fast parallel reactions. *Chemical Engineering Journal and the Biochemical Engineering Journal* **58**: 15-20, 1995.

Bourne, J. R., Kut, O. M., Lenzner, J., and Maire, H. Kinetics of the diazo coupling between 1-naphthol and diazotized sulfanilic acid. *Ind. Eng. Chem. Res.* **29**: 1761-1765, 1990.

Brandrup, J., Immergut, E. H., Grulke, E. A., Abe, A., and Bloch, D. R., editors. *Polymer handbook*, 4th ed. New York: John Wiley & Sons, Inc., 2005.

Brausam, A., Eigler, S., Jux, N., and van Eldik, R. Mechanistic investigations of the reaction of an iron(III) octa-anionic porphyrin complex with hydrogen peroxide and the catalyzed oxidation of diammonium-2,2'-azinobis(3-ethylbenzothiazoline-6-sulfonate). *Inorg. Chem.* **48**: 7667-7678, 2009.

Bredt, D. S., Glatt, C. E., Hwang, P. M., Fotuhi, M., Dawson, T. M., and Snyder, S. H. Nitric-oxide synthase protein and messenger-RNA are discretely localized in neuronal populations of the mammalian CNS together with NADPH diaphorase. *Neuron* **7**: 615-624, 1991a.

Bredt, D. S., Hwang, P. M., Glatt, C. E., Lowenstein, C., Reed, R. R., and Snyder, S. H. Cloned and expressed nitric-oxide synthase structurally resembles Cytochrome-P-450 reductase. *Nature* **351**: 714-718, 1991b.

Brucato, A., Ciofalo, M., Grisafi, F., and Tocco, R. On the simulation of stirred tank reactors via computational fluid dynamics. *Chem. Eng. Sci.* **55**: 291-302, 2000.

Burney, S., Tamir, S., Gal, A., and Tannenbaum, S. R. A mechanistic analysis of nitric oxide-induced cellular toxicity. *Nitric Oxide-Biol. Ch.* **1**: 130-144, 1997.

Buxton, G. V., Greenstock, C. L., Helman, W. P., and Ross, A. B. Critical-review of rate constants for reactions of hydrated electrons, hydrogen-atoms and hydroxyl radicals (.OH/.O^-) in aqueous-solution. *J. Phys. Chem. Ref. Data* **17**: 513-886, 1988.

Campolo, M. and Soldati, A. Numerical evaluation of mixing time in a tank reactor stirred by a magnetically driven impeller. *Ind. Eng. Chem. Res.* **43**: 6836-6846, 2004.

Chan, W. H., Nordstrom, R. J., Galvert, J. G., and Shaw, J. H. An IRFTS spectroscopic study of the kinetics and the mechanism of the reactions in the gaseous system, HONO, NO, NO_2, H_2O. *Chem. Phys. Lett.* **37**: 441-446, 1976.

Chappell, G. A. Aqueous scrubbing of nitrogen oxides from stack gases. *Adv. Chem. Ser.* **127**: 206-217, 1973.

Chen, B. and Deen, W. M. Analysis of the effects of cell spacing and liquid depth on nitric oxide and its oxidation products in cell cultures. *Chem. Res. Toxicol.* **14**: 135-147, 2001.

Chen, B., Keshive, M., and Deen, W. M. Diffusion and reaction of nitric oxide in suspension cell cultures. *Biophys. J.* **75**: 745-754, 1998.

Childs, R. E. and Bardsley, W. G. Steady-state kinetics of peroxidase with 2,2'-azino-di-(3-ethylbenzthiazoline-6-sulphonic acid) as chromogen. *Biochem. J.* **145**: 93-103, 1975.

Chin, M. P., Schauer, D. B., and Deen, W. M. Nitric oxide, oxygen, and superoxide formation and consumption in macrophages and colonic epithelial cells. *Chem. Res. Toxicol.* **23**: 778-787, 2010.

Chin, M. P., Schauer, D. B., and Deen, W. M. Prediction of nitric oxide concentrations in colonic crypts during inflammation. *Nitric Oxide-Biol. Ch.* **19**: 266-275, 2008.

Chrungoo, V. J., Singh, K., and Singh, J. Differential biochemical response of freshly isolated rat hepatocytes to paracetamol, carbon tetrachloride and *D*-galactosamine toxicity. *Indian J. Exp. Biol.* **35**: 603-610, 1997.

Daff, S. NO synthase: Structures and mechanisms. *Nitric Oxide-Biol. Ch.* **23**: 1-11, 2010.

Danckwerts, P. V. *Gas-liquid reactions*. McGraw-Hill Book Co., 1970.

Daum, P. H., Kelly, T. J., Schwartz, S. E., and Newman, L. Measurements of the chemical composition of stratiform clouds. *Atmos. Environ.* **18**: 2671-2684, 1984.

De Souza, B. D. M., Bortoluzzi, E. A., Da Silveira Teixeira, C., Felippe, W. T., Simões, C. M. O., and Felippe, M. C. S. Effect of HBSS storage time on human periodontal ligament fibroblast viability. *Dent. Traumatol.* **26**: 481-483, 2010.

Deen, W. M. *Analysis of transport phenomena*. New York: Oxford University Press, 1998.

Degering, E. F. and Berntsen, R. A. The oxidation of glucose and related compounds with oxides of nitrogen. *J. Am. Chem. Soc.* **73**: 848-849, 1951.

Denbigh, K. G. and Prince, A. J. Kinetics of nitrous gas absorption in aqueous nitric acid. *J. Chem. Soc.* 790-801, 1947.

Dendroulakis, V., Deen, W. M., and Dedon, P. C. Nucleotide pool as a target for nitrosative deamination during inflammation. *Chem. Res. Toxicol.* **20**: 2009, 2007.

Diaf, A. and Beckman, E. J. Thermally reversible polymeric sorbents for acid gases, IV. Affinity tuning for the selective dry sorption of NO_x. *React. Polym.* **25**: 89-96, 1995.

Distelhoff, M. F. W., Marquis, A. J., Nouri, J. M., and Whitelaw, J. H. Scalar mixing measurements in batch operated stirred tanks. *Can. J. Chem. Eng.* **75**: 641-652, 1997.

Dong, M. and Dedon, P. C. Relatively small increases in the steady-state levels of nucleobase deamination products in DNA from human TK6 cells exposed to toxic levels of nitric oxide. *Chem. Res. Toxicol.* **19**: 50-57, 2006.

Dong, M., Wang, C., Deen, W. M., and Dedon, P. C. Absence of 2'-deoxyoxanosine and presence of abasic sites in DNA exposed to nitric oxide at controlled physiological concentrations. *Chem. Res. Toxicol.* **16**: 1044-1055, 2003.

Donohue, P. K., Gilmore, M. M., Cristofalo, E., Wilson, R. F., Weiner, J. Z., Lau, B. D., Robinson, K. A., and Allen, M. C. Inhaled nitric oxide in preterm infants: A systematic review. *Pediatrics* **127**: E414-E422, 2011.

Douglas, G., Price, J., and Page, C. A method for the long-term exposure of rabbits to environmental pollutant gases. *Eur. Respir. J.* **7**: 1516-1526, 1994.

Dransfield, T. J., Perkins, K. K., Donahue, N. M., Anderson, J. G., Sprengnether, M. M., and Demerjian, K. L. Temperature and pressure dependent kinetics of the gas-phase reaction of the hydroxyl radical with nitrogen dioxide. *Geophys. Res. Lett.* **26**: 687-690, 1999.

Ducsay, C. A. and Myers, D. A. eNOS activation and NO function: Differential control of steroidogenesis by nitric oxide and its adaptation with hypoxia. *J. Endocrinol.* **210**: 259-269, 2011.

Dunn, M. G., Wark, K., Jr., and Agnew, J. T. Determination of the equilibrium constant for the gas-phase dissociation of nitrogen tetroxide by infrared absorption techniques. *J. Chem. Phys.* **37**: 2445-2449, 1962.

El-Hibri, M. J. and Paul, D. R. Gas transport in poly(vinylidene fluoride): Effects of uniaxial drawing and processing temperature. *J. Appl. Polym. Sci.* **31**: 2533-2560, 1986.

Ellman, G. L. Tissue sulfhydryl groups. *Arch. Biochem. Biophys.* **82**: 70-77, 1959.

England, C. and Corcoran, W. H. Kinetics and mechanisms of the gas-phase reaction of water vapor and nitrogen dioxide. *Industrial & Engineering Chemistry Fundamentals* **13**: 373-384, 1974.

Eyer, P., Worek, F., Kiderlen, D., Sinko, G., Stuglin, A., Simeon-Rudolf, V., and Reiner, E. Molar absorption coefficients for the reduced Ellman reagent: Reassessment. *Anal. Biochem.* **312**: 224-227, 2003.

Ferrer-Sueta, G. and Radi, R. Chemical biology of peroxynitrite: Kinetics, diffusion, and radicals. *ACS Chem. Biol.* **4**: 161-177, 2009.

Ford, E., Hughes, M. N., and Wardman, P. Kinetics of the reactions of nitrogen dioxide with glutathione, cysteine, and uric acid at physiological pH. *Free Radic. Biol. Med.* **32**: 1314-1323, 2002.

Forni, L. G., Moraarellano, V. O., Packer, J. E., and Willson, R. L. Nitrogen-dioxide and related free-radicals - electron-transfer reactions with organic-compounds in solutions containing nitrite or nitrate. *J. Chem. Soc., Perkin Trans. 2* 1-6, 1986.

Forstermann, U., Boissel, J. P., and Kleinert, H. Expressional control of the 'constitutive' isoforms of nitric oxide synthase (NOS I and NOS III). *FASEB J.* **12**: 773-790, 1998.

Fox, J. B., Jr. The determination of nitrite - a critical review. *CRC Crit. Rev. Anal. Chem* **15**: 283-313, 1985.

Fukuto, J. M. and Chaudhuri, G. Inhibition of constitutive and inducible nitric-oxide synthase - potential selective-inhibition. *Annu. Rev. Pharmacol. Toxicol.* **35**: 165-194, 1995.

Geller, D. A. and Billiar, T. R. Molecular biology of nitric oxide synthases. *Cancer Metastasis Rev.* **17**: 7-23, 1998.

Gerasimov, O. V. and Lymar, S. V. The yield of hydroxyl radical from the decomposition of peroxynitrous acid. *Inorg. Chem.* **38**: 4317-4321, 1999.

Gerboles, M., Buzica, D., and Amantini, L. Modification of the Palmes diffusion tube and semi-empirical modelling of the uptake rate for monitoring nitrogen dioxide. *Atmos. Environ.* **39**: 2579-2592, 2005.

Gerhardt, G. and Adams, R. N. Determination of diffusion coefficients by flow injection analysis. *Anal. Chem.* **54**: 2618-2620, 1982.

Gliszczynska-Swiglo, A. Folates as antioxidants. *Food Chem.* **101**: 1480-1483, 2007.

Goldan, P. D., Kuster, W. C., Albritton, D. L., Fehsenfeld, F. C., Connell, P. S., Norton, R. B., and Huebert, B. J. Calibration and tests of the filter-collection method for measuring clean-air, ambient levels of nitric acid. *Atmos. Environ.* **17**: 1355-1364, 1983.

Goldstein, S. and Czapski, G. Kinetics of nitric oxide autoxidation in aqueous solution in the absence and presence of various reductants. The nature of the oxidizing intermediates. *J. Am. Chem. Soc.* **117**: 12078-12084, 1995.

Goldstein, S. and Czapski, G. Mechanism of the nitrosation of thiols and amines by oxygenated NO solutions: The nature of the nitrosating intermediates. *J. Am. Chem. Soc.* **118**: 3419-3425, 1996.

Goldstein, S., Czapski, G., Lind, J., and Merenyi, G. Carbonate radical ion is the only observable intermediate in the reaction of peroxynitrite with CO_2. *Chem. Res. Toxicol.* **14**: 1273-1276, 2001.

Goldstein, S., Czapski, G., Lind, J., and Merenyi, G. Tyrosine nitration by simultaneous generation of NO and O_2^- under physiological conditions. *J. Biol. Chem.* **275**: 3031-3036, 2000.

Goldstein, S., Lind, J., and Merenyi, G. Reaction of organic peroxyl radicals with $\cdot NO_2$ and $\cdot NO$ in aqueous solution: Intermediacy of organic peroxynitrate and peroxynitrite species. *J. Phys. Chem. A* **108**: 1719-1725, 2004a.

Goldstein, S., Lind, J., and Merényi, G. Chemistry of peroxynitrites as compared to peroxynitrates. *Chem. Rev.* **105**: 2457-2470, 2005.

Goldstein, S. and Merenyi, G. The chemistry of peroxynitrite: Implications for biological activity. *Methods Enzymol.* **436**: 49-61, 2008.

Goldstein, S., Merenyi, G., and Samuni, A. Kinetics and mechanism of $^{\bullet}NO_2$ reacting with various oxidation states of myoglobin. *J. Am. Chem. Soc.* **126**: 15694-15701, 2004b.

Goldstein, S., Samuni, A., Hideg, K., and Merényi, G. Structure-activity relationship of cyclic nitroxides as SOD mimics and scavengers of nitrogen dioxide and carbonate radicals. *J. Phys. Chem. A* **110**: 3679-3685, 2006.

Goldstick, T. K. and Fatt, I. Diffusion of oxygen in solutions of blood proteins. *Chem. Eng. Prog. Symp. Ser.* **66**: 101-113, 1970.

Graetzel, M., Henglein, A., Lilie, J., and Beck, G. Pulsradiolytische untersuchung einiger elementarprozesse der oxydation und reduktion des nitritions. *Ber. Bunsen-Ges. Phys. Chem.* **73**: 646-653, 1969.

Graetzel, M., Taniguchi, S., and Henglein, A. Pulsradiolytische untersuchung der NO-oxydation und des gleichgewichts N_2O_3 <--> NO + NO_2 in waessriger loesung. *Ber. Bunsen-Ges. Phys. Chem.* **74**: 488-492, 1970.

Green, D. W. and Maloney, J. O., editors. *Perry's chemical engineers' handbook*, 7th ed. New York: McGraw-Hill, Inc., 1997.

Greenacre, S. A. B. and Ischiropoulos, H. Tyrosine nitration: Localisation, quantification, consequences for protein function and signal transduction. *Free Radic. Res.* **34**: 541-581, 2001.

Grisham, M. B., Johnson, G. G., and Lancaster Jr., J. R. Quantitation of nitrate and nitrite in extracellular fluids. *Methods Enzymol.* **268**: 237-246, 1996.

Guha, D., Dudukovic, M. P., Ramachandran, P. A., Mehta, S., and Alvare, J. CFD-based compartmental modeling of single phase stirred-tank reactors. *AIChE J.* **52**: 1836-1846, 2006.

Halliwell, B., Hu, M.-L., Louie, S., Duvall, T. R., Tarkington, B. K., Motchnik, P., and Cross, C. E. Interaction of nitrogen dioxide with human plasma. Antioxidant depletion and oxidative damage. *FEBS Lett.* **313**: 62-66, 1992.

Henry, Y. and Guissani, A. Interactions of nitric oxide with hemoproteins: Roles of nitric oxide in mitochondria. *Cell. Mol. Life Sci.* **55**: 1003-1014, 1999.

Hermann, C., Dewes, I., and Schumpe, A. The estimation of gas solubilities in salt solutions. *Chem. Eng. Sci.* **50**: 1673-1675, 1995.

Hesterberg, T. W., Bunn, W. B., McClellan, R. O., Hamade, A. K., Long, C. M., and Valberg, P. A. Critical review of the human data on short-term nitrogen dioxide (NO_2) exposures: Evidence for NO_2 no-effect levels. *Crit. Rev. Toxicol.* **39**: 743-781, 2009.

Hetzer, H. B., Bates, R. G., and Robinson, R. A. Dissociation constant of morpholinium ion and related thermodynamic quantities from 0 to 50^{o}. *The Journal of Physical Chemistry* **70**: 2869-2872, 1966.

Hodges, G. R., Marwaha, J., Paul, T., and Ingold, K. U. A novel procedure for generating both nitric oxide and superoxide in situ from chemical sources at any chosen mole ratio. First application: Tyrosine oxidation and a comparison with preformed peroxynitrite. *Chem. Res. Toxicol.* **13**: 1287-1293, 2000.

Hoffman, M. Z. and Hayon, E. Pulse radiolysis study of sulfhydryl compounds in aqueous solution. *J. Phys. Chem.* **77**: 990-996, 1973.

Horstmann, S., Jabloniec, A., Krafczyk, J., Fischer, K., and Gmehling, J. PSRK group contribution equation of state: Comprehensive revision and extension IV, including critical constants and α-function parameters for 1000 components. *Fluid Phase Equilib.* **227**: 157-164, 2005.

Hughes, M. N., Nicklin, H. G., and Shrimanker, K. Autoxidation of hydroxylamine in alkaline solutions. II. Kinetics. Acid dissociation constant of hydroxylamine. *J. Chem. Soc. A, Inorg. Phys. Theor.* 3485-3487, 1971.

Huie, R. E. and Padmaja, S. The reaction of nitric oxide with superoxide. *Free Radic. Res. Commun.* **18**: 195-199, 1993.

Ignarro, L. J. Endothelium-derived nitric-oxide – pharmacology and relationship to the actions of organic nitrate esters. *Pharm. Res.* **6**: 651-659, 1989.

Ignarro, L. J., Buga, G. M., Wood, K. S., Byrns, R. E., and Chaudhuri, G. Endothelium-derived relaxing factor produced and released from artery and vein is nitric oxide. *Proc. Natl. Acad. Sci. U. S. A.* **84**: 9265-9269, 1987.

Ignarro, L. J., Cirino, G., Casini, A., and Napoli, C. Nitric oxide as a signaling molecule in the vascular system: An overview. *J. Cardiovasc. Pharmacol.* **34**: 879-886, 1999.

Ischiropoulos, H. Protein tyrosine nitration-an update. *Arch. Biochem. Biophys.* **484**: 117-121, 2009.

Ishibe, T., Sato, T., Hayashi, T., Kato, N., and Hata, T. Absorption of nitrogen dioxide and nitric oxide by soda lime. *Br. J. Anaesth.* **75**: 330-333, 1995.

Jenkins, D. C., Charles, I. G., Thomsen, L. L., Moss, D. W., Holmes, L. S., Baylis, S. A., Rhodes, P., Westmore, K., Emson, P. C., and Moncada, S. Roles of nitric oxide in tumor growth. *Proc. Natl. Acad. Sci. U. S. A.* **92**: 4392-4396, 1995.

Jin, D.-S., Deshwal, B.-R., Park, Y.-S., and Lee, H.-K. Simultaneous removal of SO_2 and NO by wet scrubbing using aqueous chlorine dioxide solution. *J. Hazard. Mater.* **135**: 412-417, 2006.

Jin, W. and Chen, H. A new method of determination of diffusion coefficients using capillary zone electrophoresis (peak-height method). *Chromatographia* **52**: 17-21, 2000.

Joshi, R., Adhikari, S., Patro, B. S., Chattopadhyay, S., and Mukherjee, T. Free radical scavenging behavior of folic acid: Evidence for possible antioxidant activity. *Free Radic. Biol. Med.* **30**: 1390-1399, 2001.

Joubert, J. and Malan, S. F. Novel nitric oxide synthase inhibitors: A patent review. *Expert Opinion on Therapeutic Patents* **21**: 537-560, 2011.

Karoui, H., Hogg, N., Fréjaville, C., Tordo, P., and Kalyanaraman, B. Characterization of sulfur-centered radical intermediates formed during the oxidation of thiols and sulfite by peroxynitrite - ESR-spin trapping and oxygen uptake studies. *J. Biol. Chem.* **271**: 6000-6009, 1996.

Kavdia, M., Stanfield, J., and Lewis, R. Nitric oxide, superoxide, and peroxynitrite effects on the insulin secretion and viability of β-TC3 cells. *Ann. Biomed. Eng.* **28**: 102-109, 2000.

Keshive, M., Singh, S., Wishnok, J. S., Tannenbaum, S. R., and Deen, W. M. Kinetics of s-nitrosation of thiols in nitric oxide solutions. *Chem. Res. Toxicol.* **9**: 988-993, 1996.

Khan, N. E. and Adewuyi, Y. G. Absorption and oxidation of nitric oxide (NO) by aqueous solutions of sodium persulfate in a bubble column reactor. *Ind. Eng. Chem. Res.* **49**: 8749-8760, 2010.

Kim, H.-H. Electrochemical behaviors of $ABTS^{2-}$ on the thiol-modified gold electrodes. *J. Kor. Electrochem. Soc.* **9**: 113-117, 2006.

Kirby, A. J. Hydrolysis and formation of esters of organic acids. In: *Ester formation and hydrolysis and related reactions* (v 10), edited by Bamford C. H. and Tipper C. F. H.: Elsevier, 1972, p. 57-207.

Kirsch, M., Fuchs, A., and de Groot, H. Regiospecific nitrosation of N-terminal-blocked tryptophan derivatives by N_2O_3 at physiological pH. *J. Biol. Chem.* **278**: 11931-11936, 2003.

Kirsch, M., Lomonosova, E. E., Korth, H. G., Sustmann, R., and de Groot, H. Hydrogen peroxide formation by reaction of peroxynitrite with HEPES and related tertiary amines - implications for a general mechanism. *J. Biol. Chem.* **273**: 12716-12724, 1998.

Kiziltepe, T., Yan, A., Dong, M., Jonnalagadda, V. S., Dedon, P. C., and Engelward, B. P. Delineation of the chemical pathways underlying nitric oxide-induced homologous recombination in mammalian cells. *Chem. Biol.* **12**: 357-369, 2005.

Kobayashi, H., Takezawa, N., and Niki, T. Removal of nitrogen oxides with aqueous solutions of inorganic and organic reagents. *Environ. Sci. Technol.* **11**: 190-192, 1977.

Kolthoff, I. M. and Sandell, E. B. *Textbook of quantitative inorganic analysis*, 3rd Edition. New York: Macmillan, 1952.

Komori, K., Murai, K., Miyajima, S., Fujii, T., Mohri, S., Ono, Y., and Sakai, Y. Development of an in vitro batch-type closed gas exposure device with an alveolar epithelial cell line, A549, for toxicity evaluations of gaseous compounds. *Anal. Sci.* **24**: 957-962, 2008.

Kone, B. C. and Baylis, C. Biosynthesis and homeostatic roles of nitric oxide in the normal kidney. *Am. J. Physiol. Renal Physiol.* **272**: F561-F578, 1997.

Koppenol, W. H., Kissner, R., and Beckman, J. S. Syntheses of peroxynitrite: To go with the flow or on solid grounds? *Methods Enzymol.* **269**: 296-302, 1996.

Kröncke, K.-D., Brenner, H.-H., Rodriguez, M.-L., Etzkorn, K., Noack, E. A., Kolb, H., and Kolb-Bachofen, V. Pancreatic islet cells are highly susceptible towards the cytotoxic effects of chemically generated nitric oxide. *Biochim. Biophys. Acta* **1182**: 221-229, 1993.

Kuhn, D. M., Aretha, C. W., and Geddes, T. J. Peroxynitrite inactivation of tyrosine hydroxylase: Mediation by sulfhydryl oxidation, not tyrosine nitration. *J. Neurosci.* **19**: 10289-10294, 1999.

Kunas, K. T. and Papoutsakis, E. T. Damage mechanisms of suspended animal cells in agitated bioreactors with and without bubble entrainment. *Biotechnol. Bioeng.* **102**: 980-987, 2009.

Lagercrantz, C. Electron spin resonance studies of nitroxide radicals formed in reaction between nitrogen dioxide and dimethyl sulphoxide. *Acta Chem. Scand.* **23**: 3259-&, 1969.

Lamas, S., Marsden, P. A., Li, G. K., Tempst, P., and Michel, T. Endothelial nitric-oxide synthase - molecular-cloning and characterization of a distinct constitutive enzyme isoform. *Proc. Natl. Acad. Sci. U. S. A.* **89**: 6348-6352, 1992.

Lamkin-Kennard, K. A., Buerk, D. G., and Jaron, D. Interactions between NO and O_2 in the microcirculation: A mathematical analysis. *Microvasc. Res.* **68**: 38-50, 2004.

Landino, L. M., Mall, C. B., Nicklay, J. J., Dutcher, S. K., and Moynihan, K. L. Oxidation of 5-thio-2-nitrobenzoic acid, by the biologically relevant oxidants peroxynitrite anion, hydrogen peroxide and hypochlorous acid. *Nitric Oxide-Biol. Ch.* **18**: 11-18, 2008.

Lange, N. A., editor. *Lange's handbook of chemistry*, 15th ed. New York: McGraw-Hill, Inc., 1999.

Lee, Y. A., Yun, B. H., Kim, S. K., Margolin, Y., Dedon, P. C., Geacintov, N. E., and Shafirovich, V. Mechanisms of oxidation of guanine in DNA by carbonate radical anion, a decomposition product of nitrosoperoxycarbonate. *Chem. Eur. J.* **13**: 4571-4581, 2007.

Lee, Y. N. and Schwartz, S. E. Reaction kinetics of nitrogen dioxide with liquid water at low partial pressure. *J. Phys. Chem.* **85**: 840-848, 1981.

Lehmann, J. Nitric oxide donors - current trends in therapeutic applications. *Expert Opinion on Therapeutic Patents* **10**: 559-574, 2000.

Lennon, C. W., Cox, H. D., Hennelly, S. P., Chelmo, S. J., and McGuirl, M. A. Probing structural differences in prion protein isoforms by tyrosine nitration. *Biochemistry* **46**: 4850-4860, 2007.

Lewis, R. S. and Deen, W. M. Kinetics of the reaction of nitric oxide with oxygen in aqueous solutions. *Chem. Res. Toxicol.* **7**: 568-574, 1994.

Lewis, R. S., Tamir, S., Tannenbaum, S. R., and Deen, W. M. Kinetic analysis of the fate of nitric oxide synthesized by macrophages in vitro. *J. Biol. Chem.* **270**: 29350-29355, 1995a.

Lewis, R. S., Tannenbaum, S. R., and Deen, W. M. Kinetics of N-nitrosation in oxygenated nitric oxide solutions at physiological pH: Role of nitrous anhydride and effects of phosphate and chloride. *J. Am. Chem. Soc.* **117**: 3933-3939, 1995b.

Li, C.-Q., Kim, M. Y., Godoy, L. C., Thiantanawat, A., Trudel, L. J., and Wogan, G. N. Nitric oxide activation of Keap1/Nrf2 signaling in human colon carcinoma cells. *Proc. Natl. Acad. Sci. U. S. A.* **106**: 14547-14551, 2009.

Li, C.-Q., Pang, B., Kiziltepe, T., Trudel, L. J., Engelward, B. P., Dedon, P. C., and Wogan, G. N. Threshold effects of nitric oxide-induced toxicity and cellular responses in wild-type and p53-null human lymphoblastoid cells. *Chem. Res. Toxicol.* **19**: 399-406, 2006.

Li, C.-Q., Trudel, L. J., and Wogan, G. N. Genotoxicity, mitochondrial damage, and apoptosis in human lymphoblastoid cells exposed to peroxynitrite generated from SIN-1. *Chem. Res. Toxicol.* **15**: 527-535, 2002a.

Li, C.-Q., Trudel, L. J., and Wogan, G. N. Nitric oxide-induced genotoxicity, mitochondrial damage, and apoptosis in human lymphoblastoid cells expressing wild-type and mutant p53. *Proc. Natl. Acad. Sci. U. S. A.* **99**: 10364-10369, 2002b.

Li, C.-Q., Wright, T. L., Dong, M., Dommels, Y. E. M., Trudel, L. J., Dedon, P. C., Tannenbaum, S. R., and Wogan, G. N. Biological role of glutathione in nitric oxide-induced toxicity in cell culture and animal models. *Free Radic. Biol. Med.* **39**: 1489-1498, 2005.

Li, Q. and Lancaster, J. R. Calibration of nitric oxide flux generation from diazeniumdiolate ˙NO donors. *Nitric Oxide-Biol. Ch.* **21**: 69-75, 2009.

Licht, W. R., Tannenbaum, S. R., and Deen, W. M. Use of ascorbic acid to inhibit nitrosation: Kinetic and mass transfer considerations for an in vitro system. *Carcinogenesis* **9**: 365-372, 1988.

Lim, C. H. *Prediction of concentrations of reactive nitrogen species in aqueous solutions and cells* (PhD Thesis). Cambridge, MA: Massachusetts Institute of Technology, 2011.

Lim, C. H., Dedon, P. C., and Deen, W. M. Kinetic analysis of intracellular concentrations of reactive nitrogen species. *Chem. Res. Toxicol.* **21**: 2134-2147, 2008.

Lindberg, L. and Rydgren, G. Evaluation of nitrogen dioxide scavengers during delivery of inhaled nitric oxide. *Br. J. Anaesth.* **81**: 404-408, 1998.

Liu, R. H. and Hotchkiss, J. H. Potential genotoxicity of chronically elevated nitric-oxide - a review. *Mutation Research-Reviews in Genetic Toxicology* **339**: 73-89, 1995.

Liu, X., Miller, M. J. S., Joshi, M. S., Thomas, D. D., and Lancaster, J. R. Accelerated reaction of nitric oxide with O_2 within the hydrophobic interior of biological membranes. *Proc. Natl. Acad. Sci. U. S. A.* **95**: 2175-2179, 1998.

Lobachev, V. L. and Rudakov, E. S. Kinetics and mechanism of the oxidation of alkanes and alkenes with peroxynitrous acid in aqueous solution-gas phase systems. *Kinetics and Catalysis* **46**: 344-353, 2005.

Lomonosova, E. E., Kirsch, M., Rauen, U., and de Groot, H. The critical role of HEPES in SIN-1 cytotoxicity, peroxynitrite versus hydrogen peroxide. *Free Radic. Biol. Med.* **24**: 522-528, 1998.

Lymar, S. V., Jiang, Q., and Hurst, J. K. Mechanism of carbon dioxide-catalyzed oxidation of tyrosine by peroxynitrite. *Biochemistry* **35**: 7855-7861, 1996.

Mahal, H. S., Sharma, H. S., and Mukherjee, T. Antioxidant properties of melatonin: A pulse radiolysis study. *Free Radic. Biol. Med.* **26**: 557-567, 1999.

Maragos, C. M., Morley, D., Wink, D. A., Dunams, T. M., Saavedra, J. E., Hoffman, A., Bove, A. A., Isaac, L., Hrabie, J. A., and Keefer, L. K. Complexes of NO with nucleophiles as agents for the controlled biological release of nitric oxide. Vasorelaxant effects. *J. Med. Chem.* **34**: 3242-3247, 1991.

Marani, D., Patterson, J. W., and Anderson, P. R. Alkaline precipitation and aging of Cu(II) in the presence of sulfate. *Water Res.* **29**: 1317-1326, 1995.

Masha, A., Dinatale, S., Allasia, S., and Martina, V. Role of the decreased nitric oxide bioavailability in the vascular complications of diabetes mellitus. *Curr. Pharm. Biotech.* **12**: 1354-1363, 2011.

Masumoto, H. and Sies, H. The reaction of ebselen with peroxynitrite. *Chem. Res. Toxicol.* **9**: 262-267, 1996.

McCarthy, H. O., Coulter, J. A., Robson, T., and Hirst, D. G. Gene therapy via inducible nitric oxide synthase: A tool for the treatment of a diverse range of pathological conditions. *J. Pharm. Pharmacol.* **60**: 999-1017, 2008.

Merényi, G., Lind, J., Goldstein, S., and Czapski, G. Mechanism and thermochemistry of peroxynitrite decomposition in water. *J. Phys. Chem. A* **103**: 5685-5691, 1999.

Mertes, S. and Wahner, A. Uptake of nitrogen dioxide and nitrous acid on aqueous surfaces. *J. Phys. Chem.* **99**: 14000-14006, 1995.

Mezyk, S. P. Determination of the rate constant for the reaction of hydroxyl and oxide radicals with cysteine in aqueous solution. *Radiat. Res.* **145**: 102-106, 1996a.

Mezyk, S. P. Rate constant determination for the reaction of hydroxyl and glutathione thiyl radicals with glutathione in aqueous solution. *J. Phys. Chem.* **100**: 8861-8866, 1996b.

Minetti, M., Pietraforte, D., Straface, E., Metere, A., Matarrese, P., and Malorni, W. Red blood cells as a model to differentiate between direct and indirect oxidation pathways of peroxynitrite. *Methods Enzymol.* **440**: 253-272, 2008.

Miyamoto, S., Ronsein, G. E., Correa, T. C., Martinez, G. R., Medeiros, M. H. G., and Mascio, P. Direct evidence of singlet molecular oxygen generation from peroxynitrate, a decomposition product of peroxynitrite. *Dalton Transactions* 5720-5729, 2009.

Moncada, S., Palmer, R. M. J., and Higgs, E. A. Biosynthesis of nitric oxide from L-arginine: A pathway for the regulation of cell function and communication. *Biochem. Pharmacol.* **38**: 1709-1715, 1989.

Monn, C. Exposure assessment of air pollutants: A review on spatial heterogeneity and indoor/outdoor/personal exposure to suspended particulate matter, nitrogen dioxide and ozone. *Atmos. Environ.* **35**: 1-32, 2001.

Morga-Ramirez, M., Collados-Larumbe, M. T., Johnson, K. E., Rivas-Arreola, M. J., Carrillo-Cocom, L. M., and Alvarez, M. M. Hydrodynamic conditions induce changes in secretion level and glycosylation patterns of von willebrand factor (vWF) in endothelial cells. *Journal of Bioscience and Bioengineering* **109**: 400-406, 2010.

Mumtaz, F. H., Khan, M. A., Sullivan, M. E., Thompson, C. S., Mikhailidis, D. P., Morgan, R. J., and Dashwood, M. R. Potential role of endothelin and nitric oxide in physiology and pathophysiology of the lower urinary tract. *Endothelium-Journal of Endothelial Cell Research* **7**: 1-9, 1999.

Nakagawa, H. Photocontrollable nitric oxide (NO) and nitroxyl (HNO) donors and their release mechanisms. *Nitric Oxide-Biol. Ch.* **25**: 195-200, 2011.

Nakamura, M., Nagayoshi, R., Ijiri, K., Nakashima-Matsushita, N., Takeuchi, T., and Matsuyama, T. Nitration and chlorination of folic acid by peroxynitrite and hypochlorous acid, and the selective binding of 10-nitro-folate to folate receptor beta. *Biochem. Biophys. Res. Commun.* **297**: 1238-1244, 2002.

Nalwaya, N. and Deen, W. M. Analysis of the effects of nitric oxide and oxygen on nitric oxide production by macrophages. *J. Theor. Biol.* **226**: 409-419, 2004a.

Nalwaya, N. and Deen, W. M. Peroxynitrite exposure of cells cocultured with macrophages. *Ann. Biomed. Eng.* **32**: 664-676, 2004b.

Nauser, T. and Koppenol, W. H. The rate constant of the reaction of superoxide with nitrogen monoxide: Approaching the diffusion limit. *J. Phys. Chem. A* **106**: 4084-4086, 2002.

Nere, N. K., Patwardhan, A. W., and Joshi, J. B. Liquid-phase mixing in stirred vessels: Turbulent flow regime. *Ind. Eng. Chem. Res.* **42**: 2661-2698, 2003.

Niles, J. C., Wishnok, J. S., and Tannenbaum, S. R. Peroxynitrite-induced oxidation and nitration products of guanine and 8-oxoguanine: Structures and mechanisms of product formation. *Nitric Oxide* **14**: 109-121, 2006.

Nizkorodov, S. A. and Wennberg, P. O. First spectroscopic observation of gas-phase HOONO. *J. Phys. Chem. A* **106**: 855-859, 2002.

Nucifora, G., Smaller, B., Remko, R., and Avery, E. C. Transient radicals of DNA bases by pulse radiolysis. Effects of cysteine and cysteamine as radioprotectors. *Radiat. Res.* **49**: 96-111, 1972.

O'Connor, D. M. and O'Brien, T. Nitric oxide synthase gene therapy: Progress and prospects. *Expert Opinion on Biological Therapy* **9**: 867-878, 2009.

Oh, S. K. W., Nienow, A. W., Al-Rubeai, M., and Emery, A. N. The effects of agitation intensity with and without continuous sparging on the growth and antibody production of hybridoma cells. *J. Biotechnol.* **12**: 45-61, 1989.

Paige, J. S. and Jaffrey, S. R. Pharmacologic manipulation of nitric oxide signaling: Targeting NOS dimerization and protein-protein interactions. *Current Topics in Medicinal Chemistry* **7**: 97-114, 2007.

Palmer, R. M. J., Ferrige, A. G., and Moncada, S. Nitric oxide release accounts for the biological activity of endothelium-derived relaxing factor. *Nature* **327**: 524-526, 1987.

Palmes, E. D., Gunnison, A. F., DiMattio, J., and Tomczyk, C. Personal sampler for nitrogen dioxide. *Am. Ind. Hyg. Assoc. J.* **37**: 570 - 577, 1976.

Pamir, B. and Wogan, G. N. Carbon dioxide modulation of peroxynitrite-induced mutagenesis of the supF gene in pSP189. *Chem. Res. Toxicol.* **16**: 487-492, 2003.

Parkinson, J. F., Mitrovic, B., and Merrill, J. E. The role of nitric oxide in multiple sclerosis. *J. Mol. Med.* **75**: 174-186, 1997.

Pasternak, R. A., Christensen, M. V., and Heller, J. Diffusion and permeation of oxygen, nitrogen, carbon dioxide, and nitrogen dioxide through polytetrafluoroethylene. *Macromolecules* **3**: 366-371, 1970.

Perrin, D. and Koppenol, W. H. The quantitative oxidation of methionine to methionine sulfoxide by peroxynitrite. *Archives of Biochemistry and Biophysics* **377**: 266-272, 2000.

Persinger, R. L., Blay, W. M., Heintz, N. H., Hemenway, D. R., and Janssen-Heininger, Y. M. W. Nitrogen dioxide induces death in lung epithelial cells in a density-dependent manner. *Am. J. Respir. Cell Mol. Biol.* **24**: 583-590, 2001.

Pfeiffer, S., Gorren, A. C. F., Schmidt, K., Werner, E. R., Hansert, B., Bohle, D. S., and Mayer, B. Metabolic fate of peroxynitrite in aqueous solution. *J. Biol. Chem.* **272**: 3465-3470, 1997.

Pfeiffer, S., Lass, A., Schmidt, K., and Mayer, B. Protein tyrosine nitration in mouse peritoneal macrophages activated in vitro and in vivo: Evidence against an essential role of peroxynitrite. *FASEB J.* **15**: 2355-2364, 2001.

Pfeiffer, S. and Mayer, B. Lack of tyrosine nitration by peroxynitrite generated at physiological pH. *J. Biol. Chem.* **273**: 27280-27285, 1998.

Pfeiffer, S., Schmidt, K., and Mayer, B. Dityrosine formation outcompetes tyrosine nitration at low steady-state concentrations of peroxynitrite. Implications for tyrosine modification by nitric oxide/superoxide in vivo. *J. Biol. Chem.* **275**: 6346-6352, 2000.

Postlethwait, E. M. and Mustafa, M. G. Effect of altered dose-rate on NO_2 uptake and transformation in isolated lungs. *J. Toxicol. Environ. Health* **26**: 497-507, 1989.

Press, W. H. *Numerical recipes: The art of scientific computing*, 3rd Edition. Cambridge University Press, 2007.

Prütz, W. A., Mönig, H., Butler, J., and Land, E. J. Reactions of nitrogen dioxide in aqueous model systems: Oxidation of tyrosine units in peptides and proteins. *Arch. Biochem. Biophys.* **243**: 125-134, 1985.

Pryor, W. A., Cueto, R., Jin, X., Koppenol, W. H., Ngu-Schwemlein, M., Squadrito, G. L., Uppu, P. L., and Uppu, R. M. A practical method for preparing peroxynitrite solutions of low ionic strength and free of hydrogen peroxide. *Free Radic. Biol. Med.* **18**: 75-83, 1995.

Pryor, W. A., Jin, X., and Squadrito, G. L. One- and two-electron oxidations of methionine by peroxynitrite. *Proc. Natl. Acad. Sci. U. S. A.* **91**: 11173-11177, 1994.

Pryor, W. A. and Squadrito, G. L. The chemistry of peroxynitrite: A product from the reaction of nitric oxide with superoxide. *American Journal of Physiology* **268**: L699-722, 1995.

Quijano, C., Alvarez, B., Gatti, R. M., Augusto, O., and Radi, R. Pathways of peroxynitrite oxidation of thiol groups. *Biochem. J.* **322**: 167-173, 1997.

Radi, R., Beckman, J. S., Bush, K. M., and Freeman, B. A. Peroxynitrite oxidation of sulfhydryls. The cytotoxic potential of superoxide and nitric oxide. *J. Biol. Chem.* **266**: 4244-4250, 1991.

Radi, R., Rubbo, H., Thomson, L., and Prodanov, E. Luminol chemiluminescence using xanthine and hypoxanthine as xanthine-oxidase substrates. *Free Radic. Biol. Med.* **8**: 121-126, 1990.

Rafikov, R., Fonseca, F. V., Kumar, S., Pardo, D., Darragh, C., Elms, S., Fulton, D., and Black, S. M. eNOS activation and NO function: Structural motifs responsible for the posttranslational control of endothelial nitric oxide synthase activity. *J. Endocrinol.* **210**: 271-284, 2011.

Ramamurthi, A. and Lewis, R. S. Measurement and modeling of nitric oxide release rates for nitric oxide donors. *Chem. Res. Toxicol.* **10**: 408-413, 1997.

Ranade, V. V., Bourne, J. R., and Joshi, J. B. Fluid-mechanics and blending in agitated tanks. *Chem. Eng. Sci.* **46**: 1883-1893, 1991.

Rebrin, I., Bregere, C., Gallaher, T. K., and Sohal, R. S. Detection and characterization of peroxynitrite-induced modifications of tyrosine, tryptophan, and methionine residues by tandem mass spectrometry. *Methods Enzymol.* **441**: 283-294, 2008.

Rezk, B. M., Haenen, G. R. M. M., van der Vijgh, W. J. F., and Bast, A. Tetrahydrofolate and 5-methyltetrahydrofolate are folates with high antioxidant activity. Identification of the antioxidant pharmacophore. *FEBS Lett.* **555**: 601-605, 2003.

Robb, W. L. Thin silicone membranes—their permeation properties and some applications. *Ann. N. Y. Acad. Sci.* **146**: 119-137, 1968.

Robinson, K. M. and Beckman, J. S. Synthesis of peroxynitrite from nitrite and hydrogen peroxide. *Methods Enzymol.* **396**: 207-214, 2005.

Rosser, W. Thermal decomposition of nitrogen dioxide. *J. Chem. Phys.* **24**: 493, 1956.

Saha, A., Goldstein, S., Cabelli, D., and Czapski, G. Determination of optimal conditions for synthesis of peroxynitrite by mixing acidified hydrogen peroxide with nitrite. *Free Radic. Biol. Med.* **24**: 653-659, 1998.

Sampson, J. B., Ye, Y., Rosen, H., and Beckman, J. S. Myeloperoxidase and horseradish peroxidase catalyze tyrosine nitration in proteins from nitrite and hydrogen peroxide. *Arch. Biochem. Biophys.* **356**: 207-213, 1998.

Sato, S., Suzuki, M., Kanehashi, S., and Nagai, K. Permeability, diffusivity, and solubility of benzene vapor and water vapor in high free volume silicon- or fluorine-containing polymer membranes. *J. Membr. Sci.* **360**: 352-362, 2010.

Schwartz, S. E. and White, W. H. Solubility equilibria of the nitrogen oxides and oxyacids in dilute aqueous solution. *Adv. in Environ. Sci. Eng.* **4**: 1-46, 1981.

Shafirovich, V., Cadet, J., Gasparutto, D., Dourandin, A., and Geacintov, N. E. Nitrogen dioxide as an oxidizing agent of 8-oxo-7,8-dihydro-2'-deoxyguanosine but not of 2'-deoxyguanosine. *Chem. Res. Toxicol.* **14**: 233-241, 2001.

Singh, S. and Gupta, A. K. Nitric oxide: Role in tumour biology and iNOS/NO-based anticancer therapies. *Cancer Chemother. Pharmacol.* **67**: 1211-1224, 2011.

Skinn, B. T., Lim, C. H., and Deen, W. M. Nitric oxide delivery system for biological media. *Free Radic. Biol. Med.* **50**: 381-388, 2011.

Spinas, G. A. The dual role of nitric oxide in islet beta-cells. *News Physiol. Sci.* **14**: 49-54, 1999.

Srivastava, B. N. and Barua, A. K. Thermal conductivity and equilibrium constant of the system N_2O_4 <--> 2 NO_2. *J. Chem. Phys.* **35**: 329-334, 1961.

Steinhorn, R. H. Therapeutic approaches using nitric oxide in infants and children. *Free Radic. Biol. Med.* **51**: 1027-1034, 2011.

Stuehr, D. J. Mammalian nitric oxide synthases. *Biochim. Biophys. Acta* **1411**: 217-230, 1999.

Switalla, S., Knebel, J., Ritter, D., Krug, N., Braun, A., and Sewald, K. Effects of acute in vitro exposure of murine precision-cut lung slices to gaseous nitrogen dioxide and ozone in an air-liquid interface (ALI) culture. *Toxicol. Lett.* **196**: 117-124, 2010.

Szabo, C. Physiological and pathophysiological roles of nitric oxide in the central nervous system. *Brain Res. Bull.* **41**: 131-141, 1996.

Tamir, S., Burney, S., and Tannenbaum, S. R. DNA damage by nitric oxide. *Chem. Res. Toxicol.* **9**: 821-827, 1996.

Tamir, S., Lewis, R. S., Walker, T. D., Deen, W. M., Wishnok, J. S., and Tannenbaum, S. R. The influence of delivery rate on the chemistry and biological effects of nitric-oxide. *Chem. Res. Toxicol.* **6**: 895-899, 1993.

Tamir, S. and Tannenbaum, S. R. The role of nitric oxide ($NO^{\bullet}$) in the carcinogenic process. *Biochim. Biophys. Acta* **1288**: F31-F36, 1996.

Thomas, D. D., Espey, M. G., Vitek, M. P., Miranda, K. M., and Wink, D. A. Protein nitration is mediated by heme and free metals through Fenton-type chemistry: An alternative to the NO/O_2^- reaction. *Proc. Natl. Acad. Sci. U. S. A.* **99**: 12691-12696, 2002.

Thomas, D. D., Liu, X., Kantrow, S. P., and Lancaster, J. R., Jr. The biological lifetime of nitric oxide: Implications for the perivascular dynamics of NO and O_2. *Proc. Natl. Acad. Sci. U. S. A.* **98**: 355-360, 2001.

Tomadakis, M. M. and Sotirchos, S. V. Ordinary and transition regime diffusion in random fiber structures. *AIChE J.* **39**: 397-412, 1993.

Torres, J. and Wilson, M. T. The reactions of copper proteins with nitric oxide. *Biochim. Biophys. Acta* **1411**: 310-322, 1999.

Treinin, A. and Hayon, E. Absorption spectra and reaction kinetics of NO_2, N_2O_3, and N_2O_4 in aqueous solution. *J. Am. Chem. Soc.* **92**: 5821-5828, 1970.

Trujillo, M. and Radi, R. Peroxynitrite reaction with the reduced and the oxidized forms of lipoic acid: New insights into the reaction of peroxynitrite with thiols. *Arch. Biochem. Biophys.* **397**: 91-98, 2002.

Tsutsui, M., Shimokawa, H., Morishita, T., Nakashima, Y., and Yanagihara, N. Development of genetically engineered mice lacking all three nitric oxide synthases. *J. Pharmacol. Sci. (Japan)* **102**: 147-154, 2006.

Venkatasubramanian, L. and Maruthamuthu, P. Kinetics and mechanism of formation and decay of 2,2'-azinobis(3-ethylbenzothiazole-6-sulfonate) radical cation in aqueous solution by inorganic peroxides. *Int. J. Chem. Kinet.* **21**: 399-421, 1989.

Verhoek, F. H. and Daniels, F. The dissociation constants of nitrogen tetroxide and of nitrogen trioxide. *J. Am. Chem. Soc.* **53**: 1250-1263, 1931.

Wang, C. and Deen, W. M. Nitric oxide delivery system for cell culture studies. *Ann. Biomed. Eng.* **31**: 65-79, 2003.

Wang, C. and Deen, W. M. Peroxynitrite delivery methods for toxicity studies. *Chem. Res. Toxicol.* **17**: 32-44, 2004.

Wang, C., Trudel, L. J., Wogan, G. N., and Deen, W. M. Thresholds of nitric oxide-mediated toxicity in human lymphoblastoid cells. *Chem. Res. Toxicol.* **16**: 1004-1013, 2003.

Wardman, P. Evaluation of the 'radical sink' hypothesis from a chemical-kinetic viewpoint. *J. Radioanal. Nucl. Chem.* **232**: 23-27, 1998.

Wardman, P. and von Sonntag, C. Kinetic factors that control the fate of thiyl radicals in cells. *Methods Enzymol.* **251**: 31-45, 1995.

Weichenthal, S., Dufresne, A., and Infante-Rivard, C. Review: Indoor nitrogen dioxide and VOC exposures: Summary of evidence for an association with childhood asthma and a case for the inclusion of indoor ultrafine particle measures in future studies. *Indoor Built Environ.* **16**: 387-399, 2007.

Weimann, J., Hagenah, J. U., and Motsch, J. Reduction in nitrogen dioxide concentration by soda lime preparations during simulated nitric oxide inhalation. *Br. J. Anaesth.* **79**: 641-644, 1997.

Weiss, R. F. The solubility of nitrogen, oxygen and argon in water and seawater. *Deep Sea Res. Oceanogr. Abstr.* **17**: 721-735, 1970.

Wendt, J., Fabian, P., Flentje, G., and Kourtidis, K. Investigation of catalytic reduction and filter techniques for simultaneous measurements of NO, NO_2 and HNO_3. *NASA Conf. Publ.* **3266**: 870-873, 1994.

Wenger, K. S., Dunlop, E. H., and Macgilp, I. D. Investigation of the chemistry of a diazo micromixing test reaction. *AIChE J.* **38**: 1105-1114, 1992.

Wiberg, N. and Aylett, B. J., editors. *Inorganic chemistry*. San Diego: Academic Press, 2001.

Williams, D. L. H. S-nitrosation and the reactions of S-nitroso compounds. *Chem. Soc. Rev.* **14**: 171-196, 1985.

Wolfenden, B. S. and Willson, R. L. Radical-cations as reference chromogens in kinetic studies of one-electron transfer reactions: Pulse radiolysis studies of 2,2'-azinobis-(3-ethylbenzthiazoline-6-sulphonate). *J. Chem. Soc., Perkin Trans. 2* 805-812, 1982.

Xie, Q. W., Cho, H. J., Calaycay, J., Mumford, R. A., Swiderek, K. M., Lee, T. D., Ding, A. H., Troso, T., and Nathan, C. Cloning and characterization of inducible nitric-oxide synthase from mouse macrophages. *Science* **256**: 225-228, 1992.

Yoder, C. H., Agee, T. M., Ginion, K. E., Hofmann, A. E., Ewanichak, J. E., Schaeffer, C. D., Jr., Carroll, M. J., Schaeffer, R. W., and McCaffrey, P. F. The relative stabilities of the copper hydroxyl sulphates. *Mineral. Mag.* **71**: 571-577, 2007.

Yoshikawa, T., Naito, Y., Masui, K., Fujii, T., Boku, Y., Nakagawa, S., Yoshida, N., and Kondo, M. Free radical-scavenging activity of *Crassostera gigas* extract (JCOE). *Biomed. Pharmacother.* **51**: 328-332, 1997.

Zacharia, I. and Deen, W. Diffusivity and solubility of nitric oxide in water and saline. *Ann. Biomed. Eng.* **33**: 214-222, 2005.

Zauner, R. and Jones, A. G. On the influence of mixing on crystal precipitation processes - application of the segregated feed model. *Chem. Eng. Sci.* **57**: 821-831, 2002.

Zeng, Y., Liu, J., Schlicht, K. E., Khan, A., Wishnok, J. S., and Tannenbaum, S. R. Simultaneous quantification of free and protein-bound chlorotyrosine and nitrotyrosine in biological fluid an tissue by NICI GC/MS. *Chem. Res. Toxicol.* **23**: 287-287, 2010.

Zhang, H., Bhargava, K., Keszler, A., Feix, J., Hogg, N., Joseph, J., and Kalyanaraman, B. Transmembrane nitration of hydrophobic tyrosyl peptides - localization, characterization, mechanism of nitration, and biological implications. *J. Biol. Chem.* **278**: 8969-8978, 2003.

Zhang, X. Nitric oxide (NO) electrochemical sensors. In: *Electrochemical sensors, biosensors and their biomedical applications*, edited by Zhang X., Ju H. and Wang J. New York: Academic Press, 2008, p. 1-29.

Zhang, Y.-Y., Xu, A.-M., Nomen, M., Walsh, M., Keaney, J. F., and Loscalzo, J. Nitrosation of tryptophan residue(s) in serum albumin and model dipeptides. *J. Biol. Chem.* **271**: 14271-14279, 1996.

Zhao, R., Lind, J., Merenyi, G., and Eriksen, T. E. Kinetics of one-electron oxidation of thiols and hydrogen abstraction by thiyl radicals from α-amino C-H bonds. *J. Am. Chem. Soc.* **116**: 12010-12015, 1994.

Ziolo, M. T., Kohr, M. J., and Wang, H. L. Nitric oxide signaling and the regulation of myocardial function. *J. Mol. Cell. Cardiol.* **45**: 625-632, 2008.